Title
Toward Perfection of Gyros! Modeling, Analysis, and Modification of Ring-Type Resonators

Author
Behbahani, Amir Hossein

Publication Date
2018

Peer reviewed|Thesis/dissertation

UNIVERSITY OF CALIFORNIA
Los Angeles

Toward Perfection of Gyros!
Modeling, Analysis, and Modification of Ring-Type Resonators

A dissertation submitted in partial satisfaction
of the requirements for the degree
Doctor of Philosophy in Mechanical Engineering

by

Amir Hossein Behbahani

2018

ABSTRACT OF THE DISSERTATION

Toward Perfection of Gyros!

Modeling, Analysis, and Modification of Ring-Type Resonators

by

Amir Hossein Behbahani

Doctor of Philosophy in Mechanical Engineering

University of California, Los Angeles, 2018

Professor Robert Thomas M'Closkey, Chair

Gyroscopes are sensors that measure the rate of rotation of an object. One common type is a "Coriolis Vibratory Gyroscope" (CVG) which takes advantage of Coriolis coupling in sensing rotation. CVGs exploit two resonant modes for measuring the sensor's angular rate of rotation. The highest sensitivity to angular motion is achieved when the resonant modes have degenerate frequencies as this configuration provides the greatest signal-to-noise ratio (SNR) with respect to extrinsic (electronic) noise sources. One way to achieve degeneracy is to design an axisymmetric resonator such as the UCLA CVG. It is impossible to retain the symmetry during manufacturing process because small fabrication errors *detune* the modes of interest. To compensate for these fabrication errors, post-processing of the resonator to recover its optimal axisymmetric configuration is required. One process, considered here, is the perturbation of the resonator's mass distribution by removing mass from specific locations. Perturbing the stiffness of the structure is not permanent, and it requires relatively large size electronics. A technique which retains wafer-scale processing and packaging compatibility is described for customizing the dynamics of individual silicon resonators. The approach uses laser ablation of a protective conformal layer (Parylene-C) to expose silicon in regions that are targeted for mass removal by subsequent deep reactive-ion etching (DRIE). The technique is demonstrated on a planar axisymmetric resonator design whereby the frequency mismatches of a subset of the resonators are reduced to less than 100 mHz which is the mechanical bandwidth of the resonator.

The model for the resonator is based on a perturbation analysis of ring dynamics which serves

as a basis for the ring-type resonators. The perturbation expansion is found for the exact solution of imperfect rings for the case in which the damping is neglected. The results show excellent agreement with both Rayleigh-Ritz and finite element results. The perturbation model is refined and modified for multi-modal tuning where both $n = 2$ and $n = 3$ are considered. The search algorithm is also improved using linear programming and a branch and bound routine. The results are successfully demonstrated on a few devices.

The damping mechanisms of this type of resonator are also studied. The thermoelastic damping which is the dominant damping mechanism in ring-type resonators is studied in detail for a ring structure. The equation of motion is derived and solved using strong form Galerkin method for imperfect rings. The imperfections studied are caused by the manufacturing processes (e.g., etch non-uniformities) and tuning the devices in practice. The analysis demonstrates a practical limitation in the tuning process where the damping asymmetries may not necessarily be removed even for the case that the frequencies are perfectly tuned. A general design guideline based on the geometry and material of the ring is presented. The temperature profile for the different materials is shown as well.

The dissertation of Amir Hossein Behbahani is approved.

Robert N. Candler

James S. Gibson

Jason L. Speyer

Robert Thomas M'Closkey, Committee Chair

University of California, Los Angeles

2018

To Maman, Baba, and Aji!

TABLE OF CONTENTS

LIST OF FIGURES

LIST OF TABLES

ACKNOWLEDGMENTS

Foremost, I would like to express my sincere gratitude to my advisor Professor Robert M'Closkey for the continuous support of my research, his patience, motivation, and immense knowledge. Professor M'Closkey molded me into a diligent researcher, helped me flourish as a student, and grow as a professional. Through his tutelage, I came to understand the value of quality over quantity! His integrity and character as a professor and adviser have set the basis for the type of academic I aspire to be.

Besides my advisor, I would like to thank the rest of my thesis committee: Professor Jason Speyer, Professor James Gibson, and Professor Robert Candler, for their support and insightful comments. I would like to thank other instructors and professors who crossed paths with me during my time at UCLA, Dr. Vinay Goyal, Dr. Robert Kinsey, Dr. Alex Golub, Professor Tsu Chin Tsao, Professor Tetsuya Iwasaki, Professor Rajit Gadh, Professor Daniel Yang, Professor Greg Carman and Professor Stanley Dong. I am also grateful to the following university staff: Angie Castillo, Evgenia Grigorova , Benjamin Tan, Abel Lebon, Lance Kono, and Marla Cooper.

I would like to thank the Nanoelectronics Research Facility at UCLA for letting me use their equipment, and Teledyne Scientific and Imaging for the fabrication of UCLA resonators especially Dr. Philip Stupar and Dr. Jeffrey DeNatale.

I will always remember my joyful experience of being the Teaching Assistant for all my students in Mechanical and Aerospace Engineering department and Center of Excellence in Engineering and Diversity. The course that I would like to single out is MAE 107, which taught me a lot regarding teaching and dealing with various situations. The students always pushed me to be a better teacher and strengthened my love for teaching.

I do not know enough ways to thank my friends at UCLA: Ali Hatamizadeh, Alireza Haji, Hossein Sharifazadeh, Sahba Aghajani, and Hamidreza Nazaripouya.

I do not know how to express my large gratitude to all of my current and past lab-mates: Dr. Dennis Kim, Michael Andonian, Stephen Schein and Howard Ge for creating a great work environment that I am going to miss for the rest of my life. I am genuinely glad I have the pleasure

to call them my peers and close friends. I enjoyed my time at UCLA working in the same lab with them. They were always ready to help even before I ask.

I am thankful to my uncles: Daie Seyf who helped me settle down in Los Angeles and Daie Aref who checks on me despite his busy schedule. I would like to express my special gratitude toward Khaleh Zinat who always ensures, no matter how far from my family I may be, I never feel homesick. Her family took me in and never let me feel alone.

Last but not least, I would like to thank my family: my mother Nini, my father Karamat, my sister Yassaman, and my brother-in-law Mohammad. My parents have always been supportive in all aspects of all life. During my time as a graduate student, their spiritual and emotional guidance has genuinely been the pillar of my success. All the meals during visits, care packages, and phone conversations (special thanks to FaceTime!) gave me all the motivation necessary to pursue my goals. Certainly, none of this was possible without my family, but this thesis is a culmination of your commitment and faith in me. And so, I dedicate this thesis to them.

The following is the line-up of the chapters in this thesis.

Chapter 1: Introduction

The first chapter is an introduction to the gyroscope, from point mass to distributed mass gyros. It introduces the concept of the lag factor and derives it for common Coriolis coupled modes used in the ring-type resonators. The chapter also discusses the importance of having perfect symmetry in the structure and mentions the symmetry cannot be achieved even from the state of the art manufacturing technology, indicating the importance of having a post-fabrication modification process. The last part of the introduction briefly describes the damping mechanisms in the ring-type resonators. The lag factor analysis is the improved version of the results from the conference paper (Analysis of the dynamics of a perturbed ring Amir H. Behbahani, Robert T. M'Closkey Inertial Sensors and Systems, 2016 IEEE International Symposium on, February 2016, Laguna Beach).

Chapter 2: Ring Dynamics

Ring dynamics has been reprinted with modifications with permission from (Frequency analysis of a uniform ring perturbed by point masses and springs, Amir H. Behbahani, Robert T. M'Closkey

Journal of Sound and Vibration, pp. 204-221. 2017) with the addition of intermediate steps and new results on connections between the analytical results and tuning process used in practice for the resonators. The orientation of the mode shapes is also discussed in more details.

Chapter 3: Wafer-Level Compensating for the Manufacturing Imperfections for $n = 2$ Modes
Compensating for the manufacturing imperfections for n = 2 modes has been reprinted with modifications with permission from (Tailored Etch Profiles for Wafer-Level Frequency Tuning of Axisymmetric Resonators, Amir H. Behbahani, Dennis Kim, Philip Stupar, Jeffrey DeNatale, Robert T. M'Closkey Journal of Microelectromechanical Systems, pp. 333-343. 2017) with the addition of more details on the etching, modification and manufacturing process.

Chapter 4: Multi-Modal Tuning
Multi-modal tuning is a version of a paper submitted for publication by Amir H. Behbahani, Howard H. Ge, Robert T. M'Closkey discussing tuning of both $n = 2$ and $n = 3$ modes simultaneously using a refined and improved model of the resonator.

Chapter 5: Damping Mechanisms
The damping mechanism is a vastly extended version of a paper submitted for publication by Amir H. Behbahani, Robert T. M'Closkey with the addition of a discussion on the dominant damping mechanisms for the resonators, the temperature profile for different modes and a design guideline based on the geometry and material.

VITA

2013	B.S. (Mechanical Engineering), Sharif University of Technology, Tehran, Iran
2015	M.S. (Mechanical Engineering), UCLA, Los Angeles, California.
2014–2018	Teaching Assistant, Mechanical and Aerospace Engineering Department, UCLA. MAE 107: Introduction to Modeling and Analysis of Dynamic Systems (10 times), MAE 171A: Dynamic Systems Control (2 times), MAE 182A: Mathematics of Engineering (1 time), MAE 103: Introduction to Fluid Mechanics (1 time).
2014–2018	Graduate Research Assistant, Mechanical and Aerospace Engineering Department, UCLA.

PUBLICATIONS

Journal Articles:

- Tailored Etch Profiles for Wafer-Level Frequency Tuning of Axisymmetric Resonators
  Amir H. Behbahani, Dennis Kim, Philip Stupar, Jeffrey DeNatale, Robert T. M'Closkey
  Journal of Microelectromechanical Systems, pp. 333-343, 2017.

- Frequency Analysis of a Uniform Ring Perturbed by Point Masses and Springs Amir H. Behbahani, Robert T. M'Closkey Journal of Sound and Vibration, pp. 204-221, 2017.

- Thermoelastic Dissipation Analysis of Imperfect Rings
  Amir H. Behbahani, Robert T. M'Closkey, submitted.

- Multi-Modal Tuning in MEMS Axisymmetric Resonators
  Amir H. Behbahani, Howard H. Ge, Robert T. M'Closkey, submitted.

- A Model-Based Approach for Modal Parameter Estimation in MEMS Resonators
  Robert T. M'Closkey, Amir H. Behbahani, under preparation.

- Adaptive Feed-Forward Cancellation of Parasitic Feedthrough Current in a MEMS Resonator
  Howard H. Ge, Amir H Behbahani, James S. Gibson, Robert T. M'Closkey, submitted.

Refereed Conference Proceedings:

- Wafer-Scale Etch Process for Precision Frequency Tuning of MEMS Gyros
  Dennis Kim, Amir H. Behbahani, Philip Stupar, Jeffrey DeNatale, Robert T. M'Closkey Inertial Sensors and Systems, 2015 IEEE International Symposium on, March 2015, Hapuna Beach, HI.

- Analysis of the Dynamics of a Perturbed Ring
  Amir H. Behbahani, Robert T. M'Closkey Inertial Sensors and Systems, 2016 IEEE International Symposium on, February 2016, Laguna Beach, CA.

- MEMS Gyro Bias Drift Mitigation by Simultaneous Operation of the $n = 2$ and $n = 3$ Modes
  Howard H. Ge, Amir H Behbahani, Robert T. M'Closkey, Position, Location and Navigation Symposium-PLANS 2018, 2018 IEEE/ION, April 2018, Monterey, CA.

- Optimal Actuation of Dynamically Driven Serial and Hybrid Flexure Systems
  Jonathan B Hopkins, Yuanping Song, Shaoyu Wang, Amir H Behbahani, Ilya Josefson, ASME 2014 International Design Engineering Technical Conferences and Computers and Information in Engineering Conference, August 2014, Buffalo, NY.

CHAPTER 1

Introduction

Nomenclature - Chapter 1

x_1, x_2	degrees of freedom fixed to the sensor case		
k	spring constant	m	size of point mass
$\omega_n = \sqrt{\frac{k}{m}}$	natural frequency		
Ω	angular rotation rate of sensor case		
t	time	θ	angular coordinate
$\dot{(\,)}$	derivative with respect to t		
f_{exc}	excitation force	f_{reb}	force to rebalance force
a_1	amplitude function of x_1	a_2	amplitude function of x_2
ϕ_1	phase function of x_1	ϕ_2	phase function of x_2
$\psi_1(t) := \omega_n t + \phi_1(t)$	phase argument for the first degree of freedom		
$\psi_2(t) := \omega_n t + \phi_2(t)$	phase argument for the second degree of freedom		
ω_0	frequency of the signal used in rate measurement		
$\underline{\mathrm{r}}$	location vector	$\underline{\mathrm{r}}$	velocity vector
$\underline{\mathrm{a}}$	acceleration vector		
$\underline{\mathrm{e}}_r$	unit vector in radial direction		
$\underline{\mathrm{e}}_\theta$	unit vector in tangential direction		
A	cross sectional area	E	modulus of elasticity
I	cross section moment of inertia	$\bar{r}$	ring mean radius
ρ	density	j	$\sqrt{-1}$
f	radial external force per unit length		
p	tangential external force per unit length		
$\mathcal{E}$	total energy	Δ	frequency split
M	mass matrix	C	damping matrix
K	stiffness matrix		

1.1 Coriolis Vibratory Gyroscopes: Point Mass Model

A sensor that measures the rate of rotation of an object is called a "gyroscope". Gyroscopes can be found everywhere, from halteres in fruit flies [BD06] to navigation systems in aircraft [YFZ17]. They are used in biomedical engineering and ergonomics [BME18, IOP17], robotics [BEF97, ZXM17], etc. One common type is a "Coriolis Vibratory Gyroscope" (CVG). In a CVG, the underlying physical principle is that a planar vibrating point mass suspended in a "cage" tends to continue vibrating along the same line even as the cage rotates about the point mass. Thus, transducers fixed to the cage measure the apparent change in orientation of the vibratory mass –see Fig. 1.1. This simplified system is often offered as the prototypical example of a CVG. Note that although the term "gyroscope" is employed, there is no spinning mass involved in this kind of sensor. The model consists of a point mass of mass m suspended in a frame or case that is allowed to rotate in the x_1-x_2 plane about an axis that is located at the center of the case. The orthogonal x_1 and x_2 degrees of freedom are fixed to the sensor case, that is, they rotate with the case. Assume the pick-off arrangement permits the measurement of x_1 and x_2. The springs are chosen so that the restoring force is isotropic for small displacements from the case center (ignoring geometric nonlinearities) and so the effective spring rate for displacements in both the x_1 and x_2 directions is regarded as k. Writing the equations of motion for the mass assuming pure rotation about the case center (no translation) yields

$$\begin{bmatrix} \ddot{x}_1 \\ \ddot{x}_2 \end{bmatrix} + 2\Omega \begin{bmatrix} 0 & -1 \\ 1 & 0 \end{bmatrix} \begin{bmatrix} \dot{x}_1 \\ \dot{x}_2 \end{bmatrix} + \begin{bmatrix} \omega_n^2 - \Omega^2 & \dot{\Omega} \\ \dot{\Omega} & \omega_n^2 - \Omega^2 \end{bmatrix} \begin{bmatrix} x_1 \\ x_2 \end{bmatrix} = \frac{1}{m} \begin{bmatrix} f_{exc} \\ f_{reb} \end{bmatrix} \tag{1.1}$$

where Ω is the (time-varying) angular rotation rate of the sensor case (counter-clockwise positive), $\dot{\Omega}$ is its time derivative and $\omega_n = \sqrt{\frac{k}{m}}$ is the natural frequency of each degree of freedom [KM12]. Further simplifications are made by assuming $\Omega, \dot{\Omega} << \omega_n$ so that the time-varying term in stiffness matrix can be dropped.

$$\begin{bmatrix} \ddot{x}_1 \\ \ddot{x}_2 \end{bmatrix} + 2\Omega \begin{bmatrix} 0 & -1 \\ 1 & 0 \end{bmatrix} \begin{bmatrix} \dot{x}_1 \\ \dot{x}_2 \end{bmatrix} + \begin{bmatrix} \omega_n^2 & 0 \\ 0 & \omega_n^2 \end{bmatrix} \begin{bmatrix} x_1 \\ x_2 \end{bmatrix} = \frac{1}{m} \begin{bmatrix} f_{exc} \\ f_{reb} \end{bmatrix} \tag{1.2}$$

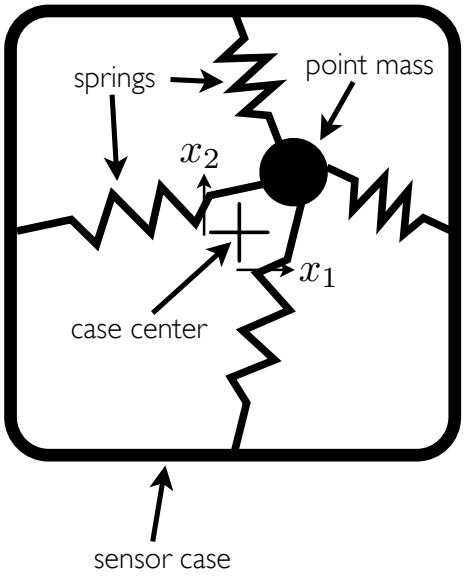

Figure 1.1: A point mass suspended by springs and attached it to the sensor case. Internal transducers measure the mass displacement or velocity in the x_1-x_2 coordinate frame (which is fixed to and rotates with the case). All motion is in-plane and it is assumed the case rotates with angular velocity Ω.

The first analysis of (1.2) reflects the so-called "whole angle mode" operation of the sensor in which the mass is allowed to move freely in the case with only the spring forces acting on it. In other words, f_{exc} and f_{reb} (excitation and force to rebalance forces) are zero. In this case, the solution of the mass position may be represented as

$$x_1(t) = a_1(t)\cos(\omega_n t + \phi_1(t)) \tag{1.3}$$

$$x_2(t) = a_2(t)\cos(\omega_n t + \phi_2(t)) \tag{1.4}$$

where a_1 and a_2 are the amplitude functions of x_1 and x_2, respectively, and ϕ_1 and ϕ_2 are the phase functions. The objective is to derive first-order differential equations for the dependent variables a_1, a_2, ϕ_1 and ϕ_2. By differentiating (1.3) and (1.4), we have

$$\dot{x}_1 = \dot{a}_1\cos(\psi_1) - a_1(\omega_n + \dot{\phi}_1)\sin(\psi_1), \tag{1.5}$$

$$\dot{x}_2 = \dot{a}_2 \cos(\psi_2) - a_2(\omega_n + \dot{\phi}_2) \sin(\psi_2), \tag{1.6}$$

where $\psi_k(t) := \omega_n t + \phi_k(t), k = 1, 2$. Following the amplitude and phase coordinate procedure, we set

$$\dot{a}_1 \cos(\psi_1) - a_1 \dot{\phi}_1 \sin(\psi_1) = 0, \tag{1.7}$$

$$\dot{a}_2 \cos(\psi_2) - a_2 \dot{\phi}_2 \sin(\psi_2) = 0, \tag{1.8}$$

which yields simplified expressions for $\dot{x}_1$ and $\dot{x}_2$,

$$\dot{x}_1 = -a_1 \omega_n \sin(\psi_1), \tag{1.9}$$

$$\dot{x}_2 = -a_2 \omega_n \sin(\psi_2), \tag{1.10}$$

Differentiating (1.9) and (1.10) and substituting into (1.2) result into the following equations.

$$-\dot{a}_1 \omega_n \sin(\psi_1) - a_1 \omega_n \dot{\phi}_1 \cos(\psi_1) + 2\Omega a_2 \omega_n \sin(\psi_2) = 0 \tag{1.11}$$

$$-\dot{a}_2 \omega_n \sin(\psi_2) - a_2 \omega_n \dot{\phi}_2 \cos(\psi_2) - 2\Omega a_1 \omega_n \sin(\psi_1) = 0 \tag{1.12}$$

By multiplying (1.7) by $+\cos(\psi_1)$ and adding it to the product of (1.11) with $\frac{-\sin(\psi_1)}{\omega_n}$, we have

$$\dot{a}_1 - 2\Omega a_2 \sin(\psi_1) \sin(\psi_2) = 0. \tag{1.13}$$

Using similar manipulation for a_2 and the phases, we conclude

$$\dot{a}_2 + 2\Omega a_1 \sin(\psi_1) \sin(\psi_2) = 0, \tag{1.14}$$

$$a_1\dot{\phi}_1 - 2\Omega a_2 \cos(\psi_1)\sin(\psi_2) = 0, \tag{1.15}$$

$$a_2\dot{\phi}_2 + 2\Omega a_1 \sin(\psi_1)\cos(\psi_2) = 0. \tag{1.16}$$

By multiplying (1.13) by a_1 and (1.14) by a_2, we have

$$a_1\dot{a}_1 - 2a_1\Omega a_2 \sin(\psi_1)\sin(\psi_2) = 0, \tag{1.17}$$

$$a_2\dot{a}_2 + 2a_2\Omega a_1 \sin(\psi_1)\sin(\psi_2) = 0. \tag{1.18}$$

Summing (1.17) and (1.18) together yields

$$a_1\dot{a}_1 + a_2\dot{a}_2 = 0, \tag{1.19}$$

which implies the norm of the amplitude is constant.

If periodic averaging is applied to (1.13) though (1.16) then the following simplified equations are derived,

$$\begin{aligned} \dot{a}_1 - \Omega a_2 \cos(\phi_2 - \phi_1) &= 0, \\ \dot{a}_2 + \Omega a_1 \cos(\phi_2 - \phi_1) &= 0, \\ a_1\dot{\phi}_1 - \Omega a_2 \sin(\phi_2 - \phi_1) &= 0, \\ a_2\dot{\phi}_2 - \Omega a_1 \sin(\phi_2 - \phi_1) &= 0. \end{aligned} \tag{1.20}$$

The later two can be manipulated to

$$a_1 a_2 \frac{\mathrm{d}}{\mathrm{d}t}(\phi_2 - \phi_1) + \Omega\left(a_2^2 + a_1^2\right)\sin(\phi_2 - \phi_1) = 0.$$

This expression is a differential equation for the difference in phases and shows that if $\phi_2(0) - \phi_1(0) = 0$, then $\phi_2(t) - \phi_1(t) = 0$ for all $t \geq 0$. In other words, $\phi_2(t) = \phi_1(t)$ which can be interpreted to mean that if the mass is set in motion along a line, it remains along that line for all

future time independent of Ω. The change in angle of the sensor case can then be inferred from the amplitudes since the first two equations in (1.20) reduce to

$$\begin{aligned} \dot{a}_1 - \Omega a_2 &= 0 \\ \dot{a}_2 + \Omega a_1 &= 0 \end{aligned} \implies \frac{\mathrm{d}}{\mathrm{d}t} \tan^{-1}\left(\frac{a_2(t)}{a_1(t)}\right) = -\Omega(t).$$

Thus, monitoring the ratio of the amplitudes yields and estimate of the change in orientation of the sensor case with respect to an initial orientation. This is what is termed "whole angle mode" and it has the advantage of measuring angles even when the sensor case experiences very large angular rates of rotation because the "physics" of the device performs the integration of angular rate into a change in angle. In practice, though, the resonator does exhibit dissipation of energy which must be replaced to sustain the oscillation on which the angle sensing mechanism depends, and it is difficult to design a replenishment strategy that does not perturb the orientation of the oscillation.

It is possible to motivate the *angular rate* sensing mode of operation with considerably less effort. Starting from (1.2), the two "actuators" are now used. The actuators produce forces along the x_1 and x_2 coordinate axes. The x_1 degree of freedom is designated the "excitation" degree of freedom and a control loop is designed whose objective is to maintain a stable harmonic oscillation of the x_1 component of the mass response. In other words, the excitation force, denoted f_{exc}, ensures that $x_1(t) = a\cos(\omega_0 t)$. There is a second controller, commonly called the "force-to-rebalance" controller, that produces the force f_{reb} along the x_2 degree of freedom. The design objective of this controller is to null, or zero out, the x_2 component of the sensor response. In other words, if we assume $x_2(t) = 0$, then

$$f_{reb}(t) = 2m\Omega(t)\dot{x}_1(t) = -2ma\omega_0\Omega(t)\sin(\omega_0 t) \tag{1.21}$$

According to (1.21), the force-to-rebalance is proportional to the Coriolis term linking two degrees of freedom. Thus, a signal proportional to Ω can be recovered by multiplying f_{reb} by measurement of $\dot{x}_1$ and then low-pass filtering the result. When noise sources are neglected the difference in modal frequencies of the two degrees of freedom has no impact on estimated angular rate signal (see Sec. 1.4).

1.2 CVG: Distributed Mass Model

There are advantages in manufacturing gyroscopes as a distributed mass instead of a point mass configuration described in Sec. 1.1. A common design of distributed mass is a ring-type resonator. In this type of resonator, the center can be constrained to be a node of vibration. Having a node at the center makes the design less susceptible to case vibrations and helps isolate the device from the environmental translational motion. The other benefit of using ring-type resonators is the symmetry that can be achieved in the design. This symmetry helps improve the signal-to-noise ratio of the sensor. On the other hand, using a design other than a point mass has its challenges as well. As opposed to the point mass case, the vibration pattern is not spatially fixed, and in fact, lags behind the structure itself. This amount of lagging is fixed for a given mode shape and needs to be calculated once. The mode shapes for the vibration must be found as well.

1.3 Lag Factor Derivation for Ring-Type Resonators

A ring resonator is the prototype structure for the many variants of planar disk resonators and, as such, can be studied to infer features associated with the dynamics of more complicated ring-like structures such as resonators in [SKS15, KBS15, CGL14] and studied in Chapters 3 and 4. The derivation presented herein is a more complete version of the derivation presented in [BM16].

For a point on the ring, the location vector $\underline{\mathrm{r}}$ can be written as

$$\underline{\mathrm{r}} = u\underline{\mathrm{e}}_r + w\underline{\mathrm{e}}_\theta, \tag{1.22}$$

where u and w are the radial and tangential displacements and $\underline{\mathrm{e}}_r$ and $\underline{\mathrm{e}}_\theta$ are the unit vectors in the radial and tangential directions, respectively (see Fig. 1.2). The ring is subject to the rotation rate Ω. Differentiating $\underline{\mathrm{r}}$ gives the velocity vector $\underline{\mathrm{v}}$.

$$\underline{\mathrm{v}} = (\dot{u} - \Omega w)\underline{\mathrm{e}}_r + (\dot{w} + \Omega u)\underline{\mathrm{e}}_\theta, \tag{1.23}$$

where the "˙" notation represents differentiation with respect to time. Differentiating (1.23) leads

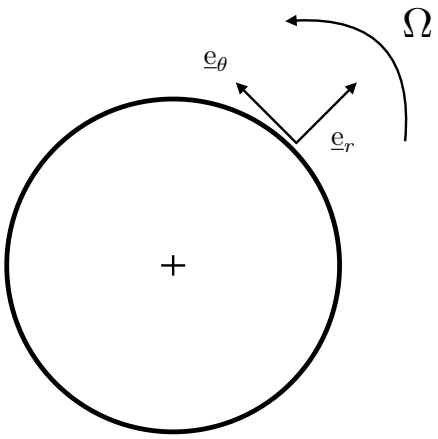

Figure 1.2: The schematic for the ring subject to the rate of rotation Ω.

to the expression for the acceleration vector $\underline{a}$ which can be written as

$$\underline{a} = (\ddot{u} - \dot{\Omega}w - 2\Omega\dot{w} - \Omega^2 u)\underline{e}_r + (\ddot{w} + \dot{\Omega}u + 2\Omega\dot{u} - \Omega^2 w)\underline{e}_\theta, \tag{1.24}$$

where $\ddot{u}$ and $\ddot{w}$ are the inertial accelerations. Assuming Ω and $\dot{\Omega}$ are small compared to $\dot{u}$, $\dot{w}$, $\ddot{u}$, and $\ddot{w}$, (1.24) can be approximated as

$$\underline{a} \approx (\ddot{u} \underbrace{-2\Omega\dot{w}}_{\text{Coriolis acceleration}})\underline{e}_r + (\ddot{w} + \underbrace{2\Omega\dot{u}}_{\text{Coriolis acceleration}})\underline{e}_\theta. \tag{1.25}$$

The accelerations caused in the radial and tangential directions due to the Coriolis effect are $-2\Omega\dot{w}$ and $2\Omega\dot{u}$, respectively.

From [Rao07] the equation of motion for a uniform, thin, inextensible ring is

$$\frac{\partial^6 w}{\partial\theta^6} + 2\frac{\partial^4 w}{\partial\theta^4} + \frac{\partial^2 w}{\partial\theta^2} + \frac{\bar{r}^4}{EI}\left(p - \frac{\partial f}{\partial\theta}\right) + \rho\frac{A\bar{r}^4}{EI}\frac{\partial^2}{\partial t^2}\left(\frac{\partial u}{\partial\theta} - w\right) = 0 \tag{1.26}$$

where $w(\theta, t)$ and $u(\theta, t)$ are the tangential and radial displacements, respectively, at angular position θ and time t, $\bar{r}$ is the ring radius, A is the ring cross-sectional area, E and I are the modulus of elasticity and moment of inertia, respectively, ρ is the ring material density and p and f are the tangential and radial external forces per unit length, respectively. The equation of motion for the ring for more general cases will be derived in Chapters 2 and 5.

To relate the equation of motion (1.26) to the forces applied to the ring from the rotation, the lag factor needs to be introduced. As opposed to the point mass case studied in Sec. 1.1, the vibration pattern is not spatially fixed when distributed mass is used. It lags behind by a certain amount depending on the mode shape. The amount of lagging is called lag factor. Lag factor for a ring was first reported by Bryan in 1890 [Bry90]. The present treatment represents a simple and intuitive derivation working from (1.26) once the Coriolis terms have been included. In particular, two "pick-off" coordinates that subtend a 45° arc are assumed, and the analysis produces the modulated amplitude equations for these coordinates. The lag factor is then readily determined from the skew-symmetric matrix in the differential equation that couples these pick-off coordinates (see Fig. 1.3).

The equation of motion of the ring in a ring-fixed frame which rotates with rate of rotation Ω with respect to an inertial frame (rotation axis is normal to the ring plane) is still given by (1.26), however, p and f are due to the Coriolis terms that appear in the ring-fixed frame and from (1.25) are given by

$$\begin{aligned} p &= 2\rho A\Omega\dot{u}, \\ f &= -2\rho A\Omega\dot{w}. \end{aligned} \tag{1.27}$$

When $\Omega = 0$ the tangential motion for the k^{th} pair of degenerate modes can be represented as

$$w(\theta, t) = (b_1 \cos(k\theta) + b_2 \sin(k\theta))\mathrm{e}^{\mathrm{j}\omega t}, \quad k = 2, 3, \ldots \tag{1.28}$$

where b_1 and b_2 are suitable constants that depend on the initial condition associated with the given pair of degenerate modes. For a nonzero rotation rate Ω, a natural extension of (1.28) is to let the constant coefficients $\{b_1, b_2\}$ vary with time,

$$w(\theta, t) = b_1(t) \cos(k\theta) + b_2(t) \sin(k\theta). \tag{1.29}$$

Note that this choice of parameterizing the ring displacement assumes that the physical pick-offs which measure the amplitudes are arranged so that they subtend the angle $90^\circ/k$. The subtended angle is 45° for $k = 2$, 30° for $k = 3$, and so forth. The fact that tangential displacement is

measured, as opposed to radial displacement which would be the case in a physical implementation, does not change the results. Using the Galerkin method (see [Mei67] and Chapter 5 for the description of the process), the equation of motion becomes

$$\begin{bmatrix} \ddot{b}_1 \\ \ddot{b}_2 \end{bmatrix} - \underbrace{\frac{4k}{k^2+1}}_{G} \Omega \underbrace{\begin{bmatrix} 0 & 1 \\ -1 & 0 \end{bmatrix}}_{S} \begin{bmatrix} \dot{b}_1 \\ \dot{b}_2 \end{bmatrix} + \underbrace{\frac{k^6 - 2k^4 + k^2}{k^2+1} \frac{EI}{\rho A \bar{r}^4}}_{\omega_0^2} \underbrace{\begin{bmatrix} b_1 \\ b_2 \end{bmatrix}}_{\boldsymbol{b}} = 0,$$

or, in compact notation,

$$\ddot{\boldsymbol{b}} - G\Omega S\dot{\boldsymbol{b}} + \omega_0^2 \boldsymbol{b} = 0. \tag{1.30}$$

When $\Omega = 0$ the two differential equations are decoupled in $\boldsymbol{b}$ coordinates and yield time harmonic solutions with frequency $\omega_0 = \sqrt{\frac{k^6-2k^4+k^2}{k^2+1}\frac{EI}{\rho A\bar{r}^4}}$ (see [Rao07] and Chapter 2). When $\Omega \neq 0$, the two equations are coupled, however, the net "energy" in the system does not change and energy is only exchanged between the modes. For example, the "strain" energy is $\frac{1}{2}\omega_0^2 \boldsymbol{b}^* \boldsymbol{b}$ and the "kinetic" energy is $\frac{1}{2}\dot{\boldsymbol{b}}^* \dot{\boldsymbol{b}}$, where $(\cdot)^*$ denotes the vector transpose. The total energy, denoted $\mathcal{E}$, is the sum of the kinetic and strain energy expressions. A simple calculation to shows $\dot{\mathcal{E}} = 0$ independent of the time history of Ω.

In order to determine how the vibration pattern (anti-node orientation) lags the case rotation we return to (1.30) and assume $\Omega(t) = \Omega_0$, i.e., constant. The constant rotation rate assumption is by no means necessary but does simplify the analysis. Consider defining a new set of coordinates, or virtual pick-offs, denoted $\boldsymbol{y} = [y_1,\, y_2]^T$ ($(\cdot)^T$ takes the transpose of the vector or matrix), that are related to the case-fixed pick-offs according to

$$\boldsymbol{b} = \underbrace{\begin{bmatrix} \cos(\Psi t) & -\sin(\Psi t) \\ \sin(\Psi t) & \cos(\Psi t) \end{bmatrix}}_{\Theta} \boldsymbol{y}.$$

Starting from $\boldsymbol{b} = \Theta \boldsymbol{y}$, we have

$$\dot{\boldsymbol{b}} = \dot{\Theta}\boldsymbol{y} + \Theta\dot{\boldsymbol{y}}, \quad \ddot{\boldsymbol{b}} = \ddot{\Theta}\boldsymbol{y} + 2\dot{\Theta}\dot{\boldsymbol{y}} + \Theta\ddot{\boldsymbol{y}}.$$

By plugging in for the expressions for $\boldsymbol{b}$, $\dot{\boldsymbol{b}}$, and $\ddot{\boldsymbol{b}}$, (1.30) can be written in terms of the new coordinate as

$$\ddot{\boldsymbol{y}} + (2\Theta^{-1}\dot{\Theta} - G\Omega\Theta^{-1}S\Theta)\dot{\boldsymbol{y}} + (\Theta^{-1}\ddot{\Theta} - G\Omega\Theta^{-1}S\dot{\Theta} + \omega_0^2\Theta^{-1}\Theta)\boldsymbol{y} = \boldsymbol{0}. \tag{1.31}$$

In order to decouple the equations represented in (1.31), the following equation must be satisfied,

$$2\Theta^{-1}\dot{\Theta} - G\Omega\Theta^{-1}S\Theta = \boldsymbol{0}. \tag{1.32}$$

Solving (1.32) leads to

$$\Psi = \frac{G}{2}\Omega = \frac{2k}{k^2+1}\Omega.$$

The expression in (1.29) can be written in terms of $\boldsymbol{y}$ as

$$w(\theta, t) = y_1 \cos(k\theta + \Psi t) + y_2 \sin(k\theta + \Psi t).$$

The "new" mode shapes are $\cos(k\theta+\Psi t)$ and $\sin(k\theta+\Psi t)$. The angle θ is measured in the rotating frame. To represent the displacements in the inertial frame, the following relationship is used

$$\theta = \Phi - \Omega t,$$

where Φ is the angle measured in the inertial frame. Now the mode shapes can be represented as

$$\begin{aligned} \cos(k\theta + \Psi t) &= \cos(k\Phi - k\Omega t + \frac{2k}{k^2+1}) = \cos(k\Phi - k\frac{k^2-1}{k^2+1}\Omega t), \\ \sin(k\theta + \Psi t) &= \sin(k\Phi - k\Omega t + \frac{2k}{k^2+1}) = \sin(k\Phi - k\frac{k^2-1}{k^2+1}\Omega t). \end{aligned} \tag{1.33}$$

The argument for cosine and sine is $k(\Phi - \frac{k^2-1}{k^2+1}\Omega t)$. Thus, the *lag factor* is defined to be

$$1 - \frac{k^2-1}{k^2+1} = \frac{2}{k^2+1}.$$

For $k = 2$, this value is $\frac{2}{5}$ or 40% (see Fig. 1.3), for $k = 3$, the lag factor is $\frac{2}{10}$ or 20%, and so forth.

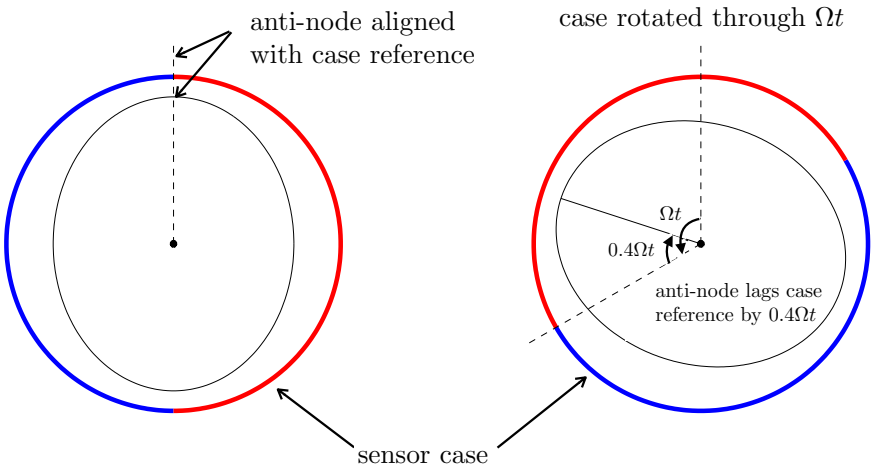

Figure 1.3: Lag factor diagram for the $k = 2$ pair of modes.

1.4 Practical Issues

The ring-type resonators can be manufactured efficiently using micro-electro-mechanical systems (MEMS) technology. During the manufacturing process, small errors break the symmetry of the structure. In practice, MEMS gyros are subjected to intrinsic noise caused by thermo-mechanical events and extrinsic noise due to thermal noise in the signal conditioning electronics. At low frequencies, the noise power spectral density (PSD) is relatively flat so integrating the rate estimate produces an angle random walk (ARW) uncertainty in the sensor orientation estimate. The ARW figure is a typical specification quoted for angular rate sensors. When noise is included in the CVG analysis, though, the difference in the natural frequencies associated with two coordinates can severely impact the sensor ARW [KM12, KM13]. The difference in the natural frequencies is caused by the imperfections that are unavoidable in the manufacturing process. Fig. 1.4 depicts the PSD for a MEMS CVG (the Boeing disk resonator gyro, or DRG) with very small frequency mismatch overlaid on the PSD associated with a 1 Hz detuning between the modal frequencies of the two companion modes. It is clear that even a 1 Hz detuning can significantly worsen the performance of the gyro. Note that the nominal modal frequencies are about 13.9 kHz. The degradation in ARW due to modal frequency detuning is perhaps the greatest motivation for fabricating

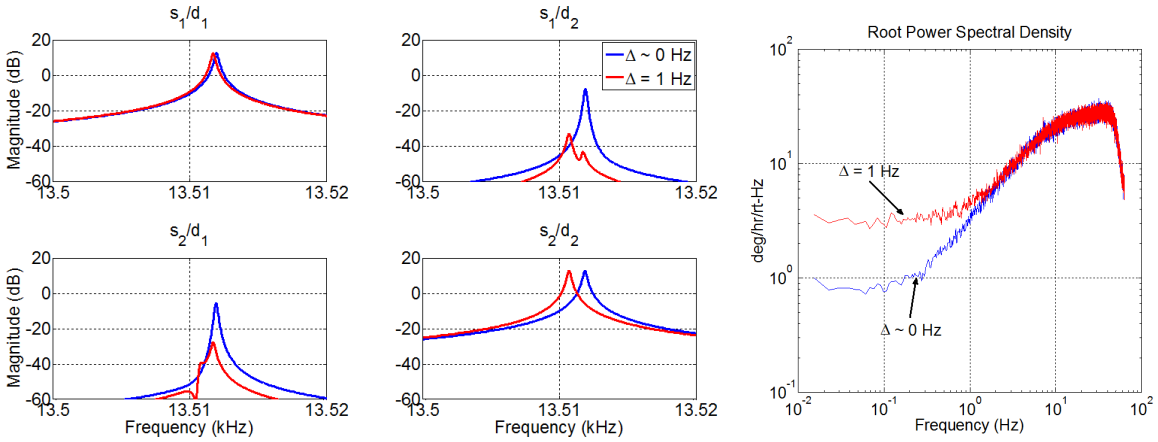

Figure 1.4: (Left) Open loop frequency response showing DRG with essentially zero detuning ($\Delta = 0$) compared to the same sensor with 1 Hz detuning ($\Delta = 1$). (Right) The low frequency angular rate PSD when $\Delta = 0$ is increased by a factor of three when $\Delta = 1$ Hz.

a symmetrically shaped MEMS CVG with inherent degenerate modal frequencies in the pair of modes that are exploited for angular rate sensing [Law98, KM12, KM13].

1.5 Compensating for Manufacturing Errors

As indicated in Sec. 1.4, the manufacturing imperfections can have a detrimental impact on the sensor's performance. So it is necessary to correct for these imperfections after the manufacturing is concluded. Modifying the dynamics of the ring-type resonators can take place by perturbing the mass and/or stiffness distribution. In a single degree-of-freedom resonator the natural frequency is given by $\omega_n = \sqrt{\frac{k}{m}}$ where m is the resonator mass, and k is the stiffness. The natural frequency can be manipulated by changing the stiffness but leaving the mass fixed [GHB05, Lel03, TSH14, KM06], changing the mass but leaving the stiffness fixed [GHB03, BBC13, KBS15, SKS15, GKM15] (see Chapters 3 and 4), or modifying both mass and stiffness.

1.5.1 Electrostatic Modification of Resonator Dynamics

The linear mechanics of a simplified CVG were given in (1.1). A more complete description of the coupled pair of modes is

$$M\ddot{x} + C\dot{x} + l\Omega S\dot{x} + Kx = f, \tag{1.34}$$

where M, C and K are real 2×2 positive definite mass, damping and stiffness matrices, respectively, S is a skew-symmetric matrix and l is the Coriolis coupling coefficient. If dedicated "tuning" electrodes are available, then the stiffness matrix is, in fact, the sum of an elastic stiffness and electrostatic stiffness. In this approach, we need to dedicate electrodes to modify K to make it a scaled version of M. The stiffness matrix can be written as the sum of a positive definite mechanical stiffness matrix, K_0, and n_e negative semi-definite electrostatic stiffness matrices, K_p, $p = 1, 2, ..., n_e$ with the corresponding bias electrode potentials, ν_p, $p = 1, 2, ..., n_e$,

$$K = K_0 + \sum_p K_p \nu_p^2. \tag{1.35}$$

In order to electrostatically "tune" the resonator, the objective is to adjust the bias voltages such that the generalized eigenvalues of M and K are equal.

The systematic electrostatic tuning problem for the Boeing DRG has been solved [KM06]. One of the challenges was how to determine the various matrices in (1.34). These parameters were determined by fitting the frequency domain version of (1.34) to the two-input/two-output empirical frequency response that can be derived from the test data described in [SKS15]. The frequency response estimates are generated at a handful of bias points so that the electrostatic stiffness matrices can be uniquely identified. Once the $\{M, K_0, K_1, \dots\}$ are known, a simple optimization problem determines the set of bias voltages to make equal modal frequencies. This approach has been successfully applied to the Boeing DRG.

Electrostatic biasing requires very stable bias voltages in practice because drift in the biases changes the resonator dynamics which in turn causes the zero rate bias signal to drift. This adds very low-frequency noise to the angular rate PSD and degrades the ARW figure. In a sense, instead of directly addressing the non-idealities in the resonator fabrication, they are accepted knowing it is possible to "fix" them, but this places stringent requirements on the biasing electronics. The electrostatic biasing approach developed in [KM06] also relies on the fact that the biases are "reversible" because once the mass and stiffness matrices are identified at fixed bias points, the correct "tuning" bias potentials are determined and then applied to the resonator. In other words, the test potentials need to be removed before the new potentials are applied.

1.5.2 Modifying the Resonator Dynamics through Mass Addition/Removal

An alternative approach for reducing the frequency detuning is to perturb the mass distribution on the resonator instead of electrostatically modifying its stiffness matrix. Changing the resonator mass distribution is permanent and reduces or eliminates the biasing support electronics. For modifying the mass matrix, we have the option to remove mass from the resonator or to add mass to the resonator. The first attempts at extending the systematic electrostatic tuning process to a mass modification scenario relied on estimating mass perturbation matrices. In other words, the stiffness matrix is now fixed, but the mass matrix is represented as

$$M = M_0 + \alpha_1 M_1 + \alpha_2 M_2 + \cdots ,$$

where M_0 represents the nominal mass matrix of the system and $\{M_1, M_2, \dots\}$ represent *perturbation matrices* that are identified after a series of mass addition experiments modify the resonator dynamics. The $\{\alpha_1, \alpha_2, \dots\}$ quantities represent the relative intensity of the perturbation (in most cases the same size mass perturbation was used for each experiment). The frequency response modeling algorithm that was developed for the electrostatic tuning was adapted for this case. The idea is that the difference in the frequency response data from one mass addition scenario to the next is due solely to changes in the resonator mass matrix. So the algorithm is forced to fit different mass matrices to each set of frequency response data while keeping the damping and stiffness matrices the same across all data sets. The procedure to reduce the frequency detuning involves determining the intensities α_k such that, again, the generalized eigenvalues of the perturbed mass matrix and stiffness matrix are equal. This procedure works quite well with large-scale axisymmetric resonators [SKS15, Sch10] but presents some problems for micro-scale resonators such as the UCLA CVG. First, it is necessary to perform *non-reversible* mass deposition experiments on the resonator to identify the perturbation matrices and, ideally, the experiments are performed in such a way that the frequency detuning is not exacerbated. Second, the intensities α_k that are computed to reduce the degree of detuning are associated with specific deposition locations on the resonator, and it is entirely possible that more mass is specified at a location than can be accommodated at that point. In other words, there was no effective way to "spread out" the added mass so that

the detuning reduction goal was realized. Finally, the modal properties of micro-scale resonators tend to exhibit fairly significant sensitivity to temperature. For this modeling process to accurately identify the perturbation matrices, the resonator would need to be tested at the same temperature for all of the frequency response tests (otherwise a gross shift in mean modal frequency due to the temperature dependence of the elastic modulus would be interpreted by the modeling algorithm to be due to the added mass). Thermal regulation of the resonator is possible but complicates the testing.

The results for tuning the modes using mass perturbations are presented in Chapters 3 and 4 and are based on the frequency analysis of imperfect rings from Chapter 2. Chapter 2 studies the effect of imperfections on a uniform ring structure. The results form a basis for the modeling used in the tuning process. Chapter 3 uses the perturbation theory and approximation methods to develop a model that can be used for tuning $n = 2$ on the wafer level. The process shown in this chapter is compatible with the other manufacturing steps since only the material is removed from the resonator. The naming convention for the modes comes from the mode shapes. For instance, for a uniform ring, the tangential and radial displacements are weighted sum of $\cos(k\theta)$ and $\sin(k\theta)$. Although the ring-type resonators are more complicated structures than uniform rings, the dominant terms in the displacements remain the same and so the name is inherited. In Chapter 4, the model is refined and a linear integer programming algorithm is used to tune both $n = 2$ and $n = 3$ modes simultaneously. The mass perturbations are applied by adding solder spheres at designated locations.

1.6 Damping Mechanisms

The problem in Sec. 1.5 does not include the effect of damping mechanisms in the structure. In general, having less damping is desirable, since this translates to a longer time constant for the sensor. Having a longer time constant is related to the "memory" of the device which means more averaging can be done, leading to more attenuation on the noise level. There are different types of damping mechanisms involved in the process such as squeeze film damping, anchor loss, and thermoelastic damping. Since the resonators ultimately operate in the vacuum, the squeeze film

damping is negligible. The anchor loss is also not significant in the ring-type structures due to the existence of a node at the stem. The thermoelastic damping, on the other hand, cannot be removed. The contributing factors in this type of damping are the design/geometry of the structure and the material. As such, researchers are switching to low-loss materials such as fused silica.

Chapter 5 takes a closer look at the effect of imperfections on the damping asymmetries of the structure. The two types of imperfections considered are width variation in the ring and point perturbations. The width variation represents the type of imperfections that can happen during the manufacturing process. The point perturbations are models for the types of corrections used in practice for tuning the devices. The results in Chapter 5 show a design guideline for different low-loss materials and modes in addition to a practical limitation in the tuning techniques. The practical limitation shows tuning the resonators using point mass perturbations does not necessarily lead to the same damping behaviors for two companion modes which can lead to damping asymmetries.

CHAPTER 2

Ring Dynamics

Nomenclature - Chapter 2

A	cross sectional area	E	modulus of elasticity
I	cross section moment of inertia	$\bar{r}$	ring mean radius
ρ	density	j	$\sqrt{-1}$
$M = 2\pi\bar{r}A\rho$	uniform ring mass		
$K = \frac{EI}{\bar{r}^3}$	nominal spring rate		
g_1	mass perturbation factor	g_2	spring perturbation factor
$\mathbb{N}(\mathbf{P})$	null space of matrix **P**	t	time
$\mathbb{R}(\mathbf{P})$	range space of matrix **P**	u	radial displacement
$\mathbb{R}(\mathbf{P})^{\perp}$	orthogonal complement of $\mathcal{R}(\mathbf{P})$	$\mathbf{v}$	weight vector
$\dim \mathcal{S}$	dimension of subspace $\mathcal{S}$	$\mathbf{v}_k$	kth term in expansion for $\mathbf{v}$
rank($\mathbf{P}$)	rank of matrix **P**	$\mathbf{v}_{k_l}$	lth partition of $\mathbf{v}_k$
$\mathbf{P}^T$	transpose of **P**	w	tangential displacement
δ	variational derivative		
$\boldsymbol{R}^n$	vector with n real elements	ϵ	perturbation parameter
$\boldsymbol{R}^{n\times m}$	$n \times m$ matrix with real elements	γ	weight vector scaling parameter
U	radial displacement eigenfunction		
W	tangential displacement eigenfunction		
$W^{(p)}$	p^{th} derivative of W with respect to θ		
$\kappa := \sqrt{\rho A\bar{r}^4/(EI)}$	time scale		
ω	frequency		
ω_k	k^{th} term in expansion for ω		
ω_{k_l}	k^{th} term in expansion for mode $l \in \{1, 2\}$		
$\mathcal{T}$	kinetic energy	$\mathcal{U}$	strain energy
$\mathcal{L} = \mathcal{T} - \mathcal{U}$	Lagrangian		
t	time	$\dot{()}$	derivative with respect to t
θ	angle coordinate		

This chapter studies the in-plane dynamics of a perturbed linearly elastic thin ring in which non-uniformities are created by point masses and massless radial springs. A perturbation approach is used to determine expansions for the natural frequencies and eigenfunctions of the exact solutions of the perturbed ring. The perturbation parameter is the point mass value normalized by the unperturbed ring mass. Massless radial springs are also included in the analysis, and their contribution relative to the point mass is quantified with an additional parameter. The perturbation results presented herein must be developed for specific scenarios, however, since the modes appear as degenerate pairs in the uniform ring, the common features among the various case studies are noted. The boundary conditions that demarcate uniform ring segments separated by the perturbation locations are developed using Hamilton's principle, and the resulting algebraic constraints on the eigenfunction weights are expanded in the perturbation parameter and sequentially solved. The case studies consider single- and two-mass perturbations and a mass-spring perturbation. Frequency expansions are developed through order-ϵ^3 and are shown to accurately predict the perturbed frequencies for large perturbations. Finite element analysis (FEA) of a thin ring is taken as the benchmark, and the results are also compared with Rayleigh-Ritz analysis using up to twenty basis functions.

Although the type of perturbations considered here seems to be quite simple, they represent a fairly accurate model of the type of modifications that can be used in practice for changing the dynamics of ring-type resonators. Studying the complete dynamics of this type of resonator is fairly complicated and impedes our full understanding of the change in their dynamics subject to non-uniformities. On the other hand, focusing on a ring as the prototype structure for the many variants of planar disk resonators can help us infer features associated with the dynamics of more complicated ring-like structures. The other issue that needs to be mentioned is the fact that the ultimate goal of the research is to use the results for making the dynamics of originally perturbed ring resonators more desirable. However, the effects of imperfections are studied on a uniform ring as the starting point for the analyses. It is not possible to uniquely figure out what the nature of perturbations was just by looking at the frequency response of a ring. But from the study of these effects on an initially uniform ring, we can learn what to do to perturb an originally imperfect ring or ring-type resonator, regardless of the nature of the imperfections, to make the dynamics more

ideal.

The in-plane equations of motion for a ring were developed more than a century ago [Bry90, Lov92], but analysis since the 1980's has focused on the dynamics of nonuniform rings because they represent more realistic structures. The analysis tool for most of these studies is the Rayleigh-Ritz method (e.g., [CP73, ASY86, Fox90, RMF01]) in which a certain number of eigenfunctions of the uniform ring are used as a solution basis. Other researchers have proposed more complicated basis functions for capturing the motion of an imperfect ring and allow general, distributed perturbations [BC07, YLY02]. For sufficiently small imperfections, many of these references also address the frequency trimming problem in which it is desired to reduce the frequency difference between a detuned pair of modes. The frequency trimming problem has recently received renewed interest from the sensor community because fabrication techniques now permit the creation of precision non-planar micro-scale resonant structures. For example, axisymmetric resonators have been recently reported [SMG14, PZT11, ZTS12, CGN12, KBK15]. The residual frequency difference after fabrication is significant enough to warrant trimming, however, for these resonators the fabrication processes are still not sufficiently developed to permit manipulation of the resonator mass distribution so no experimental trimming results have been reported. Examples in which the experimental reduction of the modal frequency differences have been achieved are given in [BBC13, SKS15, BKS17] (see Chapter 3). In [SKS15], the Rayleigh-Ritz analysis from [Fox90] was adapted to create an iterative frequency trimming procedure that employs mass deposition on a planar micro-scale resonator consisting of multiple nested rings. Using the same resonator design, a tailored etch technique has also produced trimmed devices [KBS15, BKS17] (see Chapter 3). This chapter does not address the frequency trimming procedure, however, it is shown in the case studies where the comparison with finite elements is possible that accurate prediction of the perturbed natural frequencies is achieved for large perturbations. Connections with the frequency trimming problem will be developed using FE results in Chapters 3 and 4 and will have relevance to resonators with large initial differences between the pairs of model frequencies, e.g., [TSH14]. Although only the effect of point masses and radial restoring force springs are analyzed, they are good approximations of the mass deposition, targeted etch techniques and electrostatic "springs" that have been employed to modify the dynamics of micro-scale resonators. The results are also

compared with nominal perturbations on the ring-type resonators. It should be noted that this section ignores all types of energy loss in the structure. Chapter 5 takes a closer look at different damping mechanisms in ring-type resonators.

The chapter is organized as follows. Sec. 2.1 discusses the derivation of the boundary conditions created between ring segments due to point mass or radial spring perturbations. Sec. 2.2 solves the sixth order differential equation for a uniform ring to determine the complete set of eigenfunctions. Sec. 2.3 discusses the series of algebraic problems that are derived by expanding the relations between the eigenfunction weights in the perturbation parameter and considers case studies involving single mass, dual mass, and mass-spring perturbations. Sec. 2.4 considers a thin silicon ring for the case studies and compares the perturbation results to Rayleigh-Ritz analysis and finite elements. The results are compared with a practical ring tuning problem in Sec. 2.5. The ring parameters approximate a single ring of the resonator studied in Chapters 3 and 4. Sec. 2.6 summarizes the results.

2.1 Ring Equation and Boundary Conditions

The equation of motion and boundary conditions for a uniform ring that is perturbed by a point mass and a co-located massless spring exerting a radial force are derived using Hamilton's principle. It should be noted that the damping is ignored in the derivation of the equations in this chapter. The uniform ring is defined by the parameters ρ, A, $\bar{r}$, and M which are the material density, cross-sectional area, mean radius and total mass of the ring, respectively. The ring's radial and tangential displacements, denoted $u(\theta, t)$ and $w(\theta, t)$, respectively, are dependent on the angle variable θ and the time variable t. The mass of the point-mass perturbation is $\epsilon g_1 M$, and for the boundary condition derivations its location is taken to be $\theta = 0$ without loss of generality, which is equivalent to $\theta = 2\pi$ radians due to the periodic structure of the ring (see Fig. 2.1). The spring stiffness is given by $\epsilon g_2 K$. The parameter ϵ is used to generate a perturbation expansion of the exact solution of the perturbed ring and the parameters g_1 and g_2 are used to modify the relative contributions of the perturbing mass and spring. The cases when there are more than one mass or spring perturbation can be simply extended from the analysis presented herein. Furthermore, if the

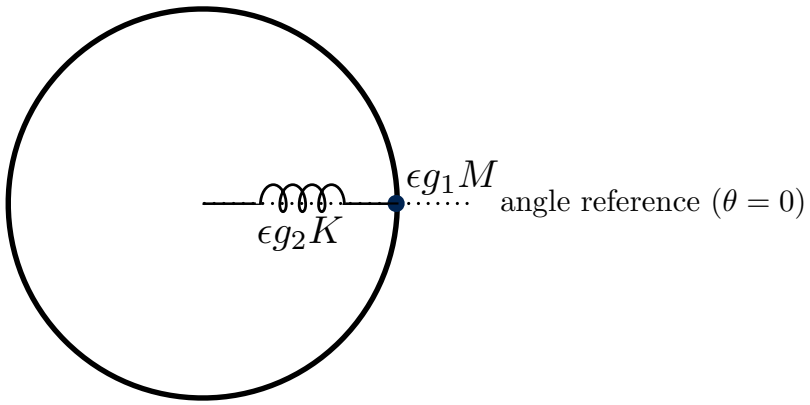

Figure 2.1: Point mass perturbation with co-located spring applied to a thin uniform ring.

mass and spring are not co-located, then g_1 or g_2 can be set to zero to obtain the desired case. The standard thin ring equation of motion governs the segments between the perturbation locations and the derived boundary conditions specify relations between the solutions for each segment. In order to apply Hamilton's principle, the kinetic and strain energies for the Lagrangian functional must be determined.

The Lagrangian functional is $\mathcal{L} = \mathcal{T} - \mathcal{U}$, where $\mathcal{T}$ and $\mathcal{U}$ are the kinetic energy and strain energy, respectively. The kinetic energy $\mathcal{T}$ is composed of the kinetic energy of the ring and the kinetic energy of the mass perturbation located at $\theta = 0$

$$\mathcal{T} = \frac{1}{2}\int_0^{2\pi} \rho A\bar{r}\left(\dot{w}^2(\theta,t) + \dot{u}^2(\theta,t)\right) \mathrm{d}r\, \mathrm{d}z + \frac{1}{2}\epsilon g_1 M\left((\dot{w}(0,t))^2 + (\dot{u}(0,t))^2\right). \tag{2.1}$$

The strain energy of the ring is computed (see [Lan49]) and summed with the strain energy of the spring,

$$\mathcal{U} = \frac{1}{2}\int_0^{2\pi} \frac{EI}{\bar{r}^3}\left(\frac{\partial^3 w}{\partial\theta^3} + \frac{\partial w}{\partial\theta}\right)^2 \mathrm{d}r\, \mathrm{d}z + \frac{1}{2}\epsilon g_2 K u^2(0,t). \tag{2.2}$$

The following small angle approximation is employed which provides a kinematic constraint between the radial and tangential velocities at a point: $u(\theta,t) = \frac{\partial w}{\partial\theta}(\theta,t)$. The derivation of the strain energy for a more complete case including the temperature effect is presented in Chapter 5. In Chapter 5, $u(\theta,t) = -\frac{\partial w}{\partial\theta}(\theta,t)$ is used instead for the sake of consistency with other references which does not ultimately affect the general results.

Hamilton's principle is applied to the Lagrangian $\mathcal{L}$ in order to derive the boundary conditions

created by a point mass and radial spring perturbation co-located at $\theta = 0^\circ$. The variation of $\mathcal{L}$ is summarized below,

$$
\begin{aligned}
&\int_{t_1}^{t_2}[-\int_0^{2\pi}\rho A\bar{r}\ddot{w}(\theta,t)\delta(w(\theta,t))\mathrm{d}r\,\mathrm{d}z \\
&-\rho A\bar{r}\frac{\partial\ddot{w}}{\partial\theta}(\theta,t)\delta(w(\theta,t))\Big|_0^{2\pi}+\int_0^{2\pi}\rho A\bar{r}\frac{\partial^2\ddot{w}}{\partial\theta^2}(\theta,t)\delta(w(\theta,t))\mathrm{d}r\,\mathrm{d}z \\
&-\epsilon g_1 M\ddot{w}(0,t)\delta(w(0,t))-\epsilon g_1 M\frac{\partial\ddot{w}}{\partial\theta}(0,t)\delta(\frac{\partial w}{\partial\theta}(0,t)) \\
&-\frac{EI}{\bar{r}^3}\left(\frac{\partial^3 w}{\partial\theta^3}\delta(\frac{\partial^2 w}{\partial\theta^2})\Big|_0^{2\pi}-\frac{\partial^4 w}{\partial\theta^4}\delta(\frac{\partial w}{\partial\theta})\Big|_0^{2\pi}+\frac{\partial^5 w}{\partial\theta^5}\delta(w)\Big|_0^{2\pi}-\int_0^{2\pi}\frac{\partial^6 w}{\partial\theta^6}\delta(w)\mathrm{d}r\,\mathrm{d}z\right) \\
&-\frac{EI}{\bar{r}^3}\left(\frac{\partial^3 w}{\partial\theta^3}\delta(w)\Big|_0^{2\pi}-\int_0^{2\pi}\frac{\partial^4 w}{\partial\theta^4}\delta(w)\mathrm{d}r\,\mathrm{d}z\right) \\
&-\frac{EI}{\bar{r}^3}\left(\frac{\partial w}{\partial\theta}\delta(\frac{\partial^2 w}{\partial\theta^2})\Big|_0^{2\pi}-\frac{\partial^2 w}{\partial\theta^2}\delta(\frac{\partial w}{\partial\theta})\Big|_0^{2\pi}+\frac{\partial^3 w}{\partial\theta^3}\delta(w)\Big|_0^{2\pi}-\int_0^{2\pi}\frac{\partial^4 w}{\partial\theta^4}\delta(w)\mathrm{d}r\,\mathrm{d}z\right) \\
&-\frac{EI}{\bar{r}^3}\left(\frac{\partial w}{\partial\theta}\delta(w)\Big|_0^{2\pi}-\int_0^{2\pi}\frac{\partial^2 w}{\partial\theta^2}\delta(w)\mathrm{d}r\,\mathrm{d}z\right) \\
&-\epsilon g_2 k\frac{\partial w}{\partial\theta}(0,t)\delta(\frac{\partial w}{\partial\theta}(0,t))]\mathrm{d}t=0.
\end{aligned}
\tag{2.3}
$$

By grouping terms associated with $\delta w(\theta,t)$, fundamental lemma of calculus of variations yields the equation of motion for the ring.

The equation of motion is

$$
-\rho A\bar{r}\ddot{w}(\theta,t)+\rho A\bar{r}\frac{\partial^2\ddot{w}}{\partial\theta^2}(\theta,t)+\frac{EI}{\bar{r}^3}(\frac{\partial^6 w}{\partial\theta^6}+2\frac{\partial^4 w}{\partial\theta^4}+\frac{\partial^2 w}{\partial\theta^2})=0, \tag{2.4}
$$

which is equivalent to the equation of motion derived from the Newtonian approach [Rao07].

The continuity of the radial and tangential motion and their derivatives at $\theta = 0$ or $\theta = 2\pi$ dictates the continuity of $u(\theta,t), \frac{\partial u}{\partial\theta}(\theta,t), w(\theta,t)$ and $\frac{\partial w}{\partial\theta}(\theta,t)$ at that point, which translates to

three essential boundary conditions

$$w(2\pi,t) = w(0,t), \tag{2.5}$$

$$\frac{\partial w}{\partial \theta}(2\pi,t) = \frac{\partial w}{\partial \theta}(0,t), \tag{2.6}$$

$$\frac{\partial^2 w}{\partial \theta^2}(2\pi,t) = \frac{\partial^2 w}{\partial \theta^2}(0,t). \tag{2.7}$$

The remaining natural boundary conditions are derived from (2.3) by gathering various terms. Noting $\delta w(0,t) = \delta w(2\pi,t)$ yields

$$-\epsilon g_1 M \ddot{w}(0,t) - \frac{EI}{\bar{r}^3}\left(\frac{\partial^5 w}{\partial \theta^5}(2\pi,t) - \frac{\partial^5 w}{\partial \theta^5}(0,t)\right) - \frac{2EI}{\bar{r}^3}\left(\frac{\partial^3 w}{\partial \theta^3}(2\pi,0) - \frac{\partial^3 w}{\partial \theta^3}(0,t)\right) = 0. \tag{2.8}$$

Furthermore, $\frac{\partial w}{\partial \theta}(0,t) = \frac{\partial w}{\partial \theta}(2\pi,t)$ implies

$$-\epsilon g_1 M \frac{\partial \ddot{w}}{\partial \theta}(0,t) - \epsilon g_2 k \frac{\partial w}{\partial \theta}(0,t) + \frac{EI}{\bar{r}^3}\left(\frac{\partial^4 w}{\partial \theta^4}(2\pi,t) - \frac{\partial^4 w}{\partial \theta^4}(0,t)\right) = 0, \tag{2.9}$$

and $\frac{\partial^2 w}{\partial \theta^2}(0,t) = \frac{\partial^2 w}{\partial \theta^2}(2\pi,t)$ implies

$$\frac{\partial^3 w}{\partial \theta^3}(2\pi,t) - \frac{\partial^3 w}{\partial \theta^3}(0,t) = 0. \tag{2.10}$$

Finally, substituting (2.10) into (2.8) simplifies the boundary condition involving the 5^{th} derivative of the tangential displacement as

$$\epsilon\omega^2 g_1 M w(0,t) - \frac{EI}{\bar{r}^3}\left(\frac{\partial^5 w}{\partial \theta^5}(2\pi,t) - \frac{\partial^5 w}{\partial \theta^5}(0,t)\right) = 0. \tag{2.11}$$

In summary, the six boundary conditions are given by (2.5), (2.6), (2.7), (2.9), (2.10) and (2.11).

Harmonic ring motion is assumed so $w(\theta,t) = W(\theta)\mathrm{e}^{\mathrm{j}\omega t}$, where W denotes the mode shape associated with natural frequency ω. The following notation is also used for the p^{th} derivative of W: $W^{(p)} = \mathrm{d}^p W/\mathrm{d}\theta^p$. The essential boundary conditions given by (2.5), (2.6) and (2.7) can be

expressed in terms of W

$$\begin{aligned} W(2\pi) - W(0) &= 0, \\ W^{(1)}(2\pi) - W^{(1)}(0) &= 0, \\ W^{(2)}(2\pi) - W^{(2)}(0) &= 0. \end{aligned} \tag{2.12}$$

The remaining natural boundary conditions given by (2.9), (2.10) and (2.11) yield

$$\begin{aligned} W^{(3)}(2\pi) - W^{(3)}(0) &= 0, \\ \epsilon\left(\omega^2 g_1 M - g_2 k\right) W^{(1)}(0) + \frac{EI}{\bar{r}^3}\left(W^{(4)}(2\pi) - W^{(4)}(0)\right) &= 0, \\ \epsilon\omega^2 g_1 M W(0) - \frac{EI}{\bar{r}^3}\left(W^{(5)}(2\pi) - W^{(5)}(0)\right) &= 0. \end{aligned} \tag{2.13}$$

2.2 Ring Eigenfunctions

The following differential equation is derived from (2.4) and may be solved for the ring eigenfunctions,

$$W^{(6)} + 2W^{(4)} + W^{(2)} + \rho A\frac{\bar{r}^4}{EI}\omega^2(W - W^{(2)}) = 0. \tag{2.14}$$

The characteristic equation associated with (2.14) is

$$\lambda^6 + 2\lambda^4 + (1 - \rho A\frac{\bar{r}^4}{EI}\omega^2)\lambda^2 + \rho A\frac{\bar{r}^4}{EI}\omega^2 = 0, \tag{2.15}$$

in which only the even powers of λ are present. A natural change of variable is $\tilde{\lambda} = \lambda^2$, which converts (2.15) into a third order equation for which closed-form solutions exist,

$$\tilde{\lambda}^3 + 2\tilde{\lambda}^2 + (1 - (\kappa\omega)^2)\tilde{\lambda} + (\kappa\omega)^2 = 0, \tag{2.16}$$

where $\kappa := \sqrt{\rho A\frac{\bar{r}^4}{EI}}$. Note that $\kappa\omega$ represents a non-dimensional frequency. The discriminant of (2.16) is

$$\Delta = 36\left(1 - (\kappa\omega)^2\right)(\kappa\omega)^2 - 32(\kappa\omega)^2 + 4\left(1 - (\kappa\omega)^2\right)^2 - 4\left(1 - (\kappa\omega)^2\right)^3 - 27(\kappa\omega)^4, \tag{2.17}$$

and has three real roots

$$(\kappa\omega)^2 = 0,$$
$$(\kappa\omega)^2 = \frac{71 \pm 17\sqrt{17}}{8}.$$

The discriminant is positive ($\Delta > 0$) when $0 < (\kappa\omega)^2 < (71 - 17\sqrt{17})/8$, or $(\kappa\omega)^2 > (71 + 17\sqrt{17})/8$, and it is negative ($\Delta < 0$) when $(71 - 17\sqrt{17})/8 < (\kappa\omega)^2 < (71 + 17\sqrt{17})/8$.

2.2.1 Eigenfunctions for $n = 2$

The sign of the discriminant determines different families of eigenfunctions, however, for the uniform thin ring, all eigenfunctions are of the form $\cos(n\theta + \psi)$, where $n = 2, 3, 4, \ldots$, and ψ is an arbitrary phase. The closed-form expression for the ring natural frequencies is $\omega^2 = \frac{n^6 - 2n^4 + n^2}{n^2+1}\frac{EI}{\rho A \bar{r}^4}$ [Rao07]. Thus, for $n = 2$, there exists a degenerate pair of modes with natural frequency $\omega_0^2 = \frac{36EI}{5\rho A\bar{r}^4}$. Substituting $(\kappa\omega_0)^2 = 36/5$ into (2.17) shows that the discriminant is negative when $n = 2$, which implies (2.16) has one real negative root and a complex conjugate pair of roots. Thus, in the perturbed ring, the six roots of (2.15) can be parameterized as $\{\pm \mathrm{j}a, \pm b \pm \mathrm{j}c\}$, where a, b and c are real-valued parameters that are dependent on the perturbed natural frequency ω. The corresponding eigenfunctions from (2.14) are given by $W(\theta) = e^{\pm \mathrm{j}a\theta}$ and $W(\theta) = e^{(\pm b \pm \mathrm{j}c)\theta}$, which can be equivalently expressed as the following set

$$\begin{aligned}
W_1(\theta) &= \cos(a\theta), & W_4(\theta) &= \cosh(b\theta)\sin(c\theta), \\
W_2(\theta) &= \sin(a\theta), & W_5(\theta) &= \sinh(b\theta)\cos(c\theta), \\
W_3(\theta) &= \cosh(b\theta)\cos(c\theta), & W_6(\theta) &= \sinh(b\theta)\sin(c\theta).
\end{aligned} \tag{2.18}$$

The perturbed natural frequencies are represented by regular perturbation expansions in the parameter ϵ, in other words,

$$\omega = \omega_0 + \epsilon\omega_1 + \epsilon^2\omega_2 + \cdots \tag{2.19}$$

Using this representation, the roots of (2.15) are also expressed as perturbation expansions. The series for the a, b and c parameters are determined to be

$$\begin{aligned}
a &= 2 + \epsilon\left(0.26001\kappa\omega_1\right) + \epsilon^2\left(-0.019181\kappa^2\omega_1^2 + 0.26001\kappa\omega_2\right) \\
&\quad + \epsilon^3\left(0.26001\kappa\omega_3 - 0.038361\kappa^2\omega_1\omega_2 + 0.0030343\kappa^3\omega_1^3\right) + \cdots, \\
b &= 1.0820 + \epsilon\left(0.19537\kappa\omega_1\right) + \epsilon^2\left(-0.025498\kappa^2\omega_1^2 + 0.19537\kappa\omega_2\right) \\
&\quad + \epsilon^3\left(0.19537\kappa\omega_3 - 0.050995\kappa^2\omega_1\omega_2 + 0.0059897\kappa^3\omega_1^3\right) + \cdots, \\
c &= 0.41330 + \epsilon\left(-0.11761\kappa\omega_1\right) + \epsilon^2\left(-0.031796\kappa^2\omega_1^2 - 0.11761\kappa\omega_2\right) \\
&\quad + \epsilon^3\left(-0.11761\kappa\omega_3 - 0.063591\kappa^2\omega_1\omega_2 - 0.0067277\kappa^3\omega_1^3\right) + \cdots.
\end{aligned} \tag{2.20}$$

Symbolic computation software is used for these calculations [Wol16].

The general solution for the perturbed ring is a weighted sum of the eigenfunctions in (2.18), in other words, $W(\theta) = \sum_{p=1}^{6} v_p W_p(\theta)$, where the set of weights $\{v_p\}$ will be determined by enforcing the constraints in (2.12) and (2.13). The process for finding these weights, and values for ω_1, ω_2 and ω_3 are described in Sec. 2.3.

2.2.2 Eigenfunctions for $n > 2$

When $n > 2$, the discriminant is positive and (2.16) has three real roots, one of which is negative. Thus, the roots of (2.15) can be parameterized as $\{\pm \mathrm{j}a, \pm b, \pm c\}$ which yields the following eigenfunctions,

$$\begin{aligned}
W_1(\theta) &= \cos(a\theta), & W_4(\theta) &= \sinh(b\theta), \\
W_2(\theta) &= \sin(a\theta), & W_5(\theta) &= \cosh(c\theta), \\
W_3(\theta) &= \cosh(b\theta), & W_6(\theta) &= \sinh(c\theta).
\end{aligned} \tag{2.21}$$

Just as for the $n = 2$ case, the parameters a, b and c can be written as a perturbation expansion in ϵ. These expansions are given in Table 2.1 for $n = 3, 4, 5$.

Table 2.1: The expansions for a, b and c for $n = 3, 4, 5$ up to order ϵ^3

$n=3$	a	$3 + \epsilon(0.16821\kappa\omega_1) + \epsilon^2(0.16821\kappa\omega_2 - 0.0048761\kappa^2\omega_1^2)$ $+\epsilon^3(0.16821\kappa\omega_3 - 0.0097522\kappa^2\omega_1\omega_2 + 0.00029030\kappa^3\omega_1^3)$
	b	$2.4328 + \epsilon(0.21262\kappa\omega_1) + \epsilon^2(0.21262\ \kappa\omega_2 - 0.010780\kappa^2\omega_1^2)$ $+\epsilon^3(0.21262\ \kappa\omega_3 - 0.021560\kappa^2\omega_1\omega_2 + 0.0012651\kappa^3\omega_1^3)$
	c	$1.0399 + \epsilon(-0.012171\kappa\omega_1) + \epsilon^2\ (-0.012171\kappa\omega_2 + 0.0029483\kappa^2\omega_1^2)$ $+\epsilon^3(-0.012171\kappa\omega_3 + 0.0058966\kappa^2\omega_1\omega_2 - 0.00067236\kappa^3\omega_1^3)$
$n=4$	a	$4 + \epsilon(0.049823\kappa\omega_1) + \epsilon^2(0.049823\ \kappa\omega_2 + 0.0027292\kappa^2\omega_1^2)$ $+\epsilon^3(0.049823\kappa\omega_3 + 0.0054584\kappa^2\omega_1\omega_2 - 0.000070159\kappa^3\omega_1^3)$
	b	$3.6028 + \epsilon(0.050394\kappa\omega_1) + \epsilon^2(0.050394\kappa\omega_2 + 0.0029990\kappa^2\omega_1^2)$ $+\epsilon^3(0.050394\kappa\omega_3 + 0.0059980\kappa^2\omega_1\omega_2 - 0.000051990\kappa^3\omega_1^3)$
	c	$1.0098 + \epsilon(-0.0029880\kappa\omega_1) + \epsilon^2(-0.0029880\kappa\omega_2 + 0.00071864\kappa^2\omega_1^2)$ $+\epsilon^3(-0.0029880\kappa\omega_3\ + 0.0014373\kappa^2\omega_1\omega_2 - 0.00016045\kappa^3\omega_1^3)$
$n=5$	a	$5 + \epsilon(0.022966\kappa\omega_1) + \epsilon^2(0.022966\kappa\omega_2 + 0.0014391\kappa^2\omega_1^2)$ $+\epsilon^3(0.022966\kappa\omega_3\ + 0.0028782\kappa^2\omega_1\omega_2 - 0.0000098823\kappa^3\omega_1^3)$
	b	$4.6896 + \epsilon(0.022918\kappa\omega_1) + \epsilon^2(0.022918\kappa\omega_2 + 0.0014626\kappa^2\omega_1^2)$ $+\epsilon^3(0.022918\kappa\omega_3\ + 0.00292522\kappa^2\omega_1\omega_2 - 0.0000067902\kappa^3\omega_1^3)$
	c	$1.0037 + \epsilon(-0.0011189\kappa\omega_1) + \epsilon^2\ (-0.0011189\kappa\omega_2 + 0.00026885\kappa^2\omega_1^2)$ $+\epsilon^3(-0.0011189\kappa\omega_3 + 0.00053770\kappa^2\omega_1\omega_2 - 0.000059818\kappa^3\omega_1^3)$

2.3 Perturbation Expansions of Solutions

This section develops perturbation expansions of the solutions for number of perturbation scenarios. The first case, a single mass perturbation and no spring perturbation, is developed in Sec. 2.3.1 for $n = 2$ and the $n = 3$ modes. Dual-mass perturbation scenarios are studied in Sec. 2.3.2 and a non co-located spring-mass perturbation is discussed in Sec. 2.3.3. The results are related to a practical problem in Sec. 2.5.

When there are $p > 0$ distinct perturbation locations, then there are p ring segments governed by (2.4), so each segment can be expressed as a sum of the appropriate eigenfunctions (either (2.18) or (2.21)) with an associated weight vector. Thus, there are $6p$ constraints generated by enforcing boundary conditions between each segment for a total of $6p$ weights. Since the weights appear linearly in the constraints, the constraint equations can be generically written as $\mathbf{A}\mathbf{v} = \mathbf{0}$ where $\mathbf{A} \in \boldsymbol{R}^{6p\times 6p}$ and the weights are collected into the vector $\mathbf{v} \in \boldsymbol{R}^{6p}$, where $\boldsymbol{R}^n$ and $\boldsymbol{R}^{n\times m}$ represent a vector with n real elements and a $n \times m$ matrix with real elements, respectively. A perturbation expansion of the expressions for the modal frequencies and eigenfunctions is derived by expanding $\mathbf{A}$ and $\mathbf{v}$ with respect to ϵ: $\mathbf{A} = \mathbf{A}_0 + \epsilon\mathbf{A}_1 + \epsilon^2\mathbf{A}_2 + \cdots$, where

$$\mathbf{A}_0 = \mathbf{A}\Big|_{\epsilon=0}, \quad \mathbf{A}_1 = \frac{\partial \mathbf{A}}{\partial \epsilon}\Big|_{\epsilon=0}, \quad \mathbf{A}_2 = \frac{1}{2}\frac{\partial^2 \mathbf{A}}{\partial \epsilon^2}\Big|_{\epsilon=0}, \ldots$$

and $\mathbf{v} = \mathbf{v}_0 + \epsilon\mathbf{v}_1 + \epsilon^2\mathbf{v}_2 + \cdots$, so

$$\left(\mathbf{A}_0 + \epsilon\mathbf{A}_1 + \epsilon^2\mathbf{A}_2 + \ldots\right)\left(\mathbf{v}_0 + \epsilon\mathbf{v}_1 + \epsilon^2\mathbf{v}_2 + \ldots\right) = \mathbf{0}. \tag{2.22}$$

$\mathbf{A}_k$ depends on frequency expansion terms ω_p, $p = 0, 1, \ldots, k$. Thus, the following set of hierar-

chical algebraic problems is solved for every perturbation scenario,

$$\mathbf{A}_0(\omega_0)\mathbf{v}_0 = \mathbf{0}, \tag{2.23}$$

$$\mathbf{A}_0(\omega_0)\mathbf{v}_1 + \mathbf{A}_1(\omega_0,\omega_1)\mathbf{v}_0 = \mathbf{0}, \tag{2.24}$$

$$\mathbf{A}_0(\omega_0)\mathbf{v}_2 + \mathbf{A}_1(\omega_0,\omega_1)\mathbf{v}_1 + \mathbf{A}_2(\omega_0,\omega_1,\omega_2)\mathbf{v}_0 = \mathbf{0}, \tag{2.25}$$

$$\mathbf{A}_0(\omega_0)\mathbf{v}_3 + \mathbf{A}_1(\omega_0,\omega_1)\mathbf{v}_2 + \mathbf{A}_2(\omega_0,\omega_1,\omega_2)\mathbf{v}_1 + \mathbf{A}_3(\omega_0,\omega_1,\omega_2,\omega_3)\mathbf{v}_0 = \mathbf{0}, \tag{2.26}$$

$$\vdots$$

The solution details depend on the particular nature of the perturbations, however, there are some features common to all cases. It is generally possible to derive closed-form expressions for ω_k by projecting the columns of $\mathbf{A}_k$ onto the orthogonal complements, or the intersections thereof, of the subspaces $\{\mathbb{R}(\mathbf{A}_0), \mathbb{R}(\mathbf{A}_1), \ldots, \mathbb{R}(\mathbf{A}_{k-1})\}$ ($\mathbb{R}(\cdot)$ represents the range space), and then selecting ω_k so that these projected components are zero. For example, the unperturbed ring possesses degenerate pairs of modes so $\dim \mathbb{R}(\mathbf{A}_0)^\perp = 2$ ($\mathbb{R}(\cdot)^\perp$ is the orthogonal complement of the matrix) and $\dim \mathbb{N}(\mathbf{A}_0) = 2$, ($\mathbb{N}(\cdot)$ represents the null space and $dim(\cdot)$ is the dimension of the subspace) independent of the number of perturbations. In the case studies that follow, basis vectors for $\mathbb{R}(\mathbf{A}_0)^\perp$ are represented by the two columns of $\mathbf{P}_0$. Multiplying (2.24) on the left by $\mathbf{P}_0^T$ ($(\cdot)^T$ is the transpose of the vector or the matrix) and restricting $\mathbf{v}_0$ to $\mathbb{N}(\mathbf{A}_0)$ yields a 2×2 matrix whose determinant must be zero. The entries of this matrix are affine in ω_1 because the elements of $\mathbf{A}_1$ are affine functions of ω_1. Thus, simple expressions can be derived for determining ω_1. In fact, as $\mathbf{A}_k$ is an affine function of ω_k, expressions for ω_k are at most quadratic. In the case studies that follow, the natural frequency expansions are computed through order ϵ^3.

2.3.1 Single Mass Perturbations

Consider the case of a single point mass perturbation ($g_1 = 1$, $g_2 = 0$) located at $\theta = 0$. For the $n = 2$ modes, the constraints in (2.12) and (2.13) yield six equations for the six to-be-determined

weights $\{v_1, \ldots, v_6\}$ associated with the $n = 2$ eigenfunctions as shown below

$$\begin{aligned}
&\sum_p v_p \left(W_p(2\pi) - W_p(0)\right) = 0, \qquad &&\sum_p v_k \left(W_p^{(1)}(2\pi) - W_p^{(1)}(0)\right) = 0,\\
&\sum_p v_p \left(W_p^{(2)}(2\pi) - W_p^{(2)}(0)\right) = 0, \qquad &&\sum_p v_k \left(W_p^{(3)}(2\pi) - W_p^{(3)}(0)\right) = 0,\\
&\sum_p v_p \left(\epsilon M\omega^2 W_p^{(1)}(0) + \frac{EI}{\bar{r}^3}\left(W_p^{(4)}(2\pi) - W_p^{(4)}(0)\right)\right) = 0,\\
&\sum_p v_p \left(\epsilon M\omega^2 W_p(0) - \frac{EI}{\bar{r}^3}\left(W_p^{(5)}(2\pi) - W_p^{(5)}(0)\right)\right) = 0.
\end{aligned} \tag{2.27}$$

In this case, $\mathbf{A} \in \boldsymbol{R}^{6\times 6}$ matrix derived from (2.27) and $\mathbf{v} = [v_1, \ldots, v_6]^T \in \boldsymbol{R}^6$ is the non-zero weight vector. For example, when the eigenfunctions are defined as shown in (2.18), the first row of $\mathbf{A}$ is determined from the first expression in (2.27)

$$\Big[1 - \cos(2\pi a), \quad -\sin(2\pi a), \quad 1 - \cosh(2\pi b)\cos(2\pi c), \quad -\cosh(2\pi b)\sin(2\pi c),$$
$$-\sinh(2\pi b)\cos(2\pi c), \quad -\sinh(2\pi b)\sin(2\pi c)\Big].$$

The second row of A is determined from the second expression in (2.27)

$$\begin{aligned}
\big[a\sin(2\pi a),\ a - a\cos(2\pi a), &\, c\cosh(2\pi b)\sin(2\pi c) - b\cos(2\pi c)\sinh(2\pi b),\\
&c - c\cos(2\pi c)\cosh(2\pi b) - b\sin(2\pi c)\sinh(2\pi b),\\
&b - b\cos(2\pi c)\cosh(2\pi b) + c\sin(2\pi c)\sinh(2\pi b),\\
&-b\cosh(2\pi b)\sin(2\pi c) - c\cos(2\pi c)\sinh(2\pi b)\big].
\end{aligned}$$

The remaining rows of A are determined from (2.27), but these expressions are too lengthy to include here. As noted in Sec. 2.2, the parameters a, b and c are functions of ϵ because they are related to the roots of the perturbed characteristic polynomial (see (2.20)). Symbolic calculation yields the matrices $\mathbf{A}_0$, $\mathbf{A}_1$, $\mathbf{A}_2, \ldots$, but because of their structure, it is useful to partition these matrices as follows: $\mathbf{A}_k = \begin{bmatrix}\mathbf{A}_{k_1} & \mathbf{A}_{k_2}\end{bmatrix}$, $k = 0, 1, 2, \ldots$, where the $\mathbf{A}_{k_1} \in \boldsymbol{R}^{6\times 2}$ and $\mathbf{A}_{k_2} \in \boldsymbol{R}^{6\times 4}$.

Similarly, $\mathbf{v}_k$ are partitioned into

$$\mathbf{v}_k = \begin{bmatrix} \mathbf{v}_{k_1} \\ \mathbf{v}_{k_2} \end{bmatrix}, \ k = 0, 1, 2, \ldots$$

which are compatible with the partitions of $\mathbf{A}_k$. The analysis is general in the sense that the computed matrices $\mathbf{A}_k$ are common to all thin ring problems with a single mass perturbation in which the non-dimensional frequency parameters $\{\kappa\omega_0, \kappa\omega_1, \ldots\}$ are used. Thus, these computations need only be performed once to the desired accuracy.

The partitions of $\mathbf{A}_0$ (see (2.28)) are constant since they are functions of the known parameter $\kappa\omega_0 = \sqrt{36/5}$. The partitions $\mathbf{A}_{0_1}$ and $\mathbf{A}_{0_2}$ are

$$\mathbf{A}_{0_1} = \begin{bmatrix} 0 & 0 \\ 0 & 0 \\ 0 & 0 \\ 0 & 0 \\ 0 & 0 \\ 0 & 0 \end{bmatrix}, \quad \mathbf{A}_{0_2} = \begin{bmatrix} 384.45 & -232.32 & 383.45 & -232.32 \\ 510.93 & -92.486 & 512.01 & -92.900 \\ 592.24 & 110.65 & 591.24 & 111.54 \\ 594.02 & 365.47 & 594.73 & 364.09 \\ 492.47 & 639.47 & 492.28 & 641.26 \\ 268.37 & 897.41 & 267.85 & 895.39 \end{bmatrix}. \tag{2.28}$$

Since rank $(\mathbf{A}_{0_2}) = 4$, the first constraint, (2.23), yields $\mathbf{v}_{0_2} = \mathbf{0}$, $\mathbf{v}_{0_1}$ is undetermined. The next set of constraints, (2.24), yields

$$\begin{bmatrix} \mathbf{0} & \mathbf{A}_{0_2} \end{bmatrix} \begin{bmatrix} \mathbf{v}_{1_1} \\ \mathbf{v}_{1_2} \end{bmatrix} + \begin{bmatrix} \mathbf{A}_{1_1} & \mathbf{A}_{1_2} \end{bmatrix} \begin{bmatrix} \mathbf{v}_{0_1} \\ \mathbf{0} \end{bmatrix} = \mathbf{0} \implies \begin{bmatrix} \mathbf{A}_{1_1} & \mathbf{A}_{0_2} \end{bmatrix} \begin{bmatrix} \mathbf{v}_{0_1} \\ \mathbf{v}_{1_2} \end{bmatrix} = \mathbf{0}, \tag{2.29}$$

where the known zero partitions have been inserted. Let the columns of $\mathbf{P}_0 \in \boldsymbol{R}^{6\times 2}$ span $\mathbb{R}(\mathbf{A}_{0_2})^{\perp}$. Singular value decompositions are used to determine $\mathbb{R}(\cdot)$, $\mathbb{R}(\cdot)^{\perp}$ and $\mathbb{N}(\cdot)$ where required. Anal-

ysis of $\mathbf{A}_0$ yields

$$\mathbf{P}_0 = \begin{bmatrix} -0.37374 & -0.50351 \\ 0.50351 & -0.37374 \\ 0.41527 & 0.55946 \\ -0.55946 & 0.41527 \\ -0.20763 & -0.27973 \\ 0.27973 & -0.20763 \end{bmatrix}. \tag{2.30}$$

The partitions of $\mathbf{A}_1$ are

$$\mathbf{A}_{1_1} = \begin{bmatrix} 0 & -1.6337\kappa\omega_1 \\ 3.2674\kappa\omega_1 & 0 \\ 0 & 6.5347\kappa\omega_1 \\ -13.069\kappa\omega_1 & 0 \\ 0 & -26.139\kappa\omega_1 - 90.478 \\ 52.278\kappa\omega_1 + 45.239 & 0 \end{bmatrix}, \tag{2.31}$$

and

$$\mathbf{A}_{1_2} = \begin{bmatrix} 299.02\kappa\omega_1 & -568.54\kappa\omega_1 & 299.02\kappa\omega_1 & -568.54\kappa\omega_1 \\ 606.13\kappa\omega_1 & -582.20\kappa\omega_1 & 606.32\kappa\omega_1 & -582.08\kappa\omega_1 \\ 985.84\kappa\omega_1 & -457.56\kappa\omega_1 & 985.33\kappa\omega_1 & -457.65\kappa\omega_1 \\ 1383.8\kappa\omega_1 & -135.61\kappa\omega_1 & 1384.7\kappa\omega_1 & -135.78\kappa\omega_1 \\ 1713.5\kappa\omega_1 & 426.28\kappa\omega_1 - 18.697 & 1712.3\kappa\omega_1 - 48.951 & 427.02\kappa\omega_1 \\ 1848.0\kappa\omega_1 + 45.239 & 1237.6\kappa\omega_1 & 1849.3\kappa\omega_1 & 1236.0\kappa\omega_1 \end{bmatrix}. \tag{2.32}$$

Left-multiplication of (2.29) by $\mathbf{P}_0^T$ yields $\mathbf{P}_0^T\mathbf{A}_{1_1}\mathbf{v}_{0_1} = \mathbf{0}$, where

$$\mathbf{P}_0^T\mathbf{A}_{1_1} = \begin{bmatrix} 12.655 + 23.581\kappa\omega_1 & 18.786 + 8.7515\kappa\omega_1 \\ -9.3931 - 17.503\kappa\omega_1 & 25.309 + 11.790\kappa\omega_1 \end{bmatrix},$$

and where $\mathbf{P}_0$ and $\mathbf{A}_{1_1}$ are given by (2.30) and (2.31), respectively. Non-trivial $\mathbf{v}_{0_1}$ will exist at

those values of $\kappa\omega_1$ where $\det\left(\mathbf{P}_0^T\mathbf{A}_{1_1}\right) = \mathbf{0}$ ($\det(\cdot)$ is the determinant of the matrix). These values, denoted $\kappa\omega_{1_1}$ and $\kappa\omega_{1_2}$, are

$$\kappa\omega_{1_1} = -2.1466, \quad \kappa\omega_{1_2} = -0.53665. \tag{2.33}$$

At these two values of $\kappa\omega_1$, rank $\left(\begin{bmatrix}\mathbf{A}_{1_1} & \mathbf{A}_{0_2}\end{bmatrix}\right) = 5$, so solutions for $\mathbf{v}_{0_1}$ and $\mathbf{v}_{1_2}$, denoted $\tilde{\mathbf{v}}_{0_1}$ and $\tilde{\mathbf{v}}_{1_2}$, respectively, are unique up to a scaling,

$$\begin{aligned}
\kappa\omega_{1_1} = -2.1466 \implies \tilde{\mathbf{v}}_{0_1} = \begin{bmatrix}0\\1\end{bmatrix}, \quad \tilde{\mathbf{v}}_{1_2} = \begin{bmatrix}-1.7534 & -9.7813 & 1.7614 & 9.8020\end{bmatrix}^T, \\
\kappa\omega_{1_2} = -0.53665 \implies \tilde{\mathbf{v}}_{0_1} = \begin{bmatrix}1\\0\end{bmatrix}, \quad \tilde{\mathbf{v}}_{1_2} = \begin{bmatrix}-2.2170 & -3.6827 & 2.2169 & 3.6731\end{bmatrix}^T.
\end{aligned} \tag{2.34}$$

The $\tilde{\mathbf{v}}_{0_1}$ partitions are normalized to unit length and this sets the scaling for all subsequent elements of the series for the weight vector. Note that the leading order terms imply that the tangential motion for a perturbation at $\theta = 0$ are close to $\sin(2\theta)$ and $\cos(2\theta)$. Thus, one radial anti-node is essentially aligned with the perturbation location at $\theta = 0°$, and the other anti-node is located near $45°$.

The perturbed natural frequencies up to order ϵ^2 can be computed from (2.25), rewritten below with the partitions,

$$\begin{bmatrix}\mathbf{0} & \mathbf{A}_{0_2}\end{bmatrix}\begin{bmatrix}\mathbf{v}_{2_1}\\ \mathbf{v}_{2_2}\end{bmatrix} + \begin{bmatrix}\mathbf{A}_{1_1} & \mathbf{A}_{1_2}\end{bmatrix}\begin{bmatrix}\mathbf{v}_{1_1}\\ \tilde{\mathbf{v}}_{1_2}\end{bmatrix} + \begin{bmatrix}\mathbf{A}_{2_1} & \mathbf{A}_{2_2}\end{bmatrix}\begin{bmatrix}\tilde{\mathbf{v}}_{0_1}\\ \mathbf{0}\end{bmatrix} = \mathbf{0}.$$

The unknown weights $\mathbf{v}_{2_2}$ and $\mathbf{v}_{1_1}$ are gathered into a single vector as follows,

$$\begin{bmatrix}\mathbf{A}_{1_1} & \mathbf{A}_{0_2}\end{bmatrix}\begin{bmatrix}\mathbf{v}_{1_1}\\ \mathbf{v}_{2_2}\end{bmatrix} + \begin{bmatrix}\mathbf{A}_{2_1} & \mathbf{A}_{1_2}\end{bmatrix}\begin{bmatrix}\tilde{\mathbf{v}}_{0_1}\\ \tilde{\mathbf{v}}_{1_2}\end{bmatrix} = \mathbf{0}. \tag{2.35}$$

Since rank $\left(\begin{bmatrix}\mathbf{A}_{1_1} & \mathbf{A}_{0_2}\end{bmatrix}\right) = 5$ when $\omega_1 = \{\omega_{1_1}, \omega_{1_2}\}$, let $\mathbf{P}_1 \in \boldsymbol{R}^6$ span $\mathbb{R}\left(\begin{bmatrix}\mathbf{A}_{1_1} & \mathbf{A}_{0_2}\end{bmatrix}\right)^{\perp}$ when $\kappa\omega_1$

is selected as either value in (2.33). Left-multiplying (2.35) by $\mathbf{P}_1^T$ yields

$$\mathbf{P}_1^T \begin{bmatrix} \mathbf{A}_{2_1} & \mathbf{A}_{1_2} \end{bmatrix} \begin{bmatrix} \tilde{\mathbf{v}}_{0_1} \\ \tilde{\mathbf{v}}_{1_2} \end{bmatrix} = 0. \tag{2.36}$$

When $\kappa\omega_{1_1} = -2.1466$, (2.36) yields $\kappa\omega_{2_1} = 3.9104$, and when $\kappa\omega_{1_2} = -0.53666$ it yields $\kappa\omega_{2_2} = 1.2159$. Expressions for both values of frequency deviations for $\mathbf{P}_1$ and $\mathbf{A}_{2_1}$ are given in (2.37), (2.38), and (2.39), respectively. The orthogonal complements of $\mathbb{R}\left(\begin{bmatrix}\mathbf{A}_{1_1} & \mathbf{A}_{0_2}\end{bmatrix}\right)$ are given by

$$\mathbf{P}_1 = \begin{bmatrix} 0 & 0.62706 & 0 & -0.69673 & 0 & 0.34837 \end{bmatrix}^T \text{ when } \kappa\omega_{1_1} = -2.1466, \tag{2.37}$$

and

$$\mathbf{P}_1 = \begin{bmatrix} 0 & 0.62706 & 0 & -0.69673 & 0 & 0.34837 \end{bmatrix}^T \text{ when } \omega_{1_2} = -0.53666. \tag{2.38}$$

The first two columns of matrix $\mathbf{A}_2$ are grouped into one sub-matrix $\mathbf{A}_{2_1}$ and is a function of the first two deviation terms in the frequency expansion $\kappa\omega_1$ and $\kappa\omega_2$.

$$\mathbf{A}_{2_1} = \begin{bmatrix} 2.6689(\kappa\omega_1)^2 & 0.24103(\kappa\omega_1)^2 - 3.2674\kappa\omega_2 \\ 0.36748(\kappa\omega_1)^2 + 6.5347\kappa\omega_2 & 5.3378(\kappa\omega_1)^2 \\ -10.676(\kappa\omega_1)^2 & 2.4340(\kappa\omega_1)^2 + 13.069\kappa\omega_2 \\ -8.2662(\kappa\omega_1)^2 - 26.139\kappa\omega_2 & -21.351(\kappa\omega_1)^2 \\ 42.703(\kappa\omega_1)^2 & -23.329(\kappa\omega_1)^2 - 158.40\kappa\omega_1 - 52.278\kappa\omega_2 \\ 60.250(\kappa\omega_1)^2 + 67.438\kappa\omega_1 + 104.56\kappa\omega_2 & 85.405(\kappa\omega_1)^2 \end{bmatrix} \tag{2.39}$$

The partitions $\mathbf{A}_{2_2}$ and $\mathbf{A}_{3_1}$ are necessary for computing the perturbed frequencies through ϵ^3, but due to their lengthly nature, they are not included in this section.

Solutions for $[\mathbf{v}_{1_1} \;\; \mathbf{v}_{2_2}]^T$ can now be determined from (2.35). Although they are not unique, they can be expressed as a unique *least norm* solution, denoted $[\tilde{\mathbf{v}}_{1_1} \;\; \tilde{\mathbf{v}}_{2_2}]^T$, plus an arbitrary vector in $\mathbb{N}\left(\begin{bmatrix}\mathbf{A}_{1_1} & \mathbf{A}_{0_2}\end{bmatrix}\right)$. From (2.29), a vector that spans the null space of this matrix is $[\tilde{\mathbf{v}}_{0_1} \;\; \tilde{\mathbf{v}}_{1_2}]^T$. Thus,

the eigenfunction weights satisfying (2.35) are

$$\begin{bmatrix} \mathbf{v}_{1_1} \\ \mathbf{v}_{2_2} \end{bmatrix} = \begin{bmatrix} \tilde{\mathbf{v}}_{1_1} \\ \tilde{\mathbf{v}}_{2_2} \end{bmatrix} + \gamma \begin{bmatrix} \tilde{\mathbf{v}}_{0_1} \\ \tilde{\mathbf{v}}_{1_2} \end{bmatrix}, \tag{2.40}$$

where γ is a real parameter. The least norm solution associated with $\kappa\omega_{1_1}$ is

$$\begin{bmatrix} \tilde{\mathbf{v}}_{1_1} \\ \tilde{\mathbf{v}}_{2_2} \end{bmatrix} = \begin{bmatrix} 1.7535 & 2.5193 & -1.5010 & 0.43081 & 1.4858 & -0.36263 \end{bmatrix}^T,$$

and the least norm solution associated with $\kappa\omega_{1_2}$ is

$$\begin{bmatrix} \tilde{\mathbf{v}}_{1_1} \\ \tilde{\mathbf{v}}_{2_2} \end{bmatrix} = \begin{bmatrix} 2.3833 & -0.43836 & -0.30261 & 0.50506 & 0.30756 & -0.51076 \end{bmatrix}^T.$$

The frequency expansion is computed up to ϵ^3 since this will yield accurate estimates of the perturbed modal frequencies even for relatively large perturbations. Expanding (2.26) into its partitions yields,

$$\begin{aligned} \begin{bmatrix} \mathbf{0} & \mathbf{A}_{0_2} \end{bmatrix} \begin{bmatrix} \mathbf{v}_{3_1} \\ \mathbf{v}_{3_2} \end{bmatrix} + \begin{bmatrix} \mathbf{A}_{1_1} & \mathbf{A}_{1_2} \end{bmatrix} \begin{bmatrix} \mathbf{v}_{2_1} \\ \tilde{\mathbf{v}}_{2_2} + \gamma\tilde{\mathbf{v}}_{1_2} \end{bmatrix} \\ + \begin{bmatrix} \mathbf{A}_{2_1} & \mathbf{A}_{2_2} \end{bmatrix} \begin{bmatrix} \tilde{\mathbf{v}}_{1_1} + \gamma\tilde{\mathbf{v}}_{0_1} \\ \tilde{\mathbf{v}}_{12} \end{bmatrix} + \begin{bmatrix} \mathbf{A}_{3_1} & \mathbf{A}_{3_2} \end{bmatrix} \begin{bmatrix} \tilde{\mathbf{v}}_{0_1} \\ \mathbf{0} \end{bmatrix} = \mathbf{0}. \end{aligned} \tag{2.41}$$

The unknown weights are $\mathbf{v}_{3_1}$, $\mathbf{v}_{3_2}$, and $\mathbf{v}_{2_1}$. Furthermore, $\mathbf{A}_{3_1}$ and $\mathbf{A}_{3_2}$ are functions of $\kappa\omega_3$. Left-multiplying (2.41) by $\mathbf{P}_1^T$ (for a particular value of $\kappa\omega_1$), eliminates $\mathbf{v}_{3_1}$, $\mathbf{v}_{3_2}$ and $\mathbf{v}_{2_1}$ and produces an expression that is only a function of $\kappa\omega_3$,

$$\mathbf{P}_1^T\mathbf{A}_{1_2}\tilde{\mathbf{v}}_{2_2} + \mathbf{P}_1^T\mathbf{A}_{2_1}\tilde{\mathbf{v}}_{1_1} + \gamma\underbrace{\mathbf{P}_1^T\left(\mathbf{A}_{1_2}\tilde{\mathbf{v}}_{1_2} + \mathbf{A}_{2_1}\tilde{\mathbf{v}}_{0_1}\right)}_{=0,\text{ per (2.36)}} + \mathbf{P}_1^T\mathbf{A}_{2_2}\mathbf{v}_{12} + \mathbf{P}_1^T\mathbf{A}_{3_1}\mathbf{v}_{0_1} = 0. \tag{2.42}$$

Although $\mathbf{A}_{2_2}$ and $\mathbf{A}_{3_1}$ are required to compute this expression, they are not given here due to their length. Nevertheless, (2.42) is affine in $\kappa\omega_3$, and when $\kappa\omega_{1_1} = -2.1466$ and $\kappa\omega_{2_1} = 3.9104$, (2.42)

yields $\kappa\omega_{3_1} = -6.0317$. Similarly, when $\kappa\omega_{1_2} = -0.53665$ and $\kappa\omega_{2_2} = 1.2159$, (2.42) yields $\kappa\omega_{3_2} = -2.7520$. Gathering the frequency terms yields the following expansions

$$\begin{aligned}\kappa\omega &= \sqrt{\frac{36}{5}} + \epsilon(-2.1466) + \epsilon^2(3.9104) + \epsilon^3(-6.0317) + \cdots, \\ \kappa\omega &= \sqrt{\frac{36}{5}} + \epsilon(-0.53665) + \epsilon^2(1.2159) + \epsilon^3(-2.7520) + \cdots.\end{aligned} \tag{2.43}$$

The role of γ will now be clarified in (2.40). Note that left-multiplication of (2.41) by $\mathbf{P}_1^T$ eliminated $\mathbf{v}_{3_1}$, $\mathbf{v}_{3_2}$, γ, and $\mathbf{v}_{2_1}$. Define $\mathbf{P}_2 \in \boldsymbol{R}^6$ such that $\mathbf{P}_1$ and $\mathbf{P}_2$ form a basis for $\mathbb{R}(\mathbf{A}_{0_2})^\perp$ (this subspace is also spanned by the columns of $\mathbf{P}_0$). Then, left-multiplication of (2.41) by $\mathbf{P}_2^T$ also eliminates $\mathbf{v}_{3_1}$ and $\mathbf{v}_{3_2}$ but yields a relation between γ and unknown vector $\mathbf{v}_{2_1}$,

$$\mathbf{P}_2^T\mathbf{A}_{1_1}\mathbf{v}_{2_1} + \mathbf{P}_2^T\left(\mathbf{A}_{1_2}\tilde{\mathbf{v}}_{2_2} + \mathbf{A}_{2_1}\tilde{\mathbf{v}}_{1_1} + \mathbf{A}_{2_2}\tilde{\mathbf{v}}_{1_2} + \mathbf{A}_{3_1}\tilde{\mathbf{v}}_{0_1}\right) + \gamma\mathbf{P}_2^T\left(\mathbf{A}_{1_2}\tilde{\mathbf{v}}_{1_2} + \mathbf{A}_{2_1}\tilde{\mathbf{v}}_{0_1}\right) = 0. \tag{2.44}$$

The solution for $\mathbf{v}_{2_1}$ can be written as a function of two parameters. First, let $\tilde{\mathbf{v}}_{2_1}$ represent the least-norm solution to (2.44) when $\gamma = 0$, that is, $\tilde{\mathbf{v}}_{2_1}$ satisfies

$$\mathbf{P}_2^T\mathbf{A}_{1_1}\tilde{\mathbf{v}}_{2_1} + \mathbf{P}_2^T\left(\mathbf{A}_{1_2}\tilde{\mathbf{v}}_{2_2} + \mathbf{A}_{2_1}\tilde{\mathbf{v}}_{1_1} + \mathbf{A}_{2_2}\tilde{\mathbf{v}}_{1_2} + \mathbf{A}_{3_1}\tilde{\mathbf{v}}_{0_1}\right) = 0. \tag{2.45}$$

It can be shown that the dimension of $\mathbb{N}(\mathbf{P}_2^T\mathbf{A}_{1_1})$ is one, so let $\mathbf{u}$ be its basis vector. All $\mathbf{v}_{2_1}$ solutions of (2.45) can be expressed as $\tilde{\mathbf{v}}_{2_1} + \tilde{\alpha}\mathbf{u}$, where $\tilde{\alpha}$ is a free parameter. If $\gamma \neq 0$, then $\tilde{\mathbf{v}}_{2_1} + \tilde{\alpha}\mathbf{u} + \gamma\tilde{\mathbf{v}}_{1_1}$ satisfies (2.44) because

$$\mathbf{P}_2^T\left(\mathbf{A}_{1_1}\tilde{\mathbf{v}}_{1_1} + \mathbf{A}_{1_2}\tilde{\mathbf{v}}_{1_2} + \mathbf{A}_{2_1}\tilde{\mathbf{v}}_{0_1}\right) = 0. \tag{2.46}$$

This is shown by first noting $\mathbf{P}_2^T\mathbf{A}_{1_1}\tilde{\mathbf{v}}_{0_1} = \mathbf{0}$. Then, left-multiplying (2.35) by $\mathbf{P}_2^T$,

$$\begin{aligned}&\mathbf{P}_2^T\begin{bmatrix}\mathbf{A}_{1_1} & \mathbf{A}_{0_2}\end{bmatrix}\begin{bmatrix}\tilde{\mathbf{v}}_{1_1} + \gamma\tilde{\mathbf{v}}_{0_1} \\ \tilde{\mathbf{v}}_{2_2} + \gamma\tilde{\mathbf{v}}_{1_2}\end{bmatrix} + \mathbf{P}_2^T\begin{bmatrix}\mathbf{A}_{2_1} & \mathbf{A}_{1_2}\end{bmatrix}\begin{bmatrix}\tilde{\mathbf{v}}_{0_1} \\ \tilde{\mathbf{v}}_{1_2}\end{bmatrix} = 0 \\ \Longrightarrow\ &\mathbf{P}_2^T\mathbf{A}_{1_1}\tilde{\mathbf{v}}_{1_1} + \gamma\underbrace{\mathbf{P}_2^T\mathbf{A}_{1_1}\tilde{\mathbf{v}}_{0_1}}_{0} + \underbrace{\mathbf{P}_2^T\mathbf{A}_{0_2}}_{0}(\tilde{\mathbf{v}}_{2_2} + \gamma\tilde{\mathbf{v}}_{1_2}) + \mathbf{P}_2^T\left(\mathbf{A}_{2_1}\tilde{\mathbf{v}}_{0_1} + \mathbf{A}_{1_2}\tilde{\mathbf{v}}_{1_2}\right) = 0,\end{aligned}$$

from which (2.46) follows. Gathering these results, the coefficient vector associated with a given

frequency expansion is

$$\mathbf{v} = \begin{bmatrix} \tilde{\mathbf{v}}_{0_1} \\ \mathbf{0} \end{bmatrix} + \epsilon \begin{bmatrix} \tilde{\mathbf{v}}_{1_1} + \gamma \tilde{\mathbf{v}}_{0_1} \\ \tilde{\mathbf{v}}_{1_2} \end{bmatrix} + \epsilon^2 \begin{bmatrix} \tilde{\mathbf{v}}_{2_1} + \tilde{\alpha}\mathbf{u} + \gamma \tilde{\mathbf{v}}_{1_1} \\ \tilde{\mathbf{v}}_{2_2} + \gamma \tilde{\mathbf{v}}_{1_2} \end{bmatrix} + \cdots$$

which is rearranged to

$$\mathbf{v} = (1 + \epsilon\gamma) \begin{bmatrix} \tilde{\mathbf{v}}_{0_1} \\ \mathbf{0} \end{bmatrix} + \epsilon(1 + \epsilon\gamma) \begin{bmatrix} \tilde{\mathbf{v}}_{1_1} \\ \tilde{\mathbf{v}}_{1_2} \end{bmatrix} + \cdots$$

Although only the first few terms in the eigenfunction weights have been calculated, it appears that γ merely scales the entire weight vector. So despite the fact that the leading order term $[\tilde{\mathbf{v}}_{0_1} \ 0]^T$ was normalized to have unit length, if $\gamma \neq 0$ the norm of this term is $1 + \epsilon\gamma$, and the other terms are also scaled by this factor as well. Thus, γ can be chosen to be zero without loss of generality.

The analysis for the $n = 3$ pair of modes follows the same sequence of steps as the $n = 2$ analysis with the exception that the eigenfunction basis is now given by (2.21) with the a, b and c parameters defined in Table 2.1. Only the final results for the perturbed natural frequencies are given,

$$\begin{aligned} \kappa\omega &= \sqrt{\frac{576}{10}} + \epsilon\,(-6.8305) + \epsilon^2\,(20.553) + \epsilon^3\,(-42.001) + \cdots, \\ \kappa\omega &= \sqrt{\frac{576}{10}} + \epsilon\,(-0.75894) + \epsilon^2\,(1.9349) + \epsilon^3\,(-4.9136) + \cdots. \end{aligned} \tag{2.47}$$

Comparisons of the perturbed frequencies are made with FE and approximate methods in Sec. 2.4.

2.3.2 Dual-Mass Perturbations

The case in which two identical masses are placed approximately 45° apart is addressed in this section. The analysis is performed for the $n = 2$ modes. The modal frequencies detune for finite perturbations when the masses are exactly 45° apart. Furthermore, when the masses are close to, but not exactly, 45° apart, the modal frequencies initially detune as ϵ is increased, become degenerate, and then detune again.

2.3.2.1 Identical Masses at $\theta = 0$ and $\theta_0 = 44^\circ$

For the case that we have Identical masses at $\theta = 0$ and $\theta_0 = 44^\circ$, the ring is divided into two segments when two mass perturbations are present and as remarked in the introduction to Sec. 2.3, $\mathbf{A} \in \boldsymbol{R}^{12\times 12}$ and $\mathbf{v} \in \boldsymbol{R}^{12}$. The locations of the perturbations are $\theta = 0$ and $\theta_0 = 44^\circ$ (the angle origin coincides with one of the perturbations). The analysis that follows is also applicable to any two-mass perturbation when $\theta_0 \neq 45^\circ$. The $\theta_0 = 45^\circ$ case is separately addressed in Sec. 2.3.2.2. The first 6 elements of $\mathbf{v}$ correspond to ring segment $\theta \in [0, \theta_0]$ and the last 6 elements of $\mathbf{v}$ correspond to the ring segment $\theta \in [\theta_0, 2\pi]$ radians. With this parameterization, $\mathbf{A}_0$ is partitioned into four submatrices $\mathbf{A}_0 = \begin{bmatrix}\mathbf{A}_{0_1} & \mathbf{A}_{0_2} & \mathbf{A}_{0_3} & \mathbf{A}_{0_4}\end{bmatrix}$, where $\mathbf{A}_{0_1}, \mathbf{A}_{0_3} \in \boldsymbol{R}^{12\times 2}$, and $\mathbf{A}_{0_2}, \mathbf{A}_{0_4} \in \boldsymbol{R}^{12\times 4}$. The partitions of $\mathbf{v}_0$ are similarly defined and compatible with the partitions of $\mathbf{A}_0$: $\mathbf{v}_0 = \begin{bmatrix}\mathbf{v}_{0_1} & \mathbf{v}_{0_2} & \mathbf{v}_{0_3} & \mathbf{v}_{0_4}\end{bmatrix}^T$. The following can be shown

$$\begin{aligned}
&\mathbf{A}_{0_3} = -\mathbf{A}_{0_1},\\
&\text{rank}\,(\mathbf{A}_{0_1}) = 2,\\
&\text{rank}\left(\begin{bmatrix}\mathbf{A}_{0_1} & \mathbf{A}_{0_2} & \mathbf{A}_{0_4}\end{bmatrix}\right) = 10.
\end{aligned}$$

Thus, $\text{rank}\,(\mathbf{A}_0) = 10$, and since the first constraint is $\mathbf{A}_0\mathbf{v}_0 = \mathbf{0}$, this implies $\mathbf{v}_{0_2} = \mathbf{0}$, $\mathbf{v}_{0_3} = \mathbf{v}_{0_1}$, $\mathbf{v}_{0_4} = \mathbf{0}$, however, $\mathbf{v}_{0_1} \neq \mathbf{0}$ and is determined after further analysis. (2.24) is

$$\begin{bmatrix}\mathbf{A}_{0_1} & \mathbf{A}_{0_2} & -\mathbf{A}_{0_1} & \mathbf{A}_{0_4}\end{bmatrix}\begin{bmatrix}\mathbf{v}_{1_1}\\ \mathbf{v}_{1_2}\\ \mathbf{v}_{1_3}\\ \mathbf{v}_{1_4}\end{bmatrix} + \begin{bmatrix}\mathbf{A}_{1_1} & \mathbf{A}_{1_2} & \mathbf{A}_{1_3} & \mathbf{A}_{1_4}\end{bmatrix}\begin{bmatrix}\mathbf{v}_{0_1}\\ \mathbf{0}\\ \mathbf{v}_{0_1}\\ \mathbf{0}\end{bmatrix} = \mathbf{0}, \tag{2.48}$$

where $\mathbf{v}_1$ is also partitioned as shown. Reusing notation from Sec. 2.3.1, let $\mathbf{P}_0 \in \boldsymbol{R}^{12\times 2}$ be defined such that its columns span $\mathbb{R}(\mathbf{A}_0)^\perp$. Left-multiplying (2.48) by $\mathbf{P}_0^T$ yields the following expression involving $\kappa\omega_1$,

$$\mathbf{P}_0^T\left(\mathbf{A}_{1_1} + \mathbf{A}_{1_3}\right)\mathbf{v}_{0_1} = \begin{bmatrix}-33.888 - 12.714\kappa\omega_1 & -8.9157 - 3.5861\kappa\omega_1\\ -9.6204 - 3.3234\kappa\omega_1 & 34.107 + 12.632\kappa\omega_1\end{bmatrix}\mathbf{v}_{0_1} = \mathbf{0} \tag{2.49}$$

Solutions for $\mathbf{v}_{0_1}$ will exist when the matrix multiplying it is singular. This yields the following values for $\kappa\omega_1$,

$$\kappa\omega_{1_1} = -2.7395, \quad \kappa\omega_{1_2} = -2.6271,$$

at which the matrix is rank 1. The values for $\kappa\omega_1$ are substituted into (2.48), which, after some rearrangement yields,

$$\begin{bmatrix} (\mathbf{A}_{1_1} + \mathbf{A}_{1_3}) & \mathbf{A}_{0_2} & \mathbf{A}_{0_1} & \mathbf{A}_{0_4} \end{bmatrix} \begin{bmatrix} \mathbf{v}_{0_1} \\ \mathbf{v}_{1_2} \\ \mathbf{v}_{1_1} - \mathbf{v}_{1_3} \\ \mathbf{v}_{1_4} \end{bmatrix} = \mathbf{0} \tag{2.50}$$

and because the matrix multiplying the coefficient vector is rank 11, the solution vector is unique up to a scaling. The weight vectors associated with $\kappa\omega_{1_1}$ are

$$\begin{aligned} \tilde{\mathbf{v}}_{0_1} &= \begin{bmatrix} -0.69466 \\ 0.71934 \end{bmatrix}, \quad \tilde{\mathbf{v}}_{1_2} = \begin{bmatrix} 0.76082 & -6.3518 & 0.23719 & 2.5828 \end{bmatrix}^T \\ \tilde{\mathbf{v}}_{1_1} - \tilde{\mathbf{v}}_{1_3} &= \begin{bmatrix} -0.69669 \\ -2.4999 \end{bmatrix}, \quad \tilde{\mathbf{v}}_{1_4} = \begin{bmatrix} 1.0402 & -27.417 & -1.0332 & 27.443 \end{bmatrix}^T. \end{aligned} \tag{2.51}$$

Similarly, for $\kappa\omega_{1_2}$ the solution vectors are

$$\begin{aligned} \tilde{\mathbf{v}}_{0_1} &= \begin{bmatrix} -0.71934 \\ -0.69466 \end{bmatrix}, \quad \tilde{\mathbf{v}}_{1_2} = \begin{bmatrix} 5.2538 & 5.9227 & -0.35983 & -12.985 \end{bmatrix}^T, \\ \tilde{\mathbf{v}}_{1_1} - \tilde{\mathbf{v}}_{1_3} &= \begin{bmatrix} 0.54526 \\ -2.4566 \end{bmatrix}, \quad \tilde{\mathbf{v}}_{1_4} = \begin{bmatrix} 6.6055 & 0.65224 & -6.6116 & -0.65018 \end{bmatrix}^T. \end{aligned} \tag{2.52}$$

The weight vectors are scaled so that the $\tilde{\mathbf{v}}_{0_1}$ partition has unit norm. The tangential displacement will be dominated by $W(\theta) = -0.69466\cos(2\theta) + 0.71934\sin(2\theta)$ and $W(\theta) = 0.71934\cos(2\theta) +$

$0.69466\sin(2\theta)$ which implies the radial displacement $U = \mathrm{d}W/\mathrm{d}\theta$ will be proportional to

$$U(\theta) \propto 0.69466\sin(2\theta) + 0.71934\cos(2\theta) = \cos\left(2(\theta - 22\pi/180)\right)$$
$$U(\theta) \propto -0.71934\sin(2\theta) + 0.69466\cos(2\theta) = \cos\left(2(\theta + 23\pi/180)\right).$$

Thus, one of the anti-nodes associated with the radial displacement lies between the locations of the perturbations at $\theta = 22^\circ$.

The expression for determining $\kappa\omega_2$ is determined by considering the ϵ^2 terms (see (2.25)) and using the fact that $\mathbf{v}_{0_2} = \mathbf{v}_{0_4} = \mathbf{0}$,

$$\begin{bmatrix}\mathbf{A}_{0_1} & \mathbf{A}_{0_2} & -\mathbf{A}_{0_1} & \mathbf{A}_{0_4}\end{bmatrix}\begin{bmatrix}\mathbf{v}_{2_1}\\ \mathbf{v}_{2_2}\\ \mathbf{v}_{2_3}\\ \mathbf{v}_{2_4}\end{bmatrix} + \begin{bmatrix}\mathbf{A}_{1_1} & \mathbf{A}_{1_2} & \mathbf{A}_{1_3} & \mathbf{A}_{1_4}\end{bmatrix}\begin{bmatrix}\tilde{\mathbf{v}}_{1_1}\\ \tilde{\mathbf{v}}_{1_2}\\ \tilde{\mathbf{v}}_{1_3}\\ \tilde{\mathbf{v}}_{1_4}\end{bmatrix} + \left(\mathbf{A}_{2_1} + \mathbf{A}_{2_3}\right)\tilde{\mathbf{v}}_{0_1} = \mathbf{0}$$

which is rearranged to

$$\begin{aligned}&\begin{bmatrix}(\mathbf{A}_{1_1} + \mathbf{A}_{1_3}) & \mathbf{A}_{0_2} & \mathbf{A}_{0_1} & \mathbf{A}_{0_4}\end{bmatrix}\begin{bmatrix}\tilde{\mathbf{v}}_{1_3}\\ \mathbf{v}_{2_2}\\ \mathbf{v}_{2_1} - \mathbf{v}_{2_3}\\ \mathbf{v}_{2_4}\end{bmatrix}\\ &+ \begin{bmatrix}(\mathbf{A}_{2_1} + \mathbf{A}_{2_3}) & \mathbf{A}_{1_2} & \mathbf{A}_{1_1} & \mathbf{A}_{1_4}\end{bmatrix}\begin{bmatrix}\tilde{\mathbf{v}}_{0_1}\\ \tilde{\mathbf{v}}_{1_2}\\ \tilde{\mathbf{v}}_{1_1} - \tilde{\mathbf{v}}_{1_3}\\ \tilde{\mathbf{v}}_{1_4}\end{bmatrix} = \mathbf{0}\end{aligned} \tag{2.53}$$

The left-most matrix is rank 11 at $\{\kappa\omega_{1_1}, \kappa\omega_{1_2}\}$ and the orthogonal complement of its range is spanned by the vector $\mathbf{P}_1 \in \boldsymbol{R}^{12}$. Left-multiplying (2.53) by $\mathbf{P}_1^T$ yields a scalar expression involving

$\kappa\omega_2$,

$$\mathbf{P}_1^T \begin{bmatrix} (\mathbf{A}_{2_1} + \mathbf{A}_{2_3}) & \mathbf{A}_{1_2} & \mathbf{A}_{1_1} & \mathbf{A}_{1_4} \end{bmatrix} \begin{bmatrix} \tilde{\mathbf{v}}_{0_1} \\ \tilde{\mathbf{v}}_{1_2} \\ \tilde{\mathbf{v}}_{1_1} - \tilde{\mathbf{v}}_{1_3} \\ \tilde{\mathbf{v}}_{1_4} \end{bmatrix} = \mathbf{0}. \tag{2.54}$$

Evaluating (2.54) at $\kappa\omega_{1_1}$ yields $\omega_{2_1} = 9.2098$, and at $\kappa\omega_{1_2}$ yields $\kappa\omega_{2_2} = 6.5597$.

The process for solving the equation associated with ϵ^3 is similar to the single mass perturbation case and leads to analysis of

$$\begin{bmatrix} (\mathbf{A}_{3_1} + \mathbf{A}_{3_3}) & \mathbf{A}_{2_2} & \mathbf{A}_{2_1} & \mathbf{A}_{2_4} \end{bmatrix} \begin{bmatrix} \tilde{\mathbf{v}}_{0_1} \\ \tilde{\mathbf{v}}_{1_2} \\ \tilde{\mathbf{v}}_{1_1} - \tilde{\mathbf{v}}_{1_3} \\ \tilde{\mathbf{v}}_{1_4} \end{bmatrix} +$$
$$\begin{bmatrix} (\mathbf{A}_{2_1} + \mathbf{A}_{2_3}) & \mathbf{A}_{1_2} & \mathbf{A}_{1_1} & \mathbf{A}_{1_4} \end{bmatrix} \begin{bmatrix} \tilde{\mathbf{v}}_{1_3} \\ \tilde{\mathbf{v}}_{2_2} \\ \tilde{\mathbf{v}}_{2_1} - \tilde{\mathbf{v}}_{2_3} \\ \tilde{\mathbf{v}}_{2_4} \end{bmatrix} + \tag{2.55}$$
$$\begin{bmatrix} (\mathbf{A}_{1_1} + \mathbf{A}_{1_3}) & \mathbf{A}_{0_2} & \mathbf{A}_{0_1} & \mathbf{A}_{0_4} \end{bmatrix} \begin{bmatrix} \tilde{\mathbf{v}}_{2_3} \\ \tilde{\mathbf{v}}_{3_2} \\ \tilde{\mathbf{v}}_{3_1} - \tilde{\mathbf{v}}_{3_3} \\ \tilde{\mathbf{v}}_{3_4} \end{bmatrix} = \mathbf{0}.$$

Left-multiplication of (2.55) by $\mathbf{P}_1^T$ yields a scalar expression for $\kappa\omega_3$ because $\mathbf{P}_1$ is orthogonal to the ranges of the latter two matrices multiplying the coefficient vectors in (2.55). Completing this analysis yields the following frequency expansions

$$\kappa\omega = \sqrt{\frac{36}{5}} + \epsilon(-2.7395) + \epsilon^2(9.2098) + \epsilon^3(-30.726) + \cdots$$
$$\kappa\omega = \sqrt{\frac{36}{5}} + \epsilon(-2.6271) + \epsilon^2(6.5597) + \epsilon^3(-24.643) \cdots .$$

Table 2.2: Frequency expansions for dual mass perturbation

Location	First mode			Second mode		
θ_0	$\kappa\omega_{1_1}$	$\kappa\omega_{2_1}$	$\kappa\omega_{3_1}$	$\kappa\omega_{1_2}$	$\kappa\omega_{2_2}$	$\kappa\omega_{3_2}$
43	-2.7955	9.4627	-31.734	-2.5710	6.4513	-24.519
44	-2.7395	9.2098	-30.726	-2.6271	6.5597	-24.643
44.5	-2.7114	9.0830	-30.221	-2.6552	6.6157	-24.708
44.8	-2.6945	9.0067	-29.918	-2.6720	6.6500	-24.749
45	-2.6833	8.9562	-29.727	-2.6833	6.6730	-24.775

Table 2.2 summarizes the expansions for additional values of θ_0. It is also evident from the table that as θ_0 approaches $45°$, the difference between $\kappa\omega_{1_1}$ and $\kappa\omega_{1_2}$ approaches zero, thus, identical mass perturbations at $\theta = \{0°, 45°\}$ only weakly detune the modal frequencies.

2.3.2.2 Identical Masses at $\theta = 0$ and $\theta_0 = 45°$

The $\theta_0 = 45°$ case is considered separately because there is an additional reduction in rank in the ϵ^1-level analysis and so additional steps are required in order to resolve the weight vectors. Since $\text{rank}(\mathbf{A}_0) = 10$, $\mathbf{P}_0$ is still defined so that its columns span $\mathbb{R}(\mathbf{A}_0)^\perp$, however, (2.49) is now

$$\begin{bmatrix} 3.6795 + 1.3713\kappa\omega_1 & 35.047 + 13.061\kappa\omega_1 \\ 35.047 + 13.061\kappa\omega_1 & -3.6795 - 1.3713\kappa\omega_1 \end{bmatrix} \mathbf{v}_{0_1} = \mathbf{0},$$

which is singular at only one value of $\kappa\omega_1$, namely $\kappa\omega_{1_1} = \kappa\omega_{1_2} = -2.6833$. In this case the matrix multiplying $\mathbf{v}_{0_1}$ evaluates to zero. Thus, $\dim \mathbb{N}\left(\left[(\mathbf{A}_{1_1} + \mathbf{A}_{1_3})\ \mathbf{A}_{0_2}\ \mathbf{A}_{0_1}\ \mathbf{A}_{0_4}\right]\right) = 2$ in (2.50). Let $\mathbf{u}_1, \mathbf{u}_2 \in \boldsymbol{R}^{12}$ form a basis for this null space and, furthermore, let the columns of $\mathbf{P}_1 \in \boldsymbol{R}^{12\times 2}$ span $\mathbb{R}\left(\left[(\mathbf{A}_{1_1} + \mathbf{A}_{1_3})\ \mathbf{A}_{0_2}\ \mathbf{A}_{0_1}\ \mathbf{A}_{0_4}\right]\right)^\perp$. Solution vectors are then represented by

$$\begin{aligned} \tilde{\mathbf{v}}_{0_1} &= \tilde{\alpha}\mathbf{u}_{1_1} + \tilde{\beta}\mathbf{u}_{2_1} \\ \tilde{\mathbf{v}}_{1_2} &= \tilde{\alpha}\mathbf{u}_{1_2} + \tilde{\beta}\mathbf{u}_{2_2} \\ \tilde{\mathbf{v}}_{1_1} - \tilde{\mathbf{v}}_{1_3} &= \tilde{\alpha}\mathbf{u}_{1_3} + \tilde{\beta}\mathbf{u}_{2_3} \\ \tilde{\mathbf{v}}_{1_4} &= \tilde{\alpha}\mathbf{u}_{1_4} + \tilde{\beta}\mathbf{u}_{2_4}, \end{aligned} \tag{2.56}$$

where $\mathbf{u}_1$ and $\mathbf{u}_2$ are partitioned in the same manner as the solution vectors, and where $\tilde{\alpha}$ and $\tilde{\beta}$ represent real parameters which will be determined at the next stage of analysis.

Left-multiplying (2.53) by $\mathbf{P}_1^T$ yields the analog of (2.54),

$$\mathbf{P}_1^T \begin{bmatrix} (\mathbf{A}_{2_1} + \mathbf{A}_{2_3}) & \mathbf{A}_{1_2} & \mathbf{A}_{1_1} & \mathbf{A}_{1_4} \end{bmatrix} \begin{bmatrix} \tilde{\alpha}\mathbf{u}_{1_1} + \tilde{\beta}\mathbf{u}_{2_1} \\ \tilde{\alpha}\mathbf{u}_{1_2} + \tilde{\beta}\mathbf{u}_{2_2} \\ \tilde{\alpha}\mathbf{u}_{1_3} + \tilde{\beta}\mathbf{u}_{2_3} \\ \tilde{\alpha}\mathbf{u}_{1_4} + \tilde{\beta}\mathbf{u}_{2_4} \end{bmatrix} = \mathbf{0}.$$

This expression is rearranged to

$$\begin{aligned} \tilde{\alpha}\mathbf{P}_1^T \big(\mathbf{A}_{1_2}\mathbf{u}_{1_2} + \mathbf{A}_{1_3}\mathbf{v}_{1_1} - \mathbf{A}_{1_3}\mathbf{u}_{1_3} + (\mathbf{A}_{2_1} + \mathbf{A}_{2_3})\mathbf{u}_{1_1}\big) \\ + \tilde{\beta}\mathbf{P}_1^T \big(\mathbf{A}_{1_2}\mathbf{u}_{2_2} + \mathbf{A}_{1_3}\mathbf{v}_{1_1} - \mathbf{A}_{1_3}\mathbf{u}_{2_3} + (\mathbf{A}_{2_1} + \mathbf{A}_{2_3})\mathbf{u}_{2_1}\big) = \mathbf{0} \end{aligned} \tag{2.57}$$

When computing $\mathbf{u}_1$, $\mathbf{u}_2$ and $\mathbf{P}_1$ from a singular value decomposition of $\big[(\mathbf{A}_{1_1} + \mathbf{A}_{1_3}) \;\; \mathbf{A}_{0_2} \;\; \mathbf{A}_{0_1} \;\; \mathbf{A}_{0_4}\big]$, (2.57) can be rewritten as

$$\begin{bmatrix} 0.31427 - 0.080763\kappa\omega_2 & 4.7283 - 0.69671\kappa\omega_2 \\ 3.0604 - 0.35681\kappa\omega_2 & 0.52256 - 0.11416\kappa\omega_2 \end{bmatrix} \begin{bmatrix} \tilde{\alpha} \\ \tilde{\beta} \end{bmatrix} = \mathbf{0},$$

which yields $\kappa\omega_{2_1} = 6.6730$ and $\kappa\omega_{2_2} = 8.9562$.

The eigenfunction weights are of interest for this perturbation scenario since the modal frequencies are degenerate to ϵ^1. For $\kappa\omega_{2_1}$, $\tilde{\alpha} = 0.33215$ and $\tilde{\beta} = 0.94323$ from which the leading order terms in the weights are determined

$$\tilde{\mathbf{v}}_0 = \begin{bmatrix} -0.70711 & -0.70711 \end{bmatrix}^T.$$

Similarly, for $\kappa\omega_{2_2}$, then $\tilde{\alpha} = -0.96528$ and $\tilde{\beta} = 0.26122$ so

$$\tilde{\mathbf{v}}_0 = \begin{bmatrix} -0.70711 & 0.70711 \end{bmatrix}^T.$$

Thus, the tangential displacements associated with the modes are dominated by $W(\theta) = \cos(2\theta) + \sin(2\theta)$ and $W(\theta) = -\cos(2\theta) + \sin(2\theta)$, which implies the radial displacements with the slightly detuned modes will be proportional to $U(\theta) \propto -\sin(2\theta) + \cos(2\theta)$ and $U(\theta) \propto \sin(2\theta) + \cos(2\theta)$. The anti-nodes of the radial displacement subtend 45° but one anti-node at $\theta = 22.5^\circ$ is located between the perturbation locations.

2.3.3 Mass-Spring Perturbation

This section considers a mass perturbation located at $\theta = 0^\circ$ and a radial spring perturbation located at $\theta = 45^\circ$. The objective is to choose the spring parameter g_2 such that the first-order expansion values for the perturbed $n = 2$ modal frequencies are equal, i.e., $\omega_{1_1} = \omega_{1_2}$ (the mass parameter g_1 is taken to be unity). This will guarantee that the $n = 2$ modes will be essentially tuned for sufficiently small ϵ, however, the behavior of the eigenfunction weight vector is of particular interest in this scenario. It will be shown that like the dual mass perturbation case, the leading order terms in the eigenfunction weight vector demonstrate that the anti-node orientations of the modes do not coincide with the $\{0, 45\}$ degree locations of the perturbations.

The nominal spring rate is the ring bending stiffness $K = EI/\bar{r}^3$. A single radial spring affects only one modal frequency in the unperturbed ring. When $g_1 = 0$ and $g_2 = 1$, the following expansion parameters are derived,

$$\kappa\omega_{1_1} = 0 \quad , \quad \kappa\omega_{1_2} = 0.047451$$

where $\kappa\omega_{1_2}$ is associated with the perturbed mode whose radial displacement anti-node is aligned with the spring at $\theta = 45^\circ$. On the other hand, a single mass perturbation at $\theta = 0^\circ$ decreases both modal frequencies (see (2.33)),

$$\kappa\omega_{1_1} = -2.1466 \quad , \quad \kappa\omega_{1_2} = -0.53665.$$

The perturbations of the modal frequencies are additive at this order, so a simultaneous perturbation

with a mass located at $\theta = 0^\circ$ and a radial spring at $\theta = 45^\circ$ yields

$$\kappa\omega_{1_1} = -2.1466 + 0g_2$$
$$\kappa\omega_{1_2} = -0.53665 + 0.047451g_2,$$

where $g_1 = 1$ and g_2 remains a parameter. By selecting $g_2 = -33.929$ (a negative spring stiffness), $\kappa\omega_{1_1} = \kappa\omega_{1_2} = -2.1466$, so for sufficiently small ϵ the modal frequencies can be considered degenerate.

The weight vectors for the perturbed modes are of interest, however, analysis of $\mathbf{A}_0\mathbf{v}_1 + \mathbf{A}_1\mathbf{v}_0 = \mathbf{0}$ yields $\kappa\omega_{1_1} = \kappa\omega_{1_2} = -2.1466$ as constructed above but not the leading-order terms in the weight vector, $\mathbf{v}_0$. To compute the weight vector, (2.50) is analyzed for this case. Since

$$\text{rank}\left(\left[(\mathbf{A}_{1_1} + \mathbf{A}_{1_3})\ \ \mathbf{A}_{0_2}\ \ \mathbf{A}_{0_1}\ \ \mathbf{A}_{0_4}\right]\right) = 10,$$

then $\mathbf{u}_1, \mathbf{u}_2 \in \boldsymbol{R}^{12}$ are defined as a basis for $\mathbb{N}\left(\left[(\mathbf{A}_{1_1} + \mathbf{A}_{1_3})\ \ \mathbf{A}_{0_2}\ \ \mathbf{A}_{0_1}\ \ \mathbf{A}_{0_4}\right]\right)$. The solution vector is parameterized using the same form as (2.56) but only the first partitions are reported because they determine $\tilde{\mathbf{v}}_{0_1}$,

$$\tilde{\mathbf{v}}_{0_1} = \tilde{\alpha}\mathbf{u}_{1_1} + \tilde{\beta}\mathbf{u}_{2_1}, \quad \mathbf{u}_{1_1} = \begin{bmatrix} -0.99856 \\ 0.053726 \end{bmatrix}, \quad \mathbf{u}_{1_1} = \begin{bmatrix} 0.36301 \\ 0.93179 \end{bmatrix}.$$

Furthermore, (2.53) reduces to

$$\begin{bmatrix} -7.8786 + 8.0818\kappa\omega_2 & 26.956 - 12.359\kappa\omega_2 \\ 44.258 - 10.352\kappa\omega_2 & 30.634 - 4.4431\kappa\omega_2 \end{bmatrix} \begin{bmatrix} \tilde{\alpha} \\ \tilde{\beta} \end{bmatrix} = \mathbf{0},$$

so the following values for $\kappa\omega_2$ and $\{\tilde{\alpha}, \tilde{\beta}\}$ are determined,

$$\kappa\omega_{2_1} = 1.7427, \quad \{\tilde{\alpha}, \tilde{\beta}\} = \{-0.65770, 0.75328\} \implies \tilde{\mathbf{v}}_{0_1} = \begin{bmatrix} 0.81285 \\ 0.58247 \end{bmatrix} \tag{2.58}$$

and

$$\kappa\omega_{2_1} = 5.0235, \quad \{\tilde{\alpha}, \tilde{\beta}\} = \{0.73174, 0.68158\} \implies \tilde{\mathbf{v}}_{0_1} = \begin{bmatrix} -0.58247 \\ 0.81285 \end{bmatrix}, \tag{2.59}$$

where the $\tilde{\mathbf{v}}_{0_1}$ are normalized to unit norm. This result demonstrates that for arbitrarily small but non-zero ϵ, the leading order terms in the eigenfunction weights are orthogonal, which implies the anti-nodes associated with the modes subtend $45°$, however, the anti-nodes are not aligned with the perturbation locations. The tangential displacements are dominated by these leading order terms and are given by $W(\theta) = 0.81285\cos(2\theta) + 0.58247\sin(2\theta)$ and $W(\theta) = -0.58247\cos(2\theta) + 0.81285\sin(2\theta)$. Thus, the radial displacements U will be proportional to

$$U(\theta) \propto -0.81285\sin(2\theta) + 0.58247\cos(2\theta) = \cos\left(2(\theta + 27.2\pi/180)\right),$$
$$U(\theta) \propto 0.58247\sin(2\theta) + 0.81285\cos(2\theta) = \cos\left(2(\theta - 17.8\pi/180)\right).$$

2.4 Comparison with Other Analyses

The perturbation results are compared to Rayleigh-Ritz analysis when the basis functions are selected to be $W(\theta) = \sum_k \Big(\tilde{\alpha}_k \cos(k\theta) + \tilde{\beta}_k \sin(k\theta)\Big)$, for $k = 2$ (two-term), and for $k = 1, \ldots, 10$ (twenty-term). These basis functions satisfy the essential boundary conditions (continuity up to the second derivative of the tangential displacement). The objective is to minimize the Lagrangian functional $\mathcal{L}$ with respect to basis function coefficients [Mei67]. The resulting generalized eigenvalue problem is numerically solved. Comparisons with finite element analysis of a thin silicon ring are also reported. The ring parameters are: $E = 170$ GPa, $\rho = 2329\,\mathrm{kg\,m^{-3}}$, ring height $L = 270\,\mu$m, ring width $h = 100\,\mu$m, $I = 1/12Lh^3$, $A = Lh$, $\bar{r} = 0.5$ cm, and $\kappa = 1.0137 \times 10^{-4}$ s. Three-dimensional free tetrahedral elements are used and generate over one hundred thousand degrees of freedom. The density of a small plug of material is manipulated to create a localized change in mass. The added mass is normalized with respect to the nominal ring mass to define ϵ.

The natural frequencies for the single added mass as a function of ϵ are depicted in Fig. 2.2

when $n = 2, 3$. The perturbation analysis, FEA and twenty-term Rayleigh-Ritz analysis produce essentially the same results for both $n = 2$ and $n = 3$ cases. The dual mass perturbation results are summarized in Figs. 2.3, 2.4 and 2.5 for the $n = 2$ pair of modes. In these figures, the absolute value of the difference between the perturbed modal frequencies as a function of ϵ are shown when identical mass perturbations subtend $43°$, $44°$ and $45°$. The modes weakly detune in these cases, however, for sufficiently large mass the perturbation expressions show closer agreement with the FEA. The results also depict interesting behavior for the dual mass perturbations when the subtended angle is not equal to $45°$: the existence of a non-zero perturbation at which the modal frequencies are equal. The finite perturbation that achieves degeneracy is quite accurately predicted by the perturbation analysis as seen in Figs. 2.3 and 2.4. Lastly, Fig. 2.6 shows the normalized modal frequency difference as a function of ϵ for the spring-mass perturbation. It can be shown that the two-term Rayleigh-Ritz analysis produces the same order-ϵ dependence as the perturbation analysis for these case studies. Thus, for sufficiently small perturbations, the two-term Rayleigh-Ritz analysis offers greater simplicity for predicting the perturbed modal frequencies. This simplicity is advantageous when deriving a trimming procedure for reducing the modal frequency difference in ring resonators as described in [Fox90]. Although the perturbation analysis appears to show greater predictive capability for large perturbations, especially with multiple masses. An effective trimming procedure based these results is still to be developed.

The discrepancy between the perturbation results and Rayleigh-Ritz analysis for large perturbations can be attributed to the fact that the third and fourth derivatives of the radial displacement with respect to θ are not continuous because of the boundary conditions in (2.13) (equivalent to the fourth and fifth derivatives with respect θ for the tangential displacement W). The discontinuity is proportional to ϵ and is essentially "built in" the perturbation solution. As the perturbation magnitude increases, the discontinuity becomes more severe, and the Rayleigh-Ritz basis functions, which have continuous derivatives of all orders have greater difficulty in approximating $W^{(4)}$ and $W^{(5)}$ in a neighborhood of the perturbation locations.

Another comparison is made between the magnitudes of the coefficients of a Fourier series expansion computed for the perturbed mode shapes. A comparison is possible between the perturbation results and finite element analysis, but not the two-term Rayleigh-Ritz analysis as it assumes

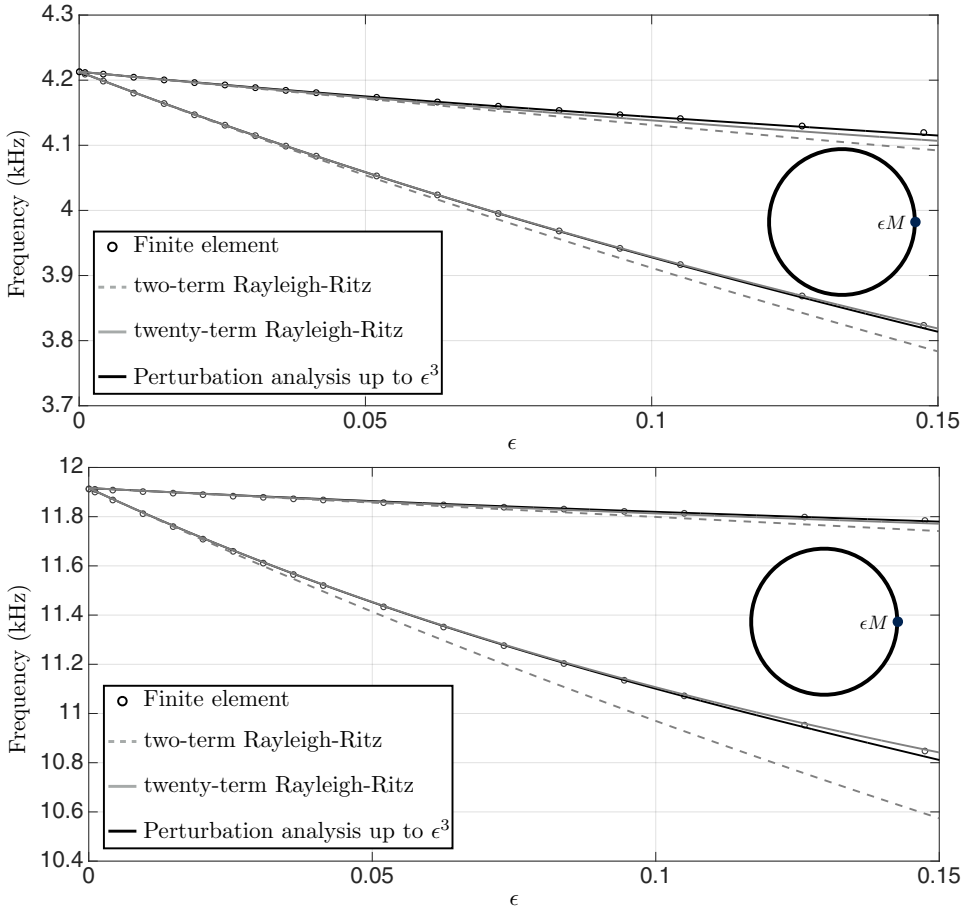

Figure 2.2: Top: The modal frequencies when $n = 2$ modes as a function of a single mass perturbation. Bottom: The modal frequencies when $n = 3$ modes as a function of a single mass perturbation.

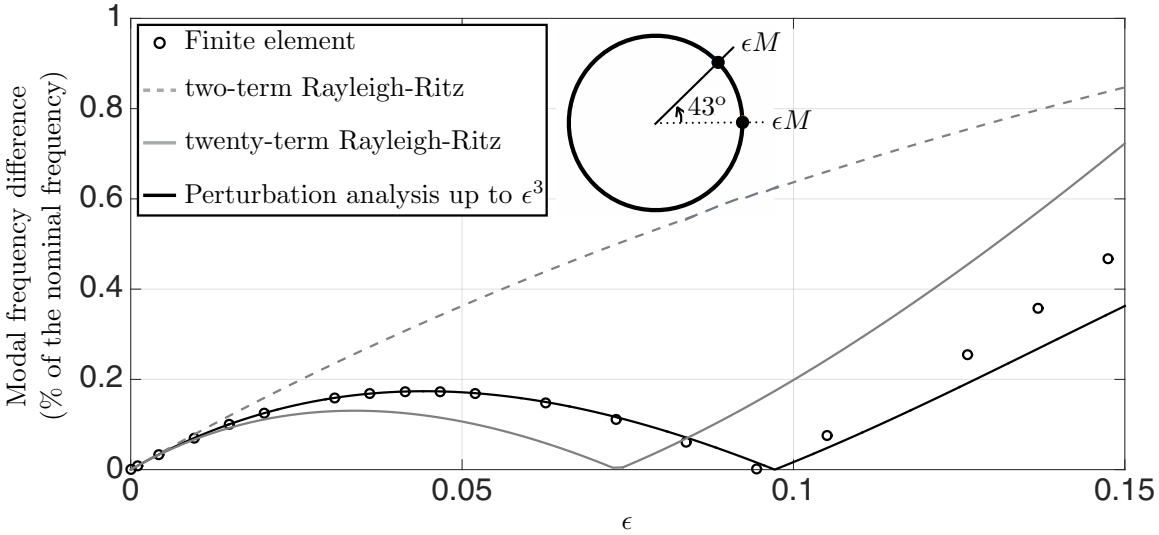

Figure 2.3: The normalized frequency split of the $n = 2$ modal frequencies with respect to ϵ when $\theta_0 = 43°$.

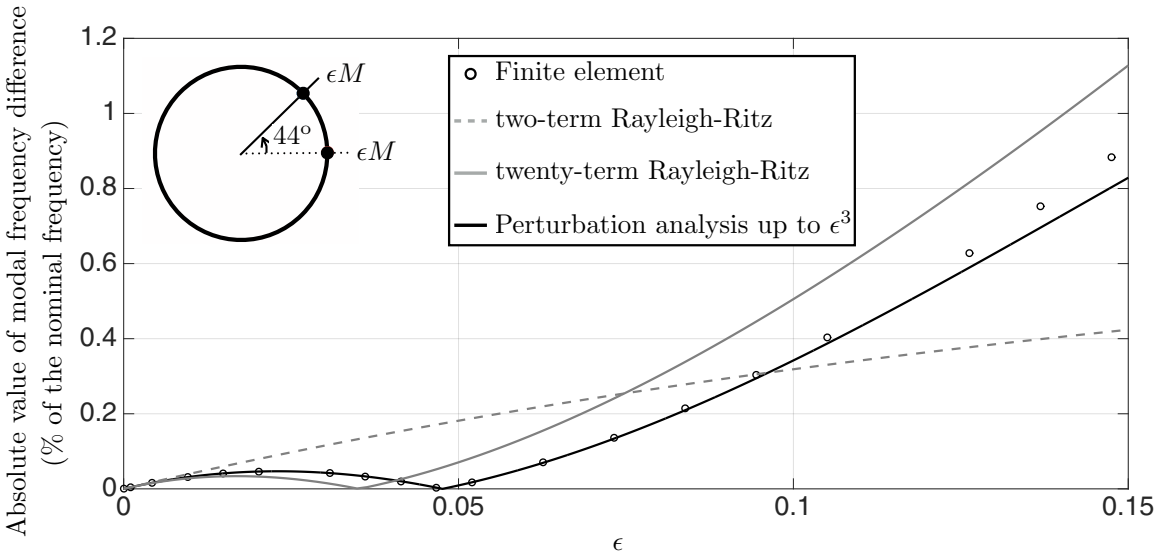

Figure 2.4: The normalized frequency split of the $n = 2$ modal frequencies with respect to ϵ when $\theta_0 = 44°$.

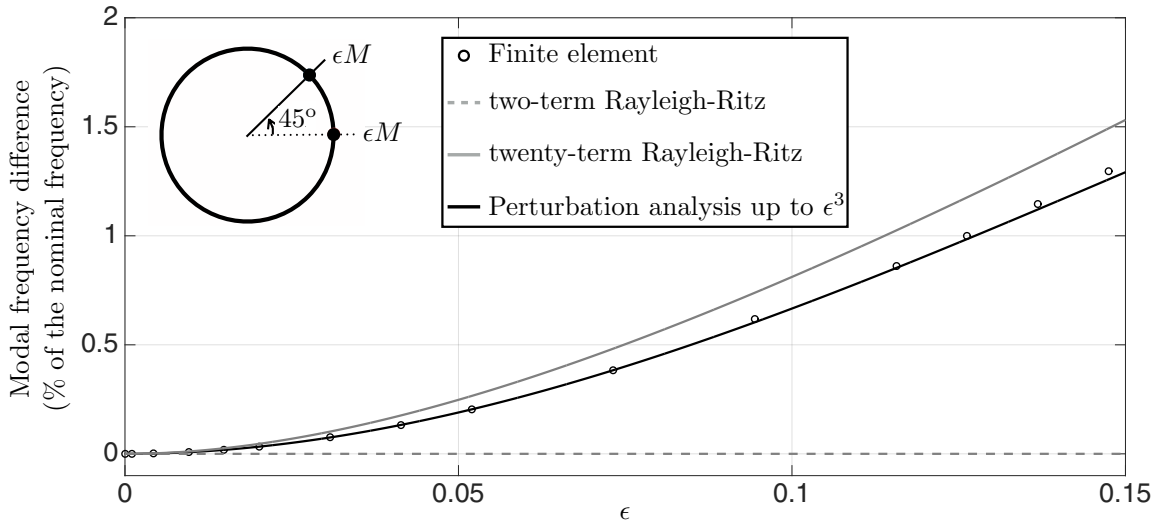

Figure 2.5: The normalized frequency split of the $n = 2$ modal frequencies with respect to ϵ when $\theta_0 = 45°$. The modal frequencies detune for a non-zero perturbation.

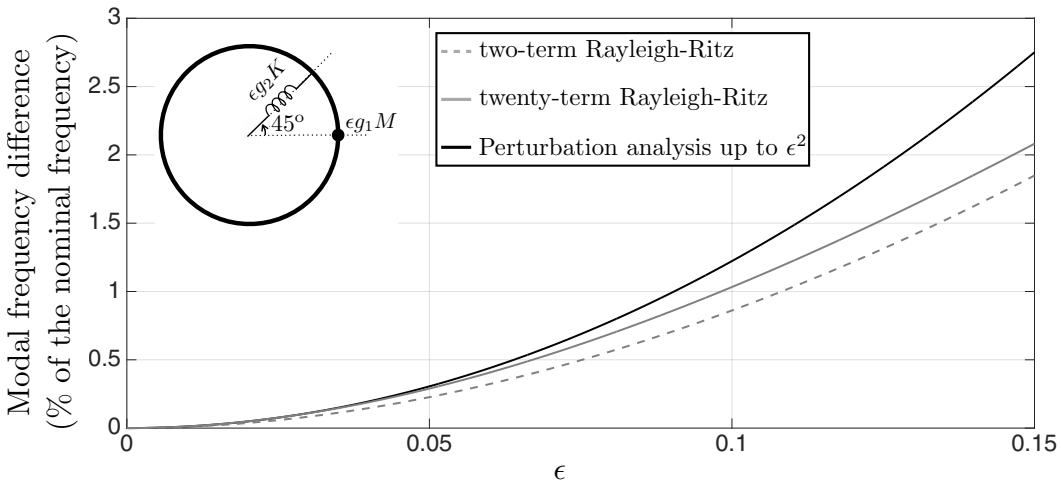

Figure 2.6: The normalized frequency split of the $n = 2$ modal frequencies with respect to ϵ for a simultaneous mass-spring perturbation.

modes of the form $\cos(2\theta)$ and $\sin(2\theta)$. The comparison with twenty-term Rayleigh-Ritz analysis is possible, but not included. For a given mass perturbation, the tangential velocities of the modes are sampled at 1000 uniformly-spaced points along the ring centerline for the finite element results. Similarly, the tangential velocity is evaluated from the eigenfunctions and coefficient vector derived from the perturbation analysis using the expansion up to ϵ and with $\gamma = 0$. Discrete Fourier series are determined for these tangential velocities, and since the dominant harmonic corresponds to the 2θ terms, the magnitudes of these Fourier coefficients are normalized to unity. The magnitude of the Fourier coefficients for each perturbed mode are compared in Figs. 2.7 and 2.8 for two perturbation sizes, $\epsilon = 0.017$ and $\epsilon = 0.069$. The perturbation and FE results are very close for the harmonic indices below 6. The largest contributions after the dominant 2θ component are the θ and 3θ components.

2.5 Comparison of the Results with a Practical Ring Problem

This section takes a closer look at the comparison of the results with a practical problem. The properties are selected based on the resonator described in Chapters 3 and 4. The mass perturbations are solder spheres (see Chapter 4). The electrostatic tuning is based on the spring perturbations. The material and geometrical properties of the ring are described in Sec. 2.4. Based on the density

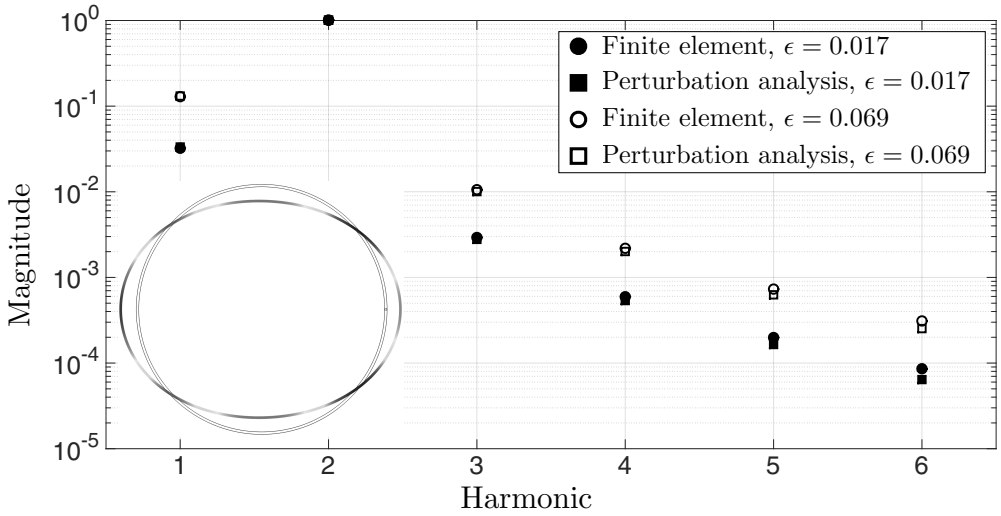

Figure 2.7: Magnitude of the coefficients of the Fourier series expansion of the lower frequency $n = 2$ mode derived from the perturbation analysis using $\tilde{\boldsymbol{v}}_0 + \epsilon\tilde{\boldsymbol{v}}_1$ as the weight vector. The agreement with finite elements is excellent at lower harmonics.

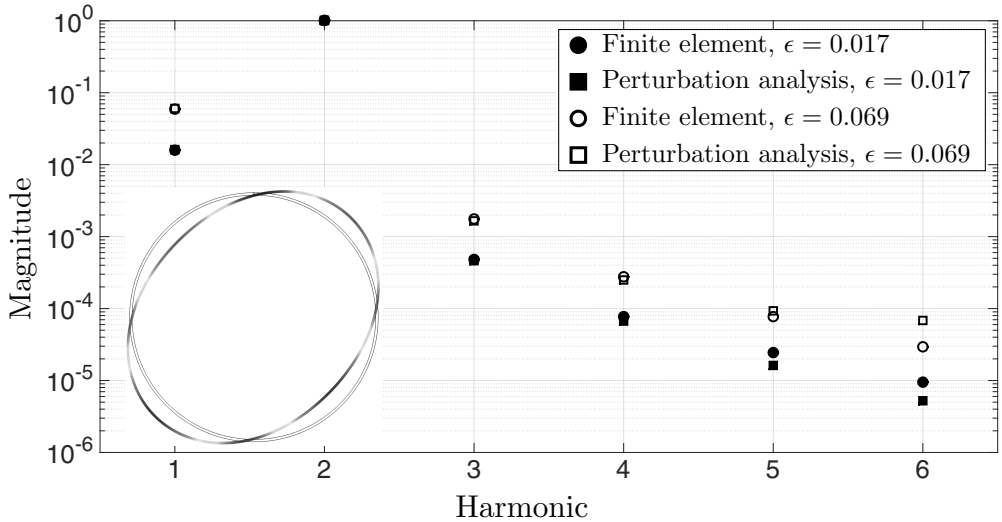

Figure 2.8: Magnitude of Fourier series coefficients of the higher frequency $n = 2$ mode.

of tin (Sn) which is the primary element in solder spheres, the relative size of the solder sphere to the silicon (Si) ring can be calculated. The density for Sn and Si are $\rho_{\text{Sn}} = 7310\text{kg/m}^3$, and $\rho_{\text{Si}} = 2329\text{kg/m}^3$. The volume for a solder sphere can be calculated as $V_{Sn} = \frac{4}{3}\pi(\frac{d}{2})^3 = \pi\frac{d^3}{6}$, where d is the diameter of the sphere. The masses for the solder sphere and the silicon ring are $m_{\text{Sn}} = \rho_{\text{Sn}}V_{\text{Sn}} = \rho_{\text{Sn}}\pi\frac{d^3}{6}$ and $M_{\text{ring}} = \rho_{\text{Si}}2\pi\bar{r}A$, respectively. The value for the perturbation parameter ϵ is equal to the ratio of the masses of the perturbation and the ring.

$$\epsilon = \frac{m_{\text{Sn}}}{M_{\text{ring}}} = \frac{\rho_{\text{Sn}}\pi\frac{d^3}{6}}{\rho_{\text{Si}}2\pi\bar{r}A} = (\frac{\rho_{\text{Sn}}}{\rho_{\text{Si}}})\frac{d^3}{12\bar{r}A}$$

Assuming that the nominal solder sphere diameter is $d = 75\mu$m, using the same parameter for the ring as in Sec. 2.4, the value of ϵ is 8.1702×10^{-4}.

2.5.1 Single Mass Perturbation Comparison

From Sec. 2.3.1, the values for the first and second frequency deviation terms are $\kappa\omega_{1_1} = -2.14662$, $\kappa\omega_{1_2} = -0.53665$, $\kappa\omega_{2_1} = 3.91039$, and $\kappa\omega_{2_2} = 1.2159$. The values of κ for the silicon ring in hand are $\kappa = \sqrt{\rho_{\text{Si}}\frac{A\bar{r}^4}{EI}} = 1.0139 \times 10^{-4}$, which lead to the following frequency deviations

$$\Delta_1 = -17.2721\text{rad/s} \quad , \quad \Delta_2 = -4.3164\text{rad/s},$$

which translate to 2.0620 Hz frequency detuning. Placing the same type perturbation on a uniform ring results in a 7.7673 Hz change in the frequency split for $n = 3$ modes. These values are in the same ballpark as the change in the frequency split resulting from a nominal solder sphere mass perturbation as will be discussed in Chapter 4.

2.5.2 Dual Mass Perturbation Comparison

For the case of having two mass perturbations one at $\theta = 0$ and one at $\theta_0 = 44^\circ$, from Sec.2.3.2.1, the frequency deviation terms are $\kappa\omega_{1_1} = -2.7395, \kappa\omega_{1_2} = 2.6271, \kappa\omega_{2_1} = 9.2098$, and $\kappa\omega_{2_2} = 6.5597,$ which result in -22.0150rad/s and -21.1268rad/s frequency deviations, which lead to a 0.1414 Hz frequency detuning. For the case that $\theta_0 = 45^\circ$ where $\kappa\omega_{1_1} = \kappa\omega_{1_2}$, the frequency

detuning is smaller for small values of ϵ. The frequency detuning for this case is only 0.0024 Hz.

2.5.3 Mass-Spring perturbation comparison

The objective is to compensate for the existence of the mass using the appropriate size spring. Based on the results from Sec.2.3.3, the relative size of the spring with respect to the mass is $g_2 = -33.929$. The spring needs to implemented electrostatically. The force from a capacitive plate is $\frac{1}{2}CV^2$, where C is the capacitance and V is the voltage. The capacitance C for two parallel plates in the vacuum can be written as $\frac{\epsilon_0 A_0}{d_0^3}$, where $\epsilon_0 = 8.854182 \times 10^{-12}$F/m, $d_0 = 25\mu$m and $A_0 = \frac{1}{8}2\pi\bar{r}L$ are the vacuum permittivity, the gap between the plates and the exposed area, respectively. So the voltage corresponding to the g_2 spring can be calculated as

$$V = \sqrt{g_2 \frac{\epsilon}{\epsilon_0} \frac{EI}{\bar{r}^3} \frac{2d_0^3}{A_0}} = 53.138\text{V},$$

The frequency split associated with this case is fairly small as expected since the relative stiffness of the spring is chosen to match the ϵ terms in the expansion and it is equal to 0.0036 Hz. The voltage value is at the same order of magnitude as the voltage values used in [KM06] for electrostatically tuning the resonators.

2.5.4 Results Based on Two-Term Rayleigh-Ritz Analysis

As discussed in Sec. 2.4, for sufficiently small perturbations, the two-term Rayleigh-Ritz analysis leads to accurate results with greater simplicity, which is advantageous for dealing with the frequency tuning problem. This section takes a closer look at the results that can be extracted from this analysis. Although, for large perturbations, the results from this analysis deviate from the actual frequency splits, for practical problems, the mass perturbations used in the tuning process are relatively small. It can be shown the location of the anti-nodes ψ for modes number n can be written as

$$\tan(2n\psi) = \frac{\Sigma_i m_i \sin(2n\phi_i)}{\Sigma_i m_i \cos(2n\phi_i)}.$$

where m_i and ϕ_i are the mass perturbation sizes and locations, respectively. The mass sizes are simply ϵM_{ring}. The resonant frequencies can be written as $\omega = \omega_0\sqrt{\frac{5}{(1+\epsilon)5\pm3\epsilon}}$ which can be expanded approximately as

$$\kappa\omega \approx \sqrt{\frac{36}{5}} - 2.14663\epsilon + 5.15190\epsilon^2,$$
$$\kappa\omega \approx \sqrt{\frac{36}{5}} - 0.53665\epsilon + 0.32199\epsilon^2,$$

for $n = 2$ modes.

The resonant frequencies for $n = 3$ modes can be written as $\omega = \omega_0\sqrt{\frac{10}{(1+\epsilon)10\pm8\epsilon}}$ which can be expanded as

$$\kappa\omega \approx \sqrt{\frac{576}{10}} - 6.83052\epsilon + 18.4424\epsilon^2,$$
$$\kappa\omega \approx \sqrt{\frac{576}{10}} - 0.758947\epsilon + 0.227684\epsilon^2.$$

As it can be seen, the expansions are the same as the expansions for the perturbation analysis (see (2.43) and (2.47)) for the ϵ term, but they start to deviate for higher order terms. For the case of dual same size mass perturbations, one at 0 and one at $44°$, we have $\phi_i = 0, 44°$, which leads to

$$\tan(2n\psi) = \frac{\Sigma_i m_i \sin(2n\phi_i)}{\Sigma_i m_i \cos(2n\phi_i)} = \frac{\sin(0) + \sin(4 \times 44°)}{\cos(0) + \cos(4 \times 44°)} \implies \psi = 22°.$$

The expansions for the resonant frequencies approximation can be written as

$$\kappa\omega \approx \sqrt{\frac{36}{5}} - 2.73947\epsilon + 8.3905\epsilon^2,$$
$$\kappa\omega \approx \sqrt{\frac{36}{5}} - 2.62709\epsilon + 7.71625\epsilon^2.$$

When the second mass is placed at 45°, $\phi_i = 0, 45^\circ$. and the frequency expansions are

$$\kappa\omega \approx \sqrt{\frac{36}{5}} - 2.6833\epsilon + 8.04984\epsilon^2,$$
$$\kappa\omega \approx \sqrt{\frac{36}{5}} - 2.6833\epsilon + 8.94984\epsilon^2.$$

Similar to the single mass perturbation case, the ϵ terms match the perturbation analysis. However, for higher order terms, the expansions deviate.

2.5.5 Anti-node Orientation and Cross Coupling

In addition to the importance of having zero frequency splits for different modes, it is also important to know the anti-node orientation ψ, which provides information about the vibration pattern. Lining up the electrodes and sensors with the anti-nodes is advantageous and reduces the amount of cross-channel coupling from one mode to the other. As it will be shown in Chapter 3, a two input two output frequency response is sufficient for finding the frequency splits and the anti-node orientations. It is ideal to isolate one mode from the other by lining up the electrodes and sensors with the vibration pattern. However, due to the existence of higher order terms in the radial and tangential displacements, the modes are not necessarily orthogonal to each other. For instance, for the case of having a single mass perturbation, which introduces about a 6 Hz frequency split in a silicon ring with geometrical properties given in Sec. 2.4, assuming that the sensor electrodes subtend 45° and they cover from -22.5° to 22.5° and from 22.5° to 67.5°, exciting the ring at $\theta = 180^\circ$ will lead to about 0.5% cross-channel coupling. This level of detuning is similar to what can be seen for manufactured resonators (see Chapter 3). The cross-coupling is about the same for the case that there are two equal size mass perturbations placed at 0 and 45°. This observation is in line with the electrostatically tuned case, where the off-diagonal terms are -40 to -50 dB smaller than the diagonal channels.

2.6 Summary of Ring Dynamics

Perturbation expansions of the solutions of an imperfect ring have been developed for several case studies when the perturbations are constrained to be point masses and massless radial springs. Although each perturbation scenario is solved on a case-by-case basis, a general procedure is outlined for determining the expressions that yield the successive terms in the frequency expansions. Boundary conditions are determined that must be satisfied by the uniform ring segments that lie between the perturbation locations, and the motion of these segments is represented as a weighted sum of the eigenfunctions for the uniform thin ring. The eigenfunctions, natural frequencies, and weights are all functions of the perturbation parameter, ϵ, which is the perturbing mass normalized by the ring mass. The expansions yield successive algebraic problems that are solved for a single perturbing mass, two masses with a varying angle between them, and a mass-spring perturbation. Rayleigh-Ritz analysis of the case studies using two- and twenty-term bases are also reported. For mass perturbations less than a few percent of the ring mass, all techniques yield essentially the same results, however, for larger mass ratios, the perturbation analysis more closely follows the finite element results in the two-mass cases. The critical issue that needs to be considered is the fact that as opposed to the practical problem in which the initial state of the ring resonator is imperfect, and the goal is to make the dynamics more desirable, this section solves the exact opposite problem. The initial state was perfect and different types of imperfections applied to the perfect ring, and their effects were studied. Although the perturbations considered in this section seem simple, they are quite accurate models of modifications we use in practice for correcting for manufacturing imperfections. By looking at the frequency response, we cannot figure out the nature of the perturbation, but we can find the type of perturbations that can correct for the initial imperfection. From the study of the effect of imperfections on an originally uniform ring, we learned what to do to perturb an originally imperfect ring, regardless of the nature of the imperfections, to make the dynamics more ideal. Chapters 3 and 4 apply the idea to a practical ring resonator.

CHAPTER 3

Wafer-Level Compensating for the Manufacturing Imperfections for $n = 2$ Modes

Nomenclature - Chapter 3

A	cross sectional area	E	modulus of elasticity
I	cross section moment of inertia	$\bar{r}$	ring mean radius
θ	angle coordinate	ω_n	natural frequency for mode n
ρ	density	j	$\sqrt{-1}$
$\omega_{1,0}$	pre-perturbation natural frequency for the first companion mode		
$\omega_{2,0}$	pre-perturbation natural frequency for the second companion mode		
ω_1	post-perturbation natural frequency for the first companion mode		
ω_2	post-perturbation natural frequency for the second companion mode		
$\Delta_0 := \omega_{2,0} - \omega_{1,0}$	pre-perturbation frequency split		
$\Delta := \omega_2 - \omega_1$	post-perturbation frequency split		
ω_0	average modal frequency		
U	spatial part of radial velocity	W	spatial part of tangential velocity
i	spoke layer	k	harmonic
$\alpha_{i,k}$	radial velocity amplitude for the k^{th} harmonic in spoke layer i		
$\beta_{i,2}$	tangential velocity amplitude for the 2^{nd} harmonic in spoke layer i		
$\tilde{\alpha}_{i,k} = \frac{\alpha_{i,k}}{\alpha_{1,2}}$	normalized radial velocity amplitude for the k^{th} harmonic in layer i		
$\tilde{\beta}_{i,2} = \frac{\beta_{i,2}}{\alpha_{1,2}}$	normalized tangential velocity amplitude for the 2^{nd} harmonic in layer i		
T_p	spatial kinetic energy change from a point mass perturbation		
$T_{1,0}$	nominal kinetic energy for the first companion mode		
$T_{2,0}$	nominal kinetic energy for the second companion mode		
T_1	kinetic energy change for the first companion mode		
T_2	kinetic energy change for the second companion mode		
$\epsilon_1 = \frac{T_1}{T_{1,0}}$	normalized kinetic energy perturbation for the first companion mode		
$\epsilon_2 = \frac{T_2}{T_{2,0}}$	normalized kinetic energy perturbation for the second companion mode		

Nomenclature - Chapter 3

$\psi_{1,k}$	phase of the k^{th} harmonic for the first companion mode		
$\psi_{2,k}$	phase of the k^{th} harmonic for the second companion mode		
Q_1	quality factor for the first companion mode		
Q_2	quality factor for the second companion mode		
m_0	nominal mass perturbation	α_T	normalization factor for amplitudes
$\gamma_{\text{g}} := \frac{1}{4}\omega_0 m_0 \alpha_T$	global sensitivity parameter	r_q	mass perturbation relative to m_0

Coriolis vibratory gyros (CVGs) which employ mode-matched resonators have the advantage of maximizing the signal-to-noise ratio (SNR) of the angular rate measurement relative to noise introduced by signal conditioning electronics. In many cases, the resonators are designed with some degree of axisymmetry such that one or more pairs of modes possess nominally degenerate modal frequencies. Small fabrication errors, however, cause the modal frequencies to detune, thereby reducing the signal-to-noise ratio that can be achieved with the associated CVG (see [KM13] for the analysis of a disk resonator). With the successful development of mode-matched micro-scale disk resonators [CGL14, SKS15, NAS13], quadruple mass resonators [TPZ11], hemispherical [BBC13, BBC14, SMG14, PZT11, ZTS12, KBK15, TSH14], and hemitoroidal [CWY14, HJC14] resonators, it has become imperative to create post-fabrication corrective procedures so that the pairs of modal frequencies can be brought back to degeneracy. This chapter reports the development and application of a wafer-level targeted silicon deep reactive-ion etching (SiDRIE) process for eliminating the modal frequency differences in a planar axisymmetric silicon resonator. The reduction of the frequency difference below 100 mHz is demonstrated for seven resonators on a wafer by selective ablation of masking resist and, in a subsequent step, a conformal layer of Parylene-C such that the mass distribution of the resonator is altered by the removal of silicon at the ablated areas with a timed etch.

There are currently few references reporting the permanent modal frequency mismatch reduction in MEMS mode-matched resonators as the current focus is to refine the fabrication processes to yield small initial modal frequency differences before any post-fabrication corrective procedures. A notable effort is [BBC14] wherein gold was ablated from the lip of a micro-scale hemispherical resonator in a post-fabrication step. Laser ablation of a ring was also reported in [GHB05]

but it degraded the quality factors. The planar resonator design in this chapter was also used for modal frequency mismatch reduction by mass-loading the resonator [SKS15] (see Chapter 4). One advantage of the present approach over the mass deposition in [SKS15] is the fact that the etch simply removes silicon and does not introduce metals or other materials that may not be compatible with downstream processing and packaging. Electrostatic tuning approaches, which do not yield permanent modification of the resonator, are not reviewed here.

The chapter is organized as follows. Sec. 3.1 briefly reviews the resonator used in this study. The test procedure is described in Sec. 3.1.1. The manufacturing of the resonator and the imperfections caused during the process are discussed in Sec. 3.1.2. Secs. 3.1.3 and 3.1.4 develop a semi-analytical model of the resonator's $n = 2$ modal frequency difference as a function of mass perturbations. A global sensitivity parameter is also defined and unifies several aspects of the model developed in [SKS15]. In the modeling for this chapter, it is assumed that the anti-node orientation remains the same before and after mass perturbations. Sec. 3.2.1 introduces the guided blanket etch, which is the first step in the simultaneous wafer-level reduction of modal frequency differences for individual die. In Secs. 3.2.2 and 3.2.3 the shortcomings of the guided blanket etch are elucidated and motivate the second step of the tuning process, which involves further targeted etching within each die. The results are discussed in Sec. 3.3 and Sec. 3.4 summarizes the results of this chapter.

3.1 Resonator Description

The resonator used in the present work is composed of nine nested rings connected by spokes of varying widths and spacing. There are twenty-four large spokes at a given radius which are targets for mass deposition or removal –see Fig. 3.1. The innermost large spoke layer is designated as the first layer ($i = 1$), and the outermost spoke layer is designated as the fourth layer ($i = 4$). The resonator is a modification of the design described in [SKS15]. The fabrication process and test procedure will be discussed here shortly. The reader is referred to [SKS15] for more information on the resonator fabrication, electrode layout, test procedure, and the process for extracting pertinent modal parameters from empirical frequency response data. In the present report, the resonator is

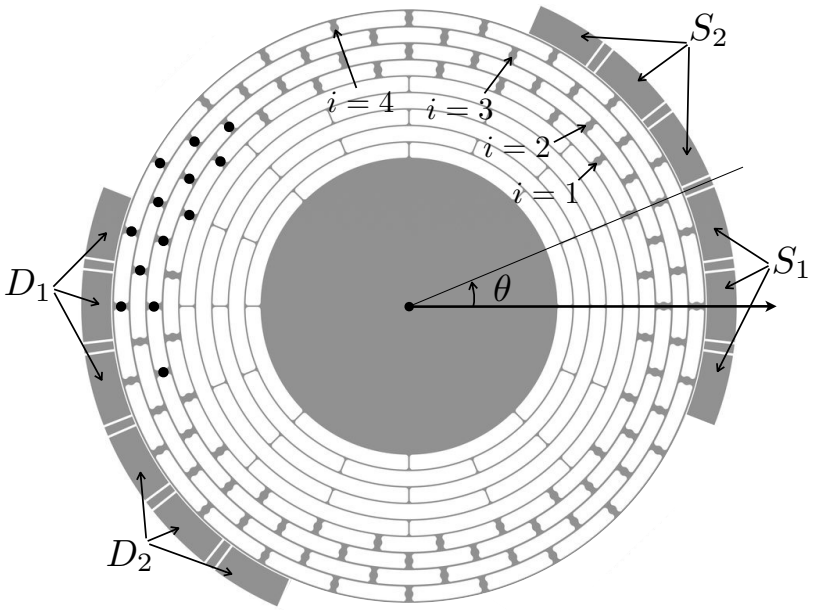

Figure 3.1: Electrode arrangement (S is a sense pick-off, and D is an electrostatic forcer), angle reference, and spoke layer indices. The dots "•" indicate the locations of perturbations for the finite element case studies.

fabricated without the gold film on, or the reservoirs in, the large spokes. Consequently, these areas are targets for further etching to selectively remove material from the resonator instead of adding material as was pursued in [SKS15]. It will be shown that material removal at the large spokes locations does not modify the stiffness properties of the resonator and so models that readily predict the changes in the resonator modal properties can be developed by assuming only the mass distribution is perturbed. The ultimate goal of this research is the wafer-level production of axisymmetric resonators with degenerate modal frequencies, but to make the post-blanket etch processing efficient, improved perturbation models of the resonator are necessary. Thus, the model developed in [SKS15] is further refined in Sec. 3.1.3 by assuming the anti-node orientation does not change by placing mass perturbations (this is a reasonable assumption for almost all cases studied in this chapter) and applied to the resonators on the 4 inch wafer shown in Fig. 3.4. The model will be further refined in Chapter 4 by removing this assumption. Probing of individual resonators is achieved with the card shown in the figure inset or by direct wire bonding between the resonator and a buffer board.

3.1.1 Test Procedure

Fig. 3.1 shows the pick-off and forcer arrangement that is optimized for testing the $n = 2$ pair. In order to optimize the observability and controllability of the $n = 2$ pair in a uniform thin ring, the centroids of the two pick-offs should subtend a 45° arc due to the fact that the $n = 2$ mode shapes are elliptical, and the orientation of one anti-node is 45° away from the other one. We dedicate three neighboring electrodes for a single pick-off because this maximizes the measurement signal associated with the $n = 2$ modes. The antipodal electrodes are configured as electrostatic forcers (the actuators), also evident in Fig. 3.1. In a non-ideal resonator, it is shown that the angle subtended by the anti-node orientations does not necessarily depart exactly 45° (see Chapter 2).

In a typical experiment, the two pick-off currents are buffered with high gain transresistance amplifiers. The amplifier outputs are then filtered with analog anti-alias filters and then sampled by the digital signal processing (DSP) analog to digital converter (ADC). The excitation signals can be directly applied by the DSP DAC since the required current is very low. Samples of the input and output sequences are stored for later processing, typically as multi-channel empirical frequency response estimates and occasionally a parametric time-domain model.

The UCLA CVG cannot operate in atmospheric pressure because squeeze film damping between the gaps created by the resonator rings and the electrodes (and other material attached to the base wafer) heavily damps the response of all modes (see Chapter 5). In fact, no modes are evident when the resonator is tested in air. Thus, the resonators are tested in a vacuum chamber in which the pressure can be reduced to several microTorr if necessary.

Using the aforementioned experimental set up yields a UCLA CVG broadband frequency response typical to that shown in Fig. 3.2. As we can see in this figure, there are three distinct peaks in the 0 to 28 kHz frequency band. They have been determined to be associated with the $n = 1, 2$ and 3 modal pairs as labeled.

Although Fig. 3.2 seems to indicate a single mode at isolated frequencies, zooming into a narrower frequency band around any of the peaks reveals that there are two modes. If the resonator where "perfectly" fabricated, only a single peak would be evident because the degenerate modes

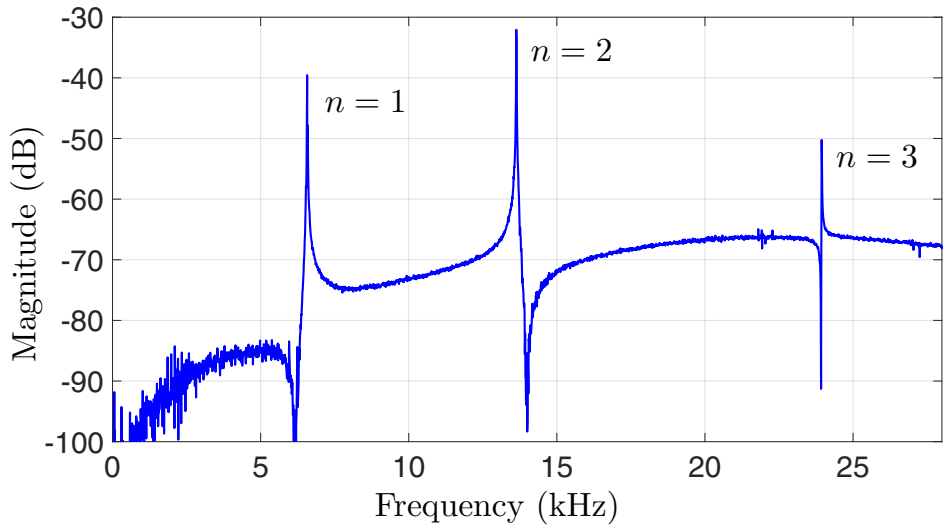

Figure 3.2: Broadband frequency response of the resonator magnitude plot showing a number of in-plane modes.

are not controllable or observable from any single forcer/pick-off pair. In fact, as the frequency detuning is eliminated, it is necessary to use the multi-input multi-output (MIMO) data to correctly build a model with the correct number of modes. As will be shown more extensively in Sec. 3.1.2 manufacturing errors "break" the resonator symmetry and lead to detuning of the various pairs of modes. This detuning will be evident in zoomed in frequency response plots.

3.1.2 Manufacturing Process and its Imperfections

Several iterations of the UCLA CVG were fabricated by Teledyne Scientific and Imaging. The resonator wafer is 270 μm thick (111) silicon (Si), and the base wafer is 450 μm thick (100) Si. The base wafer is etched to create recessed gaps for clearance of the resonator rings and thermally oxidized for electrical isolation. Openings in the oxide for substrate electrical contact are etched in the oxide layer, and gold (Au) is deposited for the wafer-wafer bonding and electrical connection between the resonator and base wafers. Separately, the resonator wafer is patterned with the mating bond metal pattern, and then the resonator and base wafers are joined using an aligned Au-Au thermo-compression bond process. Definition of the resonator rings and reservoir structures is then done using a two-level mask and deep reactive-ion etching. A resist mask is subsequently applied and patterned to define the resonator structure. The oxide layer is etched in

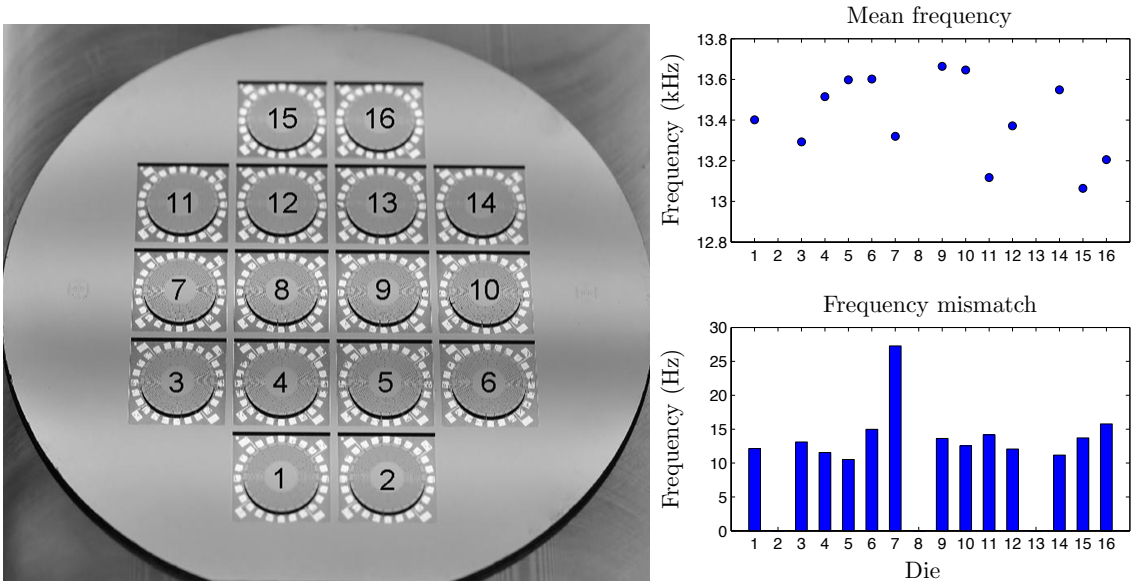

Figure 3.3: (Left) Resonators on the wafer with labels. (Right) Mean frequency and frequency mismatch

these locations, and a partial SiDRIE is performed using the same resist mask. The resist is then stripped, and the DRIE etch continued using the oxide mask to complete the etch of the resonator rings through the top wafer thickness, while simultaneously etching the shallow reservoirs into outermost spokes. The design of the UCLA CVG would, ideally, yield degenerate $n = 2$ and $n = 3$ modes, however, small manufacturing errors will always detune these modes. For example, Fig. 3.3 shows 16 resonators on a single 4-inch diameter wafer stack. The masking steps are identical for each resonator, and the resonators are simultaneously etched, however, it is evident that at the termination of the standard etch process, each mean frequency of the $n = 2$ pairs is different and so is their degree of detuning. In fact, it appears that each resonator etches in its own unique way, so it is impossible to specify or to determine *a priori* what the mean frequency will be let alone the final frequency detuning. Furthermore, the degree of detuning is so large for each resonator that it is essentially useless as a high-performance CVG in its present state. The same behavior is also seen for $n = 3$ modes.

To achieve the CVG's highest signal-to-noise ratio, it is necessary to modify the dynamics of each resonator to eliminate the frequency detuning. In this project, the focus is on perturbing the mass distribution while keeping the stiffness matrix untouched and one unique aspect of the UCLA CVG design is its ability to support research into the modification of the mass distribution

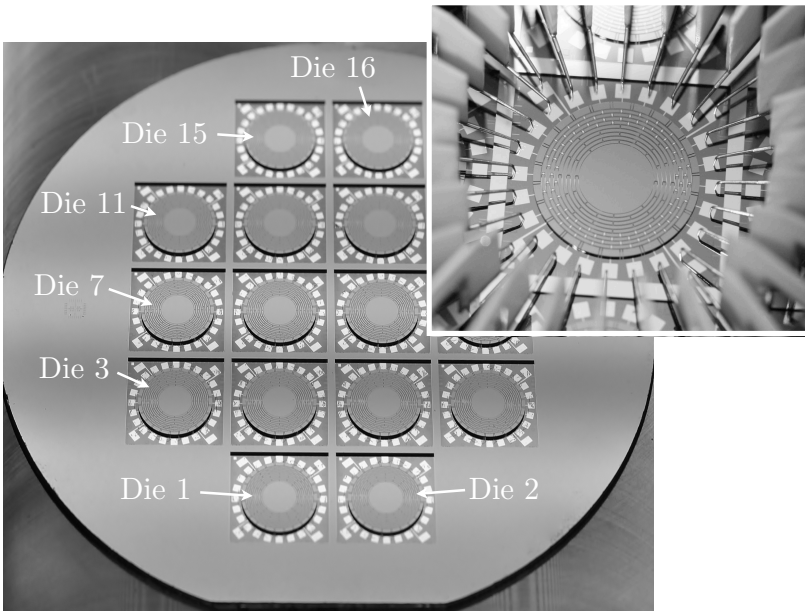

Figure 3.4: Sixteen resonators are fabricated on a 4 inch wafer. Wafer probe of a single resonator also shown.

for micro-scale axisymmetric resonators.

3.1.3 Perturbation Model

Uniform thin rings possess mode shapes given by $\cos(n\theta)$ and $\sin(n\theta)$ with associated degenerate natural frequencies $\omega_n^2 = \frac{n^6-2n^4+n^2}{n^2+1}\frac{EI}{\rho A \bar{r}^4}$, for $n = 2, 3, 4, \ldots$, where E is the modulus of elasticity, I is the ring cross-section moment of inertia, ρ is the ring material density, A is the ring cross-sectional area, and $\bar{r}$ is the ring radius. These mode shapes and frequencies are derived from a ring equation of motion that is developed under the same assumptions as those made for an Euler-Bernoulli beam [Rao07]. If the ring is perturbed, however, then, generally speaking, the mode shapes associated with the perturbed frequency ω_n are no longer simply $\cos(n\theta)$ and $\sin(n\theta)$ but will be composed of harmonics of all orders (see Chapter 2). The mode shapes associated with the resonator considered in this chapter are composed of multiple harmonics even for the "ideal" resonator because of the manner in which each ring is attached to its neighbors by the system of spokes, and despite the fact that the 2θ harmonics have the largest amplitude for ω_2 (the $n = 2$ wine glass modes), it is necessary to quantify other dominant harmonics, to build an accurate model of the spoke velocities.

Due to the complexity of the resonator design, a semi-analytical approach is adopted in order to develop a perturbation model for the resonator dynamics. As in [SKS15], the natural frequency deviation due to perturbations at the large spokes is modeled as a change in the resonator kinetic energy only –the elastic strain energy remains constant under these perturbations. This assumption is supported by finite element analysis. For example, Fig. 3.5 shows the strain energy density on a portion of the resonator for an $n = 2$ mode. The dark vertical bands on the side walls at the root of the spokes are the areas with the largest strain energy density while the white areas are where strain energy is smallest. Since the center of the spokes themselves have very little strain energy, selective etching these areas is assumed to only modify the kinetic energy of the modes.

The analysis of the perturbed kinetic energy of a given mode due to a small change in mass at the large spokes requires the radial and tangential components of the in-plane velocities at the large spokes. These velocity components can be represented as a discrete Fourier series with twelve distinct spatial harmonics since there are twenty-four spokes in a given layer. It will be shown that the ratios of the *amplitudes* of these harmonics can be assumed to be independent of the intensities and location of the mass perturbations. In other words, it is assumed that the mass perturbations are sufficiently small so that the relative amplitudes of the harmonics present in a given mode are not modified by the presence of the mass perturbations. This assumption is supported by the numerical case studies reported in Sec. 3.1.4. On the other hand, the spatial orientations (phases) are dependent on the mass perturbations. For a given mode of the $n = 2$ pair, denoted with index $p \in \{1, 2\}$, the spatial part of radial and tangential velocities at a particular spoke, defined by angle θ and spoke layer $i \in \{1, 2, 3, 4\}$, can be represented by the following partial Fourier series

$$\begin{aligned} U_{p,i}(\theta) &= \sum_{k=2,6,10} \alpha_{i,k} \cos(k(\theta - \psi_{p,k})), \\ W_{p,i}(\theta) &= \beta_{i,2} \sin(2(\theta - \psi_{p,2})), \end{aligned} \tag{3.1}$$

where the index k defines the $k\theta$ harmonic of the $n = 2$ mode shape, and $U_{p,i}$ and $W_{p,i}$ represent the radial and tangential velocity components, respectively. The amplitudes of the harmonics are represented by $\alpha_{i,k}$ and $\beta_{i,2}$ for the radial and tangential velocities, respectively, and the phases of the harmonics are represented by $\psi_{p,k}$. It should be noted that (3.1) is specific for the resonator design

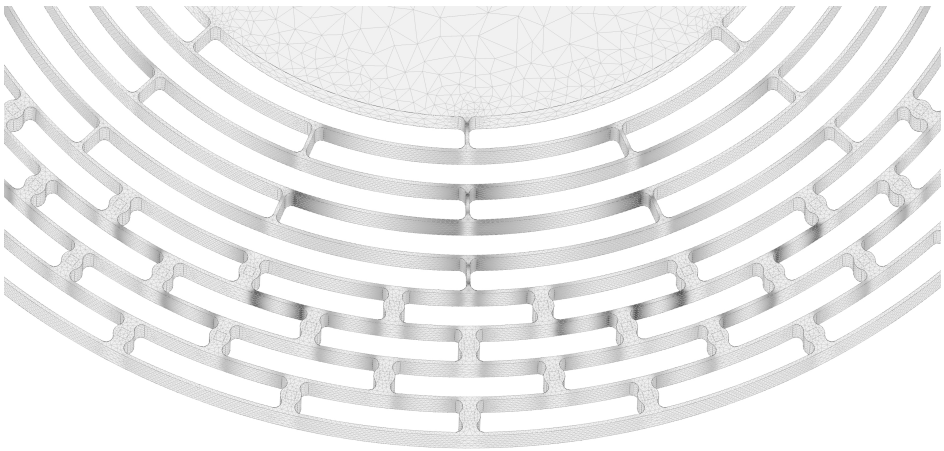

Figure 3.5: Detail of meshed resonator showing the large spokes. The dark vertical bands on the sidewalls are the areas where the strain energy density is highest.

under consideration and that other axisymmetric designs may possess a different set of dominant harmonics in the mode shapes. At the very least, $\alpha_{i,k}$ and $\beta_{i,k}$ will differ across resonator designs, however, Sec. 3.1.4 outlines a procedure that can be used to identify the important harmonics and associated parameters.

The form of (3.1) requires that the following be justified: 1) only three spatial harmonics are required to represent a spoke's radial velocity component ($k \in \{2, 6, 10\}$), 2) only one harmonic is required to represent a spoke's tangential velocity ($k = 2$), 3) the amplitudes of the harmonics are independent of θ and $n = 2$ mode under consideration (the amplitudes only depend on the layer, i, and harmonic index, k), 4) the phases $\psi_{p,k}$ depend on the mode and harmonic indices, but not the layer, and 5) the radial and tangential components have the same $k = 2$ phase. The justification is postponed until Sec. 3.1.4 so that an expression for the post-perturbation change in the differences of the modal frequencies can be developed.

A single mass perturbation of value m_0 (may be negative if mass is removed) located on the i^{th} layer at angle θ_0 creates the following spatial perturbations to the kinetic energies of each $n = 2$ mode,

$$T_p = \frac{1}{2} m_0 \left(U_{p,i}^2(\theta_0) + W_{p,i}^2(\theta_0) \right), \quad p = 1, 2. \tag{3.2}$$

The out-of-plane velocity is negligible for the $n = 2$ modes and is ignored in this analysis. The Rayleigh-Ritz method is used to estimate the perturbation of a modal frequency due to a pertur-

bation of the resonator kinetic energy [Fox90]. Consequently, the mass perturbation perturbs each modal frequency according to

$$\begin{aligned} \omega_1^2 &= \omega_{1,0}^2 \frac{1}{1+\epsilon_1} \approx \omega_{1,0}^2 \left(1-\epsilon_1\right), \\ \omega_2^2 &= \omega_{2,0}^2 \frac{1}{1+\epsilon_2} \approx \omega_{2,0}^2 \left(1-\epsilon_2\right), \end{aligned} \tag{3.3}$$

where $\omega_{1,0}$ and ω_1 are the pre- and post-perturbation natural frequencies of one of the $n = 2$ modes, respectively, and $\omega_{2,0}$ and ω_2 are the pre- and post-perturbation natural frequencies of the second companion $n = 2$ mode. When the modification on the dynamic of the structure is through point mass perturbations, the change in kinetic energy associated with a given mode is due to the new added masses relative to the new anti-nodes, plus the change in the kinetic energy associated with the point masses created the initial frequency split. The second term is caused by the change in the vibration pattern (anti-node orientation). So it should be noted that the analysis presented in this chapter is only accurate when the initial and final anti-nodes are essentially the same. This can happen in practice by adding relatively small masses anywhere (so the change in the frequency split is small compared to the initial split) or when large masses on the initial anti-node are placed since this implies that the final anti-node will then be close to the initial anti-node. Assuming preserving the anti-node orientation before and after the perturbations is reasonable for this chapter since for almost all cases the masses are placed near the anti-node orientations, because for tuning one single mode, the perturbation locations are essentially restricted to the anti-node orientation. When the objective becomes tuning multiple modes, though, the model presented herein fails to predict the results accurately. The model in this chapter is useful for studying the effect of other harmonics in the dynamics of the structure. A more accurate model for addressing this limitation is presented in Chapter 4 where there is no *a priori* information about the perturbation sites.

The relative change in kinetic energies of the modes due to the perturbation are denoted ϵ_1 and ϵ_2 and are equal to $T_1/T_{1,0}$ and $T_2/T_{2,0}$, where $T_{1,0}$ and $T_{2,0}$ are the nominal kinetic energies in each mode prior to the perturbation. It is necessary for $T_1 << T_{1,0}$ and $T_2 << T_{2,0}$ in order for these approximate expressions to be accurate, however, this requirement is satisfied in practice since the absolute change in a given modal frequency is typically less than one part in a thousand.

The mass perturbations are selected to reduce the difference in perturbed modal frequencies so it is useful to manipulate the expressions in (3.3) such that the difference is explicit,

$$\omega_2^2 - \omega_1^2 = \omega_{2,0}^2 - \omega_{1,0}^2 - \omega_{2,0}^2\epsilon_2 + \omega_{1,0}^2\epsilon_1. \tag{3.4}$$

Terms can be factored: $\omega_2^2 - \omega_1^2 = (\omega_2 - \omega_1)(\omega_2 + \omega_1)$ and $\omega_{2,0}^2 - \omega_{1,0}^2 = (\omega_{2,0} - \omega_{1,0})(\omega_{2,0} + \omega_{1,0})$. The expressions of interest are the pre- and post-perturbation differences in the modal frequencies. The pre-perturbation difference is denoted $\Delta_0 := \omega_{2,0} - \omega_{1,0}$ and the post-perturbation difference is denoted $\Delta := \omega_2 - \omega_1$, thus, (3.4) is rearranged to

$$\Delta = \Delta_0 \frac{\omega_{2,0} + \omega_{1,0}}{\omega_2 + \omega_1} - \frac{\omega_{2,0}^2}{\omega_2 + \omega_1}\epsilon_2 + \frac{\omega_{1,0}^2}{\omega_2 + \omega_1}\epsilon_1. \tag{3.5}$$

Let ω_0 represent the average modal frequency of the $n = 2$ modes for the resonator under consideration, then, the leading order value of the ratio $(\omega_{2,0} + \omega_{1,0})/(\omega_2 + \omega_1)$ is 1 and the leading order value for the ratios $\omega_{2,0}^2/(\omega_2 + \omega_1)$ and $\omega_{1,0}^2/(\omega_2 + \omega_1)$ is $\omega_0/2$. Thus, the following relation approximately relates the pre- and post-perturbation values of the frequency difference,

$$\Delta = \Delta_0 - \frac{\omega_0}{2}\left(\frac{T_2}{T_{2,0}} - \frac{T_1}{T_{1,0}}\right). \tag{3.6}$$

Substituting (3.2) into (3.6) yields an expression relating the pre- and post-perturbation modal frequency *differences* due to a mass perturbation of size m_0 located on the i^{th} layer at angle θ_0

$$\begin{aligned}\Delta = \Delta_0 &- \frac{\omega_0 m_0 \alpha_{1,2}^2}{4T_{2,0}}\left[\left(\sum_k \tilde{\alpha}_{i,k}\cos(k(\theta_0 - \psi_{2,k}))\right)^2 + \left(\tilde{\beta}_{i,2}\sin\left(2(\theta_0 - \psi_{2,2})\right)\right)^2\right] \\ &+ \frac{\omega_0 m_0 \alpha_{1,2}^2}{4T_{1,0}}\left[\left(\sum_k \tilde{\alpha}_{i,k}\cos(k(\theta_0 - \psi_{1,k}))\right)^2 + \left(\tilde{\beta}_{i,2}\sin(2(\theta_0 - \psi_{1,2}))\right)^2\right],\end{aligned} \tag{3.7}$$

where k is summed over indices $\{2, 6, 10\}$. In this expression the radial harmonic amplitude for $k = 2$ and $i = 1$, i.e. $\alpha_{1,2}$, is factored out of the kinetic energy expressions and is used to normalize the remaining amplitudes. In other words, $\tilde{\alpha}_{i,k} := \alpha_{i,k}/\alpha_{1,2}$ and $\tilde{\beta}_{i,2} = \beta_{i,2}/\alpha_{1,2}$. It will be shown in Sec. 3.1.4 that these normalized amplitudes can be assumed to be independent of the mode

under consideration and independent of the size of the (small) mass perturbation. The fact that $\tilde{\alpha}_{i,k}$ and $\tilde{\beta}_{i,2}$ are the same for both $n = 2$ modes, and the fact that they are independent of the mass perturbation, implies that the kinetic energy in a given mode is determined by specifying any one of the harmonic amplitudes. In this analysis, it is convenient to specify $\alpha_{1,2}$, which is why it is factored out of the expressions in (3.7). Thus, further consolidation in (3.7) is possible because $\alpha_{1,2}^2/T_{1,0} = \alpha_{1,2}^2/T_{2,0}$. These ratios are denoted by the parameter α_T. Thus, the constant multiplying the sums with the normalized velocity components is defined as the *resonator sensitivity parameter*, denoted γ_{g},

$$\gamma_{\mathrm{g}} := \frac{1}{4}\omega_0 m_0 \alpha_T. \tag{3.8}$$

This single global sensitivity parameter represents, in a general sense, the change in the modal frequency difference for a mass perturbation of value m_0 (the unit of γ_{g} is rad/s). It will be numerically estimated in Sec. 3.1.4 and experimentally estimated in Sec. 3.2.2. Note that γ_{g} can be used for all resonators of a specific design, i.e., it is not necessary to measure the parameter for each resonator. This definition also removes a shortcoming of the model developed in [SKS15] which required the estimation of a separate sensitivity parameter for each layer of spokes. This unified treatment is also applied to a more accurate model in Chapter 4. The global sensitivity idea will be applied to both $n = 2$ and $n = 3$ modes which leads to global sensitivity value for each mode.

Multiple mass perturbations can be addressed by extending (3.7). In fact, the effect of simultaneous perturbations on the modal frequency difference are additive because the perturbed kinetic energies of the modes are simply a sum of the individual perturbations, i.e. these terms are added to (3.2). Thus, if there are l mass perturbations, located at angles θ_q, $q = 1, 2, \ldots, l$, and spoke layer $i_q \in \{1, 2, 3, 4\}$ with mass $r_q m_0$, where r_q represents the mass perturbation relative to m_0, then the expression for Δ is

$$\begin{aligned}\Delta = \Delta_0 - \gamma_{\mathrm{g}} \sum_{q=1}^{l} r_q \Bigg[&\Big(\sum_k \tilde{\alpha}_{i_q,k} \cos(k(\theta_q - \psi_{2,k}))\Big)^2 + \Big(\tilde{\beta}_{i_q,2} \sin\left(2(\theta_q - \psi_{2,2})\right)\Big)^2 \\ &- \Big(\sum_k \tilde{\alpha}_{i_q,k} \cos(k(\theta_q - \psi_{1,k}))\Big)^2 - \Big(\tilde{\beta}_{i_q,2} \sin(2(\theta_q - \psi_{1,2}))\Big)^2 \Bigg].\end{aligned} \tag{3.9}$$

It should be noted that the expression in (3.9) is a representation of the relationship of the

frequency split before and after perturbations assuming that the anti-node orientation does not change due to the perturbations.

It is worthwhile reviewing what information is required to use (3.9) to predict Δ. First, Δ_0 is estimated from frequency response measurements of the resonator prior to the mass perturbation using the modeling process described in [SKS15]. The normalized radial and tangential velocity amplitudes are determined from finite element analysis (FEA) in Sec. 3.1.4 and yield a numerical estimate of γ_{g} (a series of experiments in Sec. 3.2.2 provide an experimental estimate). Finally, the phases of the harmonics, $\psi_{p,k}$, must be considered. The phases must be experimentally determined because they will be different for every fabricated resonator and will change (slightly) after a perturbation cycle. This analysis provides insight into what should be measured for employing a comprehensive model of the frequency perturbation as a function of the mass perturbation. For the resonator design under consideration, however, it is only possible to reliably measure the phase of the $k = 2$ harmonic. This is discussed in more detail in Sec. 3.2.

3.1.4 Numerical Case Studies

This section provides numerical justification for the assumptions that were invoked in claiming (3.1) is a reasonable model for the spoke velocities. Since the resonator dynamics are difficult to quantitatively analyze using a first principles approach, modal analysis of the structure using finite elements is used to compute the radial and tangential velocity components at all large spokes. The finite element model is not fit to a given empirical frequency response as this would be a time consuming and ultimately fruitless pursuit since it is not known how to estimate the local variations in mass and stiffness that produce the observed deviations from a modally degenerate "ideal" resonator. Thus, the modal analysis is used to identify features in the modes which appear to be invariant under small perturbations. All continuous structural systems have an infinite number of natural frequencies and finite element analysis can be used to estimate a subset of these natural frequencies and their associated mode shapes. Although these numerical techniques are not useful for predicting the dynamics of given physical resonator, they can at least be used to estimate approximate values for the modal frequencies. As the UCLA CVG exploits two resonant modes

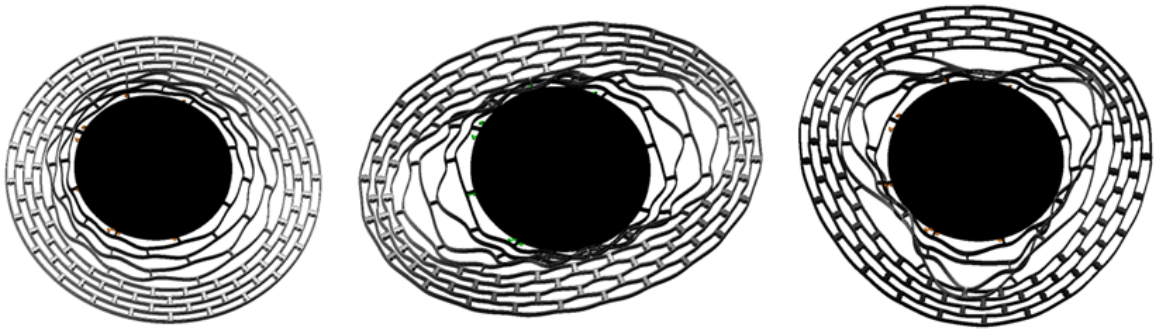

$n = 1$ $n = 2$ $n = 3$

Figure 3.6: In-plane mode shapes for the UCLA CVG with approximate modal as follows: $\omega_1 \approx 8.1$ kHz, $\omega_2 \approx 14.6$ kHz, $\omega_3 \approx 27.8$ kHz.

for measuring the rotation or angular rate of rotation the primary focus in the modal analysis is on the mode shapes that have significant Coriolis coupling terms. Furthermore, the analysis also is mainly concerned with mode shapes that are primarily in-plane because these are the only modes that can be effectively detected with the on-board electrodes. Several commercial software packages are used for the FEA (SolidWorks and Comsol Multiphysics) and Fig. 3.6 depicts the three lowest frequencies of in-plane modes in the UCLA CVG. Each of the modes shown in this figure has a "companion" mode in very close proximity, however, the orientation of the mode shape will be different for the companion mode.

The Coriolis coupling between $n = 1$ in-plane modes is significant, however, these modes are easily excited by vibration of the central stem and so they are not typically used in CVGs, however, they can be used in accelerometers. The first pair of modes that are nominally isolated from stem vibrations is the $n = 2$ pair. Furthermore, of all of the pairs that are nominally isolated, the Coriolis coupling term is largest for this pair. Other pairs of interest are the $n = 3$ and $n = 4$ pairs and they enjoy the advantage of having much higher nominal frequencies that serve to even further isolate from the vibration spectra that are typical in vehicles and aircraft. Note that although the $n = 2, 3, 4$ pairs in UCLA CVG are nominally isolated from stem vibration, in practice, there is some coupling due to the imperfect mass and stiffness distribution associated with these modes. The disadvantage of the $n = 3, 4$ pairs, though, is the fact that the Coriolis coupling term is weaker than in the $n = 2$ pair. It should be noted that although the Coriolis coupling is weaker for $n = 3$ modes, having two tuned pair on one device can improve the quality of the measurements. The

results for $n = 3$ modes will be postponed until Chapter 4.

An example of the fine mesh that is used in the FEA is shown in Fig. 3.5. The modal analysis yields the Cartesian velocity components at any point in the resonator but because mass is removed from the large spokes in the physical resonators, the spoke velocity components are of particular interest. For the FEA study, the mass at the large spokes is manipulated by changing the density of the elements in an 80μm$\times 80\mu$m patch in the center of the spokes (also shown in Fig. 3.5), Thus, the Cartesian velocity components are determined at the center of each large spoke on the top surface of the resonator and then transformed into radial and tangential components. Then, the discrete Fourier series of the radial and tangential components are computed for each spoke layer (twenty-four spokes per layer). Each perturbation "experiment," in which the density of the square patch is varied, yields Fourier series for the velocity components for each mode. A total of twenty-four perturbation case studies were performed: there are thirteen single spoke perturbations at the locations shown in Fig. 3.1. In addition to the single spoke perturbations, multi-mass perturbations involving pairs of spokes were also conducted. The modal analysis shows that the *ratios* of the amplitudes of Fourier series coefficients for the radial and tangential velocity components can be assumed to be constant and independent of the $n = 2$ mode under consideration, even when the resonator is perturbed. A similar analysis will be performed on $n = 3$ modes in Chapter 4.

The results of all twenty-four case studies are summarized in Fig. 3.7. The largest magnitude Fourier coefficient in all cases corresponds to $\alpha_{1,2}$, that is, the $k = 2$ harmonic in the radial velocity at the innermost spoke layer ($i = 1$). All other Fourier coefficient magnitudes in each experiment are normalized by $\alpha_{1,2}$ to yield the normalized Fourier coefficient magnitudes (denoted $\tilde{\alpha}$ and $\tilde{\beta}$) shown in this figure. The following may be concluded from Fig. 3.7: 1) only the $k \in \{2, 6, 10\}$ terms of radial velocity harmonics, and $k = 2$ term for the tangential velocity harmonics, need to be retained for an accurate description of the spoke velocities since these Fourier components are dominant, 2) for a given i and k, the normalized amplitudes are the same for each mode in the $n = 2$ pair, and 3) the normalized amplitudes can be assumed to be *independent* of the mass perturbation intensity and location due to the clustering of normalized amplitudes for a given harmonic and spoke layer. The values of the normalized amplitudes that are retained for the analysis are summarized in Table 3.1. It can be argued that retaining the $k = 1$ and 3 radial velocity harmonics

is justified due to their amplitude relative to $k = 10$, however, due to the limited sensing in the present resonators, it is not possible to measure all of the harmonic phases necessary for predicting the post-perturbation frequency difference, so these terms are neglected in the analysis.

The phases associated with the Fourier series must also be addressed. The Fourier analysis has treated each spoke layer separately, however, the numerical experiments show that for a given test case, the phases for each harmonic are the same for all spoke layers. This vastly simplifies the analysis because all the layers will have the same pattern of motion with different amplitudes only. This is the reason that the frequency perturbation model (3.7) assumes for a given harmonic, that the phases of each layer are equal. This property is appealing because it means that it is necessary to measure the phase of only one spoke layer when determining the phase of the $k\theta$ harmonic. Numerical evidence supports this hypothesis. For this part of the discussion, the notation will be modified to avoid a proliferation of indices. The phase of a particular harmonic is still denoted by ψ, however, the subscript will now indicate the particular spoke layer. The mean value of the set of phase differentials across layers $\{\psi_4 - \psi_3, \psi_4 - \psi_2, \psi_4 - \psi_1\}$ for the radial $k = 2$ harmonic, considering both $n = 2$ modes, and then averaging over the entire set of numerical cases is -0.0042° with a standard deviation of 0.0123°. The same computation for the radial $k = 6$ harmonic yields a mean value of 0.5326° with a standard deviation of 0.2930°. Finally, for the $k = 10$ harmonic, the mean value of $\psi_2 - \psi_1$ is 0.5117° with a standard deviation of 0.4582°. These results justify the form for the radial velocity $U_{p,i}$ in (3.1) in which the phases are independent of the ring under consideration.

The phases of Fourier series coefficients for the spoke tangential velocities must be studied in order to justify the representation of $W_{p,i}$ in (3.1). Only the $k = 2$ harmonic is significant in the Fourier series of the tangential velocities according to Fig. 3.7. The mean value of the set of phase differentials across layers $\{\psi_4 - \psi_3, \psi_4 - \psi_2, \psi_4 - \psi_1\}$ for the tangential $k = 2$ harmonic, considering both $n = 2$ modes, and averaged over the set of numerical cases is -0.0066° with a standard deviation of 0.0250°. This implies that the phase of the $k = 2$ tangential harmonics are equal across the spoke layers. Furthermore, for a given $n = 2$ mode, computation of the phase difference between the $k = 2$ harmonics for the radial and tangential velocities is 45.00° with a standard deviation of 0.0194°, which implies the phases are locked. In other words, measurement

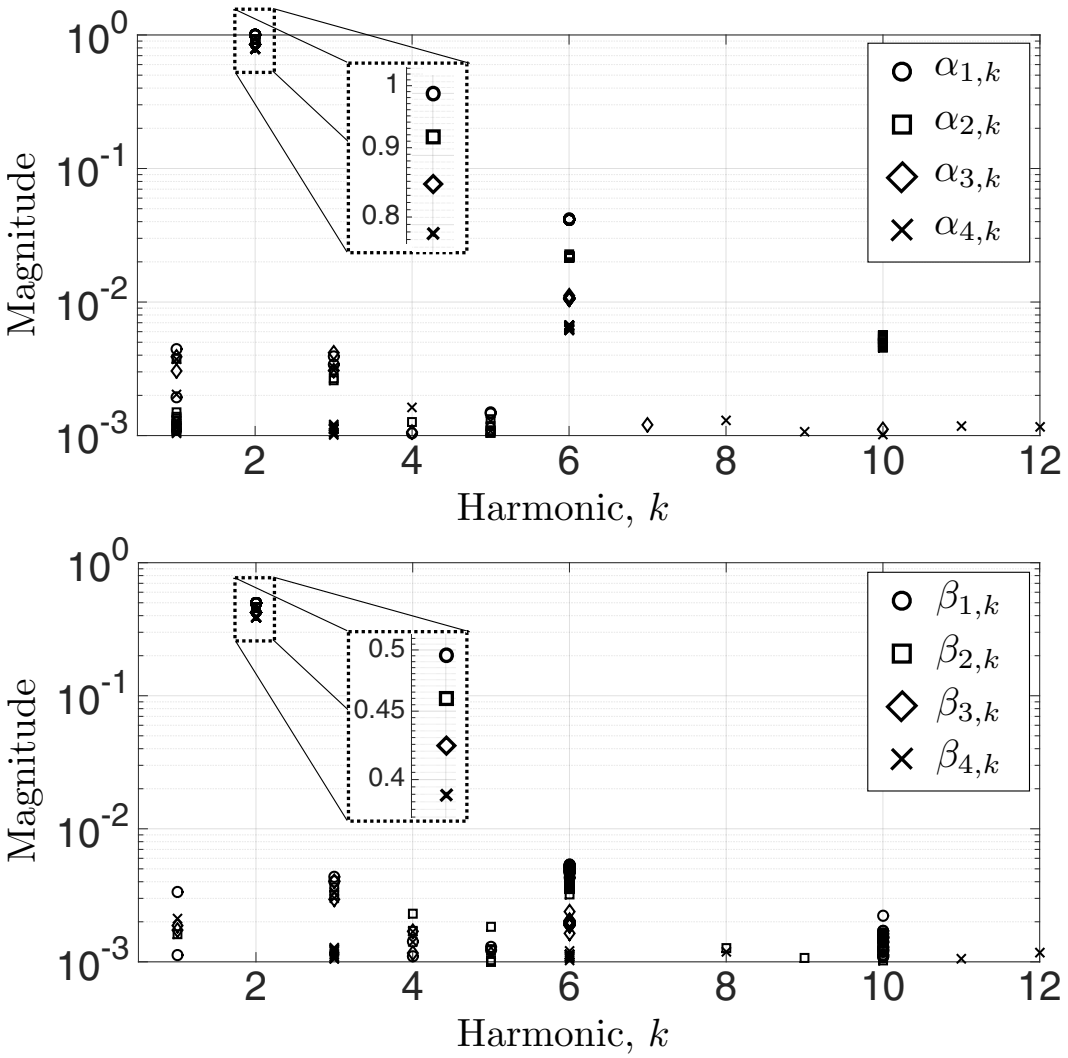

Figure 3.7: (Top) The magnitude of the Fourier series coefficients for the spoke radial velocities at different layers. All the harmonics are negligible except for $k \in \{2, 6, 10\}$. (Bottom) The magnitude of the Fourier series coefficients for the spoke tangential velocities. All harmonics are negligible except for $k = 2$.

of the $k = 2$ phase associated with the radial velocity also determines the phase associated with the tangential velocity. This analysis is required to justify (3.1) since the 45° phase difference between the tangential velocities and radial velocities is accommodated by using the sine function in $W_{p,i}$ instead of the cosine function with the 45° offset. It is interesting to note that for a thin, uniform, inextensible ring the kinematic relationship $U = \mathrm{d}W/\mathrm{d}\theta$ exists between the in-plane radial and tangential velocities, which implies the phases of the $k = 2$ radial and tangential velocity harmonics differ by 45° [Rao07].

Additional information can be extracted from the finite element analysis of the perturbation cases. Considering a single test case, the phase difference between each mode for a given harmonic can be computed and then these values can be averaged over all test cases. Using the same phase notation as (3.1), the following is determined for each test case: $\psi_{2,k} - \psi_{1,k}$, separately for $k = 2, 6, 10$. Averaging over all test cases yields a value of 44.9954° for $k = 2$ with a standard deviation of 0.0125°, 15.0200° for $k = 6$ with a standard deviation of 0.6451°, and 9.0038° for $k = 10$ with a standard deviation of 0.0414°. This shows that the $k\theta$ harmonics of the two $n = 2$ modes in a given test case can be assumed to be spatially orthogonal in the sense that $|\psi_{2,k} - \psi_{1,k}| = 90^\circ/k$. The velocity components (3.1) do not make explicit use of this property because it is assumed that $\psi_{p,k}$ are available from measurements, however, this property will be assumed when using (3.9) to compute a range for Δ for a given perturbation scenario due to unmeasured phases. Finally, for the cases where the mass perturbations are placed near the anti-node (to ensure preserving the anti-node orientation), the FEA is also estimated the sensitivity parameter

$$\gamma_{\text{FEA}} = 0.325\,\text{Hz} \tag{3.10}$$

for a mass of $m_0 = 0.1193\,\mu$g. This mass is equivalent to an $80\,\mu\text{m} \times 80\,\mu\text{m} \times 8\,\mu\text{m}$ rectangular prism of silicon which corresponds to a nominal amount of silicon to be removed in the experiments in Sec. 3.2.2.

Table 3.1: Normalized amplitudes of velocity harmonics (standard deviation in parenthesis)

layer, i	$\tilde{\alpha}_{i,2}$	$\tilde{\alpha}_{i,6}$	$\tilde{\alpha}_{i,10}$	$\tilde{\beta}_{i,2}$
1	1	0.0413	0.0287	0.4969
	(0)	(0.00021)	(0.00015)	(0.00031)
2	0.9289	0.0218	0.0055	0.4603
	(0.00011)	(0.00023)	(0.00040)	(0.00036)
3	0.8506	0.0107	0	0.4214
	(0.00034)	(0.000071	($\star$)	(0.00010)
4	0.7868	0.0065	0	0.3886
	(0.00013)	(0.00020)	($\star$)	(0.00025)

3.2 Wafer-Scale Frequency Tuning

The targeted etch approach for reducing the frequency split across all resonators proceeds in two steps. The first step, after the standard blanket etch concludes, is to ablate photoresist on the resonators in strategic areas so that continued etching will reduce the $n = 2$ modal frequency differences to a greater degree than the standard blanket etch alone. The perturbation model developed in Sec. 3.1.3 is used to select ablation locations. However, it is shown that it is not possible to fine-tune the modal frequencies since etching with small areas exposed on the spokes (denoted the *guided blanket etch*) will still globally etch the resonator and modify its dynamics in a manner that is not predicted by the perturbation model. Indeed, the test results in Sec. 3.2.1 suggest that the mass removal modifies the stiffness and mass distribution of the resonator in a complicated and unpredictable manner. The second step of targeted etching occurs once the photoresist is stripped from the wafer and a conformal coat of Parylene-C is applied. The coating is then ablated in desired areas, and a timed etch commences, but because the conformal coat withstands the etch, only the exposed areas have material removed, and the perturbation model in this case accurately predicts the post-etch modal frequency difference. Thus, the model can be used as a guide for selecting the areas for conformal coat ablation. The second step is discussed in Sec. 3.2.3.

3.2.1 Guided Blanket Etch and Initial Steps Toward Wafer-Level Silicon Ablation

At the conclusion of the standard blanket etch, there is an opportunity to selectively remove material from the large spokes by ablating the photoresist and continuing the etch. It is necessary to estimate the modal parameters to use (3.7) to search for ablation locations such that Δ is reduced to the desired level. As only one wafer was available for experimentation, the sensitivity parameter γ_{g} was estimated from the FEA (see (3.10)), although experimental estimates of γ_{g} are obtained later. The limited sensing in the resonator (the radial velocity of the outermost ring is measured by electrodes that subtend a 15° arc, [SKS15]) means that it is not possible to reliably measure $\psi_{p,6}$ and $\psi_{p,10}$ because the normalized amplitudes associated with the outermost spokes ($i = 4$) is about two orders of magnitude smaller than the amplitudes of the $k = 2$ harmonics. Furthermore, the spatial filtering of the electrodes further reduces the gain of these harmonics. The ideal locations in the resonator for measuring $\psi_{p,6}$ and $\psi_{p,10}$ are in the innermost spoke layers ($i = 1$) where electrodes do not currently exist for measuring the in-plane motion. The perturbation model (3.9) is truncated to include only the $k = 2$ harmonics for purposes of selecting the ablation sites. In other words, the following expression is used to search over θ and i to determine suitable locations for perturbations that will reduce $|\Delta|$ below a desired value,

$$\begin{aligned}\Delta = \Delta_0 - \gamma_{\mathrm{g}} \sum_{q=1}^{l} r_q \Big[& \tilde{\alpha}_{i_q,2}^2 \cos^2(2(\theta_q - \psi_{2,2})) + \tilde{\beta}_{i_q,2}^2 \sin^2(2(\theta_q - \psi_{2,2})) \\ & - \tilde{\alpha}_{i_q,2}^2 \cos^2(2(\theta_q - \psi_{1,2})) - \tilde{\beta}_{i_q,2}^2 \sin^2(2(\theta_q - \psi_{1,2})) \Big].\end{aligned} \tag{3.11}$$

Nevertheless, (3.9) will be used to estimate upper and lower bounds for Δ by assuming worst-case values for the unmeasured phases $\psi_{p,6}$ and $\psi_{p,10}$. In order for (3.11) to yield accurate results, the search space is constrained to anti-node orientations.

The modal parameters of each resonator on the 16-die wafer (Fig. 3.4) can be estimated after the standard blanket etch concludes even with the photoresist present. The photoresist mass-loads the resonator and dampens the modes, however, reliable estimates of the modal frequency *difference*, i.e., Δ_0, and the $k = 2$ phases can be obtained. The next step is to selectively ablate the photoresist from certain exaggerated spokes with the objective of exposing the top surface of the silicon in the

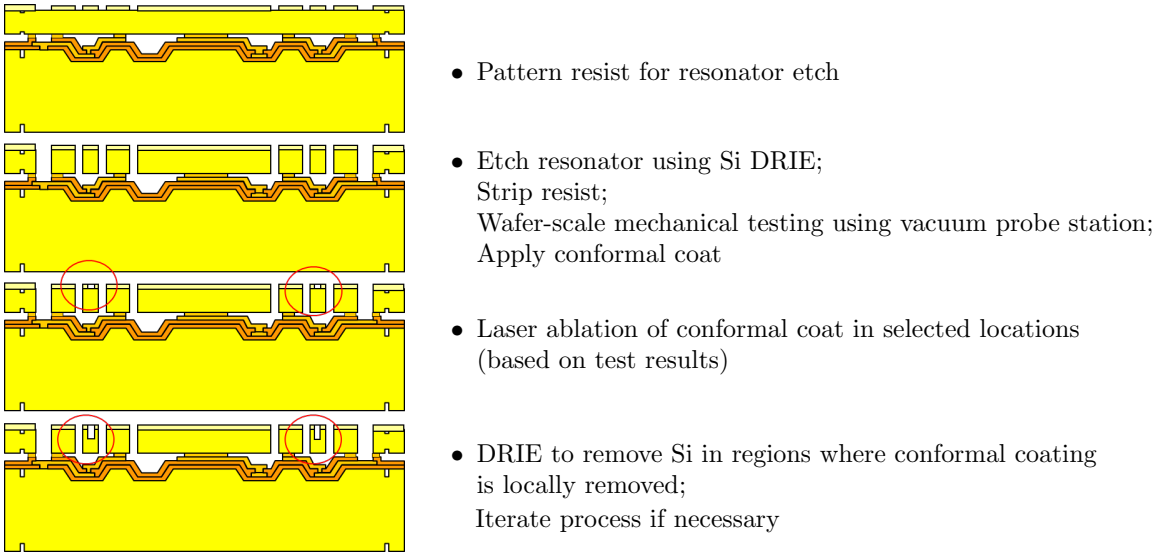

Figure 3.8: Process for photoresist ablation for the guided blanket etch [KBS15].

ablated areas –refer to Fig. 3.8. The wafer is then inserted back into the etcher for a short timed etch. The ablated areas are selected to be near the anti-nodes of the lower frequency mode of the $n = 2$ pair since removing mass from this mode will have the effect of raising its modal frequency to a greater extent than that of the companion mode, i.e., the frequency detuning will be reduced. The etch time is estimated based on the desired amount of mass to be removed at the spokes.

The measured modal frequencies are summarized in Table 3.2. Die 2, 8, and 13 are non-functional and are not included in the table. The $n = 2$ modal frequencies extend from 13.057 kHz to 13.657 kHz, and the modal frequencies differences extend from 10.52 Hz to 27.27 Hz. This range of mean frequencies and initial differences suggests that each die will require a custom etch profile. The modal frequency differences reported here are always positive because ω_2 is always assigned to higher frequency $n = 2$ mode once the measurements have been made. Thus, the phase $\psi_{2,2}$ in (3.11) is associated with the higher frequency mode as well. It is possible that the models (3.9) and (3.11) will predict $\Delta < 0$, however, if a subsequent cycle of etching is desired, then the labels on the modes will be switched along with their corresponding phases.

The spokes that are selected for ablation are determined by searching over a handful of ablation sites in a neighborhood of the lower frequency mode anti-node such that a reduction of the frequency differences of approximately 8 Hz is achieved for all resonators as predicted by (3.11),

Table 3.2: Summary of standard blanket etch results

Die	ω_1 (Hz)	ω_2 (Hz)	Δ_0 (Hz)
1	13394.90	13407.03	12.13
3	13285.87	13298.98	13.11
4	**13508.92**	**13520.46**	**11.54**
5	13592.69	13603.21	10.52
6	13594.35	13609.33	14.98
7	13306.43	13333.70	27.27
9	13657.04	13670.67	13.63
10	13640.40	13652.94	12.54
11	13110.13	13124.30	14.17
12	**13365.44**	**13377.51**	**12.07**
14	**13543.59**	**13554.77**	**11.18**
15	13056.97	13070.67	13.70
16	**13197.65**	**13213.42**	**15.77**

i.e., due to the large spread in Δ_0, the guided blanket etch is designed to achieve $\Delta - \Delta_0 \leq 8\,\text{Hz}$. Die 4, 12, 14 and 16 are used for experimental controls and are not ablated. In other words, these die will continue to be etched using the standard process, while the ablated resonators will experience the targeted etch at the spokes in addition to the standard process. The ablation is performed using a New Wave Research QuikLaze laser cutting system. The ablated areas are approximately 80 μm by 80 μm. A DRIE timed etch is performed such that the modal frequency difference would be reduced by 8 Hz in the absence of any other factors that could influence the modal frequencies. The etch time is defined by the desired etch depth to remove the targeted mass of material. Using a calibrated etch rate, the corresponding time is calculated. Due to the large size of the ablated features and the short etch depths, etch rate consistency run-to-run is typically within a few percent. The sensitivity parameter γ_{FEA} is used to estimate the duration of the timed etch based on the desired etch depth. The results of the guided blanket etch are shown in Table 3.3 and it is clear that the ablated die experience more significant reductions in modal frequency differences compared to the control die. Thus, the guided blanket etch appears to successfully reduce the frequency split to a greater degree than the standard blanket etch.

The challenge with the guided blanket etch, though, is the fact that the resonator stiffness is also clearly modified in addition to the mass distribution. This is evident from the data in Fig. 3.9

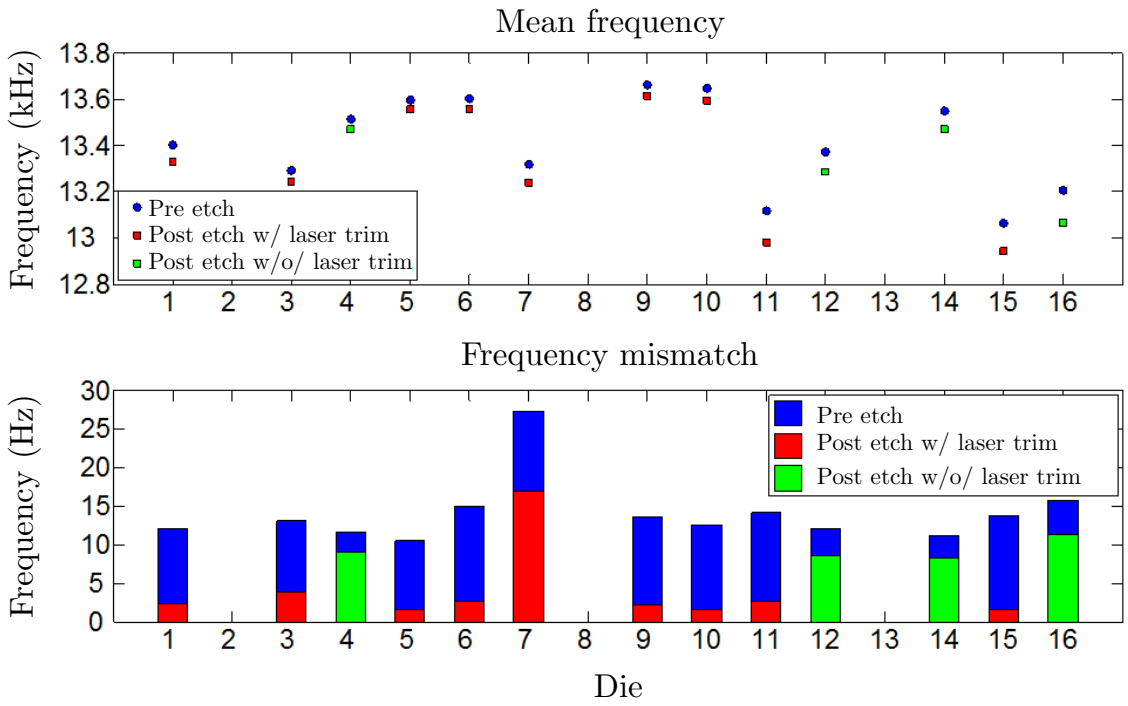

Figure 3.9: Summary of standard and guided blanket etch on the mean $n = 2$ modal frequencies and the frequency mismatch. The guided blanket etch is effective in reducing the $n = 2$ modal frequency mismatch.

which shows that the mean modal frequencies of the $n = 2$ modes are *decreased* by a significant amount (compared to the detuning that must be eliminated). Figs. 3.10 and 3.11 show empirical frequency responses of two measurement channels for Die 14 (a control die) and Die 3, respectively, before and after the guided blanket etch. In Table 3.3, the modal parameter measurements were made after the photoresist was stripped, so that accurate damping values are obtained. Note that continuing the blanket etch on the control die further reduces the modal frequency differences. The reductions range from 2.5 to 4.4 Hz depending on the die, but it illustrates the unfeasibility of using the blanket etch to eliminate the frequency differences across all die, especially since the range of starting Δ_0 is large. Note, however, that the ablated die all experience significant reductions in their modal frequency differences but the variability introduced from etching other areas of the resonator still creates too much uncertainty to accurately predict the final modal frequency difference. Nevertheless, this exercise demonstrates that the guided blanket etch can be used to systematically reduce Δ and provides a good starting point for the targeted etching that follows.

Changing stiffness simultaneously with the mass modification makes it very difficult to predict

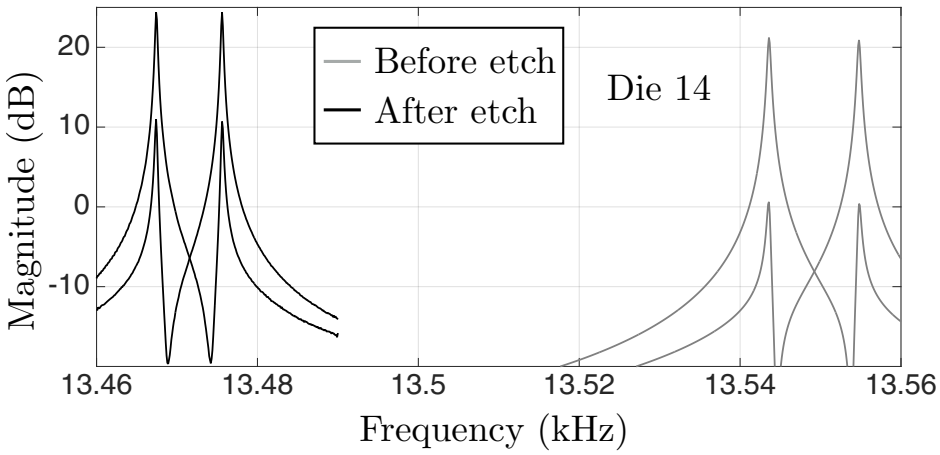

Figure 3.10: Mean modal frequencies reduce with further blanket etching. The modal frequency difference also has a modest reduction.

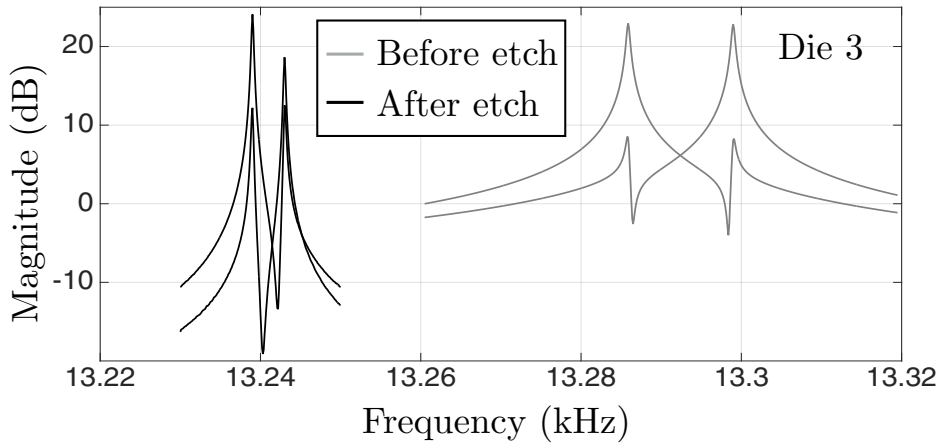

Figure 3.11: Modal frequencies after photoresist ablation on selected spokes and further blanket etching experiences larger reduction in frequency difference.

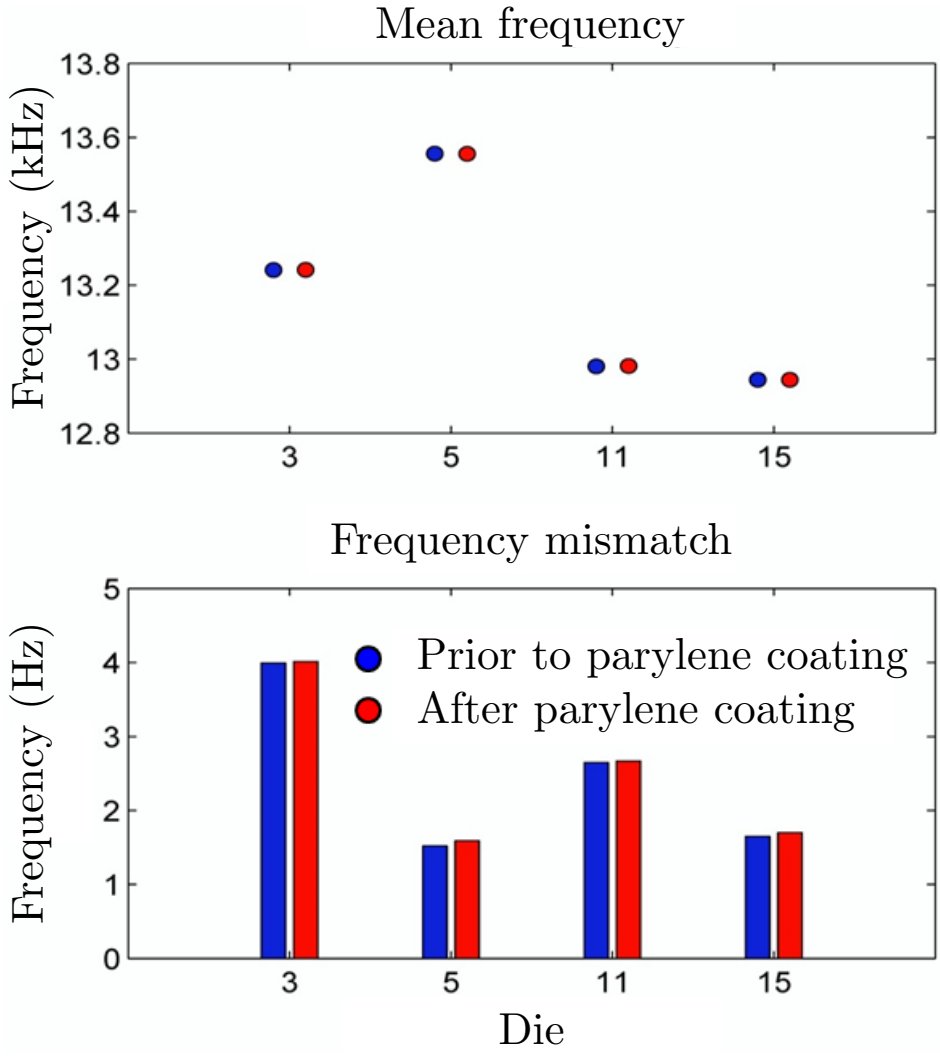

Figure 3.12: Parylene protection experiment shows that the coat protects the resonators from etching. This implies that we can now control the etching on individual resonators by ablating the parylene in selected areas.

the effect on the modal properties of the resonator. To resolve this issue, the photoresist has been replaced with a material which can protect all unexposed areas of the resonators (even on the underside) from "unwanted" etching effects. The second step was to use a conformal coat of parylene for this purpose.

An experiment was designed to check new coating's capability of protecting the silicon, with the results summarized in Fig. 3.12. First, a few resonators were selected, and their modal properties were recorded after the photoresist had been stripped by before the parylene was deposited. Then, a conformal coating of parylene is applied to the entire wafer. After that, the resonator was

placed into the etcher for timed etch of four minutes. The conformal coating was then removed, and the previously selected resonators were tested again. The results show that the parylene is able to protect the resonator from any etching. Fig. 3.12 demonstrates that the mean $n = 2$ frequency as well as frequency mismatch remain unchanged.

A coating of Parylene C, approximately 1 μm in thickness, is applied to the wafer at the conclusion of the guided blanket etch. Parylene was selected based on its capability of getting ablated without damaging the underlying silicon, and on its conformality, which protects the sidewalls of the structure during the etch in addition to the top surface. This sidewall coating prevents lateral etching, which impacts the width (and hence stiffness) of the device. Besides, the parylene is deposited using a vapor-deposition process, avoiding wet processing, and it can be cleanly removed using an oxygen plasma.

One of the challenges in switching from the photoresist to parylene was the ablation of parylene. As opposed to the ablation of photoresist which was relatively easy to do, the ablation process for parylene is quite challenging because parylene does not absorb the laser wavelength very well. An exhaustive search through all of the possible combination of different parameters in our laser trimming device was performed. The laser trimming device and some of the ablation results are shown in Fig. 3.13. Based on these experiments, a laser trimming recipe has been developed with some results shown in Fig. 3.14 which shows a resonator with trimmed spoke (after parylene ablation and etch) with a scanning electron microscope (SEM). The ablated areas using established recipe are clean and repeatable. The ultra-violet wavelength is used in the process. The Wyko measurements for the timed etch results can be seen in Fig. 3.15.

3.2.2 Sensitivity Parameter Measurements

The initial objective is to experimentally estimate γ_{g} from a series of tests on the control Die 4, 12, 14 and 16. Four rounds of experiments are conducted on these die in which four square patches, approximately $80\,\mu$m $\times$ $80\,\mu$m, are opened on a selected spoke layer in a compass-points pattern. A timed etch removes approximately $8\,\mu$m of material from these areas for each round of experiments. A single round targets different spoke layers on the different die. For example, in the

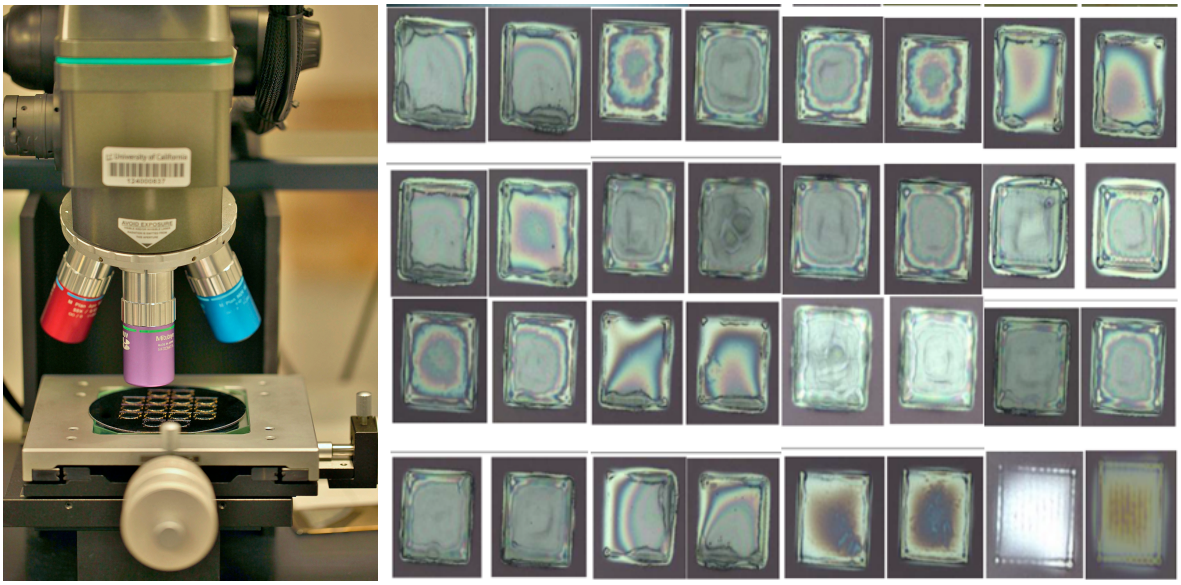

Figure 3.13: (Left)The laser system and wafer ready for trimming (Right) Some of the laser ablation results

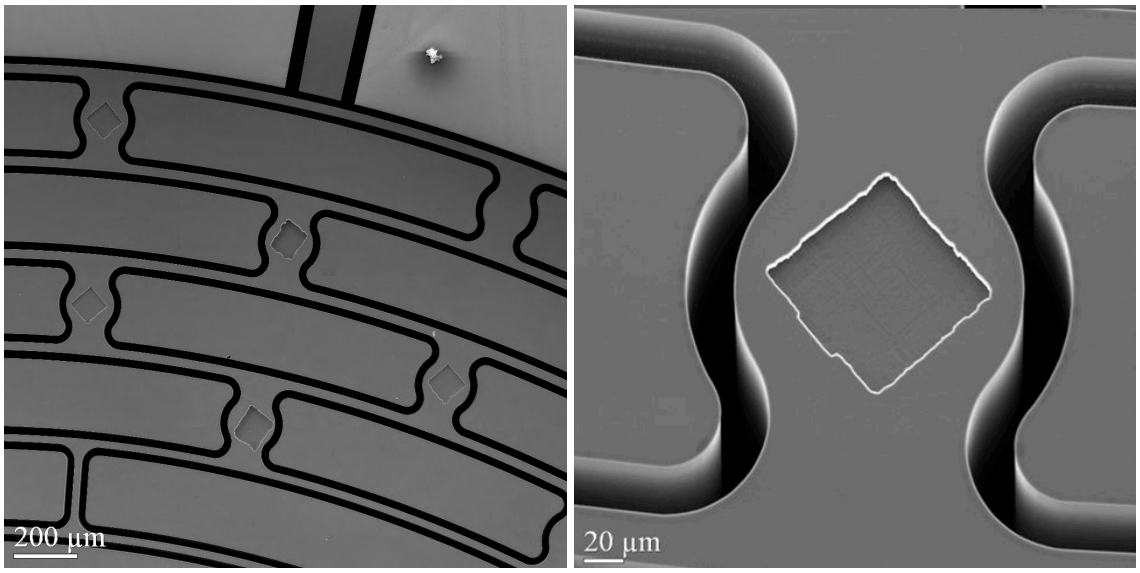

Figure 3.14: Etched areas on resonator after parylene ablation.

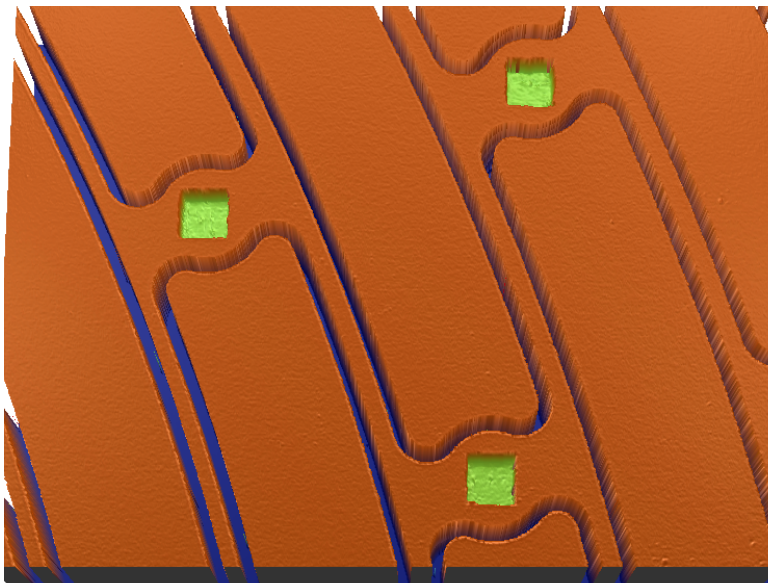

Figure 3.15: The Wyko measurements after removing the parylene coating. The depth is about 8 μm.

Table 3.3: Summary of guided blanket etch results

Die	ω_1 (Hz)	ω_2 (Hz)	Q_1 (k)	Q_2 (k)	Δ (Hz)
1	13327.14	13329.49	47.0	47.2	2.35
3	13239.00	13242.99	48.7	48.6	3.99
4	**13465.70**	**13474.78**	**45.9**	**46.0**	**9.08**
5	13554.99	13556.51	46.7	42.8	1.52
6	13557.38	13560.13	46.7	46.9	2.75
7	13231.85	13248.81	46.0	48.1	16.96
9	13613.48	13615.77	40.9	42.4	2.29
10	13592.83	13594.45	46.3	46.4	1.62
11	12979.60	12982.25	44.4	50.3	2.65
12	**13282.89**	**13291.49**	**47.9**	**48.2**	**8.60**
14	**13467.45**	**13475.62**	**47.4**	**47.4**	**8.17**
15	12943.30	12944.95	47.9	50.8	1.65
16	**13063.30**	**13074.64**	**46.2**	**49.5**	**11.34**

first round, Die 4 has material removed from the third spoke layer, but Die 12 has material removed from the second spoke layer. The results of the experiments are collected in Table 3.4. The volume that is associated with γ_{g} is $80\times80\times8\ \mu\mathrm{m}^3$, which corresponds to a mass of $m_0 = 0.1193\,\mu\mathrm{g}$. At the conclusion of each round of etching, the modal parameters are measured, and precise dimensions of the material removed are obtained with a Wyko profilometer. Then, the parameter r_m is determined which relates the actual mass perturbation estimated from the Wyko measurements relative to the canonical mass m_0. The fact that $r_m < 0$ indicates that material has been removed, and if $|r_m| > 1$, then more mass was removed than the mass m_0. The sensitivity parameter is then estimated from (3.11), where γ_{g} is replaced by $r_m\gamma$. Note that Δ, Δ_0, $\psi_{2,2}$ and $\psi_{1,2}$ are known from the pre- and post-etch modal parameter measurements, θ_0 and index i are defined by the etched spoke locations, and $\tilde{\alpha}_{i,2}$ and $\tilde{\beta}_{i,2}$ are known from the FEA. Thus, the estimated γ_{g} is calculated for each round and reported in Table 3.4. The estimates with the lowest variance correspond to spoke layer $i = 4$, i.e., the outermost layer of spokes. This can be attributed to the fact that the neglected $k = 6, 10$ harmonics in (3.11) have little effect on the spoke velocities in this layer. Thus, the mean value obtained from perturbations to the outermost spoke layer are used for the estimate of

$$\gamma_{\text{EXP}} = 0.339\,\text{Hz}. \tag{3.12}$$

Note that the estimates from the other spoke layers are very close to this value as is the value for γ_{FEA}. It is worthwhile mentioning that since the size of the mass perturbations is small, the anti-node orientation after the perturbations is essentially the same as its orientation before, which means that the model used herein is accurate.

The sensitivity parameter experiments also provide an opportunity to determine to what extent the modal properties of the non-ablated die have changed. Measurements were made on the four die shown in Table 3.5 and demonstrate that the parylene prevents material removal over the short duration of the timed etch (see Fig. 3.12). The mean frequencies are reported along with the modal frequency difference before and after the etch. The mean frequencies can vary due to small fluctuations in wafer temperature (the wafer is not temperature regulated during the tests). Furthermore, the small differences in pre- and post-etch Δ are within the accuracy of the model that is fit to the

Table 3.4: Summary of sensitivity parameter estimates

Die	round	layer, i	Δ_0 (Hz)	Δ (Hz)	r_m	γ_g (Hz)
4	1	3	9.08	8.16	-1.2661	0.3334
4	2	1	8.16	7.08	-1.0200	0.3526
4	3	2	7.08	6.20	-1.0105	0.3724
4	4	4	6.20	5.69	-0.9654	0.3295
12	1	2	8.60	7.69	-1.1579	0.3643
12	2	4	7.69	7.18	-1.0196	0.3453
12	3	1	7.18	6.10	-1.0541	0.3484
12	4	3	6.10	5.33	-1.0279	0.3534
14	1	4	8.17	7.39	-1.2352	0.3438
14	2	2	7.39	6.29	-1.2798	0.3379
14	3	3	6.29	5.63	-0.9766	0.3214
14	4	1	5.63	4.67	-0.9858	0.3428
16	1	1	11.34	10.15	-1.1542	0.3431
16	2	3	10.15	9.33	-1.0689	0.3526
16	3	4	9.33	8.74	-1.0276	0.3369
16	4	2	8.74	7.88	-1.0160	0.3636

Table 3.5: Modal parameters associated with non-ablated die

	Before Etch		**After Etch**	
Die	**Mean** ω (Hz)	Δ (Hz)	**Mean** ω (Hz)	Δ (Hz)
3	13241.00	3.99	13241.80	4.01
5	13555.75	1.52	13555.70	1.60
11	12980.92	2.65	12981.45	2.66
15	12944.12	1.65	12944.35	1.70

frequency response data and from which the modal parameters are extracted.

3.2.3 Wafer-Level Elimination of Modal Frequency Differences

The sensitivity parameter experiments were conducted using Die 4, 12, 14 and 16 to provide an estimate of γ_g but it is evident in Table 3.4 that the ablation locations were also selected to reduce Δ, although not to a specified target. Now the objective is to use γ_{EXP} and (3.11) to select ablation locations on the complementary "test" die in order to achieve $\Delta \approx 0$ for these die. Several parylene deposition-ablate-etch-measure cycles were performed with the wafer because of the approximate nature of (3.11) in predicting the post-etch frequency difference, however, during each cycle all

Table 3.6: Summary of parylene etch results

Die	ω_1 (Hz)	ω_2 (Hz)	Q_1 (k)	Q_2 (k)	Δ (Hz)
1	13332.12	13332.16	51.7	47.6	0.04
3	13245.40	13245.73	45.5	45.1	0.33
5	13557.81	13557.84	46.7	48.4	0.03
6	13562.83	13562.89	47.9	43.7	0.06
7	13234.18	13249.51	49.6	48.8	15.33
9	13617.82	13617.86	49.2	49.5	0.04
10	13596.72	13596.77	49.8	49.9	0.05
11	12984.00	12984.06	51.3	48.0	0.06
15	12946.57	12946.61	54.7	55.0	0.04

test die were modified to demonstrate the feasibility of *simultaneously* reducing Δ across all die on the wafer. Between each cycle, the parylene is removed with an oxygen plasma etch. In order to achieve the simultaneous reduction of Δ, it is necessary to ablate areas of differing sizes on the spoke surfaces so as to customize the material removal for each die since each round of etching penetrates the same depth for all die (typically about 8 μm). For these experiments areas of dimensions 22μm $\times$ 22μm to 87μm $\times$ 87μm were ablated. The model (3.11) includes the scaling r_q to account for the deviation of the expected material removal with respect to the mass m_0. The final results are compiled in Table 3.6. All modal frequency differences are reduced below 100 mHz except for Die 3 and 7, the latter of which was used for continued sensitivity parameter experiments. The success of this approach is easily seen in Figs. 3.16 and 3.17, which show the empirical frequency responses of each test die (with the exception of Die 7) before and after the targeted etch process.

3.3 Discussion on Wafer-Level $n = 2$ Modes Tuning

Tailored etching using the parylene deposition-ablation-etch cycle appears to be successful in reducing modal frequency differences to below the bandwidth of the resonances when starting from initial frequency differences of about 3 Hz or less. The guided blanket etch was an important step in realizing these starting values for the parylene cycles. The challenge with the guided blanket etch, though, is the fact that the stiffness associated with the $n = 2$ modes is also clearly mod-

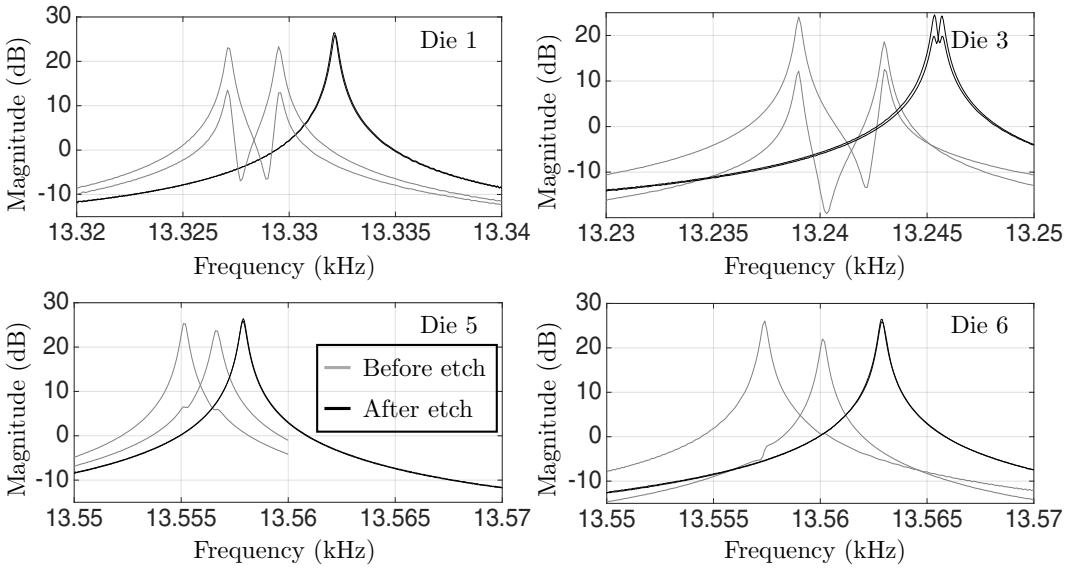

Figure 3.16: Comparison of resonator frequency responses before and after the parylene ablation-etch cycles for Die 1, 3, 5 and 6. The S_1/D_1 and S_2/D_2 channels are graphed for the resonators before and after the etch cycles.

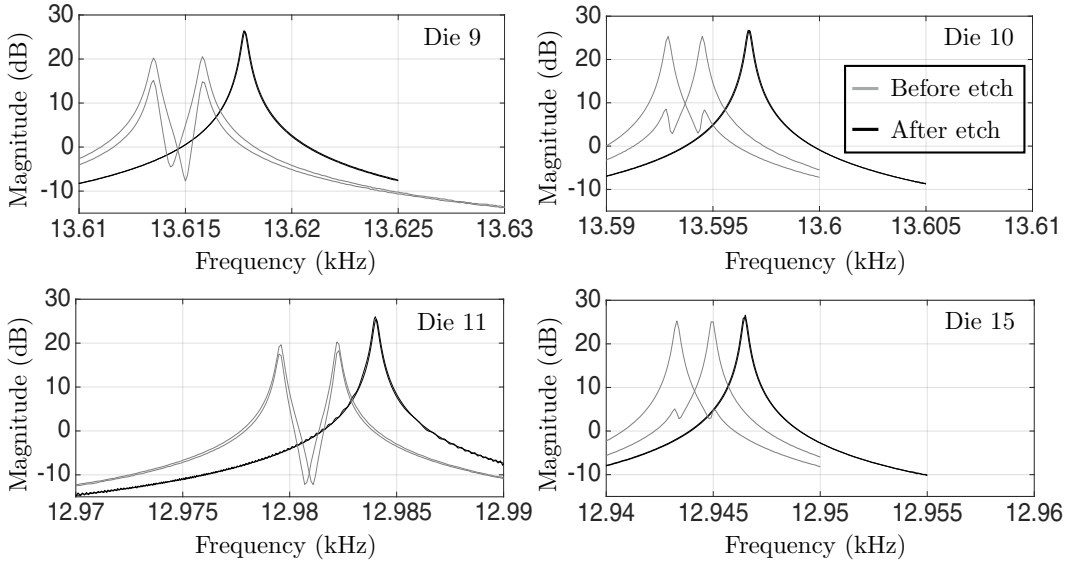

Figure 3.17: Comparison of resonator frequency responses before and after the parylene ablation-etch cycles for Die 9, 10, 11, and 15. The S_1/D_1 and S_2/D_2 channels are graphed for the resonators before and after the etch cycles.

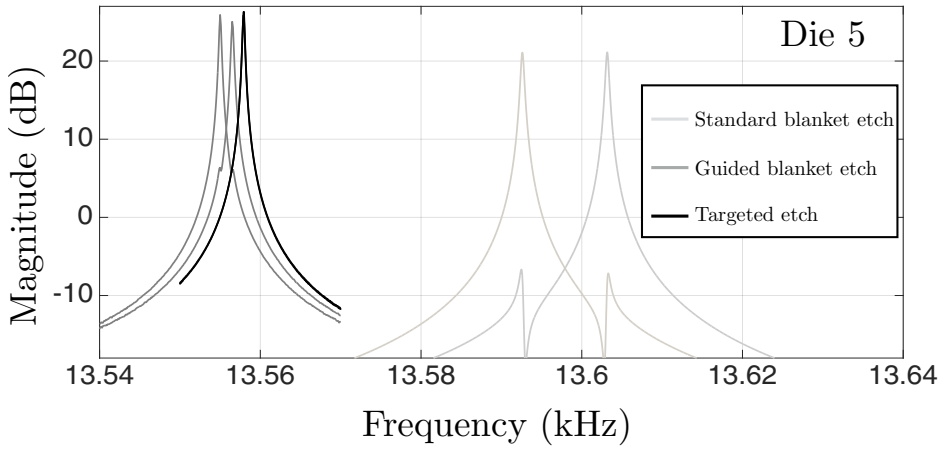

Figure 3.18: Summary for Die 5 after major etch steps. Both S_1/D_1 and S_2/D_2 channels are graphed after each major etch step.

ified in addition to the mass distribution of the resonator. This is evident by comparing the data summarized in Tables 3.2 and 3.3 but is more clearly observed in Fig. 3.18, which shows the frequency response of Die 5 after the major etch steps, and Fig. 3.19, which shows a bar chart of the frequency differences for all die after the major etch steps. Note that the mean modal frequencies of the $n = 2$ modes *decrease* by a significant amount by continuing the blanket etch. This fact – uncontrolled modification of the resonator stiffness – renders the guided blanket etch a useful tool but one that cannot be used to effectively eliminate the modal frequency difference. It is also interesting to note that the control die also experience a reduction in modal frequency difference during the guided blanket etch, although not to the extent of the die with ablated photoresist. Thus, it appears that after the initial release of the resonators, continued etching reduces the modal frequency differences although in a largely unpredictable manner. The mechanism is attributed to continued lateral etching of the exposed resonator sidewalls, impacting both local stiffness and mass.

Performing a timed etch after deposition, and then ablation, of parylene, produces highly repeatable and predictable results because the areas where the material removal occurs, i.e., the large spokes, has little impact on the $n = 2$ stiffness properties and so can be modeled as purely a perturbation to the resonator mass distribution. This was the basis of the perturbation model (3.9). Evidence of mass-only perturbations is also supported by Figs. 3.16 and 3.17 where it is clear that material removal uniformly increases the modal frequencies of the $n = 2$ modes. This demonstrates that the conformal parylene coating is effective in preventing sidewall etching during the

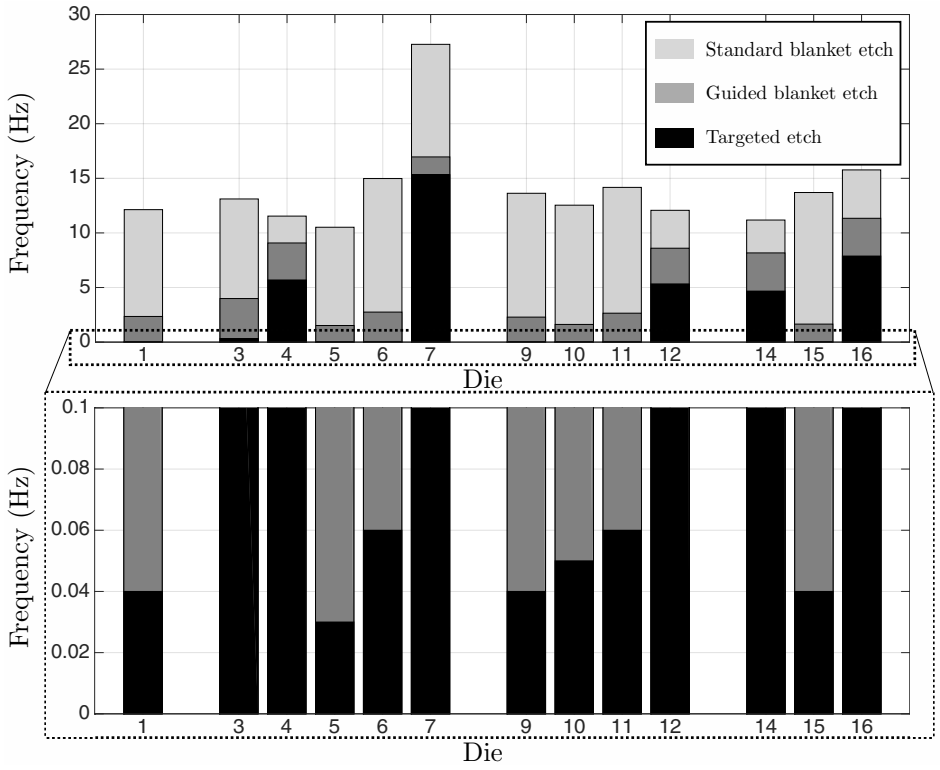

Figure 3.19: Bar graph summarizing the $n = 2$ modal frequency differences for all die after the major etch steps.

site-specific mass removal. Ideally, the comprehensive perturbation model (3.9) would be used to search for ablation sites, but due to the limited sensing of the outer ring radial motion, it is not possible to reliably estimate all of the parameters necessary for application of (3.9). In particular, the phases associated with the $k \in \{6, 10\}$ harmonics are not known. The analysis shows that the largest $k \in \{6, 10\}$ harmonic amplitudes are located in spoke layer $i = 1$ and have amplitudes that are approximately 4% and 3% of $k = 2$ harmonic amplitude. Thus, locating sense electrodes in this area of the resonator would be advantageous for measuring these phases. Nevertheless, bounds on Δ can be computed using (3.9) by searching for worst-case values of $\psi_{p,6}$ and $\psi_{p,10}$ where the relations $|\psi_{1,6} - \psi_{2,6}| = 15^\circ$ and $|\psi_{1,10} - \psi_{2,10}| = 9^\circ$ are assumed based on the finite element results. Profilometer measurements provide accurate estimates of the mass removal so the largest uncertainty in the parameters in (3.9) are the unknown phases. The bounds are shown in Table 3.7 and are computed using accurate mass removal estimates starting from the resonator states after the guided blanket etch but before any targeted etching with the parylene has occurred. The bounds demonstrate that Δ can significantly deviate from the final desired modal frequency difference of approximately zero. The real utility of the bounds is in showing the possible range of outcomes for Δ if only a single ablation-etch cycle is permitted in which the simplified model (3.11) is used to reduce Δ to approximately zero. The bounds imply that the absolute modal frequency difference may be as large as 0.4 Hz (excluding Die 7). These potentially large deviations were avoided by employing several ablation-etch cycles, thus, this method has been demonstrated to be compatible with iterative execution, enabling repeated application to achieve increasingly small frequency splits. Ultimately, however, a single ablation-etch cycle is most desirable, but this will necessitate the measurement of the unknown phases and using the more accurate model (see Chapter 4).

Finally, the quality factors are reported and appear to have experienced modest changes over the course of the experiments. In some cases, the quality factors have increased, and in others, they have decreased, but in general, they appear to remain high throughout the post-fabrication steps.

3.4 Summary of Wafer-Level $n = 2$ Modes Tuning

A wafer-level post-fabrication technique has been demonstrated for simultaneous reduction of the

Table 3.7: Bounds for Δ computed from (3.9)

Die	Δ_{min} (Hz)	Δ_{max} (Hz)
1	-0.36	0.07
3	-0.32	0.42
5	-0.03	0.31
6	0.05	0.41
7	15.35	15.52
9	0.05	0.27
10	-0.13	0.17
11	-0.15	0.37
15	0.07	0.26

modal frequency differences between the $n = 2$ modes in an axisymmetric resonator. The resonator is designed, so that mass removal at the large spokes creates a readily predictable perturbation to its dynamics. Using a model-based approach to select these areas, a laser is used to ablate the masking resist and, subsequently, a conformal layer of Parylene-C, to expose the silicon for further etching with SiDRIE. The lateral dimensions can be tightly controlled with a fixed mask for the laser, and the depth is controlled through a timed etch. Since only silicon is removed from the resonator, the process is compatible with any further processing, including wafer-level packaging operations. The underlying assumption for the model used in this chapter is that the anti-node orientation before and after perturbations is essentially the same which can happen by having sufficiently small masses or by placing them close to the anti-node orientation. This assumption is justified in practice when the objective is tuning one of the modes. A more accurate model will be derived in Chapter 4.

CHAPTER 4

Multi-Modal Tuning

Nomenclature - Chapter 4

ω	modal frequency prior to the perturbations		
$\tilde{\omega}$	modal frequency after the perturbations		
θ	angle coordinate	i	spoke layer
ϵ_S	change in the strain energy	ϵ_T	change in the kinetic energy
ϵ_{T_1}	kinetic energy change for the first modal frequency within the n^{th} pair		
ϵ_{T_2}	kinetic energy change for the second modal frequency within the n^{th} pair		
$\omega_{n,1}$	the first modal frequency within the n^{th} pair before perturbations		
$\omega_{n,2}$	the second modal frequency within the n^{th} pair before perturbations		
$\tilde{\omega}_{n,1}$	the first modal frequency within the n^{th} pair after perturbations		
$\tilde{\omega}_{n,2}$	the second modal frequency within the n^{th} pair after perturbations		
$\delta_{n,1}$	frequency deviation for the first modal frequency within the n^{th} pair		
$\delta_{n,2}$	frequency deviation for the second modal frequency within the n^{th} pair		
$\psi_{n,1}$	anti-node orientation of the modes associated with frequency $\omega_{n,1}$		
$\psi_{n,2}$	anti-node orientation of the modes associated with frequency $\omega_{n,2}$		
$\tilde{\psi}_{n,1}$	anti-node orientation of the modes associated with frequency $\tilde{\omega}_{n,1}$		
$\tilde{\psi}_{n,2}$	anti-node orientation of the modes associated with frequency $\tilde{\omega}_{n,2}$		
$\omega_{n,0}$	average modal frequency within the n^{th} pair		
$\alpha_{n,i}$	radial velocity amplitude for within the n^{th} pair in spoke layer i		
$\beta_{n,i}$	tangential velocity amplitude within the n^{th} pair in spoke layer i		
$\Delta_n := \omega_{n,2} - \omega_{n,1}$	initial frequency split		
$\tilde{\Delta}_n := \omega_2 - \omega_1$	post-perturbation frequency split		
$p = 1, 2$	mode number	m_0	nominal size of mass perturbation
m_q	size of point mass perturbations	μ_q	mass perturbation relative to m_0
θ_q	location of mass perturbations		
$\bar{m}$	size of the initial point mass perturbation		
$\bar{\mu}$	initial point mass perturbation relative to m_0		

Nomenclature - Chapter 4

$T_{n,1}$	nominal kinetic energy for the first companion mode within the n^{th} pair		
$T_{n,1}$	nominal kinetic energy for the second companion mode within the n^{th} pair		
$T_{n,0}$	mean value of the nominal kinetic energies within the n^{th} pair		
γ_{r_n}	ring sensitivity within the n^{th} pair		
$\mathcal{C}$	objective function	j	$\sqrt{-1}$
W_2	weight associated with $n = 2$ modes	W_3	weight associated with $n = 3$ modes
$\mathbb{Z}$	set of integer numbers		
$\boldsymbol{R}^n$	vector with n real elements	$\boldsymbol{R}^{n\times m}$	$n \times m$ matrix with real elements

As discussed in Chapter 1, having asymmetries in the structure degrades the signal-to-noise ratio (SNR) significantly [KM13]. Also mentioned are the most common and efficient manufacturing techniques for small sized axisymmetric resonators found in micro-electro-mechanical systems (MEMS) manufacturing such as masking and etching. In Chapter 3, it is shown that the presence of the asymmetries is unavoidable even with state of the art MEMS technology and are caused by etch non-uniformities and mounting stresses. The level and nature of the imperfection is random and varies for each resonator even if all are on the same wafer [BKS17] (see Fig. 3.3). Based on the randomness of asymmetries, post-fabrication modification seems to be the most practical option to correct for these imperfections (see Chapter 3).

Changing the dynamics of the structure can be done by either perturbing the stiffness or the mass distribution. A combination of these two would also alter the dynamics, but the process is complex and not practical. Pure change of the stiffness can be achieved electrostatically by applying voltage at specific locations [KM06]. This process is equivalent to adding or removing point springs to the ring [BM17]. Although this method is easy to implement, the modification is not permanent and requires relatively large equipment to maintain a "tuned" status.

Due to the distributed mass nature of the resonators, any addition or removal of mass not only affects the mass distribution (kinetic energy perturbation), but also alters the stiffness (potential energy perturbation). The coupling between the kinetic and potential energies is the key reason for the complexity of the tuning problem. The resonator used in this chapter is the same as the one used in Chapter 3. The design is specified to address this coupling issue. By changing the

shape of the connections (spokes) between the four outermost rings, the spokes' strain energy is minimized [BKS17] (see Fig. 3.5). Therefore, the adjustment of mass at these fat spokes does not affect the stiffness of the structure.

Tuning via mass addition and wafer-level mass removal is presented for $n = 2$ Coriolis coupled modes in [SKS15] and [BKS17], respectively. Although the $n = 2$ is the most common pair used for sensing the angular rotation and rate sensors, there are other modes that can be used such as the $n = 3$ Coriolis coupled modes. The lag factor is smaller for this pair of modes, but the pair can still be used in a gyroscope. It has been shown that using two mode pairs ($n = 2$ and $n = 3$) as rate sensors in one device provides two independent measurements with correlated long-term biases. This long-term bias correlation can be used for improving the quality of the measurements [GM17]. However, each mode used as a rate sensor needs to be tuned. The tuning of the mode for [GM17] has been done in an *ad-hoc* manner. The challenge is that both modes need to be considered in the tuning process and at the end, both modes must have essentially zero frequency splits.

In tuning the $n = 2$ modes, the neighborhood of the search for the mass perturbations can be found from the uniform ring model with point asymmetries (see [Fox90] and [BM17]). The constrained search space makes the computational aspect of the problem relatively easy. This means the anti-node orientation is usually preserved during the perturbation process, so the model used in Chapter 3 is accurate. On the other hand, for simultaneous tuning of $n = 2$ and $n = 3$ modes, the search space is essentially all the spokes in the four outermost rings. Due to the complexity of the problem, the tuning needs to be pursued systematically and the assumption about preserving the anti-node during the perturbation process must be removed from the model.

The chapter is organized as follows. Sec. 4.1 reviews the effect of point mass perturbations on a simple ring without restricting the anti-node orientation and generalizes the idea to the resonator used in this study. The results from a finite element analysis are presented to find the connection between point mass size and location and kinetic energy perturbation. The tuning equation is also derived at the end of Sec. 4.1. The linear integer programming problem is studied in Sec. 4.2. The objective function and the practical constraints are introduced and written in a format compatible with linear programming. The section shows why the solution to the tuning problem always exists in practice by properly choosing the size of the nominal mass perturbation. The process of testing

and the results for two devices are presented in Sec. 4.3. Sec. 4.4 summarizes the results of the section.

4.1 Modeling

The reader is referred to [SKS15] and Chapter 3 for information on the resonator design and fabrication. The modal parameter estimation method used for this chapter is more sophisticated than the one used in [SKS15] and it contains two inputs and eight outputs for each of the modes. The method is especially more accurate when a given companion mode's frequencies are approximately equal. In this case, the improved model yields a more accurate anti-node orientation. The ultimate goal of this research is the systematic and simultaneous modification of the two Coriolis coupled modes in axisymmetric resonators to achieve degenerate modal frequencies. After tuning, the two modes can be used to provide independent measurements in one device with correlated bias errors.

This section is divided into two parts. The first portion discusses the effect of point mass perturbations on a ring for different modes. The second half applies the idea to the resonator in hand using finite element (FE) analysis of the structure.

4.1.1 Effect of Point Mass Perturbations

The modal frequencies in a vibrating structure are perturbed from their nominal values by changes in the structure's mass and/or stiffness distribution. The pre- and post-perturbation modal frequencies in a linear elastic structure are related by,

$$\tilde{\omega}^2 = \omega^2 \frac{1+\epsilon_S}{1+\epsilon_T}, \tag{4.1}$$

where ω is the modal frequency prior to the perturbations, $\tilde{\omega}$ is the modal frequency after the perturbations, and ϵ_S and ϵ_T are the changes in the strain and kinetic energies of the perturbed mode, respectively, normalized by the unperturbed energies [Mei67].

In the case of a vibrating ring we are interested in the behavior of two "companion" modes, which in a uniform thin ring have degenerate modal frequencies [Rao07]. The modal pairs are

indexed by $n = 1, 2, 3, \ldots$, which refers to the fact that the mode shapes associated with a given pair are represented by the radial displacement functions $\cos(n\theta)$ and $\sin(n\theta)$, defined relative to the nominal, undeformed ring radius. The angular coordinate θ identifies a point on the ring relative to some datum. The two modal frequencies within the n^{th} pair are denoted $\omega_{n,1}$ and $\omega_{n,2}$. In a uniform ring $\omega_{n,2} = \omega_{n,1}$, but, in general, $\omega_{n,2} \neq \omega_{n,1}$ in an imperfect ring. The mode-shapes in an imperfect ring are still well-approximated by $\cos(n(\theta - \psi_{n,1}))$ and $\cos(n(\theta - \psi_{n,2}))$, where $\psi_{n,1}$ and $\psi_{n,2}$ denote the anti-node orientation of the modes associated with frequencies $\omega_{n,1}$ and $\omega_{n,2}$, respectively. Furthermore, $\psi_{n,2} - \psi_{n,1} \approx \pm 90^\circ/n$ so the second mode-shape reduces to $\pm \sin(n(\theta - \psi_{n,1}))$.

The "tuning problem" consists of perturbing the imperfect resonator so that the post-perturbation frequencies satisfy $\tilde{\omega}_{n,2} = \tilde{\omega}_{n,1}$. This may be desired at only one value of n (typically $n = 2$ for axisymmetric resonators used in Coriolis Vibratory Gyros - see Chapter 3), or, as is addressed in this chapter, when $n = 2, 3$. Assuming a perturbation only modifies the kinetic energy in the modes, then

$$\frac{\tilde{\omega}_{n,1}^2}{\omega_{n,1}^2} - \frac{\tilde{\omega}_{n,2}^2}{\omega_{n,2}^2} = \frac{1}{1 + \epsilon_{T_1}} - \frac{1}{1 + \epsilon_{T_2}} \approx \epsilon_{T_2} - \epsilon_{T_1} \tag{4.2}$$

where ϵ_{T_1} represents the change in kinetic energy of the $\omega_{n,1}$ mode due to the perturbation normalized by its pre-perturbation kinetic energy T_1, and so forth. The post-perturbation frequencies are related to the pre-perturbation frequencies by the frequency deviations $\delta_{n,1}$ and $\delta_{n,2}$: $\tilde{\omega}_{n,1} = \omega_{n,1} + \delta_{n,1}$ and $\tilde{\omega}_{n,2} = \omega_{n,2} + \delta_{n,2}$. The left-hand side of (4.2) can be approximated as

$$\frac{\tilde{\omega}_{n,1}^2}{\omega_{n,1}^2} - \frac{\tilde{\omega}_{n,2}^2}{\omega_{n,2}^2} \approx 2\left(\frac{\delta_{n,1}}{\omega_1} - \frac{\delta_{n,2}}{\omega_2}\right) \approx 2\left(\frac{\delta_{n,1} - \delta_{n,2}}{\omega_{n,0}}\right), \tag{4.3}$$

where $\omega_{n,0}$ is the mean value of $\omega_{n,1}$ and $\omega_{n,2}$, and where the terms with $\delta_{n,1}^2$ and $\delta_{n,2}^2$ have been neglected. Thus, the difference between the modal frequency deviations due to a perturbation is approximated as

$$\delta_{n,1} - \delta_{n,2} \approx \frac{\omega_{n,0}}{2}\left(\epsilon_{T_2} - \epsilon_{T_1}\right). \tag{4.4}$$

If the initial state of the ring is such that $\omega_{n,2} \neq \omega_{n,1}$, then this state is the starting point for any "tuning" strategy which aspires to modify the resonator in such a manner so as to remove the differ-

ences in these modal frequencies, i.e. $\tilde{\omega}_{n,2} = \tilde{\omega}_{n,1}$, with an appropriate perturbation. It is assumed that $\omega_{n,1}$, $\omega_{n,2}$ and $\psi_{n,1}$ (and, hence, $\psi_{n,2}$) are known at the outset. The physical perturbations at our disposal for the resonator depicted in Fig. 4.1 of the subsequent section are the deposition of quantized masses at the large spoke locations. These quantized masses modify the distribution of resonator mass and therefore change the modal properties of, generically, all modes. Thus, for the study of a slightly imperfect ring, it is assumed that point masses can be loaded onto the structure. Despite the fact that point masses can be safely assumed to not modify the ring stiffness at the point of attachment (a design feature of the resonator in Fig. 4.1), it is nevertheless possible that the normalized strain energy associated with a perturbed mode is different from the normalized strain energy associated with the mode in its initial state. The difference in normalized strain energies caused by a pure mass perturbation is due to non-uniformity of local bending stiffness in the ring: a mass perturbation will generally modify the anti-node orientation which will produce different strain energy. Although there appears to be little rationale for *a priori* assuming the normalized strain energy is invariant with respect to $\psi_{n,1}$, this assumption is made here because not only does it yield a tractable relationship for the degree of frequency detuning as a function of point-mass perturbations but, more importantly, the model is able to predict with high accuracy the changes in modal frequencies in actual resonators. Henceforth, it is assumed that the bending stiffness in the ring is uniform and so any change in the normalized strain energy can be neglected compared to changes in the kinetic energy.

A consequence of assuming the normalized strain energy is invariant with respect to $\psi_{n,1}$ is any difference in observed modal frequencies can be assumed to be produced by a single point-mass of appropriate size. Indeed, affixing a point mass to a uniform thin ring will create an anti-node at the attachment point that is associated with the lowest frequency mode in the pair. The difference in modal frequencies will be proportional to the perturbing mass. This is the source of the imbalance parameters discussed in [Fox90, SKS15]. When mass is added to ring in order to modify its modal properties, the change in kinetic energy can be computed based on the new added mass relative to the new anti-nodes as well as the original mass with respect to the new anti-nodes.

It is assumed the point mass $\bar{m}$ is attached to the uniform thin ring at $\psi_{n,1}$, which creates an anti-node at $\psi_{n,1}$ associated with frequency $\omega_{n,1}$. The mass size is adjusted so that the initial

frequency split $\Delta_n := \omega_{n,2} - \omega_{n,1} > 0$ matches the measured difference in frequencies (without loss of generality, $\omega_{n,2}$ is always assigned as the higher frequency mode in the n^{th} pair). This is the initial state of the ring. In this case, the radial and tangential displacements relative to the undeformed ring are

$$\alpha_n \cos(n(\theta - \psi_{n,1})) \quad \text{(radial)},$$
$$\beta_n \sin(n(\theta - \psi_{n,1})) \quad \text{(tangential)},$$

for mode $\omega_{n,1}$, and

$$\alpha_n \cos(n(\theta - \psi_{n,2})) = \pm\alpha_n \sin(n(\theta - \psi_{n,1})) \quad \text{(radial)},$$
$$\beta_n \sin(n(\theta - \psi_{n,2})) = \beta_n \cos(n(\theta - \psi_{n,1})) \quad \text{(tangential)},$$

for mode $\omega_{n,2}$. It appears the radial and tangential components are constrained to have the same amplitudes in both modes. Further, the normalized change in kinetic energy for each mode is amplitude independent so one may assume the amplitudes to be the same. Likewise, the post-perturbation radial and tangential displacements are given by

$$\alpha_n \cos(n(\theta - \tilde{\psi}_{n,1})) \quad \text{(radial)},$$
$$\beta_n \sin(n(\theta - \tilde{\psi}_{n,1})) \quad \text{(tangential)},$$

for mode $\tilde{\omega}_{n,1}$, and

$$\alpha_n \cos(n(\theta - \tilde{\psi}_{n,2})) = \pm\alpha_n \sin(n(\theta - \tilde{\psi}_{n,1})) \quad \text{(radial)},$$
$$\beta_n \sin(n(\theta - \tilde{\psi}_{n,2})) = \beta_n \cos(n(\theta - \tilde{\psi}_{n,1})) \quad \text{(tangential)},$$

for mode $\tilde{\omega}_{n,2}$. The post-perturbation frequency difference is defined $\tilde{\Delta}_n := \tilde{\omega}_{n,2} - \tilde{\omega}_{n,1}$ and note that $\tilde{\Delta}_n < 0$ is possible and depends on the details of the perturbation.

Suppose a set of point masses $\{m_q\}$ are placed on the slightly imperfect ring at points $\{\theta_q\}$. Based on the harmonic assumption for the radial and tangential displacements, the spatial portion

of the kinetic energy associated with these masses in the perturbed resonator is

$$\frac{1}{2}\sum_q m_q \left(\alpha_n^2 \cos^2(n(\theta_q - \tilde{\psi}_{n,p})) + \beta_n^2 \sin^2(n(\theta_q - \tilde{\psi}_{n,p}))\right),$$

where $p = 1, 2$ for the first and second companion modes, respectively. This spatial potion of kinetic energy is hereby referred to the kinetic energy. For the original mass $\bar{m}$ that created the initial imperfect ring, the change in kinetic energy associated with this mass due to the change in anti-node orientations is

$$\begin{aligned}\frac{1}{2}\bar{m} \times [&\left(\alpha_n^2 \cos^2(n(\psi_{n,1} - \tilde{\psi}_{n,p})) + \beta_n^2 \sin^2(n(\psi_{n,1} - \tilde{\psi}_{n,p}))\right) \\ &- \left(\alpha_n^2 \cos^2(n(\psi_{n,1} - \psi_{n,p})) + \beta_n^2 \sin^2(n(\psi_{n,1} - \psi_{n,p}))\right)].\end{aligned}$$

where $p = 1, 2$ for the first and second companion modes, respectively. Thus, the change in normalized kinetic energy associated with mode $\omega_{n,1}$ ($p = 1$) is

$$\begin{aligned}\epsilon_{T_1} = \frac{1}{2T_{n,1}} \times [\sum_q m_q &\left(\alpha_n^2 \cos^2(n(\theta_q - \tilde{\psi}_{n,1})) + \beta_n^2 \sin^2(n(\theta_q - \tilde{\psi}_{n,1}))\right) \\ &+ \bar{m} \times (\alpha_n^2 \cos^2(n(\psi_{n,1} - \tilde{\psi}_{n,1})) + \beta_n^2 \sin^2(n(\psi_{n,1} - \tilde{\psi}_{n,1})) - \alpha_n^2))],\end{aligned} \tag{4.5}$$

where $T_{n,1}$ is the nominal kinetic energy for the first companion mode of the pair. The expression in (4.5) can be simplified as

$$\begin{aligned}\epsilon_{T_1} = \frac{1}{4T_{n,1}} \times [\sum_q m_q &\left(\left(\alpha_n^2 + \beta_n^2\right) + \left(\alpha_n^2 - \beta_n^2\right)\cos(2n(\theta_q - \tilde{\psi}_{n,1}))\right) \\ &+\bar{m}\left(-\left(\alpha_n^2 - \beta_n^2\right) + \left(\alpha_n^2 - \beta_n^2\right)\cos(2n(\psi_{n,1} - \tilde{\psi}_{n,1}))\right)].\end{aligned} \tag{4.6}$$

The expression for the change in normalized kinetic energy associated with mode $\omega_{n,2}$ ($p = 2$) is similarly derived as

$$\begin{aligned}\epsilon_{T_2} = \frac{1}{4T_{n,2}} \times [\sum_q m_q &\left(\left(\alpha_n^2 + \beta_n^2\right) + \left(\alpha_n^2 - \beta_n^2\right)\cos(2n(\theta_q - \tilde{\psi}_{n,2}))\right) \\ &+\bar{m}\left(\left(\alpha_n^2 - \beta_n^2\right) + \left(\alpha_n^2 - \beta_n^2\right)\cos(2n(\psi_{n,1} - \tilde{\psi}_{n,2}))\right)],\end{aligned} \tag{4.7}$$

where $T_{n,2}$ is the nominal kinetic energy associated with the second companion mode of the pair. Assuming α_n and β_n are the same for two companion modes, the nominal kinetic energies are the same as well,

$$T_{n,1} \approx T_{n,2} \approx T_{n,0},$$

where $T_{n,0}$ is the mean value of $T_{n,1}$ and $T_{n,2}$.

Using the orthogonality condition for the two companion modes for both before and after perturbations,

$$\tilde{\psi}_{n,2} - \tilde{\psi}_{n,1} \approx \psi_{n,2} - \psi_{n,1} \approx \pm 90^\circ / n.$$

From (4.6) and (4.7), the relative change in normalized kinetic energies is

$$\begin{aligned} \epsilon_{T_2} - \epsilon_{T_1} = -2\frac{\alpha_n^2}{4T_{n,0}} \left((\frac{\alpha_n}{\alpha_n})^2 - (\frac{\beta_n}{\alpha_n})^2 \right) \\ \times [\sum_q m_q \left(\cos(2n(\theta_q - \tilde{\psi}_{n,1})) \right) + \bar{m} \left(-1 + \cos(2n(\psi_{n,1} - \tilde{\psi}_{n,1})) \right)]. \end{aligned} \tag{4.8}$$

From (4.4) and (4.8), the difference in the frequency deviations can be written in terms of the change in the kinetic energy as

$$\begin{aligned} \delta_{n,2} - \delta_{n,1} \approx \frac{m_0 \omega_{n,0} \alpha_n^2}{4T_{n,0}} \times [\sum_q \mu_q \left((\frac{\alpha_n}{\alpha_n})^2 - (\frac{\beta_n}{\alpha_n})^2 \right) \left(\cos(2n(\theta_q - \tilde{\psi}_{n,1})) \right) \\ + \bar{\mu} \left((\frac{\alpha_n}{\alpha_n})^2 - (\frac{\beta_n}{\alpha_n})^2 \right) \left(-1 + \cos(2n(\psi_{n,1} - \tilde{\psi}_{n,1})) \right)], \end{aligned} \tag{4.9}$$

where m_0 is the nominal perturbation size ($m_q = \mu_q m_0$ and $\bar{m} = \bar{\mu} m_0$). Based on the definition of the frequency deviations, the left hand side of (4.9) is $\tilde{\Delta}_n - \Delta_n$. By defining the ring sensitivity γ_{r_n} for the n^{th} pair as $\frac{m_0 \omega_{n,0} \alpha_n^2}{4T_{n,0}}$, (4.9) can be written as

$$\begin{aligned} \tilde{\Delta}_n - \Delta_n = \gamma_{r_n} \times [\sum_q \mu_q \left((\frac{\alpha_n}{\alpha_n})^2 - (\frac{\beta_n}{\alpha_n})^2 \right) \left(\cos(2n(\theta_q - \tilde{\psi}_{n,1})) \right) \\ + \bar{\mu} \left((\frac{\alpha_n}{\alpha_n})^2 - (\frac{\beta_n}{\alpha_n})^2 \right) \left(-1 + \cos(2n(\psi_{n,1} - \tilde{\psi}_{n,1})) \right)]. \end{aligned} \tag{4.10}$$

The ring sensitivity multiplied by $\left((\frac{\alpha_n}{\alpha_n})^2 - (\frac{\beta_n}{\alpha_n})^2 \right)$ is the change in the frequency split when the

mass perturbation of size m_0 is placed on the anti-node. As such, $\bar{\mu}$ can be related to the frequency split before perturbations Δ_n as

$$\bar{\mu} = \frac{\Delta_n}{\gamma_{r_n}\left((\frac{\alpha_n}{\alpha_n})^2 - (\frac{\beta_n}{\alpha_n})^2\right)}. \tag{4.11}$$

Plugging in for $\bar{\mu}$ from (4.11) in (4.10) leads to

$$\tilde{\Delta}_n - \Delta_n = \gamma_{r_n} \times \sum_q \mu_q \left((\frac{\alpha_n}{\alpha_n})^2 - (\frac{\beta_n}{\alpha_n})^2\right) \cos(2n(\theta_q - \tilde{\psi}_{n,1})) - \Delta_n + \Delta_n \cos(2n(\psi_{n,1} - \tilde{\psi}_{n,1})), \tag{4.12}$$

which can be written as

$$\begin{aligned}\tilde{\Delta}_n =& \gamma_{r_n} \times \sum_q \mu_q \left((\frac{\alpha_n}{\alpha_n})^2 - (\frac{\beta_n}{\alpha_n})^2\right) \cos(2n\theta_q)\cos(2n\tilde{\psi}_{n,1}) \\ &+ \gamma_{r_n} \times \sum_q \mu_q \left((\frac{\alpha_n}{\alpha_n})^2 - (\frac{\beta_n}{\alpha_n})^2\right) \sin(2n\theta_q)\sin(2n\tilde{\psi}_{n,1}) \\ &+ \Delta_n \cos(2n\psi_{n,1})\cos(2n\tilde{\psi}_{n,1}) + \Delta_n \sin(2n\psi_{n,1})\sin(2n\tilde{\psi}_{n,1}).\end{aligned} \tag{4.13}$$

The anti-node orientation after placing the mass perturbations can be written as

$$\frac{\tilde{\Delta}_n}{\tilde{\Delta}_n}\tan(2n\tilde{\psi}_{n,1}) = \frac{\Delta_n \sin(2n\psi_{n,1}) + \gamma_{r_n}\sum_q \mu_q \left((\frac{\alpha_n}{\alpha_n})^2 - (\frac{\beta_n}{\alpha_n})^2\right)\sin(2n\theta_q)}{\Delta_n \cos(2n\psi_{n,1}) + \gamma_{r_n}\sum_q \mu_q \left((\frac{\alpha_n}{\alpha_n})^2 - (\frac{\beta_n}{\alpha_n})^2\right)\cos(2n\theta_q)}. \tag{4.14}$$

Using (4.14), the expression in (4.13) yields

$$\begin{aligned}\tilde{\Delta}_n \cos(2n\tilde{\psi}_{n,1}) &= \Delta_n \cos(2n\psi_{n,1}) + \gamma_{r_n} \sum_q \mu_q \left((\frac{\alpha_n}{\alpha_n})^2 - (\frac{\beta_n}{\alpha_n})^2\right)\cos(2n\theta_q), \\ \tilde{\Delta}_n \sin(2n\tilde{\psi}_{n,1}) &= \Delta_n \sin(2n\psi_{n,1}) + \gamma_{r_n} \sum_q \mu_q \left((\frac{\alpha_n}{\alpha_n})^2 - (\frac{\beta_n}{\alpha_n})^2\right)\sin(2n\theta_q).\end{aligned} \tag{4.15}$$

In compact form, using Euler's formula, (4.15) can be written as

$$\tilde{\Delta}_n e^{j2n\tilde{\psi}_{n,1}} = \Delta_n e^{j2n\psi_{n,1}} + \gamma_{r_n} \sum_q \mu_q \left((\frac{\alpha_n}{\alpha_n})^2 - (\frac{\beta_n}{\alpha_n})^2\right) e^{j2n\theta_q}, \tag{4.16}$$

where j $= \sqrt{-1}$. The kinetic energy model for a ring in (4.16) will be extended to ring-type resonators using finite element analysis. As discussed for $n = 2$ modes in Chapter 3, the only difference between various rings is the amplitude of vibration.

4.1.2 Generalization to Ring-Type Resonators

The expression in (4.16) is general in the sense that it can be used for all modes. However, it is should be noted (4.16) is derived only for a single ring. For the ring-type structures such as the one in hand, (4.16) needs to be generalized. The main difference between different rings in a resonator is the variation in the radial and tangential amplitudes (or the α_n and β_n values in the mode shapes). As discussed in Chapter 3, there is a fixed relationship between the radial and tangential amplitudes for different rings. For the resonator in hand, since the mass perturbation is restricted to the four outermost rings (see Fig. 4.1), the sensitivities must be found for those rings for $n = 2$ and $n = 3$ modes. As the structure is fairly complicated, FE is used for finding the relative amplitudes. The process of numerical case studies is similar to [BKS17] (explained in Chapter 3 and will be briefly reviewed here) and is also extended to $n = 3$ modes as well. The modal analysis yields the Cartesian velocity components at any point in the resonator, but because the mass at the large spokes is perturbed, the spoke velocity components are of particular interest. The FE analysis yields the velocities at the center of each spokes. The velocities are decomposed into radial and tangential components and the discrete Fourier series are computed for each spoke layer. The largest magnitude Fourier coefficient in all cases corresponds to n^{th} harmonic radial motion of the innermost ring (out of the four rings). Thus, all other Fourier coefficient magnitudes are normalized by this value in each experiment to yield the normalized Fourier coefficient magnitudes shown in Figs. 4.2 and 4.3 for $n = 2$ and $n = 3$ modes, respectively. In the current study, all the harmonics are neglected except for the n^{th} one due to the fact that there are other sources of uncertainties in the process. The most important uncertainty would be the variation in the size of the mass perturbations. Also, sensing the other harmonics orientations is not possible from the outermost ring due to the relatively small sizes of them. Keeping all the harmonics is not practical and does not necessarily impact the tuning process in a positive way. The values of the normalized amplitudes retained for the analysis are summarized in Tables 4.1 and 4.2. for $n = 2$ and $n = 3$

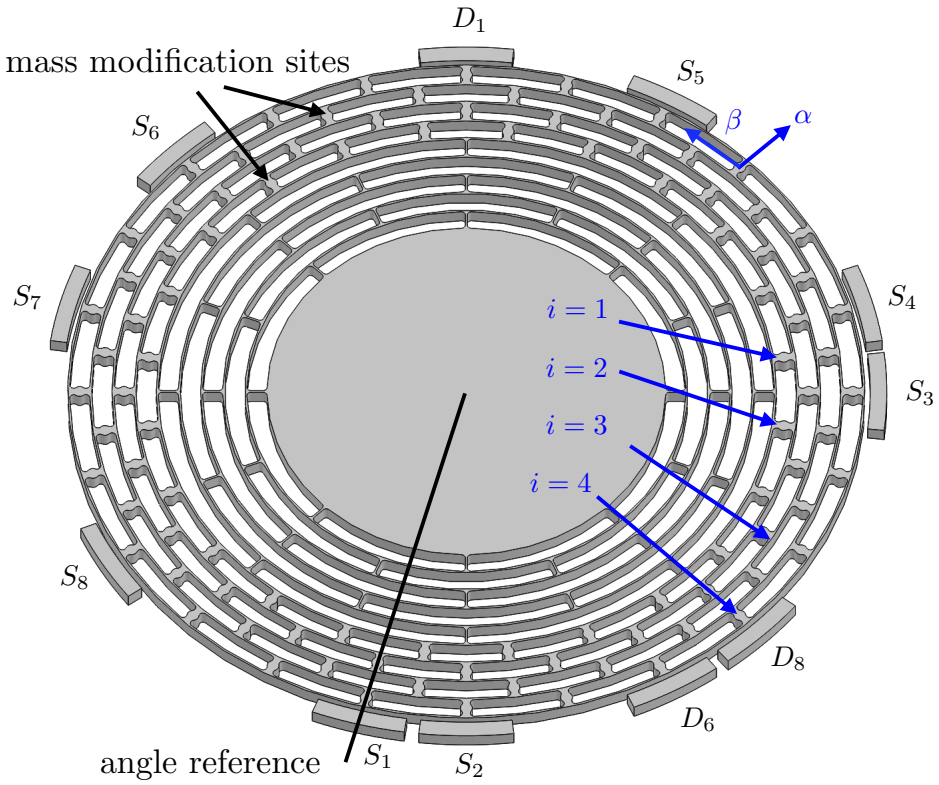

Figure 4.1: An isometric view of the resonator showing the mass perturbation sites and the electrodes used in driving and data collecting.

modes, respectively. By labeling these amplitudes as $\alpha_{n,i}$ and $\beta_{n,i}$ for the radial and tangential components for the modes n in the k^{th} layer, a unified model can be derived for both $n = 2$ and $n = 3$ modes. The sensitivity of the innermost ring, γ_{n_1}, can be taken as the universal sensitivity for mode n where the amplitude of the radial velocity $\alpha_{n,1}$ is the largest. The normalization then takes place based on this value. It should be noted the term $\left((\frac{\alpha_{n,i}}{\alpha_{n,1}})^2 - (\frac{\beta_{n,i}}{\alpha_{n,1}})^2\right)$ is unit-less and is a characteristic of the resonator's design. This multiplicative factor needs to be found from FEA. For an arbitrary design, FEA yields the ratio of different harmonics for the mass perturbation sites.

Table 4.1: Normalized amplitudes of velocity harmonics for $n = 2$ modes

layer, i	$\alpha_{2,i}$	$\beta_{2,i}$
1	1	0.4969
2	0.9289	0.4603
3	0.8506	0.4214
4	0.7868	0.3886

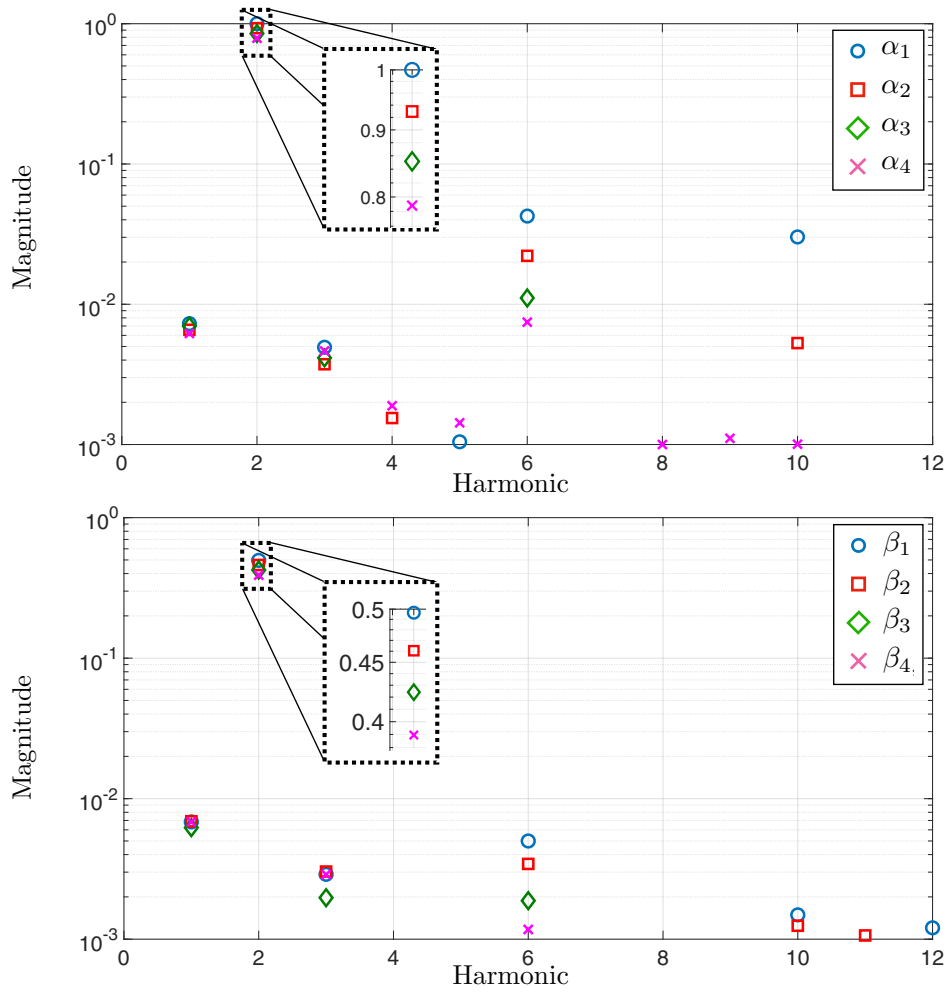

Figure 4.2: (Top) The magnitude of the Fourier series coefficients for the spoke radial velocities at different layers for $n = 2$ modes. (Bottom) The magnitude of the Fourier series coefficients for the spoke tangential velocities at different layers for $n = 2$ modes. All harmonics are negligible except for the second one.

Table 4.2: Normalized amplitudes of velocity harmonics for $n = 3$ modes

layer, i	$\alpha_{3,i}$	$\beta_{3,i}$
1	1	0.3257
2	0.8741	0.2878
3	0.7543	0.2492
4	0.6750	0.2171

Extending (4.16), the kinetic energy model for a practical ring-resonator can be written as

$$\tilde{\Delta}_n e^{j2n\tilde{\psi}_{n_1}} = \Delta_n e^{j2n\psi_{n_1}} + \gamma_n \sum_q \mu_q \left((\frac{\alpha_{n,r(q)}}{\alpha_{n,1}})^2 - (\frac{\beta_{n,r(q)}}{\alpha_{n,1}})^2 \right) e^{j2n\theta_q}, \tag{4.17}$$

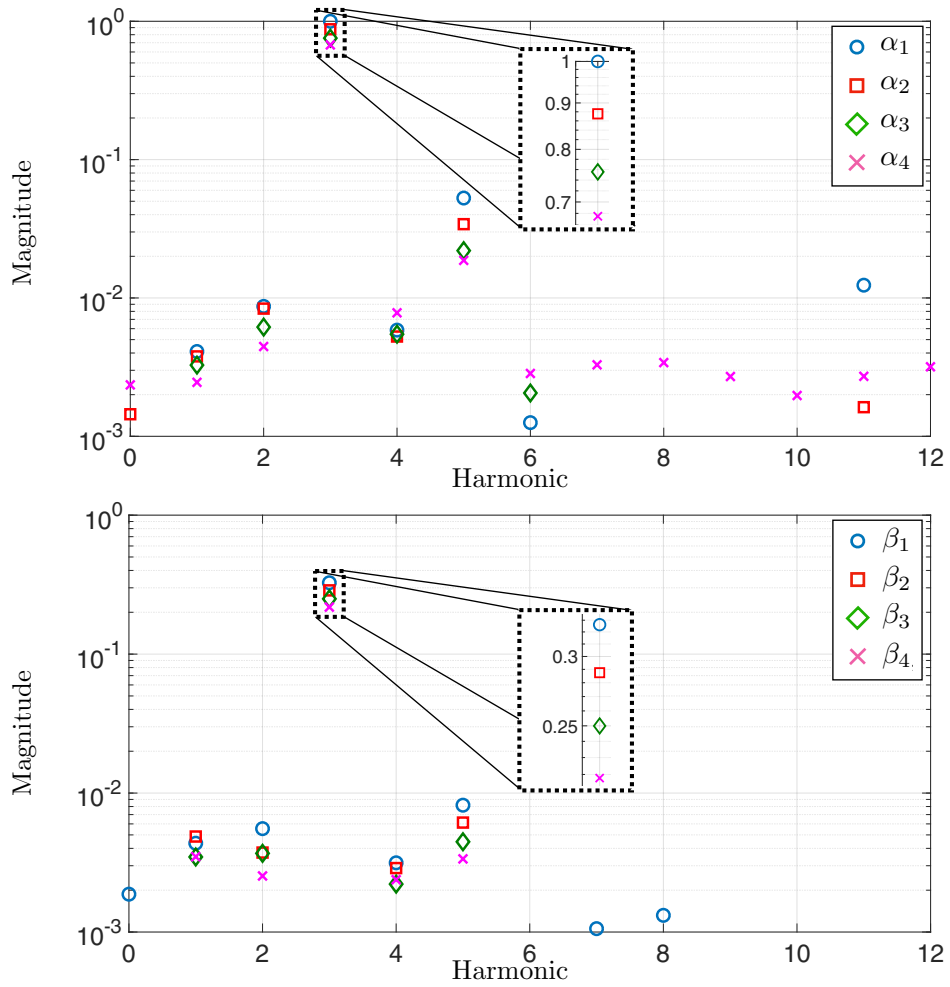

Figure 4.3: (Top) The magnitude of the Fourier series coefficients for the spoke radial velocities at different layers for $n = 3$ modes. (Bottom) The magnitude of the Fourier series coefficients for the spoke tangential velocities at different layers for $n = 3$ modes. All harmonics are negligible except for the third one.

where γ_n is the universal sensitivity for the resonator, μ_q is an integer indicating the number of fixed size point mass perturbations placed at angle θ_q, and $r(i)$ is a function with integer output ranging from 1 to 4 which indicates the layer associated with the mass perturbations. The values for $\alpha_{n,r(q)}$ and $\beta_{n,r(q)}$ can be found from Tables 4.1 and 4.2. The expression in (4.17) is used in simultaneous tuning of $n = 2$ and $n = 3$ modes of the axisymmetric resonator. This expression is more general than the tuning expression used in [SKS15] and [BKS17]. It is worthwhile mentioning that the model in (4.17) allows the variation of the anti-node orientations due to the mass perturbations as opposed to the model developed in Chapter 3 which is meant to be used for single mode tuning.

4.2 Solution via Integer Linear Programming

4.2.1 Relaxed Linear Programming Problem

In order to tune the $n = 2$ and $n = 3$ modes, both of the frequency splits must be reduced to essentially zero. To capture both modes in one expression, a combination of the two frequency splits can be used as the objective function that needs to be minimized (it will be discussed that the frequency splits should remain essentially positive). The objective function $\mathcal{C}$ is

$$\begin{aligned}\mathcal{C} = {} & W_2\tilde{\Delta}_2\cos(4\tilde{\psi}_2) + W_2\tilde{\Delta}_2\sin(4\tilde{\psi}_2) \\ & + W_3\tilde{\Delta}_3\cos(6\tilde{\psi}_3) + W_3\tilde{\Delta}_3\sin(6\tilde{\psi}_3),\end{aligned} \tag{4.18}$$

where W_2 and W_3 are the weights associated with the $n = 2$ and $n = 3$ frequency splits, respectively.

There are some practical constraints that should be taken into consideration in the optimization problem. In a nutshell, the optimization problem and the constraints can be written as

$$\begin{aligned}&\underset{\mu_q\in\mathbb{Z}}{\text{minimize}} \quad \mathcal{C} \\ &\text{subject to} \qquad \tilde{\Delta}_2\cos(4\tilde{\psi}_{2_1}) \leqslant d_2,\ \tilde{\Delta}_2\sin(4\tilde{\psi}_{2_1}) \leqslant d_2, \\ &\qquad\qquad -\tilde{\Delta}_2\cos(4\tilde{\psi}_{2_1}) \leqslant d_2,\ -\tilde{\Delta}_2\sin(4\tilde{\psi}_{2_1}) \leqslant d_2, \\ &\qquad\qquad \tilde{\Delta}_3\cos(6\tilde{\psi}_{3_1}) \leqslant d_3, \quad \tilde{\Delta}_3\sin(6\tilde{\psi}_{3_1}) \leqslant d_3, \\ &\qquad\qquad -\tilde{\Delta}_3\cos(6\tilde{\psi}_{3_1}) \leqslant d_3,\ -\tilde{\Delta}_3\sin(6\tilde{\psi}_{3_1}) \leqslant d_3.\end{aligned} \tag{4.19}$$

where d_2 and d_3 are two positive bounds that need to be selected by the user. The justification for using (4.19) will be postponed to later in this section where the linear programming will be explained.

Defining the objecting function as in (4.18) allows us to favor one mode more than the other if necessary. For instance, if only tuning $n = 2$ frequency split is desired, then W_2 and W_3 can be picked to be 1 and 0, respectively. For simultaneous tuning, a reasonable choice is $W_2 = W_3 = 1$ which are the selected values for the weights in all the case studies in this chapter. The reason

the frequency splits did not appear in the objective function as $\tilde{\Delta}_2 + \tilde{\Delta}_3$ is the fact that we cannot benefit from the linear programming algorithms in such a case (see (4.17)).

From (4.17), the frequency split and anti-node orientation can be estimated after the perturbations if the frequency split and the anti-node orientation of any of the modes before the perturbations are known as well as the size and location of the mass perturbations. However, the actual problem is different and the perturbations are not known. The only set of information available contains the frequency splits and the anti-node orientations prior to the perturbations. Further, there may be some practical constraints for the problem, yet the goal is always the same: reducing the frequency splits to essentially zero. The solution to this problem is the size and location of the mass perturbations. Assuming a nominal size mass is used, the solution can be written as a vector containing the number of masses at each of the locations dedicated to mass perturbations. The number of masses is represented by $\mu_q \in \mathbb{Z}$, where $\mathbb{Z}$ is the set of integer numbers. Changing the size of the nominal mass perturbation affects the solution.

Although, the kinetic energy perturbation model (see (4.17)) is applicable to both $n = 2$ and $n = 3$ with minor modifications, tuning both modes simultaneously is significantly more complicated than the tuning of one mode. From the dynamics of perturbed rings, the neighborhood of the mass perturbations can be selected quite easily when the objective is tuning one of the modes. Knowing this constraint makes the numerical problem and search algorithm much easier. However, when the focus is tuning both modes, the search space cannot be restricted in general (except for rare cases, such as coincidence of the anti-nodes of two modes) and finding the solution to the tuning problem requires sophisticated search algorithm.

This section takes a closer look at the search process and a relaxed version of the problem is solved using linear programming. The relaxed assumption is the solution may have a non-integer number of perturbations at a given location. A branch and bound technique yields the integer solution by removing the relaxation assumption for the number of a nominal point mass perturbations at each location. In Sec. 4.2.3, it is shown that the tuning process is feasible in practice by adjusting the size of the mass perturbation.

The first step for finding the optimal solution to the tuning problem is defining the objective

function (see (4.18)) and the constraints. The constraints are mostly practical limitations in placing the mass perturbations. The main constraints encountered in the tuning process are

- Integer number of perturbations at each location
- Number of point mass perturbations in one location
- Total number of point mass perturbations
- Positiveness of the frequency splits

Below, each of the aforementioned constraints is discussed in more detail.

Integer Number of Perturbations at Each Location

As discussed in Sec. 4.1.1, the sensitivity is defined based on a nominal fixed size point mass perturbation. One is allowed to have an integer number of point mass perturbations at each of the predefined locations. Even when there is an infinite resolution for mass perturbations (see [BKS17]), defining a nominal mass size is practical. For mass addition, the technique used in this work, defining the mass quanta is inevitable.

Number of Point Mass Perturbations in One Location

Based on the size of the mass perturbation compared to the dedicated spokes, the number of mass perturbations that can be placed at one location varies. In the case studies of this chapter, two types of mass perturbations are used: a large and a small perturbation. For the larger one, only one perturbation can be placed at each location. However, for the smaller perturbation, up to three masses can be used at a spoke. This is a practical constraint for the tuning problem and, depending on the size of the spoke as well as the type and size of the mass perturbations, the limit needs to be set.

Total Number of Point Mass Perturbations

The constraint on the total number of perturbations is more concerned with the practicality of the solution. The total number of mass perturbations that can be used is set to make sure the tuning algorithm can be solved in a reasonable amount of time.

Positiveness of the Frequency Splits

For solving the tuning problem, the objective function must be minimized. However, having a large negative frequency split is as undesirable as having a large positive frequency split. A constraint that guarantees the absolute values of the frequency splits are minimized is therefore necessary.

As mentioned in Sec. 4.2.1, the ultimate goal is to have an integer number of nominal point masses at each of the spokes. However, it is common to solve a relaxed version of the problem by removing the integer constraint. For this case, a linear programming problem will be solved for minimizing the objective function $\mathcal{C}$ subject to the other constraints (all but having integer number of perturbations at each spoke). There are several different methods for solving linear programming optimizations. One of the common methods is the simplex method. This method is used as the default version for the command `linprog`, a built-in command in the optimization toolbox in MATLAB. Instead of explaining about the steps of the simplex method, the steps for writing the optimization in a format compatible to this command are shown. The command `linprog` can solve for x which leads to a minimum value of $f^T x$ subject to

- $Ax \leqslant b$,
- $lb \leqslant x \leqslant ub$,

where f, x, b, lb, and ub are vectors, and A is a matrix.

The first step is to write the objective function as $f^T x$ where the f is fixed and x is the solution to the optimization problem. The variable x contains the information about the number of point

mass perturbations at each location. The vector $f \in \boldsymbol{R}^{97}$ is equal to

$$\begin{bmatrix} W_2\Delta_2 h(4\psi_{2_1}) + W_3\Delta_3 h(6\psi_{3_1}) \\ W_2\gamma_2(\alpha_{2,r}^2 - \beta_{2,r}^2)h(4\theta) + W_3\gamma_3(\alpha_{3,r}^2 - \beta_{3,r}^2)h(6\theta) \end{bmatrix}, \tag{4.20}$$

where $h(\theta) = \cos(\theta) - \sin(\theta)$. The first element $W_2\Delta_2 h(4\psi_{2_1}) + W_3\Delta_3 h(6\psi_{3_1})$ is a scalar and the second portion of (4.20) is a 96×1 vector based on the locations of the dedicated areas in the resonator for mass perturbations. The values of $\alpha_{2,r}$, $\beta_{2,r}$, $\alpha_{3,r}$ and $\beta_{3,r}$ are selected based on the layer of the spoke and Tables 4.1 and 4.2 whereas the angle θ specifies the location of the spoke with respect to the angle origin. The angle origin can be selected arbitrarily as long as it is the same as the angle used for the anti-node orientations. In order to get the objective function $\mathcal{C}$ to be in the form of $f^T x$, the first element in the 97×1 vector x has to be 1 and the other 96 elements are the solutions to the optimization problem.

The vectors lb and ub give the minimum and the maximum number of perturbations at each spoke. For the first element of x, both the lower and upper bound are equal to 1. For the rest of the elements, the lower bound is always equal to 0 and the upper bound depends on the size of the nominal perturbation. For the larger perturbation, the upper bound is 1 at the first step. The upper bound can set to be 0 for the locations we wish to avoid due to the pre-existence of mass perturbation.

The other constraint is on the maximum number of point mass perturbations. In order to get the total number, all the elements in the vector x need to be summed except for the very first one. So, the first row in the matrix A is called A_1 and is composed of a 0 stacked next to 96 elements all equal to 1. The first element in the vector b is called b_1 and is the maximum number of masses allowed.

The last constraint is based on the fact that the frequency splits cannot be large negative numbers which would lead to a smaller objective function which is not desirable in practice. In order to avoid such a scenario, we want to have the following constraints.

$$|\tilde{\Delta}_2| \leqslant d_2', \quad |\tilde{\Delta}_3| \leqslant d_3', \tag{4.21}$$

where $|\cdot|$ gives the absolute value and d_2' and d_3' are two positive bounds that need to be selected by the user. These two numbers are usually selected based on the initial frequency splits and the sensitivity of the fixed size point mass perturbation used in tuning. Implementing (4.21) for a linear optimizer is practically very difficult. Instead, the constraints used are

$$\begin{aligned} |\tilde{\Delta}_2 \cos(4\tilde{\psi}_{2_1})| \leqslant d_2, \quad |\tilde{\Delta}_2 \sin(4\tilde{\psi}_{2_1})| \leqslant d_2, \\ |\tilde{\Delta}_3 \cos(6\tilde{\psi}_{3_1})| \leqslant d_3, \quad |\tilde{\Delta}_3 \sin(6\tilde{\psi}_{3_1})| \leqslant d_3, \end{aligned} \tag{4.22}$$

where d_2 and d_3 are two positive bounds that need to be selected by the user. The expressions in (4.22) need to be written in a linear format as

$$\begin{aligned} \tilde{\Delta}_2 \cos(4\tilde{\psi}_{2_1}) \leqslant d_2, \qquad \tilde{\Delta}_2 \sin(4\tilde{\psi}_{2_1}) \leqslant d_2, \\ -\tilde{\Delta}_2 \cos(4\tilde{\psi}_{2_1}) \leqslant d_2, \quad -\tilde{\Delta}_2 \sin(4\tilde{\psi}_{2_1}) \leqslant d_2, \\ \tilde{\Delta}_3 \cos(6\tilde{\psi}_{3_1}) \leqslant d_3, \qquad \tilde{\Delta}_3 \sin(6\tilde{\psi}_{3_1}) \leqslant d_3, \\ -\tilde{\Delta}_3 \cos(6\tilde{\psi}_{3_1}) \leqslant d_3, \quad -\tilde{\Delta}_3 \sin(6\tilde{\psi}_{3_1}) \leqslant d_3. \end{aligned} \tag{4.23}$$

The expressions in (4.23) can be implemented as $A_2 x \leqslant b_2$ and they will be stacked together with the constraint on the total number of point mass perturbations. The matrix $A_2 \in \boldsymbol{R}^{8\times 97}$ and each row of A_2 is associated with one of the inequalities in (4.23). The construction of one row is explained here. The first element of the first row is $\Delta_2 \cos(4\psi_{2_1})$ and the remaining elements are $\gamma_2(\alpha_{2,r}^2 - \beta_{2,r}^2)\cos(4\theta)$, where $\alpha_{2,r}$, $\beta_{2,r}$ and θ are the same as the terms in (4.20). The other rows of the matrix A_2 are constructed similarly. The first four elements in the vector b_2 are d_2 and the last four elements are d_3 (Sec. 4.2.1). The matrix $A \in \boldsymbol{R}^{9\times 97}$ matrix and the 9×1 vector b can be written as

$$A = \begin{bmatrix} A_1 \\ A_2 \end{bmatrix}, \quad b = \begin{bmatrix} b_1 \\ b_2 \end{bmatrix}. \tag{4.24}$$

The optimization problem can be solved easily using the simplex method. However, the solution vector contains non-integer components which makes the implementation very difficult.

4.2.2 Integer Linear Programming

Now the relaxation assumption made in Sec. 4.2.1 regarding potentially non-integer number of nominal mass perturbations at the spokes is revoked. To properly reformulate the problem, a branch and bound technique is used. The version of the branch and bound routine that is explained here is for the binary case meaning that there is either one or zero nominal point mass at each spoke. The same idea can be extended to the scenario when the number of perturbations can be greater than one.

The binary assumption is typically the first step for tuning these resonators with larger point mass perturbations. Since there are 96 perturbation sites, the number of different permutations is 2^{96}. Considering all of these scenarios is impossible in practice, and so a systematic method needs to be implemented for significantly reducing the number of cases. The branch and bound method is a clever way of enumerating all solutions and solves the problem more efficiently. The process starts with one node for which there is no restriction on the values of different variables. At each node, a "branch" on an integer variable is formed, where on each branch, the integer variable is restricted to take certain values. Assume that all the spokes are numbered from 1 to 96. The first branch puts a constraint on the value of the first variable and assumes it is either 1 or 0. There are no constraints on the other 95 variables. The value for the objective function is calculated based on the frequency splits and anti-node orientations prior to the mass perturbations from (4.18) and is called the stored optimal objective. The linear programming is solved using the built-in command for each case. It is clear that the objective function value for the relaxed problem is smaller than the non-relaxed version of the problem, since the solution to the non-relaxed version is a subset of the relaxed case. So if the relaxed version's solution is insufficient, then the node can be deactivated. After "pruning" a node, there is no need for branching from it. We need to continue the process while there are some active nodes in the branch and bound graph. Fig. 4.4 summarizes the branch and bound routine as it applies to the binary mass tuning problem.

The optimization toolbox in MATLAB has also a built-in command that implements this routine efficiently which is called `intlinprog`. The results from this command and the branch and bound algorithm described here are essentially the same.

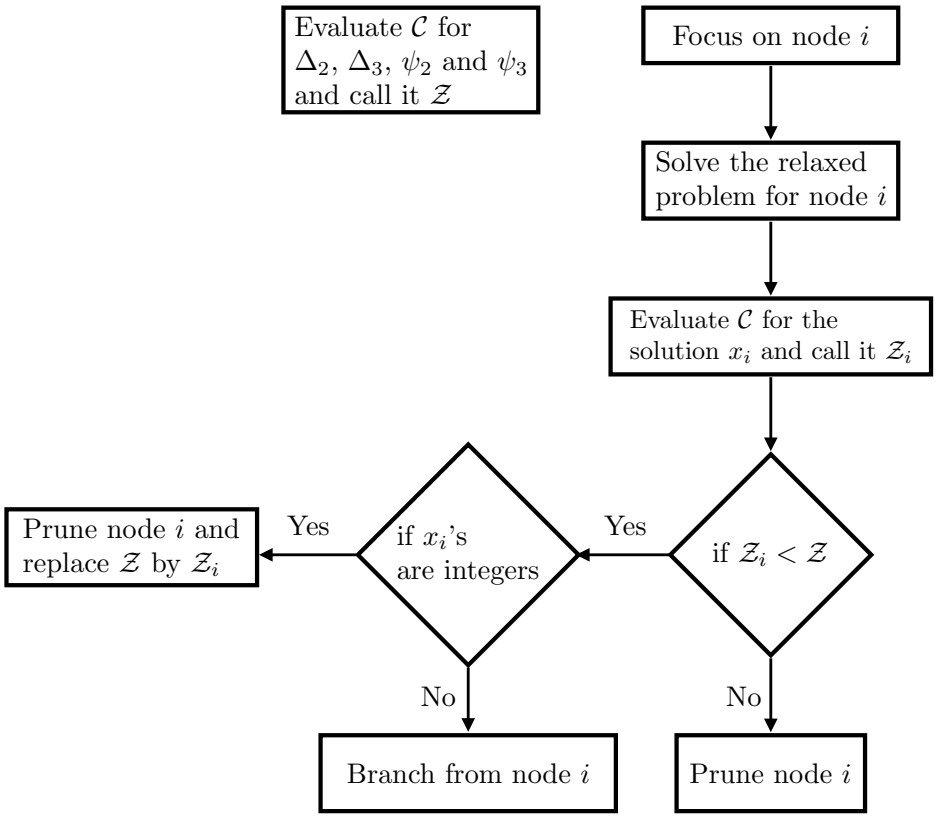

Figure 4.4: Flowchart summary of the branch and bound routine.

4.2.3 Existence of a Solution

The general idea is to use the expression in (4.17) to get sufficiently small values for both $n = 2$ and $n = 3$ frequency splits after the perturbations ($\tilde{\Delta}_2$ and $\tilde{\Delta}_3$). The sufficient reduction depends on the application. This section studies why the solution for the problem necessarily exists in practice. Without loss of generality, the process can be restricted to either mass addition or mass removal. Here, mass addition is considered to be the only type of mass perturbations. The proof is essentially the same for the mass removal case.

Assume the frequency splits and the anti-node orientations for the smaller frequencies for $n = 2$ and $n = 3$ modes are (Δ_2, ψ_{2_1}) and (Δ_3, ψ_{3_1}), respectively. The frequencies are sorted in this analysis such that the frequency splits are assumed to be always positive ($\omega_{n_2} > \omega_{n_1}$) without loss of generality (negative frequency split would lead to the change in the orientation of the anti-node).

From [BM17], we know that placing two same sized perturbations at 45° (or 135°) will not change the frequency split for $n = 2$ modes for sufficiently small perturbation size. Now the objective becomes reducing the frequency split for $n = 3$ modes using two point masses of the same size that are 45° apart. First of all, based on the quantized location constraints, the two locations with 45° spacing can always be found assuming the practical constraints allow. For two point mass perturbations 45° apart with the size of fixed nominal mass perturbation located at θ_0 and $\theta_0 + 45^\circ$ at a given layer, (4.17) becomes

$$\begin{aligned} \tilde{\Delta}_3 \cos(6\tilde{\psi}_{3_1}) &= \Delta_3 \cos(6\psi_{3_1}) + g_3 \left(\cos(6\theta_0) + \cos(6(\theta_0 + 45^\circ))\right), \\ \tilde{\Delta}_3 \sin(6\tilde{\psi}_{3_1}) &= \Delta_3 \sin(6\psi_{3_1}) + g_3 \left(\sin(6\theta_0) + \sin(6(\theta_0 + 45^\circ))\right), \end{aligned} \tag{4.25}$$

where g_3 is the sensitivity for $n = 3$ modes for a nominal mass multiplied by appropriate factors based on the layer. The expression in (4.25) can be simplified as

$$\begin{aligned} \tilde{\Delta}_3 \cos(6\tilde{\psi}_{3_1}) &= \Delta_3 \cos(6\psi_{3_1}) + g_3 \left(\cos(6\theta_0) + \sin(6\theta_0)\right), \\ \tilde{\Delta}_3 \sin(6\tilde{\psi}_{3_1}) &= \Delta_3 \sin(6\psi_{3_1}) + g_3 \left(\sin(6\theta_0) - \cos(6\theta_0)\right), \end{aligned} \tag{4.26}$$

The frequency split after the perturbation can be found from the square root of the sum of the

squares of the right hand sides of (4.26),

$$\tilde{\Delta}_3 = \sqrt{\Delta_3^2 + 2g_3^2 + 2\Delta_3 g_3 \left(\cos(6(\psi_{3_1} - \theta_0)) - \sin(6((\psi_{3_1} - \theta_0))\right)}. \tag{4.27}$$

For the case of mass addition, $g_3 > 0$. In order for the frequency split to decrease, the following inequality should hold.

$$\cos(6(\psi_{3_1} - \theta_0)) - \sin(6(\psi_{3_1} - \theta_0)) < -\frac{g_3}{2\Delta_3}, \tag{4.28}$$

which can be simplified as

$$\cos(6(\psi_{3_1} - \theta_0) + \frac{\pi}{4}) < -\frac{g_3}{2\sqrt{2}\Delta_3}. \tag{4.29}$$

The solution for θ_0 to (4.29) is always a non empty set as long as the size of mass associated with g_3 is selected properly according to the frequency split Δ_3. This shows it is always possible to reduce the $n = 3$ frequency split by preserving the $n = 2$ frequency splits by sufficiently small size mass perturbations. A similar argument can be made about reducing $\tilde{\Delta}_2$ using two equally sized perturbations 30° or 90° apart from each other. This shows that each pair can be tuned while leaving the other split unperturbed. The optimization algorithm addresses the practical constraints.

4.3 Demonstration

The systematic simultaneous tuning for $n = 2$ and $n = 3$ modes are demonstrated for two resonators in this section. First, the electrode configuration is described for the drive and sense channels, followed by the results are presented for different rounds of measurements.

4.3.1 Electrode Configuration

For this chapter, a single electrode is used for all the sense and drive channels as opposed to [SKS15], [BKS17] and the experiments done in Chapter 3. Two drive and eight sense channels are used for finding the frequency response estimates for each of the modes. It should be noted

that looking at two sense channels is sufficient for finding the frequency split and the anti-node orientation especially when the frequency split is sufficiently large [SKS15]. On the other hand, by focusing on two channels only when the frequency splits are small, the frequency response estimates from the regular chirp signal can be misleading. For the cases with small splits, it is suggested to look at all of the sense channels to ensure accurate frequency splits for both modes. Fig. 4.5 shows the electrodes' configuration. All the sense electrodes and D_1 are used for both modes while D_8 and D_6 are used for $n = 2$ and $n = 3$, respectively. The electrodes associated with the gyro bias are removed from the figure for clarity. By using eight sense channels in addition to three drive channels, close proximity between some of the channels is inevitable and causes a relatively high feedthrough which can mask the resonance peak. In order to avoid this, a frequency response with the same frequency range needs to be recorded at atmospheric pressure and is subtracted from the frequency response in the vacuum. A demodulation technique is used for removing the feedthrough from different channels.

The locations of the sense channels are selected to obtain as many independent measurements as possible from the outermost ring to see if there is any other harmonics present that can be sensed. Although finite element suggests other harmonics are present in the motion, due to their small sizes compared to the dominant harmonics in the outermost ring, it is not possible to sense them even with eight single sense electrodes. The orientation of the anti-nodes for three innermost rings is the same as the one measured for the outermost ring (see [BKS17] and Chapter 3). For this study, the angle origin is assumed to be the same for both $n = 2$ and $n = 3$ modes. However, having the same origins for two modes is not necessary. On the other hand, having the same angle origin for reading the anti-node and the locations of the mass perturbations is required. This is the assumption made in (4.17). Ultimately, having two inputs and two outputs are sufficient for getting a decent frequency response for a resonator especially when the frequency split is large enough. In Sec. 4.3.2, the results are presented for two-input two-output case.

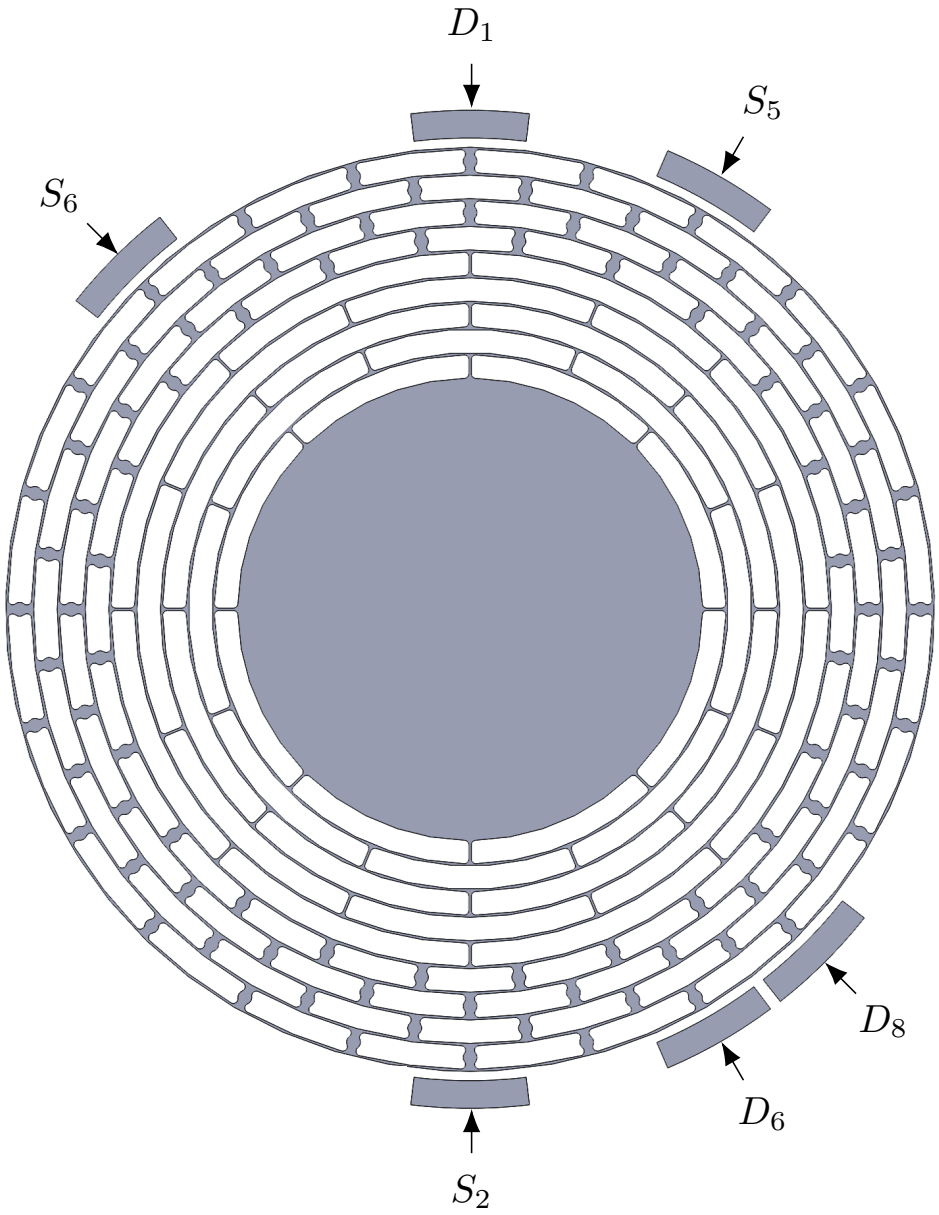

Figure 4.5: The electrodes configuration for testing $n = 2$ and $n = 3$ modes. All the sense electrodes and D_1 are used for both modes. D_8 and D_6 are used for $n = 2$ and $n = 3$, respectively. The electrodes associated with the gyro bias are removed from the figure.

4.3.2 Test Results

In this section, the results for two resonators are presented. The two resonators are selected from the same wafer. First of all, the generalized sensitivities for $n = 2$ and $n = 3$ modes need to be found. This can be done by placing mass perturbations on the resonator and comparing the frequency splits and anti-node orientations before and after perturbations using (4.17) modified for $n = 2$ and $n = 3$ modes. The sensitivities can be estimated using FEA. There are two mass perturbations used in this study. The larger mass is about 10 times larger than the smaller one. Once the sensitivities are found for the larger masses, the sensitivities for the smaller ones are also known. According to the specifications of the larger masses, the diameters can vary by about 5%. Based on the spherical shape of the masses prior to melting, this variation in the diameter can lead to up to 30% variation in the volume. However, the variation between the masses selected from the box for tuning is much smaller and it is about $10 - 15\%$ of the volume, resulting in the sensitivities having up to 15% uncertainty. The general idea in the tuning process is to use the larger solder spheres to reduce the frequency splits to less than a couple of hertz and then use the smaller solder spheres to tune both modes. If the uncertainties were less significant, the tuning could have always happened in two rounds: one with large and one with small spheres. However, due to the uncertainties, addition of an extra round to the process may be necessary. In almost all cases, the tuning can be done systematically in a maximum of three rounds.

The frequency splits and anti-node orientations from the frequency response of the resonator must be estimated. The frequency splits and the anti-node orientations are the inputs to the tuning algorithm. In the test results presented here, due to the faster turn around time, the mass addition technique used is not compatible with wafer-level manufacturing as opposed to the technique introduced in Chapter 3. The first level of reduction happens with larger mass perturbations which are solder spheres with about 75μm diameter. The sensitivities for this nominal mass can be estimated with FE and confirmed with test results. These sensitivity values are the other inputs for the tuning algorithm. At this step, the constraints are the total number of mass perturbations (for this problem, the limit is set to be 9) and the fact that we cannot have more than one mass at each location. The tuning algorithm gives the locations that need to be targeted. The frequency splits seen

Table 4.3: Summary of tuning steps for the first device

Round	Δ_2 (Hz)	Δ_3 (Hz)	Perturbations
Initial testing	23.4896	2.4251	N/A
After round #1	3.6749	1.0647	9 large masses
After round #2	0.7192	1.1691	5 large masses
After round #3	**0.1050**	**0.1601**	8 small masses

after the first round differ from the ones predicted from the model by about 10% and are caused by the variation in the solder sphere size (sensitivities). The frequency splits and the anti-nodes are used one more time to find the target locations. The large spheres are used for this round and an additional constraint excising the locations used in the previous round is imposed. This limitation comes from a practical point of view and results from the difficulty of placing a large solder sphere on top of another one. Five locations are selected by the algorithm in this round.

The last round is with the smaller mass perturbations which have sensitivities 10 times smaller than the larger solder spheres. There is no need for having constraints on the possible target locations. The small masses can be placed on top of larger solder spheres. Also, two or three small point masses can be used in one spoke. For this part of the problem, an extended version of the branch and bound routine described in Sec. 4.2.2 needs to be used to accommodate for potentially having more than one mass at a spoke. Fig. 4.6 shows frequency response magnitude plots of $n = 2$ and $n = 3$ modes for two of the channels after total of three rounds of perturbations. The modes are essentially tuned and the frequency splits are reduced to 105 mHz and 160 mHz for $n = 2$ and $n = 3$ modes, respectively.

Fig. 4.7 shows a close up view of solder spheres melted on the resonator. The final mapping of the target locations is shown in Fig. 4.8. Different marks are used for large and small mass perturbations. Table 4.3 summarizes the tuning steps for the first device.

The frequency response magnitude plots for $n = 2$ and $n = 3$ modes are shown before and after perturbations in Fig. 4.9 for another device. The tuning process is done in two rounds using large masses. The targeted locations are depicted in Fig. 4.10. Table 4.4 summarizes the tuning steps for the second device.

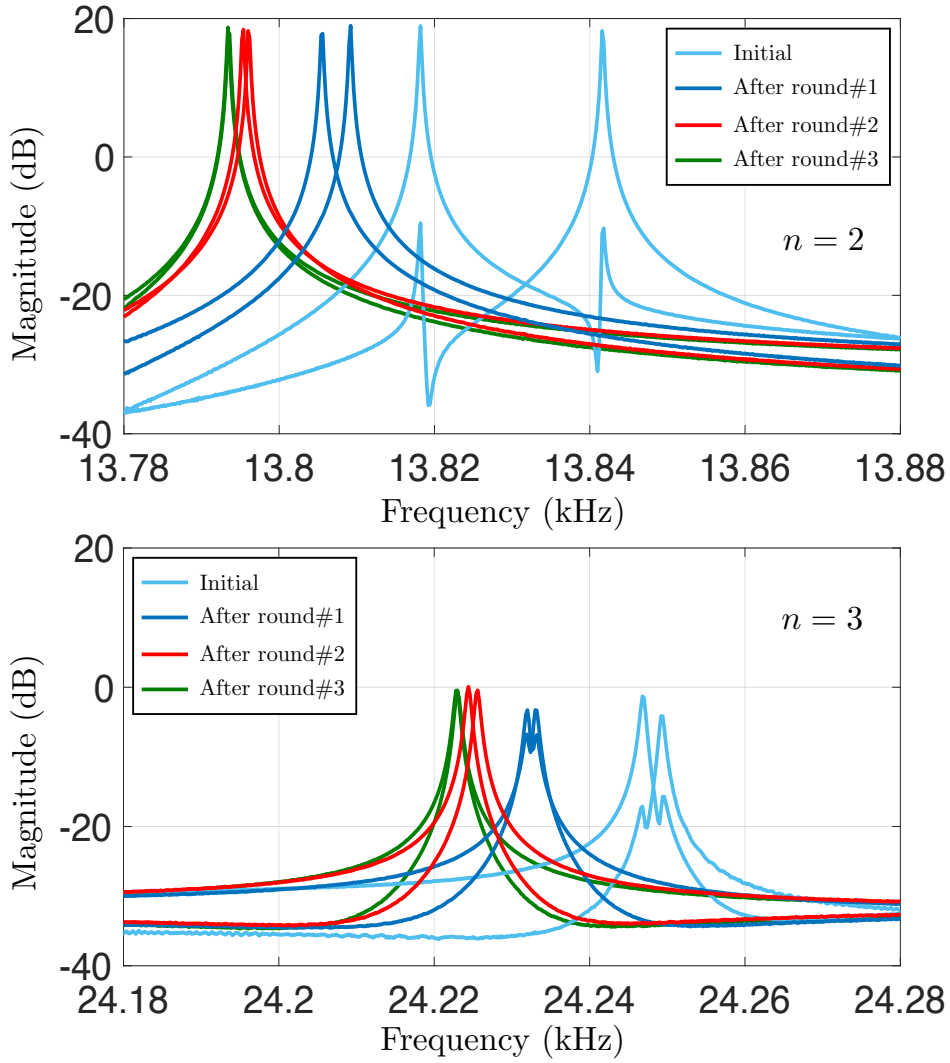

Figure 4.6: The frequency response magnitude plots of $n = 2$ and $n = 3$ for two of the channels at the initial testing after each round of perturbations show reduction from 23.4896 Hz and 2.4251 Hz to 105 mHz and 160 mHz frequency splits for $n = 2$ and $n = 3$ modes, respectively

Table 4.4: Summary of tuning steps for the second device

Round	Δ_2 (Hz)	Δ_3 (Hz)	Perturbations
Initial testing	6.8724	8.5496	N/A
After round #1	1.3898	0.8297	7 large masses
After round #2	**0.1227**	**0.0585**	6 large masses

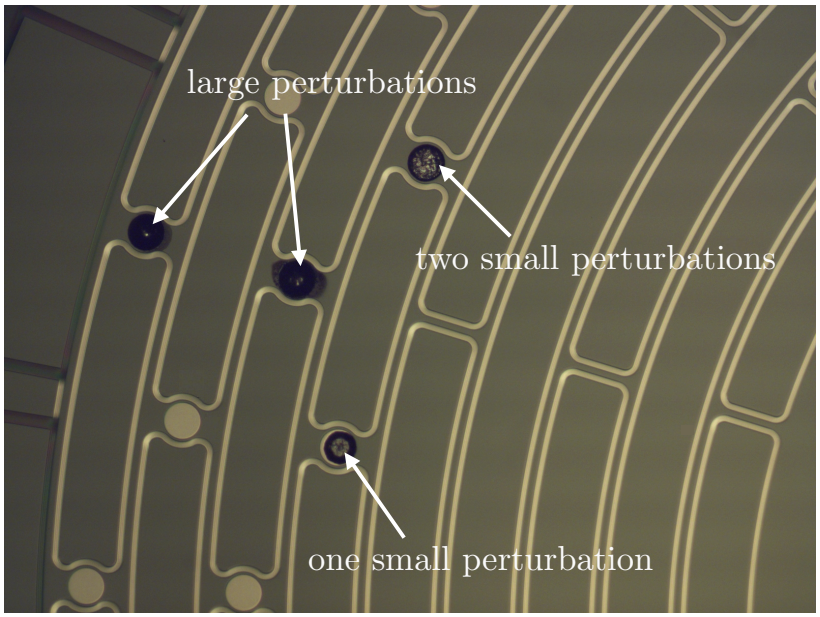

Figure 4.7: A close up view of solder spheres melted on the resonator spokes.

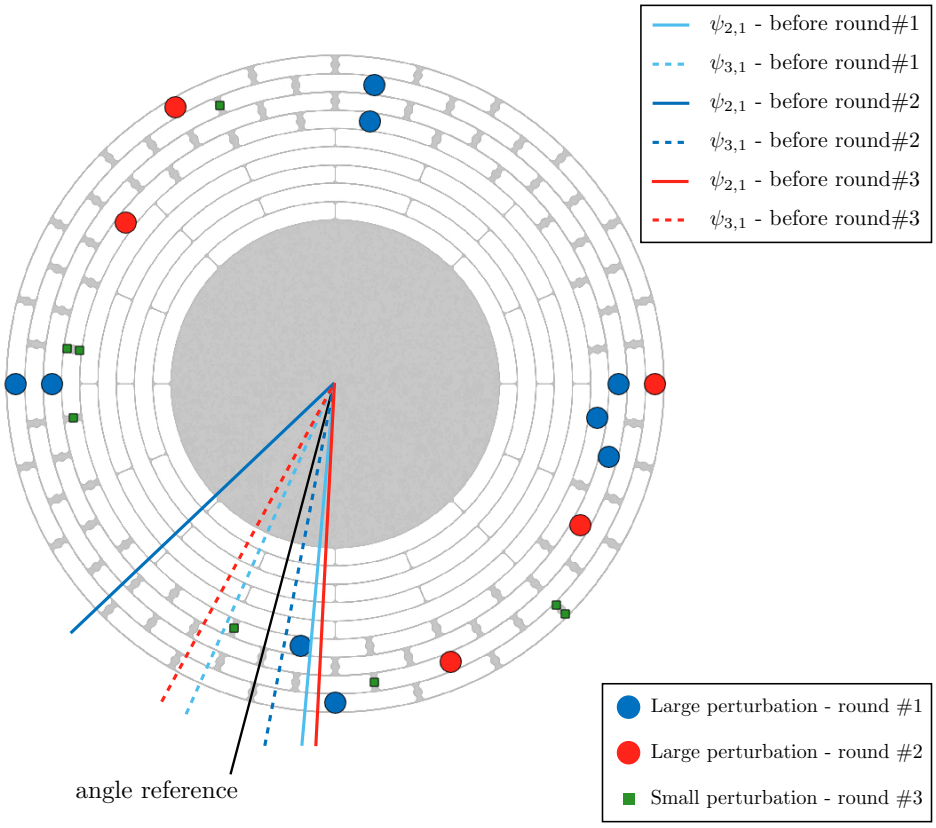

Figure 4.8: The map of different masses placed on the resonator in different rounds and the location of the anti-nodes for $n = 2$ and $n = 3$ modes at the initial testing and after each round. As seen, the locations are not necessarily selected near the anti-nodes.

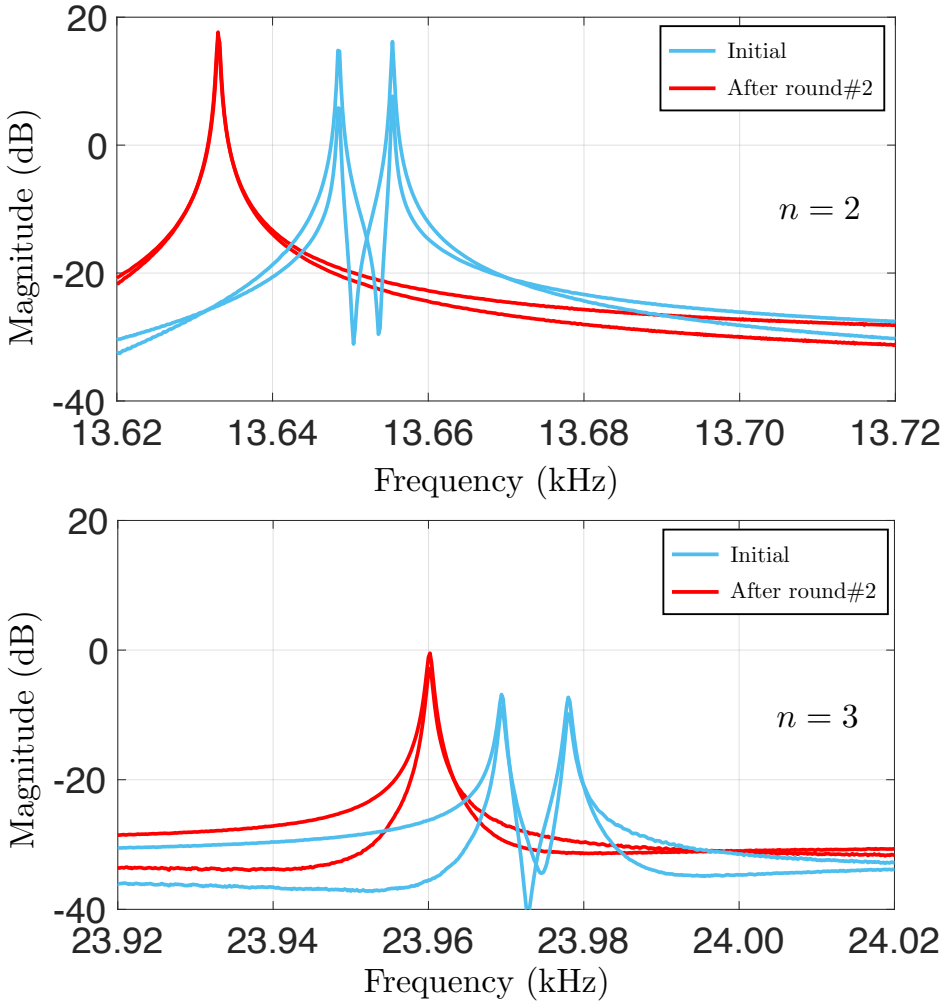

Figure 4.9: The frequency response magnitude plots of $n = 2$ and $n = 3$ modes for two of the channels at the initial testing and after two rounds of perturbations show reduction from 6.8724 Hz and 8.5496 Hz to 122.7 mHz and 58.5 mHz frequency splits for $n = 2$ and $n = 3$ modes, respectively.

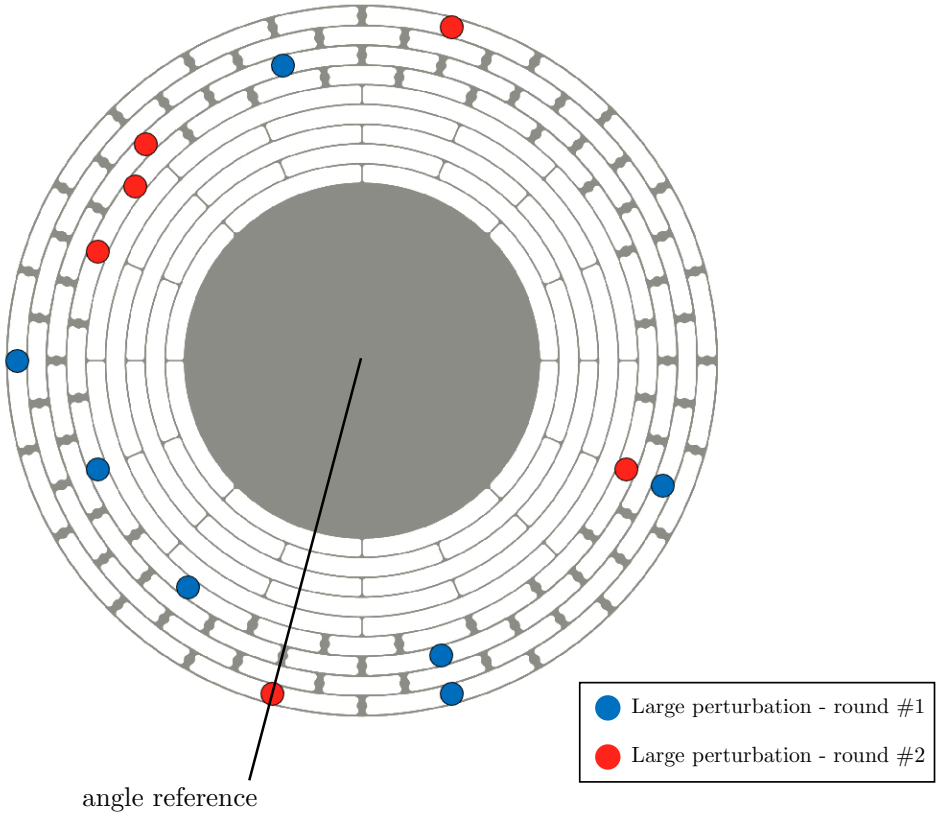

Figure 4.10: The map of different masses placed on the resonator in different rounds.

4.4 Multi-Modal Tuning Summary

A systematic post-fabrication technique has been demonstrated for simultaneous reduction of the modal frequency differences between the $n = 2$ and $n = 3$ modes in an axisymmetric resonator. The resonator is designed so mass removal at the large spokes creates a readily predictable perturbation to its dynamics. The mass addition on the large spokes can be assumed to be a pure mass perturbation with no effect on the potential energy of the structure. Finite element analysis is used to generalize the idea of perturbing the dynamics of a simple ring to a ring-type resonator. The dynamics are resonator-specific and the analysis needs to be done once for each resonator. The tuning equation is derived for both $n = 2$ and $n = 3$ modes by defining the universal sensitivities for each mode for a nominal fixed mass. The values for the sensitivities can be found in the first round of testing or from FEA and scaled for smaller or larger mass perturbations. The objective function is defined based on the absolute values of the frequency splits of two modes. The objective function and the constraints which are mostly based on the practical limitations of the process are written. A branch and bound routine is implemented based on a relaxed version of the problem by removing the assumption of having integer nominal point mass perturbations at each spoke. The relaxed version of the problem is solved using linear programming algorithm (simplex method) with a built-in command in optimization toolbox of MATLAB. The optimization problem is solved and two devices are tuned based on the solution systematically in two and three rounds.

CHAPTER 5

Damping Mechanisms

Nomenclature - Chapter 5

r	radial coordinate	ϵ_r	radial strain
θ	angle coordinate	ϵ_θ	tangential strain
z	out-of-plane coordinate	ϵ_z	out-of-plane strain
t	time	$\gamma_{z\theta}$	shear strain
u	radial displacement	σ_θ	tangential stress
w	tangential displacement	Q	quality factor
v	out-of-plane displacement	τ	time constant
$\bar{r}$	ring mean radius	$\mathrm{Re}(\cdot)$	real part
h	ring width	$\mathrm{Im}(\cdot)$	imaginary part
h_0	nominal ring width	W	tangential displacement eigenfunction
L	ring thickness	j	$\sqrt{-1}$
ρ	density	ω	modal frequency
ρ_0	nominal density	$\mathcal{T}$	kinetic energy
T	temperature	$\mathcal{U}$	strain energy
T_0	spatial temperature profile	$\mathcal{L}$	Lagrangian
T_{amb}	ambient temperature	$\mathcal{U}_0$	strain energy for no temperature change
E	modulus of elasticity	$\Delta_\mathcal{W}$	energy dissipation over one cycle
k	thermal conductivity	$(\cdot)_{,\theta}$	derivative with respect to θ
C_v	specific heat in constant volume	$(\cdot)_{,m\theta}$	m^{th} derivative with respect to θ
α	thermal diffusivity	$\dot{(\,)}$	derivative with respect to t
β	thermal expansion coefficient	$\lvert\cdot\rvert$	absolute value

Newly devised methods for fabricating micro-scale resonators have enabled the production of many axisymmetric designs that are finding application in compact, high-performance Coriolis vibratory gyros (CVGs) [ZTS12, CWY14, KBK15, BBC13, SAT14]. The axisymmetry produces modal frequency degeneracy which is desirable for reducing the effect of electronic buffer noise

on the measured angular rate [KM13]. Furthermore, the resonator attachment points to the sensor case are nodes of the modes that are exploited for the angular rate sensing –this decouples the modes from case motion and limits the transfer of energy from the modes into the supporting structure. Any physical resonator, however, suffers from some degree of imperfection which typically causes detuning of modal frequencies and couples the modes to the sensor case (see Chapter 3). The modal frequency detuning can be corrected by using electrostatic forces to essentially create springs between the resonator and its support [GHB05, KM06], or by perturbing the mass distribution of the resonator [SKS15, BKS17] (see Chapters 3 and 4). Both methods are effective in practice and have been used to create compact and very low noise CVGs [CGL14, GM17].

Modal time constants are also important factors in CVG performance. For example, the low-frequency root spectral density of the angular rate measurement is inversely proportional to the modal time constant [KM13]. Furthermore, time constant asymmetry appears in the expression for the zero-rate offset in CVGs: if τ_1 and τ_2 represent the time constants associated with the modes, then $1/\tau_1 - 1/\tau_2$ is a multiplicative factor that scales the rate offset [IEE04]. Of the many factors contributing to resonator energy dissipation, thermoelastic dissipation (TED), which is determined by the resonator material and geometry, is a source of energy loss that cannot be eliminated. Thus, sensor designers have strived to increase the modal time constants by fabricating resonators from low-loss materials like fused silica [PZT11]. There are other low-loss materials such as Invar, Zerodur and Corning ULE, which are ideal as far as the thermoelastic dissipation properties are concerned, but they have their challenges such as difficulties in their manufacturing process. In general, as opposed to the most common material for these types of resonators, silicon, the manufacturing process for other materials can be challenging.

Physically realizable resonators such as those found in CVGs have complicated geometries and are not analytically tractable (see Chapter 2). Ring resonators, on the other hand, are simple analogs of modally degenerate CVG resonators and although they lack a means of attachment to the sensor case, they are analytically tractable and provide conceptual guidance without delving into the complexity associated with practical resonator designs. Within this context, this chapter analyzes thermoelastic dissipation in ring resonators that are perturbed from uniformity. As discussed in Chapter 2, the dynamic analysis of a thin uniform ring with no dissipation was studied over a

century ago [Lov92]. The analysis has focused on the dynamics of nonuniform rings in the past three decades since they represent a more realistic model for manufactured structures. The analysis tool for most of these studies is the approximation method (e.g., [**?**, Fox90, BC07, YLY02]) in which a certain number of eigenfunctions of the uniform ring are used as a solution basis. The expansion of the exact solution for a uniform thin ring subject to point mass and spring perturbations can be found in Chapter 2 [BM17].

The problem of thermoelastic dissipation was first considered by Zener in the context of a vibrating beam [Zen37]. Thermoelastic dissipation in a uniform thin silicon ring resonator was studied in [WFM06] based on modifying the beam model proposed in [LR00]. The in-plane vibration of ring structure with multiple finite-sized imperfections is studied in [KK16] where the imperfections are modeled using the Heaviside step function. The effect of abrupt changes in the ring thickness on the frequencies, quality factors, and mode shapes were quantified. Step changes in ring thickness, however, are not typical of the imperfections caused by masking errors and etch non-uniformity during the fabrication of micro-scale resonators. Thermoelastic dissipation is considered for a ring with legs in [HMP16]. This is a more realistic model of a resonator since it provides a means of attachment to a substrate. The effect of the legs on the dynamics of the structure is analyzed, however, imperfections are not considered. Modifications to the geometry of tuning fork resonators and micro-scale hemispherical resonators are considered in [ZSP14] and [DSC17], respectively. Although TED plays a role in these studies, the primary objective was to mitigate anchor loss via coupling of the modes to the substrate to which the resonator is mounted.

An objective of this chapter is to address potential differences between the time constants of paired modes in perturbed ring resonators. In fact, it is shown that some imbalance in modal time constants is to be expected even when thermoelastic dissipation is the only energy loss mechanism. This chapter combines the temperature relationship in [WFM06] with the approach in [BC07] and [BM17] to derive the general equation of motion including thermoelastic effects for a thin ring subjected to ring width variation and point-mass perturbations. The gradual variation in structural member width is a typical model for capturing manufacturing imperfections whereas point-mass perturbations (either through mass loading or removal at specific locations on the ring) have been implemented as a post-fabrication technique for manipulating the resonator modal proper-

ties, primarily the frequencies of paired modes. The width perturbations are modeled as low-order harmonic variations and are not intended to capture abrupt changes in ring width.

The chapter is organized as follows. The equation of motion, which includes thermoelastic effects, is derived in Sec. 5.1 for a thin ring whose width and density are allowed to be functions of the angular variable θ. Galerkin's method employing a partial set of eigenfunctions of the unperturbed ring is used to estimate modal frequencies and mode shapes of the perturbed ring in Sec. 5.2. In the fully coupled problem, the modal frequencies are complex-valued with the imaginary parts being related to the time constants of the modes. This section also considers the weakly coupled approximation in which the perturbed ring equation in the absence of thermal effects is analyzed. The solution to the elastic problem is subsequently used to determine the temperature distribution in the ring and, finally, the work done over one period of harmonic motion is computed. Several case studies are considered in Sec. 5.3 for uniform and imperfect rings. The resonant frequencies and time constants for different geometries and different materials are plotted for $n = 2$ and $n = 3$ modes. The temperature profiles are compared for silicon and fused silica for a given geometry. The effects of 1-θ and 2-θ perturbations of the ring width, as well as point-mass perturbations, are determined for fused silica ring resonators on the scale of the resonator discussed in [CGL14]. The width perturbations are used to model fabrication imperfections that can be introduced by mask errors and etch non-uniformities in microscale resonators, while point-mass perturbations are good models for the post-fabrication approaches that have been developed for reducing the differences between the modal frequencies in disk resonators, e.g., [SKS15, BKS17]. A case study shows that degeneracy between modal frequencies is possible, however, differences between the modal time constants still exist and thus reveals limitations of the mass trimming techniques that have been employed for post-fabrication correction. The weakly coupled approximation is also performed, and it is shown that the modal frequencies and time constants derived from the weakly coupled analysis are indistinguishable from the fully-coupled analysis results.

5.1 Ring Model

The equation of motion for a nonuniform ring is derived. Fig. 5.1 shows the schematic of a thin ring in which the ring width, denoted h, is assumed to be small compared to the nominal mean radius $\bar{r}$, but may vary as a function of θ. The ring thickness, L, is constant. The following are assumed for this analysis:

1. There is no out-of-plane motion so the out-of-plane displacement, denoted v, and all the derivatives with respect to the out-of-plane coordinate denoted z, are equal to zero.

2. The structure experiences small deformation which leads to a geometrical constraint between the radial and tangential displacements.

3. Since the beam thickness h is much smaller than the mean radius $\bar{r}$, Poisson's ratio is zero and derivatives of displacement variables with respect to the radial coordinate r are zero.

4. The beam width h is defined with respect to the mean radius $\bar{r}$, i.e., on each side of the mean radius circle, the width is $h/2$. So in the polar cylindrical coordinates, the radial component is between $-h/2$ and $h/2$. This assumption is reasonable because of the small beam width compared to the ring radius.

5. Heat transfer occurs only in the radial direction even though the width is a function of θ. Thus, the temperature profile scales according to the local thickness.

The last assumption is justified because the perturbation of the width is at most 15% of the nominal width h_0 and, furthermore, no abrupt changes in width are considered, so width perturbations are slowly varying as a function of θ.

The equation of motion is determined once the kinetic and strain energies are computed. The kinetic energy only depends on the geometry of the structure and is independent of temperature, however, the strain energy is a function of the temperature profile. Due to the simplicity of the heat diffusion problem, a closed-form expression for the temperature profile is determined and then substituted into the strain energy expression and in this way, the derived equation of motion incorporates thermoelastic effects. Solutions are then approximated using Galerkin's procedure.

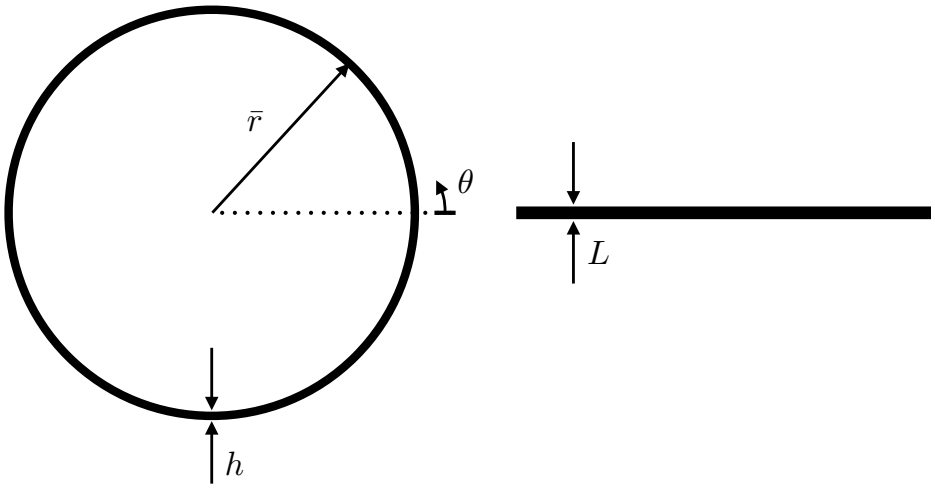

Figure 5.1: Ring parameters. Note that h is not a function of θ in this figure, although it is for the analysis.

5.1.1 Kinetic Energy

The kinetic energy $\mathcal{T}$ of the ring is

$$\mathcal{T} = \int_0^{2\pi} \frac{1}{2}\rho(\theta)h(\theta)L\bar{r}\Big(\dot{w}^2(\theta,t) + \dot{u}^2(\theta,t)\Big)\mathrm{d}\theta, \tag{5.1}$$

where ρ and h are the θ-dependent density and beam thickness, respectively, L and $\bar{r}$ are the constant out of plane height and mean radius, $w(\theta,t)$ and $u(\theta,t)$ are the in-plane tangential and radial displacements, respectively. The out-of-plane displacement is zero and does not appear in the kinetic energy expression.

5.1.2 Strain Energy

Langhaar derives the strain tensor components for a thin elastic shell under the assumption of constant temperature [Lan49]. These results can be simplified for a ring by assuming no out-of-plane motion. Furthermore, since the ring is assumed to be thin in both the radial and out-of-plane directions, the derivatives of any kinematic variables with respect to r and z are zero. Consequently, Poisson's ratio can also be assumed to be zero for a thin ring for in-plane motion. The origin of r is the centerline of the ring, and it is assumed that perturbations to the ring width are symmetric

about the centerline. Lastly, small displacements imply that a geometric constraint exists between the radial and tangential displacements, i.e., $u_{,\theta} = -w$. The sign depends on the assumed direction of positive displacement and is consistent with [Lan49] and is different from Chapter 2. The strain components for a thin ring at constant temperature reduce to

$$\epsilon_\theta = \frac{1}{\bar{r}^2}\Big(w_{,\theta} + w_{,3\theta}\Big)r, \quad \epsilon_z = 0, \quad \epsilon_r = 0, \quad \gamma_{z\theta} = 0. \tag{5.2}$$

The following shorthand notation is used to make the expressions more compact: $w_{,\theta} = \partial w/\partial\theta$, $w_{,k\theta} = \partial^k w/\partial\theta^k$. There is only one non-zero stress component,

$$\sigma_\theta = \frac{E}{\bar{r}^2}\Big(w_{,\theta} + w_{,3\theta}\Big)r. \tag{5.3}$$

where E is the modulus of elasticity of the material.

When temperature variation is included, the strain components are modified to

$$\epsilon_\theta = \frac{\sigma_\theta}{E} + \beta T(r,\theta,t), \quad \epsilon_r = \epsilon_z = \beta T(r,\theta,t), \quad \gamma_{z\theta} = 0, \tag{5.4}$$

where β is the linear coefficient of thermal expansion and T is the temperature within the ring (assumed to be a function of r, θ and t). Even with temperature variation, σ_θ is given by (5.3). Due to the fact that σ_θ is the only non-zero stress component, the strain energy at time t simplifies to

$$\mathcal{U} = \frac{1}{2}\int_0^{2\pi}\int_0^L\int_{-\frac{h}{2}}^{\frac{h}{2}} \sigma_\theta\epsilon_\theta \,\mathrm{d}r\,\mathrm{d}z\,\bar{r}\,\mathrm{d}\theta = \frac{\bar{r}L}{2E}\int_0^{2\pi}\left(\int_{-\frac{h}{2}}^{\frac{h}{2}}\left(\sigma_\theta^2 - \beta E T\sigma_\theta\right)\mathrm{d}r\right)\mathrm{d}\theta. \tag{5.5}$$

Further manipulation is possible once the temperature profile T is determined.

5.1.3 Temperature Profile

The strain energy computation requires the ring temperature T. The temperature profile for a uniform thin ring was derived in [WFM06] under the assumption of small deviations of the ring temperature relative to the ambient temperature. It was also shown in this reference that the ring temperature can be approximated as a one-dimensional problem. The source term in the diffusion

equation governing the ring temperature is the azimuthal strain, ϵ_θ, and so T is a function of θ, however, the diffusion can be considered to occur only in the radial direction due to the small ratio of nominal ring width to the ring radius, i.e., h_0/a, where h_0 is the nominal ring width. Thus, [WFM06] showed the following differential equation to be a reasonable approximation of the ring temperature,

$$\frac{\partial T}{\partial t}\left(1+2\frac{E\beta^2 T_{\text{amb}}}{C_{\text{v}}}\right)-\alpha\frac{\partial^2 T}{\partial r^2}=-\frac{E\beta T_{\text{amb}}}{C_{\text{v}}}\frac{\partial \epsilon_\theta}{\partial t}, \tag{5.6}$$

where α is the thermal diffusivity of the material, C_{v} is the heat capacity per unit volume, and T_{amb} is the ambient temperature of the ring when not in motion.

The solution of (5.6) is obtained by representing the temperature and tangential displacement as $T(r,\theta,t)=T_0(r,\theta)\text{e}^{\text{j}\omega t}$ and $w(\theta,t)=W(\theta)\text{e}^{\text{j}\omega t}$, where ω is complex-valued, and $\text{j}=\sqrt{-1}$. Thus, (5.6) can be written as

$$\frac{\partial^2 T_0}{\partial r^2}-\text{j}\omega\frac{\mu}{\alpha}T_0=\text{j}\omega\frac{1}{\alpha}\frac{\Delta_E}{\bar{r}^2\beta}\left(W_{,\theta}+W_{,3\theta}\right)r. \tag{5.7}$$

where $\Delta_E=E\beta^2 T_{\text{amb}}/C_{\text{v}}$ and $\mu=1+2\Delta_E$. Assuming negligible heat flow between the surfaces of the ring and the environment, the boundary conditions for (5.7) are $\partial T_0/\partial r(\pm h/2,\theta)=0$. Note h is assumed to be a function of θ, but as heat diffusion in the azimuthal direction is ignored, the temperature profile derived from (5.7) is simply scaled to the local ring width. The temperature profile can then be determined as function of the tangential mode shape W,

$$T_0(r,\theta)=-\frac{\Delta_E}{\mu\bar{r}^2\beta}\left(W_{,\theta}+W_{,\theta\theta\theta}\right)\left[r-\frac{1}{K}\sec\left(\frac{hK}{2}\right)\sin(Kr)\right], \tag{5.8}$$

where the parameter K is defined to be $\sqrt{-\text{j}\omega/\alpha}$.

5.1.4 Equation of Motion and Boundary Conditions

In Sec. 5.1.1 the expression for the kinetic energy $\mathcal{T}$ is given, however, the final expression for the strain energy $\mathcal{U}$ is determined by combining (5.5) and (5.8),

$$\mathcal{U} = \frac{EL}{2\bar{r}^3}\int_0^{2\pi} (w_{,\theta} + w_{,\theta\theta\theta})^2 \times \left[\frac{h^3}{12}\left(1 + \frac{\Delta_E}{\mu} + \frac{\Delta_E}{\mu}\left(\frac{hK - 2\tan(\frac{hK}{2})}{K^3}\right)\right)\right] \mathrm{d}\theta. \tag{5.9}$$

Thus, the Lagrangian $\mathcal{L} = \mathcal{T} - \mathcal{U}$ is determined from (5.1) and (5.9). The ring equation of motion is found by computing the first variation of $\mathcal{L}$ and then applying Hamilton's principle,

$$\begin{aligned}
&-\rho(\theta)h(\theta)L\bar{r}\ddot{w} + \rho_{,\theta}hL\bar{r}\ddot{w}_{,\theta} + \rho h_{,\theta}L\bar{r}\ddot{w}_{,\theta} + \rho hL\bar{r}\ddot{w}_{,2\theta} \\
&\quad + \kappa\Big(w_{,\theta} + w_{,3\theta}\Big)\left[\left(1 + \frac{\Delta_E}{\mu}\right)g_{,3\theta} + \frac{\Delta_E}{\mu}f_{,3\theta}\right] \\
&\quad + 3\kappa\Big(w_{,2\theta} + w_{,4\theta}\Big)\left[\left(1 + \frac{\Delta_E}{\mu}\right)g_{,2\theta} + \frac{\Delta_E}{\mu}f_{,2\theta}\right] \\
&\quad + \kappa\Big(w_{,\theta} + 4w_{,3\theta} + 3w_{,5\theta}\Big)\left[\left(1 + \frac{\Delta_E}{\mu}\right)g_{,\theta} + \frac{\Delta_E}{\mu}f_{,\theta}\right] \\
&\quad + \kappa\Big(w_{,2\theta} + 2w_{,4\theta} + w_{,6\theta}\Big)\left[\left(1 + \frac{\Delta_E}{\mu}\right)g + \frac{\Delta_E}{\mu}f\right] = 0,
\end{aligned} \tag{5.10}$$

where

$$\kappa = \frac{EL}{12\bar{r}^3}, \quad g(\theta) = h^3, \quad f(\theta,\omega) = \frac{12}{K^3}\left(hK - 2\tan\left(\frac{hK}{2}\right)\right). \tag{5.11}$$

It should be noted that h and ρ are permitted to be functions of θ. Furthermore, K depends on the complex frequency ω.

5.2 Approximate Solutions

5.2.1 Galerkin Procedure

Solutions of (5.10) are approximated using the strong form Galerkin (SFG) method [Mei67]. The most sensible choice of basis functions are the eigenfunctions associated with the uniform thin ring, i.e., $\cos(k\theta)$ and $\sin(k\theta)$ for integer values of k, because they satisfy both the essential and

natural boundary conditions. Thus, the trial solution, denoted $\tilde{W}$, is given by

$$\tilde{W}(\theta) = \sum_{k=1}^{N} b_{2k-1}\cos(k\theta) + b_{2k}\sin(k\theta), \tag{5.12}$$

where $\{b_1, b_2, \cdots, b_{2N}\}$ is the set of basis function weights. The trial solution does not typically satisfy the equation of motion, so upon substitution of $\tilde{W}(\theta)\mathrm{e}^{\mathrm{j}\omega t}$ into (5.10), the left-hand side of (5.10) becomes the residual, denoted R, which is a function of ω and θ. The basis function weights are selected so that each basis function is orthogonal to R. In other words, the system of equations for the weights are generated from the conditions

$$\int_0^{2\pi} R(\omega,\theta)\cos(k\theta)\mathrm{d}\theta = 0, \quad \int_0^{2\pi} R(\omega,\theta)\sin(k\theta)\mathrm{d}\theta = 0.$$

By increasing the number of basis functions in the trial solution, the accuracy of the approximate solution improves, however, the computational complexity also increases.

The orthogonality between R and each basis function generates a row in a $2N \times 2N$ matrix that is denoted $\mathcal{R}$. The constraints are gathered as $\mathcal{R}\boldsymbol{b} = 0$, where $\boldsymbol{b}$ is the vector of basis function weights. Note that $\mathcal{R}$ is a function of ω, however, it can be expressed in terms of a mass matrix, denoted $\mathcal{M}$, and stiffness matrix, denoted $\mathcal{K}$. In other words, $\mathcal{R} = -\mathcal{M}\omega^2 + \mathcal{K}(\omega)$. While the mass matrix is constant, the stiffness matrix depends on ω as noted. Thus, Galerkin's method produces a non-standard eigenvalue problem due to the ω-dependence of $\mathcal{K}$, however, an iterated procedure for determining the weight vectors and frequencies appears to work well in practice: an initial frequency "guess", ω_0, is used to determine $\mathcal{K}(\omega_0)$, then the eigenvalue problem $\left(-\mathcal{M}\tilde{\omega}^2 + \mathcal{K}(\omega_0)\right)\tilde{\boldsymbol{b}} = 0$ is solved for $\tilde{\omega}$ and $\tilde{\boldsymbol{b}}$; the process is repeated by setting $\omega_0 = \tilde{\omega}$. Convergence after one or two iterations is typical for the examples in Sec. 5.3, however, no proof of convergence is offered. The starting value for ω_0 can be chosen as the (real) frequency of the uniform ring with same nominal width and radius. Once the iterations terminate and ω is in hand, the quality factor Q and time constant τ can be computed

$$Q = \frac{1}{2}\frac{\mathrm{Re}(\omega)}{\mathrm{Im}(\omega)}, \quad \tau = \frac{2Q}{\mathrm{Re}(\omega)}, \tag{5.13}$$

where ω is expressed in rad/s, and where $\mathrm{Re}(\cdot)$ and $\mathrm{Im}(\cdot)$ are the real and imaginary parts of the argument, respectively.

5.2.2 Weakly Coupled Analysis

Time constants can also be estimated using a weakly coupled approximation [DCK06]. For low-loss materials like fused silica, the TED results from the weakly coupled approximation are indistinguishable from the TED results derived from fully-coupled equations when the same set of basis functions are used in the analyses. The weakly coupled approximation offers some advantages over the coupled analysis mainly deriving from the simpler equation of motion, the standard eigenvalue problem generated by applying Galerkin's method, and the routine calculations to compute the work done over one cycle of oscillation of harmonic motion. The ring equation derived under the assumption of no thermoelastic effects is obtained from (5.10) by setting f and its derivative zero. When analyzing this system, the mass matrix $\mathcal{M}$ is unchanged, however, $\mathcal{K}$ is now independent of ω so the eigenvalue problem yields mode shapes and (real-valued) modal frequencies.

The energy change over one cycle of harmonic motion, denoted $\Delta_{\mathcal{W}}$, is given by

$$\Delta_{\mathcal{W}} = \frac{1}{2\pi} \int_0^{\frac{2\pi}{\omega}} \int_V \mathrm{Re}(\sigma_\theta)\mathrm{Re}\left(\dot{\epsilon}_\theta\right)\, \mathrm{d}r\, \mathrm{d}z\, a\, \mathrm{d}\theta\, \mathrm{d}t, \tag{5.14}$$

where V denotes the ring volume. This quantity is negative since energy is dissipated over one cycle. The quality factor Q can be determined from the ratio of the total strain energy $\mathcal{U}_0$ to the energy lost $|\Delta_{\mathcal{W}}|$,

$$Q = \frac{\mathcal{U}_0}{|\Delta_{\mathcal{W}}|}. \tag{5.15}$$

The expression for $\mathcal{U}_0$ in this case omits temperature effects and so (5.9) is simplified accordingly.

It is rewarding to further study (5.14) because the role of the thermal conductivity α can be more clearly identified. Since all variables are assumed to be time-harmonic, $\mathrm{Re}(\sigma_\theta)$ is

$$\mathrm{Re}(\sigma_\theta) = \frac{E}{\bar{r}^2}\left(W_{,\theta} + W_{,3\theta}\right) r\cos(\omega t). \tag{5.16}$$

Furthermore,

$$\begin{aligned}\text{Re}\left(\dot{\epsilon}_\theta\right) &= \text{Re}\left(\frac{\dot{\sigma}_\theta}{E} + \beta\dot{T}\right) \\ &= -\frac{\omega}{\bar{r}^2}\left(W_{,\theta} + W_{,3\theta}\right) r\sin(\omega t) - \omega\beta\left(\text{Im}(T_0)\cos(\omega t) + \text{Re}(T_0)\sin(\omega t)\right),\end{aligned} \tag{5.17}$$

where T_0 is given by (5.8) in which ω is real and known. The terms in (5.16) and (5.17) that are in time-quadrature evaluate to zero in (5.14), thus, the energy dissipated is given by

$$\Delta_{\mathcal{W}} = \int_V -\frac{E\beta}{2\bar{r}}\left(W_{,\theta} + W_{,3\theta}\right) r\text{Im}(T_0)\,\mathrm{d}r\,\mathrm{d}z\,\mathrm{d}\theta. \tag{5.18}$$

As noted, T_0 is given by (5.8). However, an approximation can be made under the condition

$$e^{-h/\sqrt{\alpha/\omega}} << 1, \tag{5.19}$$

and in this case,

$$\int_{-\frac{h}{2}}^{\frac{h}{2}} r\text{Im}(T_0)\mathrm{d}r \approx \frac{\alpha}{\omega}\frac{\Delta_E}{\bar{r}^2\beta}\left(W_{,\theta} + W_{,3\theta}\right)\left(\sqrt{\frac{2\alpha}{\omega}} - h\right).$$

Thus, the energy dissipation over one cycle can be approximated by

$$\Delta_{\mathcal{W}} = -\frac{\alpha}{\omega}\frac{\Delta_E EL}{2\bar{r}^3}\int_0^{2\pi}\left(W_{,\theta} + W_{,3\theta}\right)^2\left(\sqrt{\frac{2\alpha}{\omega}} - h\right)\mathrm{d}\theta. \tag{5.20}$$

This expression is only valid when (5.19) is satisfied. This is the case for the fused silica ring case studies in Sec. 5.3 because $e^{-h/\sqrt{\alpha/\omega}} \approx 1.3 \times 10^{-5}$ for the dimensions used. On the other hand, this approximation is not valid for silicon rings of similar dimensions, and thus the complete expression for T_0 must be used in computing (5.18).

5.3 Thermoelastic Damping-Case Studies

This section presents several case studies for rings made out of silicon and low-loss materials such as fused silica, Invar, Zerodur and Corning ULE. The material properties used in the analysis are given in Table 5.1. It is assumed that the ambient temperature is $T_{\text{amb}} = 300\,\text{K}$. The first set of case

studies determines the modal frequencies and time constants for uniform thin rings (no variations in beam thickness or density) as a function of ring width and radius. In these cases, the modal frequencies appear in degenerate pairs with equal time constants. The resonant frequencies and time constants for $n = 2$ and $n = 3$ modes for different materials and various geometries are shown. Although, the manufacturing can still be an important issue for materials such as Invar or fused silica, knowing the potential advantages of different designs can be a quite useful guide for the researchers in the field. The result of the chapter will be a general guideline for researchers in the field for estimating the time constant that can be potentially achieved for a "non-standard" material. Obviously the process of machining and manufacturing materials other than silicon is more expensive and more difficult. However, taking into the account the potential upside, it may be a worthwhile investment based on the application. After choosing the material, getting the most out of that material is an essential task for the designers. This study will provide an optimization tool for this task. The optimization of the geometry can be used for any material and helps the researchers to get the best possible outcome for a given material. The temperature profiles for $n = 2$ and $n = 3$ modes for fused silica and silicon in a given geometry are studied to shed light on why low-loss materials have small damping.

	E (GPa)	β (K^{-1})	C_v (J m^{-3})	ρ (kg m^{-3})	α ($m^2 s^{-1}$)
Silicon	165	2.56×10^{-6}	1.64×10^{6}	2330	86×10^{-6}
fused silica	71.7	0.59×10^{-6}	1.55×10^{6}	2203	1.4×10^{-6}
Invar	142	1.5×10^{-6}	4.18×10^{6}	8100	3.2×10^{-6}
Zerodur	90.3	0.02×10^{-6}	2.02×10^{6}	2530	0.72×10^{-6}
Corning ULE	67.6	30×10^{-9}	1.70×10^{6}	2210	0.79×10^{-6}

Table 5.1: Material properties for silicon, fused silica, Invar, Zerodur and Corning ULE

The second set of case studies considers perturbed rings with small deviations from the uniform ring with a fixed nominal radius and width. The perturbations consist of variations in ring width, expressed in terms of harmonics in θ, and local changes in density to model point mass perturbations on the ring. The perturbation scenarios are considered both in isolation and in various combinations. The harmonic variations in thickness are intended to model manufacturing imperfections. In truth, it is unlikely for only one harmonic to be present in the width variation, but individually studying each harmonic provides insights into how different harmonics can affect

both the resonant frequencies and dissipation. The point mass perturbations are intended to model the kinds of "trimming" techniques that are likely to be used for eliminating modal frequency differences in micro-scale resonators, e.g., [SKS15, BKS17] (see Chapters 3, and 4). A scenario is also studied in which width variation is combined with point mass perturbations to yield degenerate modal frequencies for the "elliptical" pair of modes, however, the modes possess different time constants. The second set of case studies is presented for fused silica only. However, the results are also applicable to other materials.

5.3.1 Uniform Rings

5.3.1.1 Resonant Frequencies and Time constants for Different Geometries and Materials

The modal frequencies and time constants are computed for various geometries of a uniform ring. For fixed radii $\bar{r} \in \{0.25, 0.5, 0.75, 1\}$ cm, the modal frequencies and time constants are graphed versus ring width. The modes of interest are the elliptical pair, commonly referred to as the "$n = 2$ modes" (the mode shapes are given by $\cos(2\theta)$ and $\sin(2\theta)$) and "$n = 3$ modes" (the mode shapes are given by $\cos(3\theta)$ and $\sin(3\theta)$). Indeed, for the uniform ring, these are exactly the eigenfunctions associated with the modes. The out-of-plane dimension L does not play any role in the ring in-plane motion analysis. The modal frequencies and time constants for rings made out of fused silica for the $n = 2$ and $n = 3$ modes are shown in Fig. 5.2. The resonant frequencies and time constants for the $n = 2$ and $n = 3$ modes for silicon, Invar, Zerodur and Corning ULE for different geometries are given in Figs. 5.3, 5.4, 5.5 and 5.6, respectively.

5.3.1.2 Temperature Discussion

The temperature profile for the ring structure depends on the radial variable r, angle variable θ and time t. In Sec. 5.2, the temperature profile and the displacement are assumed to be harmonic. The time independent portion of the temperature variation $T_0(r, \theta)$ can be found from (5.8). However, the expression in (5.8) depends on the tangential displacement $W(\theta)$. For each of the modes, the corresponding time-independent temperature profile can be written once the tangential displacement $W(\theta)$ is found. Because of the existence of the term $K = \sqrt{-\mathrm{j}\frac{\omega\mu}{\alpha}}$ in (5.8) and the fact that

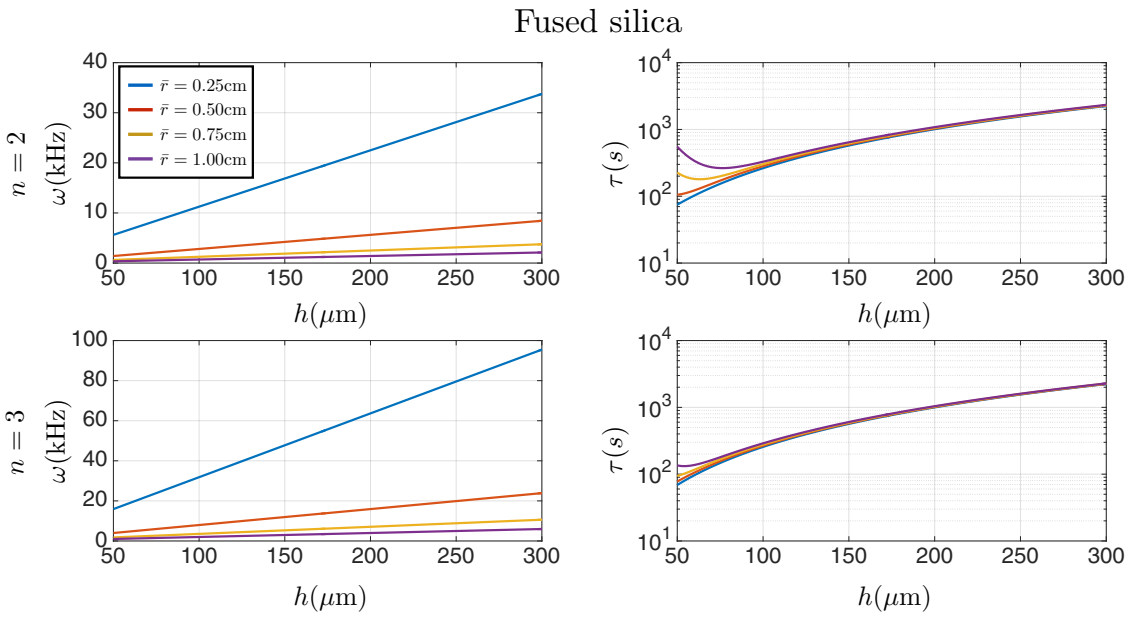

Figure 5.2: The comparison between ω and τ for $n = 2$ and $n = 3$ modes for fused silica rings for different geometries.

the frequency itself is a complex number, the temperature can be written as

$$T_0(r, \theta) = T_{0\mathrm{R}} + \mathrm{j}T_{0\mathrm{I}},$$

where $T_{0\mathrm{R}}$ and $T_{0\mathrm{I}}$ are the real and imaginary parts of the time independent temperature profile, respectively. The resonant frequency of the structure ω which appears in $\mathrm{e}^{\mathrm{j}\omega t}$ can be written as $\omega_{\mathrm{R}} + \mathrm{j}\omega_{\mathrm{I}}$, where ω_{R} and ω_{I} are real and imaginary parts of the frequency, respectively. Based on the harmonic motion assumption, the temperature profile can be written as

$$\begin{aligned} T(r, \theta, t) &= T_0(r, \theta)\mathrm{e}^{\mathrm{j}\omega t} \\ &= \big(T_{0\mathrm{R}} + \mathrm{j}T_{0\mathrm{I}}\big)\mathrm{e}^{\mathrm{j}(\omega_{\mathrm{R}} + j\omega_{\mathrm{I}})t} \\ &= \Big(T_{0\mathrm{R}} + \mathrm{j}T_{0\mathrm{I}}\Big) \times \Big(\cos(\omega_{\mathrm{R}}t) + \mathrm{j}\sin(\omega_{\mathrm{R}}t)\Big)\mathrm{e}^{-\omega_{\mathrm{I}}t} \\ &= \Big(T_{0\mathrm{R}}\cos(\omega_{\mathrm{R}}t) - T_{0\mathrm{I}}\sin(\omega_{\mathrm{R}}t)\Big)\underbrace{\mathrm{e}^{-\omega_{\mathrm{I}}t}}_{\text{decaying term}} \\ &\quad + \mathrm{j}\Big(T_{0\mathrm{R}}\sin(\omega_{\mathrm{R}}t) + T_{0\mathrm{I}}\cos(\omega_{\mathrm{R}}t)\Big)\mathrm{e}^{-\omega_{\mathrm{I}}t}. \end{aligned} \tag{5.21}$$

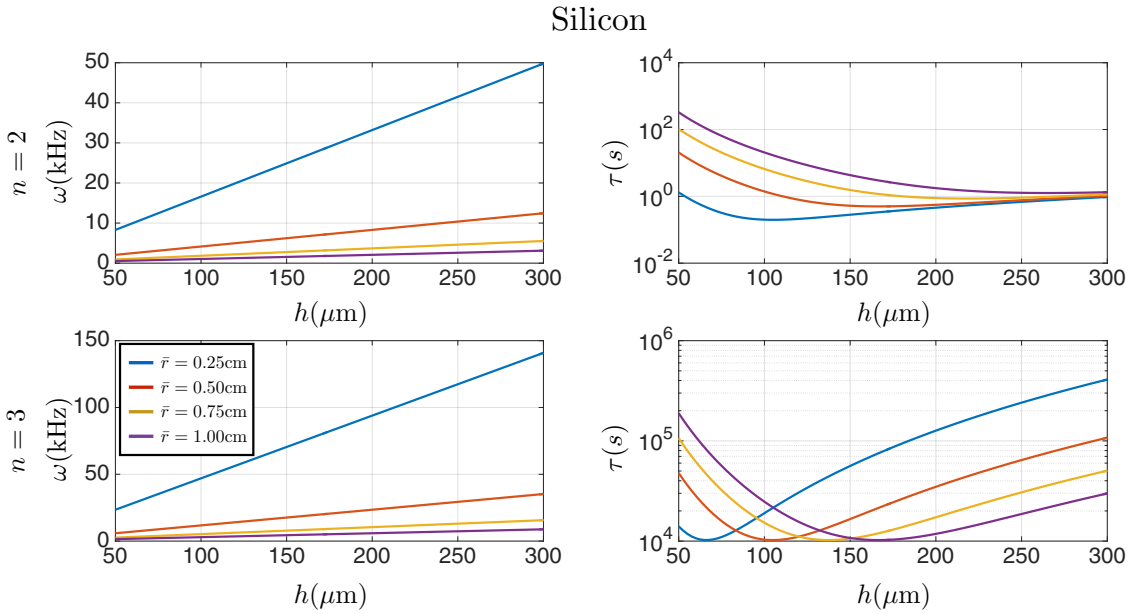

Figure 5.3: The comparison between ω and τ for $n = 2$ and $n = 3$ modes for silicon rings for different geometries.

For the case that the real part of the harmonic motion is considered, the real part of the the temperature profile needs to be taken as the actual temperature. So, the temperature profile for the ring structure from (5.21) is

$$T(r,\theta,t) = \Big(T_{0\mathrm{R}}\cos(\omega_{\mathrm{R}}t) - T_{0\mathrm{I}}\sin(\omega_{\mathrm{R}}t)\Big)\mathrm{e}^{-\omega_{\mathrm{I}}t}. \tag{5.22}$$

The expression in (5.22) is general and can be used for both uniform (constant beam width h and density ρ for throughout the whole ring) and imperfect rings.

To get a better understanding of the temperature profiles for different materials, the expression from (5.22) will be evaluated for a perfect ring with a given geometry based on the outer most ring of resonator presented in [BKS17] for silicon and fused silica. Although the analysis presented in this section is for a perfect ring, it can be easily extended to any other case studies by simply replacing $W(\theta)$ by the appropriate expression from the SFG analysis. For a uniform ring, the solution for $W(\theta)$ for $n = k$ modes are simply $\cos(k\theta)$ and $\sin(k\theta)$. For instance, for $n = 2$ modes in a uniform ring, the tangential displacement for one of the modes can be represented as a constant multiplied by $\cos(2\theta)$, and for the other mode it is simply proportional to $\sin(2\theta)$.

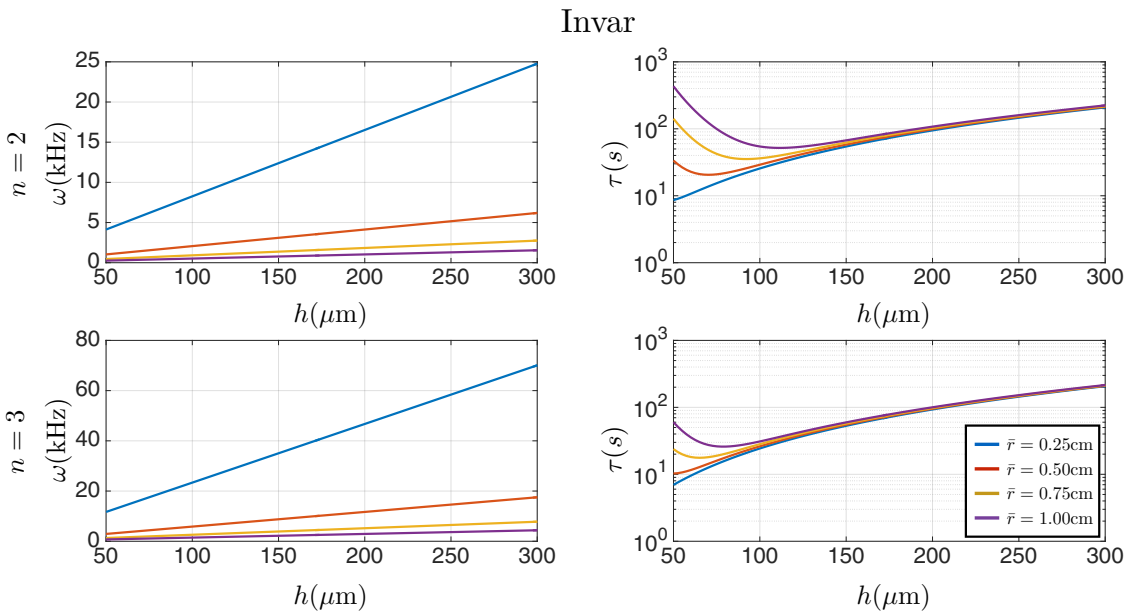

Figure 5.4: The comparison between ω and τ for $n = 2$ and $n = 3$ modes for Invar rings for different geometries.

For the case that the ring is not uniform, the tangential displacement for each of the modes is $B_1 \cos(k\theta) + B_2 \sin(k\theta)$, where B_1 and B_2 should be found from SFG.

In the analysis presented herein, since the tangential displacement can be scaled with any arbitrary scalar value in the eigenfrequency analysis, the temperature will be scaled with the same scaling factor. So, the absolute value of the temperature is not related to any physical variable, and the plots can only be used for comparing relative magnitudes of the temperature profiles. Although the absolute values for the temperatures cannot be extracted from this analysis, comparing the results is reasonable since the same weights for the basis functions are considered for both silicon and fused silica. The ring structure is opened and is presented as a rectangle with the length of 2π radians or 360° and width of h. The results are plotted over one period by looking at different phases. The times are selected based on the real part of the resonant frequency of the structure, which are 0, $0.25\mathbf{T}$, $0.5\mathbf{T}$, $0.75\mathbf{T}$ and $\mathbf{T}$, where $\mathbf{T}$ is the period of the motion which is equal to $\frac{2\pi}{\omega_R}$. The plot is a gradient plot normalized based on the largest present temperature variation in the problem. The purple color corresponds to the cooler temperature which is equivalent to less temperature variation, and the cyan color shows the hotter area which is equivalent to more temperature variation. Fig. 5.7 compares the normalized temperature profiles for silicon and fused silica

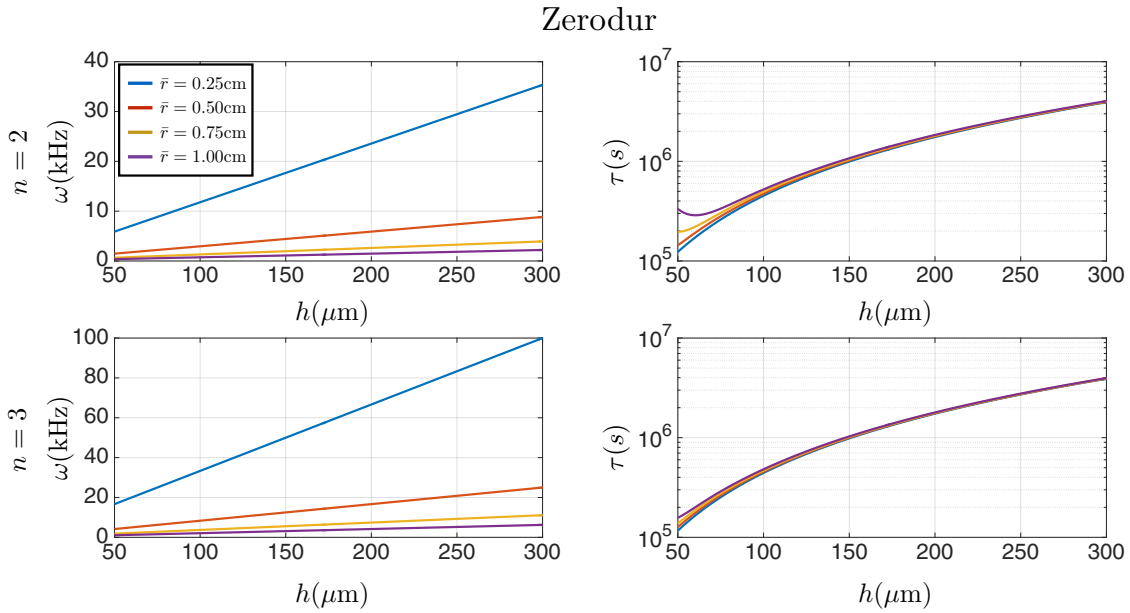

Figure 5.5: The comparison between ω and τ for $n = 2$ and $n = 3$ modes for Zerodur rings for different geometries.

for one of the $n = 2$ modes. The variation in silicon is much more significant because the thermal expansion coefficient is larger compared to fused silica. The other interesting observation is the phase of the temperature profiles which is different for the two materials. So, the lag is different for each material with respect to the displacement.

Fig. 5.8 depicts the normalized temperature profiles for silicon and fused silica for one of the $n = 3$ modes. The resonant frequency for which the times are selected is now based on the real part of the $n = 3$ resonant frequency of the structure. Fig. 5.8 clearly shows a much wider range of variation for silicon which leads to more loss in the motion and lower quality factor.

The lower thermal expansion coefficient which leads to less generated energy within the structure due to a given strain, and lower thermal diffusivity which causes a different energy distribution or temperature variation within the structure are the main reasons for less energy dissipation in "low-loss" materials such as fused silica.

5.3.2 Fused Silica Ring with a Single Perturbation

This section studies the effect of single perturbations on the n = 2 modes of the rings made out

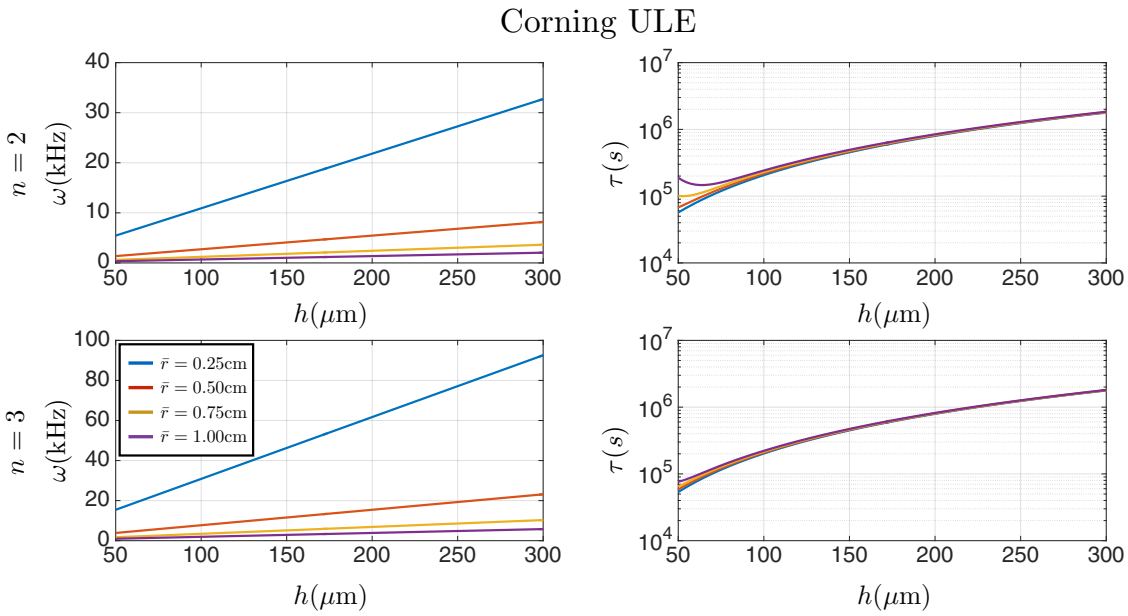

Figure 5.6: The comparison between ω and τ for $n = 2$ and $n = 3$ modes for Corning ULE rings for different geometries.

of fused silica. The analysis is readily applicable to other modes and other materials. When the ring is perturbed by variations in its width or density, for example, other harmonics are produced in the eigenfunctions for the $n = 2$ modes, however, as the perturbations are assumed to be small, the eigenfunctions are dominated by 2θ terms. Nevertheless, the trial function (5.12) includes harmonics 1 through 5, i.e., $N = 5$, for accurate estimates of the modal properties and their trends as a function of the perturbation magnitude. The first type of perturbations that are considered is the point mass perturbation. The second type of perturbations is individual harmonic change to the ring width. In all cases the nominal ring radius and width are $\bar{r} = 0.5\,\text{cm}$ and $h_0 = 100\,\mu\text{m}$, respectively. The $n = 2$ modal frequencies and time constants for a uniform fused silica ring of these dimensions are approximately 2813 Hz and 282 seconds, respectively, and so the perturbed ring parameters deviate from these values.

For the case of having one point mass perturbation, the ring width is assumed to be constant, however, the density varies as a function of θ. The density variation is impulsive and so creates a point mass perturbation at angle θ_0 on the ring. Without loss of generality, θ_0 can be set to 0 for a uniform ring. The perturbing mass magnitude is $\epsilon_\rho M_0$, where $M_0 = 2\pi\rho_0 h_0 \bar{r} L$ is the nominal ring

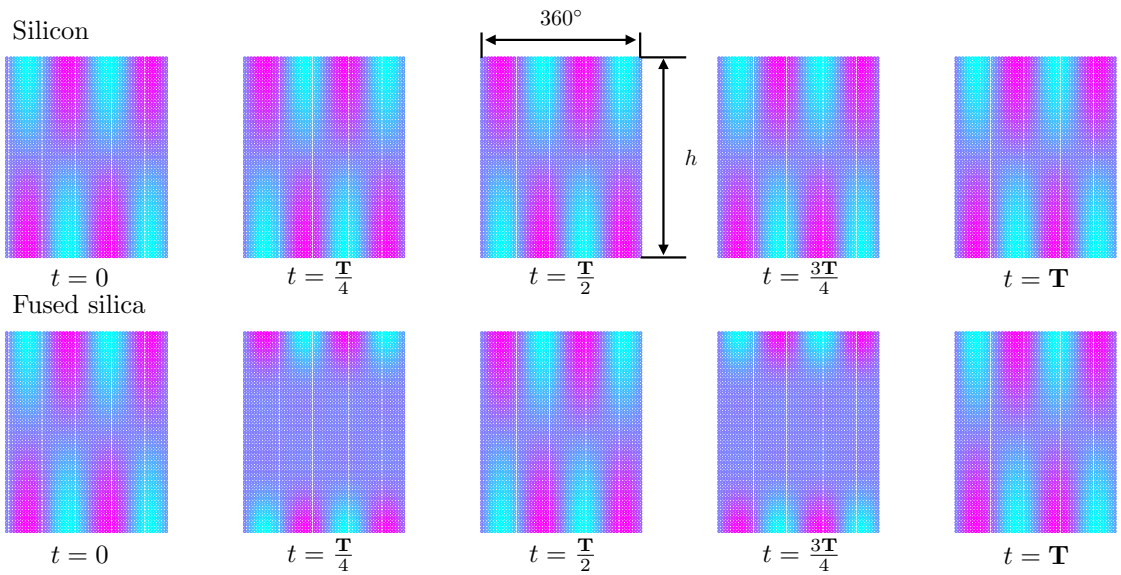

Figure 5.7: The normalized temperature profile over one period for silicon and fused silica for a given ring and same tangential displacement amplitude for one of the $n = 2$ modes.

mass. The ring thickness, L, is $270\,\mu$m. The density is defined to be

$$\rho(\theta) = \rho_0 + 2\pi\epsilon_\rho\rho_0\delta(\theta - \theta_0). \tag{5.23}$$

Figures 5.9 and 5.10 summarize the behavior of the $n = 2$ modal frequencies and the corresponding time constants. These figures also show the results of weakly coupled analysis in which the time constant is determined after computing (5.20).

For the case of having thickness variation, the density is assumed to be constant, ρ_0, but the ring width varies with respect to θ,

$$h(\theta) = h_0 + \epsilon h_0 \cos(s\theta), \tag{5.24}$$

where $s = 1, 2$, reveals the effect of single harmonic perturbations of the width. Fig. 5.11 shows exaggerated 1-θ and 2-θ width perturbations. The perturbed resonant frequencies and time constants for $n = 2$ modes are shown in Figs. 5.12 and 5.13.

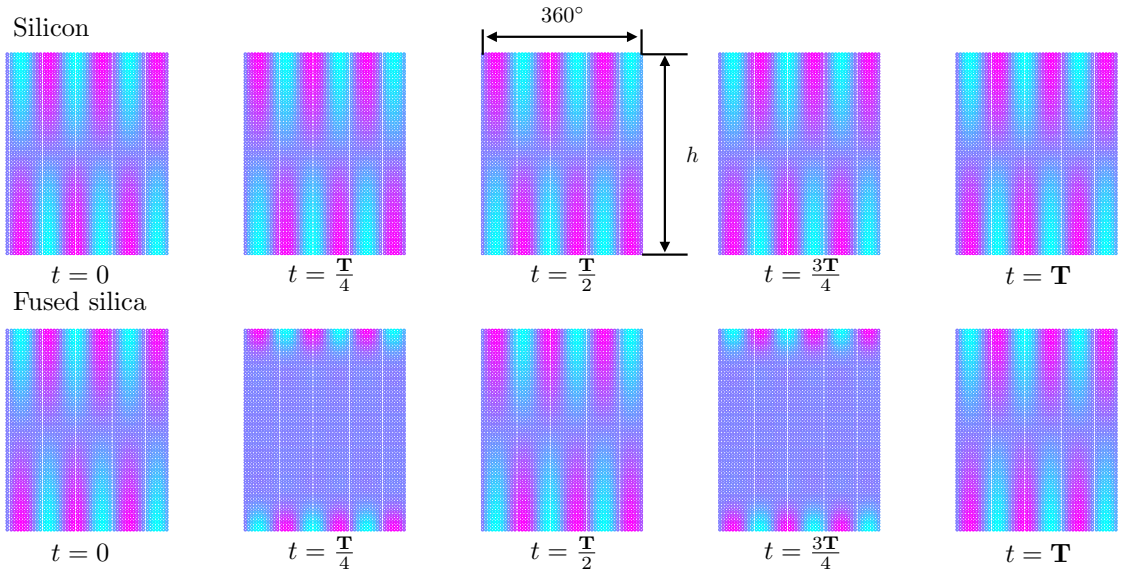

Figure 5.8: The normalized temperature profile over one period for silicon and fused silica for a given ring and same tangential displacement amplitude for one of the $n = 3$ modes.

5.3.3 Fused Silica ring with Multiple Perturbations

This section considers scenarios in which there exist a combination of point mass and thickness perturbations given by

$$\begin{aligned} h(\theta) &= h_0 + \epsilon_2 \cos(2\theta), \\ \rho(\theta) &= \rho_0 + 2\pi\epsilon_\rho \rho_0 \delta(\theta - \pi). \end{aligned} \tag{5.25}$$

In this perturbation scenario the "phase" of the width perturbation relative to the point mass perturbation is important. The point mass location is chosen to be near the anti-node of the higher frequency mode when considering only the 2θ width variation. Fig. 5.11 shows location of the point mass perturbation relative to the 2-θ width perturbation. The higher frequency mode is preferentially "loaded" and its modal frequency is more susceptible to the presence of the perturbing mass than the companion mode. This permits, for a given width perturbation, the calculation of the perturbing mass size to bring the modal frequencies into degeneracy. Thus, as the 2θ variation in width is changed from 0 to 15% of the nominal ring width, the point mass magnitude is calculated to yield equal modal frequencies. The point mass value given by ϵ_ρ is shown as a function of the amplitude of the width perturbation, given by ϵ_2, in Fig. 5.14. The corresponding frequencies and time constants are shown in Figs. 5.15 and 5.16. It is clear from these cases that "tuning" the

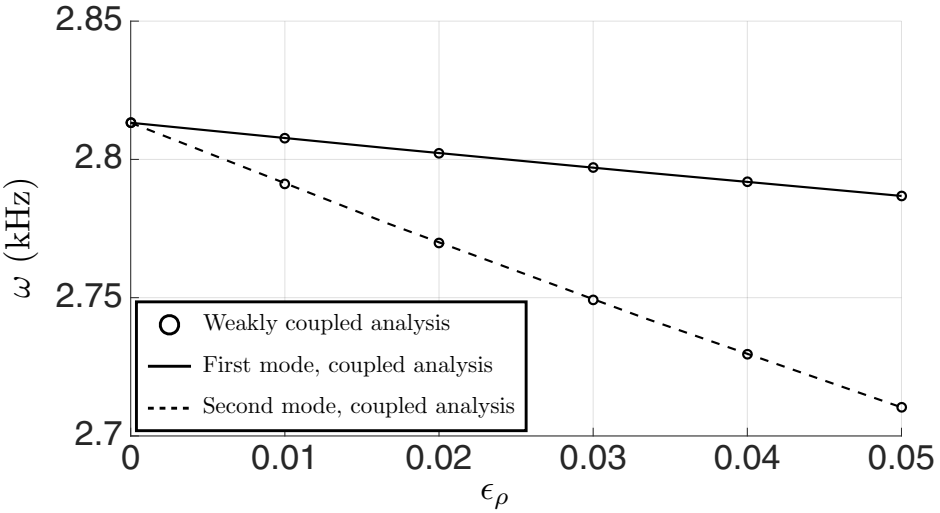

Figure 5.9: The two resonant frequencies of the $n = 2$ modes for single mass perturbation case.

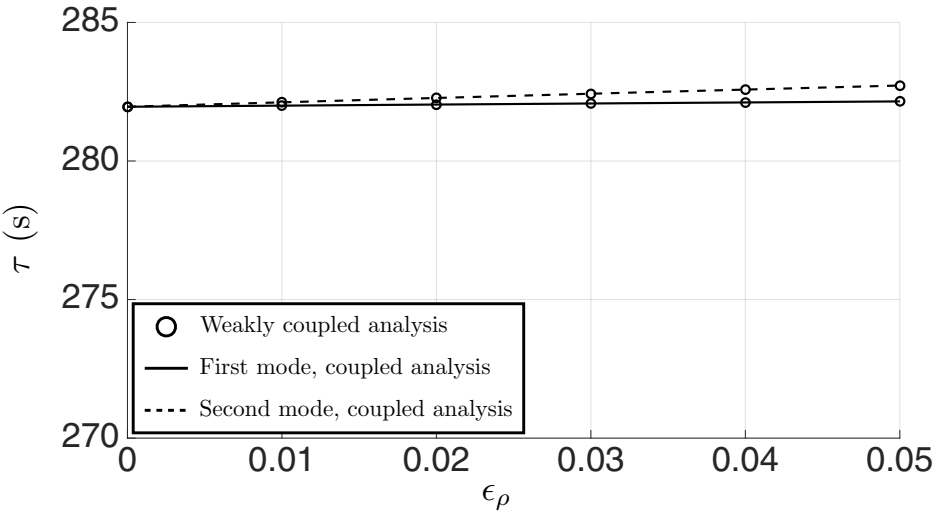

Figure 5.10: The two time constants of the $n = 2$ modes for single mass perturbation case.

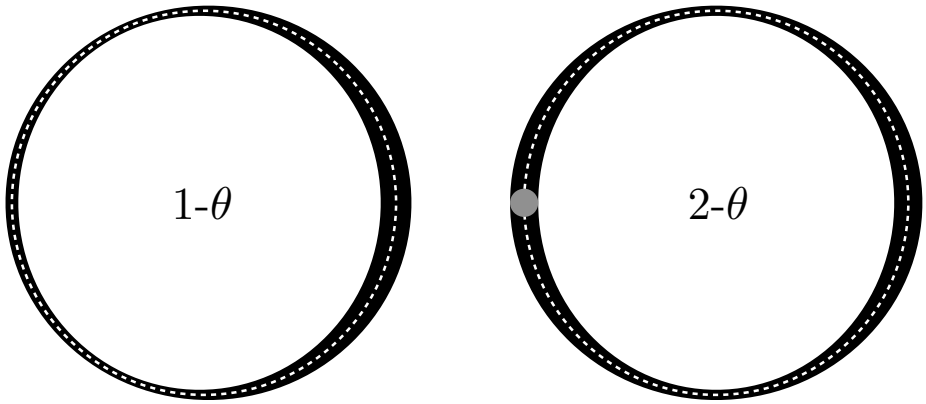

Figure 5.11: (Left) Exaggerated 1-θ ring width perturbation. (Right) Exaggerated 2-θ ring width perturbation. The location of the point-mass perturbation (solid grey disk) relative to the phase of the 2-θ ring width variation is also shown for the multi-perturbation case in Sec. 5.3.3

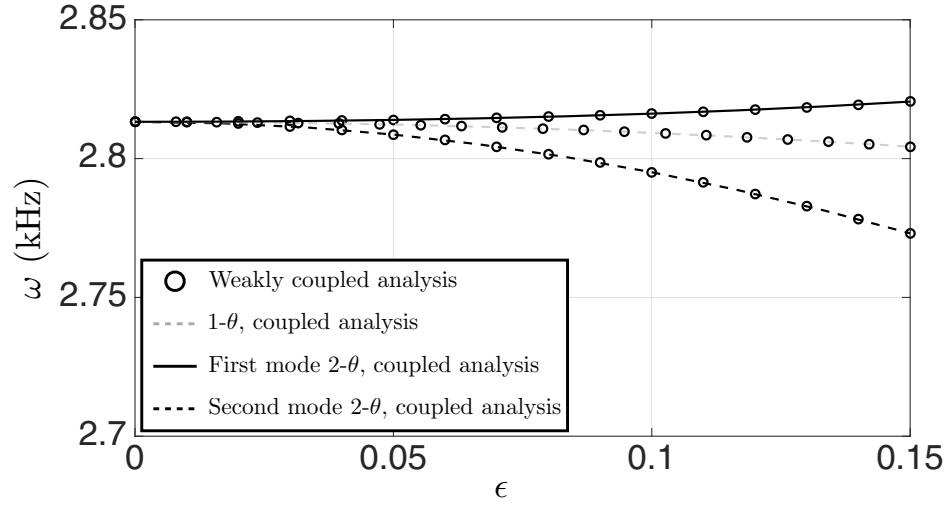

Figure 5.12: The modal frequencies of the $n = 2$ modes for 1-θ and 2-θ width variation. A 1-θ width variation does not detuning of the modal frequencies.

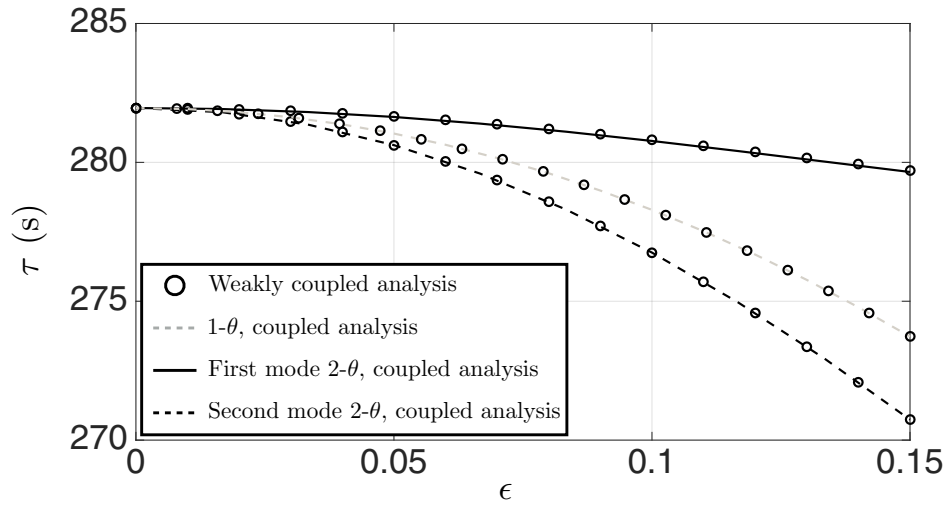

Figure 5.13: The time constants of the $n = 2$ modes for 1-θ and 2-θ width variation. The time constants for the 1-θ case are essentially the same, however, the 2-θ width perturbation does introduce differences in the time constants.

resonant frequencies does not necessarily produce matching time constants.

5.4 Thermoelastic Damping Discussion

The point-mass perturbation analysis reveals that both modal frequencies decrease when the ring is loaded with additional mass, however, the modal time constants are insensitive to this kind of perturbation. Thus, the point-mass perturbations are useful for manipulating the modal frequencies without modification of the modal time constants as far as thermoelastic dissipation is concerned. Point mass perturbations may have a significant impact on anchor loss, though, and so care is required when using point-mass perturbations to modify modal frequencies.

The ring thickness variations have a markedly different impact on the modal properties depending on the harmonic of the variation. The 1-θ variation does not create a split between the modal frequencies or time constants of $n = 2$ modes although both quantities are decreased. Thus, this perturbation is relatively benign from the perspective of TED. However, if one considers its impact on anchor loss, then the 1-θ perturbation may have a significant effect on the time constants. The 2-θ thickness variation, on the other hand, creates a split in both the modal frequencies and time constants. The last perturbation scenario shows that the frequency detuning created by the 2-θ

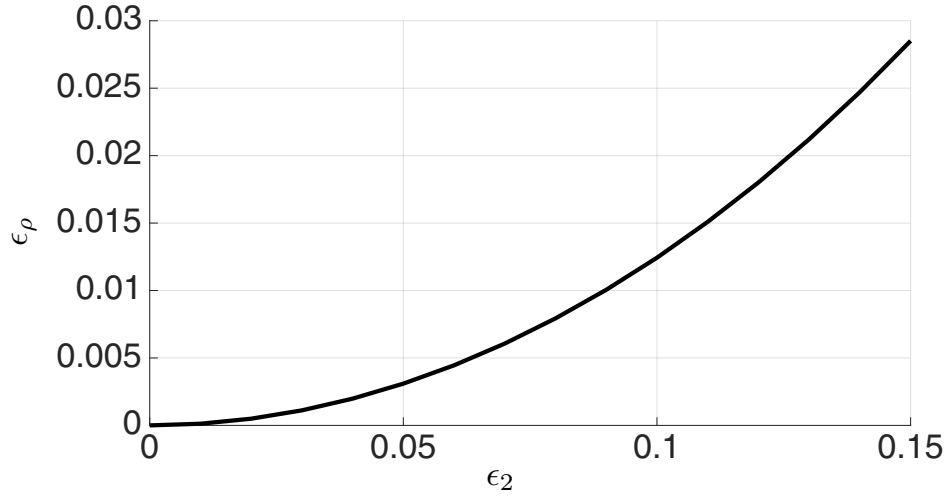

Figure 5.14: The size of the point mass given by ϵ_ρ that is required to eliminate the modal frequency split caused by a 2-θ width variation.

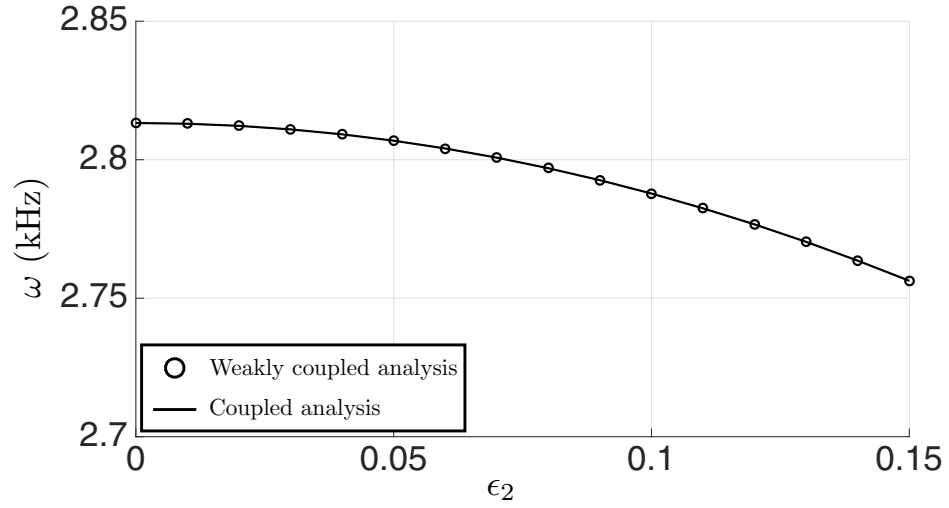

Figure 5.15: Both $n = 2$ modal frequencies are rendered equal for different values of ϵ_2 by appropriate choice of ϵ_ρ.

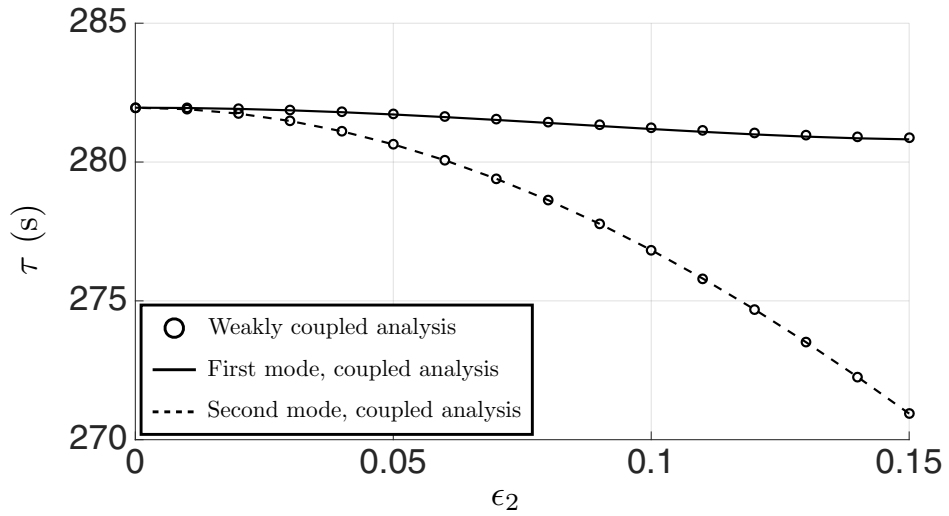

Figure 5.16: The $n = 2$ time constants as a function of ϵ_2. Although the frequencies are equal, the time constants are not.

thickness variation can be "corrected" by point-mass loading, however, the time constant split due to the thickness variation remains largely intact in the "tuned" resonator.

The weakly coupled analysis yields results which are indistinguishable from the coupled analysis and, furthermore, the weakly coupled analysis has the advantage of greater simplicity since the ring equation of motion without thermoelastic effects yields a standard eigenvalue problem in contrast to the *ad hoc* iterative approach that was used to analyze the coupled case. An approximate expression for the dissipated energy (5.20) was derived from making the quantity α/ω explicit. This estimate of $\Delta_{\mathcal{W}}$ is useful because it shows how a small ratio (relative to other materials) of thermal diffusivity to modal frequency essentially scales the energy loss, so a significant factor of TED in fused silica rings is derived from α/ω in addition to widely recognized importance of the thermal expansion coefficient, β.

5.5 Summary for Thermoelastic Damping

The equation of motion for a perturbed ring including thermoelastic effects was derived. A total of ten basis functions were used to approximate solutions using the strong form Galerkin method. The resonant frequencies and time constants were calculated for the $n = 2$ modes under different perturbation scenarios. In one interesting case study, it was shown how a 2-θ ring width pertur-

bation creates not only detuning of the modal frequencies, but also introduced differences in their time constants. In another case study, the modal frequency detuning was eliminated by point-mass loading, however, since point-mass loading has little impact on the time constants, a difference in the time constants remains even for "tuned" modes. Thus, it appears that some degree of time constant mismatch will always exist in so far as thermoelastic dissipation is concerned because the elimination of the differences would require actual modification of the 2-θ harmonic in the resonator width. Measuring these harmonics, much less correcting for them, has not been demonstrated in micro-scale resonators. On the other hand, point-mass loading has been demonstrated to be practical for certain planar axisymmetric resonators.

CHAPTER 6

Concluding Remarks

From the study of ring-type resonators in this thesis, the following remarks can be made as a summary.

- A gyroscope is a sensor that measures the rate of rotation of an object. One common type is a "Coriolis Vibratory Gyroscope" (CVG) which takes advantage of Coriolis coupling in sensing rotation. There are advantages in manufacturing the resonator, the heart of the CVG, as a distributed mass. The challenge of using distributed mass is finding the mode shapes and associated lag factors.

- The greatest sensitivity to angular motion is achieved when the resonant modes have degenerate frequencies since this configuration provides the greatest signal-to-noise ratio with respect to electronics. One way to achieve degeneracy is to design an axisymmetric resonator.

- Ring-type resonators can be manufactured efficiently with the techniques used in micro-electro-mechanical systems (MEMS). Even with the state of the art MEMS technology, small fabrication errors are introduced which break the symmetry of the structure.

- To recover the symmetry of the structure, post-fabrication processing is required. The mass, stiffness or combination of both can be modified to achieve this recovery. Changing the stiffness is not permanent, so adding/removing mass is desirable. Two custom recipes for selectively removing from and adding mass to the resonator are developed.

- The perturbation model is developed for imperfect rings. The results are in excellent agreement with Rayleigh-Ritz and finite element analysis. The analysis is extended to the ring-

type resonator in hand to study the effect of the mass perturbations to compensate for the asymmetries introduced from the manufacturing.

- The refined model is used for tuning multiple modes simultaneously. Having two tuned modes is advantageous for providing two independent measurements from one device. The correlation between the measurements can be used to enhance the quality of the sensor.

- The linear programming and a branch and bound algorithm are implemented to systematically tune both $n = 2$ and $n = 3$ modes. The results are successfully implemented for $n = 2$ modes on seven devices using a custom etching technique which is compatible with other manufacturing steps and can be implemented at the wafer-level. The results for simultaneous tuning are successfully implemented on two devices using a mass addition technique.

- The damping mechanisms are studied for ring-type resonators. The equation of motion with the dominant damping mechanism as thermoelastic damping is derived and solved using strong form Galerkin for imperfect rings. The types of the imperfections considered come from manufacturing imperfections, such as etch non-uniformities, and arise in practice for (point mass) tuning. A practical limitation is demonstrated when mass addition/removal is used for tuning the resonant frequencies as far as the damping asymmetry is concerned. A design guide is developed based on the geometry and material properties. The temperature profile is compared for silicon, a common material used in manufacturing, and fused silica as a low-loss material. It is shown that in addition to the thermal expansion coefficient of the material, the effect of its thermal diffusivity is a key player in the thermoelastic dissipation of a given structure.

REFERENCES

[ASY86] D. Allaei, W. Soedel, and T.Y. Yang. "Natural Frequencies and Modes of Rings that Deviate from Perfect Axisymmetry." *Journal of Sound and Vibration*, **111**(1):9–27, 1986.

[BBC13] J.J. Bernstein, M.G. Bancu, E.H. Cook, M.V. Chaparala, W.A. Teynor, and M.S. Weinberg. "A MEMS Diamond Hemispherical Resonator." *Journal of Micromechanics and Microengineering*, **23**(12):1 – 8, Oct. 2013.

[BBC14] J. Bernstein, M. Bancu, E. Cook, T. Henry, P. Kwok, T. Nyinjee, G. Perlin, W. Teynor, and M. Weinberg. "Diamond Hemispherical Resonator Fabrication by Isotropic Glass Etch." In *Proc. Solid-State Sensors, Actuators and Microsystems Workshop*, pp. 273–276, Hilton Head, SC, June 2014.

[BC07] P. Bisegna and G. Caruso. "Frequency Split and Vibration Localization in Imperfect Rings." *Journal of Sound and Vibration*, **306**(3-5):691–711, 2007.

[BD06] J. A. Bender and M. H. Dickinson. "A Comparison of Visual and Haltere-Mediated Feedback in the Control of Body Saccades in Drosophila Melanogaster." **209**(23):4597–4606, 2006.

[BEF97] J. Borenstein, H. R. Everett, L. Feng, and D. Wehe. "Mobile Robot Positioning-Sensors and Techniques." Technical report, Naval Command Control and Ocean Surveillance Center, 1997.

[BKS17] A. H. Behbahani, D. Kim, P. Stupar, J. DeNatale, and R. T. M'Closkey. "Tailored Etch Profiles for Wafer-Level Frequency Tuning of Axisymmetric Resonators." *Journal of Microelectromechanical Systems*, **26**(2):333–343, April 2017.

[BM16] A. Behbahani and R.T. M'Closkey. "Analysis of the Dynamics of a Perturbed Ring." In *Inertial Sensors and Systems, 2016 IEEE International Symposium on*, pp. 1–4, Laguna Beach, CA, February 2016.

[BM17] A. H. Behbahani and R. T. M'Closkey. "Frequency Analysis of a Uniform Ring Perturbed by Point Masses and Springs." *Journal of Sound and Vibration*, **397**:204 – 221, 2017.

[BME18] A. Baghdadi, F. M. Megahed, E. T. Esfahani, and L. A. Cavuoto. "A Machine Learning Approach to Detect Changes in Gait Parameters Following a Fatiguing Occupational Task." *Ergonomics*, **0**(0):1–14, 2018.

[Bry90] G.H. Bryan. "On the Beats in the Vibrations of a Revolving Cylinder or Bell." In *Proc. Cambridge Philosophical Society*, volume VII, pp. 101–111, Nov. 1890.

[CGL14] A.D. Challoner, H.H. Ge, and J.Y. Liu. "Boeing Disc Resonator Gyroscope." In *Position, Location and Navigation Symposium-PLANS 2014, 2014 IEEE/ION*, pp. 504–514, Monterey, CA, May 2014.

[CGN12] J. Cho, J.A Gregory, and K. Najafi. "High-Q, 3kHz Single-Crystal-Silicon Cylindrical Rate-Integrating Gyro (CING)." In *Proc. IEEE MEMS*, pp. 172–175, Paris, Jan 2012.

[CP73] T. Charnley and R. Perrin. "Perturbation Studies with a Thin Circular Ring." *Acustica*, **28**(3):140–146, 1973.

[CWY14] Jae Yoong Cho, Jong-Kwan Woo, Jialiang Yan, R.L. Peterson, and K. Najafi. "Fused-Silica Micro Birdbath Resonator Gyroscope (μ-BRG)." *Journal of Microelectromechanical Systems*, **23**(1):66 – 77, Feb 2014.

[DCK06] A. Duwel, R. N. Candler, T. W. Kenny, and M. Varghese. "Engineering MEMS Resonators with Low Thermoelastic Damping." *Journal of Microelectromechanical Systems*, **15**(6):1437–1445, Dec 2006.

[DSC17] A. Darvishian, B. Shiari, J. Y. Cho, T. Nagourney, and K. Najafi. "Anchor Loss in Hemispherical Shell Resonators." *Journal of Microelectromechanical Systems*, **26**(1):51–66, Feb 2017.

[Fox90] C. H. J. Fox. "A Simple Theory for the Analysis and Correction of Frequency Splitting in Slightly Imperfect Rings." *Journal of Sound and Vibration*, **142**(2):227–243, 1990.

[GHB03] B.J. Gallacher, J. Hedley, J.S. Burdess, A.J. Harris, and M.E. McNie. "Multimodal Tuning of a Vibrating Ring Using Laser Ablation." *Proc. Inst. Mech. Eng., Part C*, **217**(5):557–576, 2003.

[GHB05] B.J. Gallacher, J. Hedley, J.S. Burdess, AJ. Harris, A Rickard, and D.O. King. "Electrostatic Correction of Structural Imperfections Present in a Microring Gyroscope." *Journal of Microelectromechanical Systems*, **14**:221–234, April 2005.

[GKM15] H. Ge, D. Kim, and R.T. M'Closkey. "Simultaneous Exploitation of the Fundamental and Higher order Wineglass Modes in a Vibratory Gyro." In *Inertial Sensors and Systems, 2015 IEEE International Symposium on*, pp. 1–4, Hapuna Beach, HI, March 2015.

[GM17] H. Ge and R. M'Closkey. "Simultaneous Angular Rate Estimates Extracted From a Single Axisymmetric Resonator." *IEEE Sensors Journal*, **17**(22):7460–7469, Nov 2017.

[HJC14] R.D. Horning, B.R. Johnson, R. Compton, and E. Cabuz. "Hemitoroidal Resonator Gyroscope.", 2014.

[HMP16] S. T. Hossain, S. McWilliam, and A. A. Popov. "An Investigation on Thermoelastic Damping of High-Q Ring Resonators." *International Journal of Mechanical Sciences*, **106**:209 – 219, 2016.

[IEE04] "IEEE Standard Specification Format Guide and Test Procedure for Coriolis Vibratory Gyros." *IEEE Std 1431-2004*, pp. 1–78, Dec 2004.

[IOP17] O. J. Isaac-Lowry, S. Okamoto, S. A. Pedram, R. Woo, and P. Berkelman. "Compact Teleoperated Laparoendoscopic Single-Site Robotic Surgical System: Kinematics, Control, and Operation." *The International Journal of Medical Robotics and Computer Assisted Surgery*, **13**(4):e1811–n/a, 2017. e1811 RCS-16-0121.R2.

[KBK15] M. Kanik, P. Bordeenithikasem, D. Kim, N. Selden, A. Desai, R. M'Closkey, and J. Schroers. "Metallic Glass Hemispherical Shell Resonators." *Journal of Microelectromechanical Systems*, **24**(1):19–28, Jan 2015.

[KBS15] D. Kim, A. Behbahani, P. Stupar, J. DeNatale, and R.T. M'Closkey. "Wafer-Scale Etch Process for Precision Frequency Tuning of MEMS Gyros." In *Inertial Sensors and Systems, 2015 IEEE International Symposium on*, pp. 1–2, Hapuna Beach, HI, March 2015.

[KK16] J. H. Kim and J. H. Kim. "Thermoelastic Damping Effect of the Micro-Ring Resonator with Irregular Mass and Stiffness." *Journal of Sound and Vibration*, **369**:168 – 177, 2016.

[KM06] D.J. Kim and R.T. M'Closkey. "A Systematic Method for Tuning the Dynamics of Electrostatically Actuated Vibratory Gyros." *IEEE Transactions on Control Systems Technology*, **14**:69–81, Jan. 2006.

[KM12] D. J. Kim and R.T. M'Closkey. "Dissecting Tuned MEMS Vibratory Gyros." In J. J. Gorman and B. Shapiro, editors, *Feedback Control of MEMS to Atoms*. Springer, 2012.

[KM13] D. Kim and R.T. M'Closkey. "Spectral Analysis of Vibratory Gyro Noise." *IEEE Sensors Journal*, **13**:4361–4374, Nov. 2013.

[Lan49] H. L. Langhaar. "A Strain-Energy Expression for Thin Elastic Shells." *Journal of Applied Mechanics*, pp. 183–189, Jun 1949.

[Law98] A. Lawrence. "Natural Frequencies and Modes of Rings that Depart from Perfect Axisymmetry." 1998.

[Lel03] R.P. Leland. "Adaptive Mode Tuning for Vibrational Gyroscopes." *IEEE Transactions on Control Systems Technology*, **11**(2):242–247, mar 2003.

[Lov92] A E. H. Love. *A Treatise on the Mathematical Theory of Elasticity*. Cambridge University press, 1892.

[LR00] R. Lifshitz and M. L. Roukes. "Thermoelastic Damping in Micro- and Nanomechanical Systems." *Physical Review B*, **61**:5600–5609, Feb 2000.

[Mei67] L. Meirovitch. *Analytical Methods in Vibration: Macmillan Series in Advanced Mathematics and Theoretical Physics*. Macmillan, 1967.

[NAS13] S. Nitzan, C.H. Ahn, T.-H. Su, M. Li, E.J. Ng, S. Wang, Z.M. Yang, G. O'Brien, B.E. Boser, T.W. Kenny, and D.A Horsley. "Epitaxially-Encapsulated Polysilicon Disk Resonator Gyroscope." In *Proc. IEEE MEMS*, pp. 625–628, Taipei, Jan. 2013.

[PZT11] I.P. Prikhodko, S.A. Zotov, A.A. Trusov, and A.M. Shkel. "Microscale Glass-Blown Three-Dimensional Spherical Shell Resonators." *Journal of Microelectromechanical Systems*, **20**(3):691 – 701, June 2011.

[Rao07] Singiresu S. Rao. *Vibration of Continuous Systems*. John Wiley & Sons, Hoboken, NJ, 2007.

[RMF01] A.K. Rourke, S. McWilliam, and C.H.J. Fox. "Multi-Mode Trimming of Imperfect Rings." *Journal of Sound and Vibration*, **248**(4):695–724, 2001.

[SAT14] D. Senkal, M.J. Ahamed, A.A. Trusov, and A.M. Shkel. "Achieving Sub-Hz Frequency Symmetry in Micro-Glassblown Wineglass Resonators." *Journal of Microelectromechanical Systems*, **23**:30–38, Feb 2014.

[Sch10] D. Schwartz. *Mass Perturbation Techniques for Tuning and Decoupling of a Disk Resonator Gyroscope*. PhD thesis, University of California, Los Angeles, 2010.

[SKS15] D.M. Schwartz, D. Kim, P. Stupar, J. DeNatale, and R.T. M'Closkey. "Modal Parameter Tuning of an Axisymmetric Resonator via Mass Perturbation." *Journal of Microelectromechanical Systems*, **24**(3):545–555, June 2015.

[SMG14] P. Shao, C.L. Mayberry, X. Gao, V. Tavassoli, and F. Ayazi. "A Polysilicon Microhemispherical Resonating Gyroscope." *Journal of Microelectromechanical Systems*, **23**:762–764, Aug 2014.

[TPZ11] A. A. Trusov, I. P. Prikhodko, S. A. Zotov, and A. M. Shkel. "Low-Dissipation Silicon Tuning Fork Gyroscopes for Rate and Whole Angle Measurements." *IEEE Sensors Journal*, **11**(11):2763–2770, Nov 2011.

[TSH14] P. Taheri-Tehrani, T.-H. Su, A. Heidari, G. Jaramillo, C. Yang, S. Akhbari, H. Najar, S. Nitzan, D. Saito, L. Lin, and D.A. Horsley. "Micro-Scale Diamond Hemispherical Resonator Gyroscope." In *Proc. Solid-State Sensors, Actuators and Microsystems Workshop*, pp. 289 – 292, Hilton Head, SC, June 2014.

[WFM06] S.J. Wong, C.H.J. Fox, and S. McWilliam. "Thermoelastic Damping of the In-Plane Vibration of Thin Silicon Rings." *Journal of Sound and Vibration*, **293**(12):266 – 285, 2006.

[Wol16] Wolfram Research, Inc. *Mathematica, Version 10.4*. Wolfram Research, Inc., Champaign, Illinois, 2016.

[YFZ17] X. Yu, Y. Fu, and Y. Zhang. "Aircraft Fault Accommodation with Consideration of Actuator Control Authority and Gyro Availability." *IEEE Transactions on Control Systems Technology*, 2017.

[YLY02] Y.J. Yoon, J.M. Lee, S.W. Yoo, and H.G. Choi. "A New Method for In-Plane Vibration Analysis of Circular Rings with Widely Distributed Deviation." *Journal of Sound and Vibration*, **254**(4):787–800, 2002.

[Zen37] C. Zener. "Internal Friction in Solids I. Theory of Internal Friction in Reeds." *Physical Review*, **52**:230–235, Aug 1937.

[ZSP14] S. A. Zotov, B. R. Simon, I. P. Prikhodko, A. A. Trusov, and A. M. Shkel. "Quality Factor Maximization Through Dynamic Balancing of Tuning Fork Resonator." *IEEE Sensors Journal*, **14**(8):2706–2714, Aug 2014.

[ZTS12] S.A. Zotov, A.A. Trusov, and A.M. Shkel. "Three-Dimensional Spherical Shell Resonator Gyroscope Fabricated Using Wafer-Scale Glassblowing." *Journal of Microelectromechanical Systems*, **21**(3):509 – 510, June 2012.

[ZXM17] S. Zheng, J. Xie, C. Ma, H. Liao, and C. Chen. "Improving Dynamic Response of AMB Systems in Control Moment Gyros Based on a Modified Integral Feedforward Method." *IEEE/ASME Transactions on Mechatronics*, **22**(5):2111–2120, 2017.